KINGSTON UNIVERSITY LONDON

On-line Measurement of Broken Rice Percentage from Image Analysis of Length and Shape

by

Charles D. Mallah

A thesis submitted in partial fulfillment for the degree of Doctor of Philosophy

in the

Faculty of Science, Engineering and Computing
School of Computing and Information Systems

May 2013

Declaration of Authorship

This thesis, titled: *On-line Measurement of Broken Rice Percentage from Image Analysis of Length and Shape*, is one output from the On-line Sensor research programme part-sponsored by Buhler Sortex Ltd.; starting from the 2nd October 2009. It remains **company confidential** for five years starting from publication.

I, Charles D. Mallah, declare that this thesis and the work presented in it are my own. I confirm the following: That these doctoral studies were conducted under the supervision of Gabriel Hamid and James Orwell. That the work submitted in this thesis is a result of original research carried out by myself, except where acknowledged, while enrolled as a PhD student in the Department of Science, Engineering and Computing at Kingston University, London. Finally, that this thesis has not been submitted for any other degree or award.

Signed: _____

Date: _____

KINGSTON UNIVERSITY LONDON

Abstract

Faculty of Science, Engineering and Computing
School of Computing and Information Systems

Doctor of Philosophy

by Charles D. Mallah

This thesis investigates the design of an on-line signal processing system to measure the percentage of a batch of rice grains that are broken. The objectives of the investigation were: to provide information contributing to the hardware design; to devise one or more approaches for each processing stage; to evaluate and validate these approaches, where necessary recommending the most suitable; and to verify the overall accuracy and robustness of the proposed system. The fundamental processing stages were proposed and, for each stage, the possible approaches were investigated. A configurable experimental apparatus was assembled to enable an iterative development of algorithm and hardware design: an important aspect of the methodology was to locate an acceptable operating point in the space of possible configurations. The processing stages comprised geometric camera calibration; segmentation of the grains from the background; detection of single grains; measurement of grain length and characterisation of shape; classification; and finally corrections for bias and conversion to the required unit of measurement, percentage by mass. For each stage, an analysis of error and uncertainty was undertaken. This provides an indication of the expected accuracy and bias of the proposed system. There were several elements of novel work completed in the course of this investigation. Some novel components were introduced into the calibration procedure; a tiled approach was used in the segmentation stage, to accommodate diverse illumination across the field of view. For the shape analysis, an innovative method is employed to estimate the posterior class density, and the analysis of expected bias includes a treatment of finite aperture but also how the probability of observing a single grain is conditional upon its length. The results obtained from the experimental apparatus and prototype device indicate that it is feasible to obtain on-line measurements that are well within the required tolerance. This would enable such a device to be deployed in a number of important industrial applications.

Acknowledgements

I would like to thank Gabriel Hamid for his vision, insight and motivation during my PhD studies.

I would also like to thank Professor Alistair Forbes, of the National Physical Laboratory, London; for his continuous expertise and support.

My gratitude is extended to many working people from the industrial sponsor. In particular, many thanks to David Gherardi, Gopal Trikkur, and Bismillah Kani for their hard work, assistance and diligence when working with me on this project.

Many thanks to James Cope, fellow PhD student at Kingston University, for allowing us to work with the leaves data-set captured in partnership with the Royal Botanical Gardens, Kew, London.

Contents

List of Figures

List of Tables

Abbreviations

Acc	The overall classification accuracy, from the confusion matrix.
AR	The area descriptor of a grain kernel.
AS	The asymmetry coefficient descriptor of a grain kernel.
BoundingBox	The bounding box length definition.
BDM	Brown's Distortion Model calibration method.
EdgeCanny	The Canny edge detection method.
CCDC	The centroid contour distance curve shape descriptor.
CH	The curvature histogram shape descriptor.
CO	The compactness descriptor of a grain kernel.
ConfMat	The confusion matrix feature of the novel K-NN estimator.
Distance	The distance feature of the novel K-NN estimator.
EdgeLoG	The Laplacian of Gaussian edge detector method.
GlobalHist	The optimised global histogram threshold method.
HybridHist	The novel GlobalHist method performed on local windows.
K-NN	The K-Nearest Neighbour classifier.
LocalVar	Local image segmentation method.
LocalVarRatio	Local segmentation based on the LocalVar method.
LongestChord	The longest chord length definition.
LongestCentroidChord	The longest centroid chord length definition.
LK	The length of a grain kernel.
LKG	The groove length descriptor of a grain kernel.
LSE	Lattice of Scale Estimates calibration method.
LP	The mean log posterior of a vector of density estimates.
LWC	The length-width-corner algorithm for detecting single grains.
Mar	A fine scale margin descriptor.

ME	Misclassification Error, an evaluation metric for image segmentation.
MHD	Modified Hausdorff Distance, an evaluation metric for image segmentation.
MinErrorThresh	The minimum error thresholding method.
MinimumBoundingBox	The minimum bounding box length definition.
ML	The Miles-Lantuejoul measurement.
NaiveThresh	Naive global thresholding method for image segmentation.
NN	The Nearest Neighbour classifier.
ParallelPrincipalAxis	The parallel principal axis length definition.
PE	The perimeter descriptor of a grain kernel.
PL, PW	The petal length, and width of a flower.
PRM	Parametric Regression Model calibration method.
PrincipalAxis	The principal axis length definition.
Pre	The mean classification precision.
Prop	The proportional K-NN density estimator.
Rank	The rank feature of the novel K-NN estimator.
Rec	The mean classification recall.
RotatingCalipers	The rotating callipers length definition.
SEME	Simple Edge Mismatch Error, an evaluation metric.
Sha	A shape descriptor.
SL, SW	The sepal length, and width of a flower.
SLSE	Smoothed Lattice of Scale Estimates calibration method.
SmoothHybridHist	The novel HybridHist method with a smoothing filter.
Tex	A texture descriptor.
TP, FP	True positive, and false positive.
TN, FN	True negative, and false negative.
VEL	The velocity shape descriptor.
VotingSplit	The voting split feature of the novel K-NN estimator.
WK	The width of a grain kernel.
Wprop	The weighted proportional K-NN density estimator.

Symbols

Δ	The difference between two points.
$\Lambda(\mathbf{u}, \mathbf{v})$	The axial distance between all $e(\mathbf{u}, \mathbf{v})$ points in the rotated space by angle ϕ.
Ω	A proportion of probability mass, assigned to prevent model failure.
ε_σ, ε_μ	The standard deviation error, and the mean error from the ground truth $\mu - G$.
η	The minimum threshold parameter for the peak detection algorithm.
θ, ψ	The internal angles of a grain, for modelling quantisation error.
$\mu(\cdot)$	The arithmetic mean of a data sample.
$\sigma(\cdot)$	The standard deviation of a data sample.
ϑ, φ	A radial and tangential distortion coefficient.
τ	The threshold value of a length distribution for estimating broken rice percentage.
ψ	A scale factor and Euclidean distance between two points.
ω	A weighting multiplier.
$\mathcal{A}$	The intrinsic parameters of a camera.
$\mathcal{B}(\mathbf{u}, \mathbf{v})$	The binary image.
$\mathcal{C}$	The set of control points of the calibration pattern in image space.
$\mathcal{G}(\mathbf{u}, \mathbf{v})$	The greyscale image.
A, M	The area, and mass of an object.
B	The broken percentage of rice.
C	The number of class labels within a problem domain.
$F_\mathbf{u}$, $F_\mathbf{v}$	The focal lengths of the camera, in pixels.
G	A ground truth measurement.
$G_\mathcal{B}(\mathbf{u}, \mathbf{v})$	The ground-truth binary image, for evaluation of $\mathcal{B}(\mathbf{u}, \mathbf{v})$.

$\mathbf{I}(\cdot)$	An identity operator to obtain a test vector's label.
K	The parameter of the number of neighbours in the K-NN classifier.
$\hat{L}(\cdot)$	A likelihood.
$O_{\mathbf{u}}$, $O_{\mathbf{v}}$	The principal point in the image.
$P(\mathbf{u}, \mathbf{v})$	The pixels of an object in the image.
$\mathcal{P}(\cdot)$	A prior probability.
$[\mathcal{R}\,\mathcal{T}]$	The extrinsic camera parameters, consisting of a rotation and translation matrix.
$\mathcal{Y}$, $\mathcal{X}$	The training and test vector sets, respectively.
$\mathbf{X}$, $\mathbf{Y}$, $\mathbf{Z}$	The horizontal, vertical and depth coordinates of a point in the world.
a, b, r	The coefficients for conversion from area to mass.
c, $\bar{c}$	The definition that a grain of rice is completely within view, and partially occluded.
d	The Euclidean distance between two points.
$e(\mathbf{u}, \mathbf{v})$	The edge perimeter pixels of an object in the image.
n_{Row}, n_{Col}	Number of rows and columns of the calibration pattern.
l	The calibrated length between two points in the world (mm).
$\hat{l}$	The length between two points in the image (pixels).
$\hat{p}(\cdot)$, $p^*(\cdot)$	A density estimator, and the Bayes estimate.
$\hat{\mathbf{p}}(\cdot)$	A combined density estimate, of up to S estimates.
t	The global threshold value for image segmentation.
s, $\bar{s}$	The definition that a grain of rice is single, and touching.
$\mathbf{u}$, $\mathbf{v}$	The horizontal and vertical coordinates of a point on the image.
v	The definition that a grain is visible to the system, *i.e.* both s and $\bar{s}$.
w	The window size of a kernel or function.
$\lvert x - y \rvert$	The cardinality between two points, x and y.
$\lvert\lvert x - y \rvert\rvert$	The Euclidean distance operator between two points, x and y.

To my father.

Chapter 1

Introduction

There are a number of scientific and industrial applications that require an accurate measurement that is based on the shape of organic matter. In the industrial scenario, there is the need for quality control of rice grains by producers. The uniformity of rice kernel dimensions is important to a rice producer, as most post-harvest processes are sensitive to these dimensions [1]. However, defining rice grain quality with accuracy is a difficult problem. For each of the grower to the miller to the consumer, there may be a different set of characteristics, with varying levels of emphasis, that define the rice quality [2]. For the miller, the quality of the rice is based on the total recovery of head rice, *i.e.* unbroken whole grains, in proportion to the rough rice from the field. However, in the case of white rice, the miller attempts to whiten the rice to the maximum degree available while still remaining unbroken.

The rice milling process [3, 4] consists of a series of the following steps: cleaning of the rough rice from leaves, stems and foreign matter; shelling or dehulling; milling and polishing of the remaining brown rice; finally, separation of head rice from broken kernels. Cracks and fissures can be caused during these processes by factors such as environmental humidity and temperature, kernel moisture content, and stresses during milling [5]. These factors can eventually lead to the undesired effect of breakage. Accurate measurements of the levels of broken rice made before and after any rice milling process in the mill is extremely useful in identifying the cause issues of rice breakage; *i.e.* robust measurements made before and after a process could potentially allow a feedback-loop to correct any ill-performing component of the rice processing line, and thus reduce breakage on-the-fly.

Additionally, from a chemical level, broken and whole rice kernels have similar starch yields and protein contents; however, broken kernels have been reported to have significantly greater surface lipid content and rate of lipid hydrolysis than head rice [6, 7],

i.e. the chemical bonds breakdown at a greater rate. This results in increased oxidisation, which forms off-flavors (bad taste) and an increased yellow hue of broken rice kernels. Additionally, when cooked, the rice consistency is affected: becoming more mushy. These factors significantly effect the quality levels of the rice, and are highly undesirable due to wastage and loss of economic value. Broken rice is valued at roughly 50 to 60% that of head rice [8], *i.e.* a reduction in the head rice recovery can result in severe economic consequences to rice producers [7, 9].

In addition to the economic incentives of such a measurement system, there is potential to influence to the world food sustainability issue; where food security is an urgent and global problem [10–12]. The Royal Society expect that the situation is to worsen given the trending levels of growth over the past fifty years. There has been increasing growth in agricultural production, however at the cost of being unsustainable with respects to the environment. The International Rice Research Institute estimate that approximately 20% of food calorie intake in the world is supplied by rice, and more than half of the people in the world depend heavily on rice [13, 14]. However, an additional 8 to 10 million tons of rice needs to be produced every year to keep rice prices stable and affordable. Professor Sir David Baulcombe, chair of the Royal Society, emphasises this point by stating: "*To meet a demand for 50 per cent more food by 2050, we shall need a whole range of science-based approaches, alongside social science and economic innovations*" [15].

The main objective of this thesis is the design, implementation, and accuracy evaluation of an on-line system for the measurement of broken rice grains, *i.e.* a temporary storage and retrieval of the sensor data in order to produce the measurement. This thesis was partially funded by Buhler Sortex Ltd, London, UK; who manufactures and sells optical sorting machines for the bulk food industry. As such, expertise and assistance was given in building the measurement prototypes, in addition to some of the final experimental results of the complete system. The remainder of this chapter is organised as the following: section 1.1 discusses the principal objectives of the research; section 1.2 lists the key contributions; section 3.0.1 contains the outline of the thesis; and finally the chapter is concluded with a summary.

1.1 Principal Objectives

One of the main criteria for determining if a rice is broken is its length. However, this is hard to consistently measure accurately in the field as it is both time consuming and prone to error from manual measurement [3, 4]. A standard definition of a broken grain is a milled rice grain with a length of less than three quarters but more than one

quarter of the average length of the whole kernel [16–18]. The state-of-the-art system in rice mills around the world consists of hand-made measurements by counting or using laboratory equipment (off-line).

An example of this equipment consists of a metal or rubber plate configured with a series of circular wells [19]. Cleaned rice is manually placed (or shaken) on to the plate. Broken rice kernels fall in to the sharp edged wells, leaving unbroken grains loose on the surface of the plate. The percentage of broken rice is manually calculated as a 'by-mass' measurement given as the ratio of the weight of the broken rice and the total weight of broken and head rice. The following sub section enumerates the main requirements for an on-line sensor for the measurement of broken rice, and section 1.1.2 discusses how the problem was generally approached.

1.1.1 Sensor Requirements

With the industrial sponsor, Buhler Sortex Ltd, a set of targets for the measurement sensor were originally outlined. The expectation is that these are the minimum requirements in order to produce a viable on-line sensor. These are the following:

1. On-Line broken rice measurement of a sparse feed of long white blemish free rice, in motion at roughly 1 metre per second.
2. A target accuracy of 0.5% of this measurement, however this depends on the rice population. A more tangible target is an error of length measurement of 0.1 millimetres (for both).
3. The implemented algorithms need to be suitable for realisation in an on-line system for measuring roughly 10,000 grains in less than 10 minutes. It is planned that the proposed system will run on a CPU-architecture, rather than specialised digital signal processor or field-programmable gate array based hardware system.
4. That the system only requires a one-off calibration routine, before use in the field. However, the ability to be recalibrated in the field if there is any need to make a change to the mechanical or optical component of the sensor.

A set of assumptions of the proposed system are the following:

1. The imaging device consists of a monochromatic area camera, with a short exposure time of the charge-coupled device, and high spatial resolution.
2. The illumination set-up consists only of foreground illumination using a dark field stroboscopic source.

3. The rice gains are viewed by the imaging device sliding down a glass chute, with a sparse feed level, *i.e.* not many grains are touching together as they flow.

4. The imaging device views the product from underneath the glass chute, so as not to require any cleaning.

1.1.2 Approach to the Problem

The study begins with the measurement of the length of rice grains in stasis. This allows the construction and analysis of a machine to measure rice on a flat glass plane. This measurement system works exclusively on the assumption that rice grains are placed in the viewing area without touching one another. Then, the research is extended by migrating the system to work with rice-in-motion prototype, and consequently addresses the issues associated with this, and bias from touching rice grains and measurement aperture edge effects. The rice grains free-flow down a glass chute, with a sparse feed, *i.e.* a low level of touching grains (between 10 and 20%). The estimation of the percentage broken rice grains is applied.

For both prototypes and related bodies of work, the rice length is used as the classification criterion for a broken grain, by the industry standard definition that a broken grain is less than three quarters of the average head rice grain. Therefore, in the final body of work in this study, shape information is incorporated to assist with the classification process. A K-Nearest Neighbours posterior class density model framework is built to allow the union of these separate features in a robust and straightforward approach. Both the state-of-the-art and a novel approach are included in this part of the study. Given the necessity for an unbiased estimate of the proportion of broken grains, it is important to demonstrate the accuracy of such methods on data-sets with more than two classes. In particular, a challenging data-set consisting of multi-class problem for leaf species identification using various modalities such as shape, texture and fine scale edge features.

From the literature identified in chapter 2, a set of hardware plans were developed, and have directed the project. Chapter 3 begins with a detailed description of the sensor hardware that has been used in the development and testing of the software algorithm for the automatic measurement sensor of broken rice.

It is essential that the proposed computer vision is real-time, to facilitate useful measurements in the field. Real-time in this thesis refers to reporting the aggregate measurement of a sample of 10,0000 rice grains with a maximum time delay of 10 minutes (starting from the first grain). The experiments conducted during this research survey were performed on a workstation using the Microsoft Windows XP operating system with a

3.2 GHz processor and 3 GB of RAM; the algorithm was implemented in the Matlab programming environment.

The Matlab programming environment was chosen due to the speed of rapid prototyping and personal level of expertise. While it is commonly accepted that Matlab implementations typically run quite slowly compared to other programming languages, there are special techniques that can be used to speed up the implemented code; such as memory pre-allocation, and avoidance of for-loops with vectorised code. I implemented all experimental code and algorithms from the literature as MATLAB functions. A prototype user interface to the general measurement algorithm was also development with the built in MATLAB interface tool GUIDE. Part of each component of the algorithm was tested and timed, to keep track of computational bottlenecks; throughout the experiments in this thesis, some of the results of these timing exercises are presented to the reader.

It would normally be expected that the algorithms would be more efficient and run real-time when implemented in C/C++. However, this was not required during the scope of this thesis. The algorithm, operating on the aforementioned hardware, measures approximately 25,000 single rice grains within 5 minutes. An example of the selection and measurement process of the system is demonstrated in figure 1.1

1.2 Key Contributions

The study advances the state-of-the-art in two respects: by reducing the bias in measurements made for broken rice percentage; and by performing the measurement on-line. The key contributions are the following:

1. A robust, accurate, automated measurement of the percentage of broken rice grains provided from a self-contained apparatus with a maximum measurement time of 10 minutes for 10,000 grains of rice.

2. A fast and accurate correction procedure for the removal of lens distortion and real world unit conversion of small objects.

3. A tiled approach for image segmentation, to improve the stability of the rice grain contour that is extracted from the monochromatic area camera image.

4. A corrective approach for the bias errors caused by finite aperture size and the length of touching objects within the viewing plane; derived from Bayes Theorem, using the relevant conditional probabilities of the system seeing a single grain depending on its length.

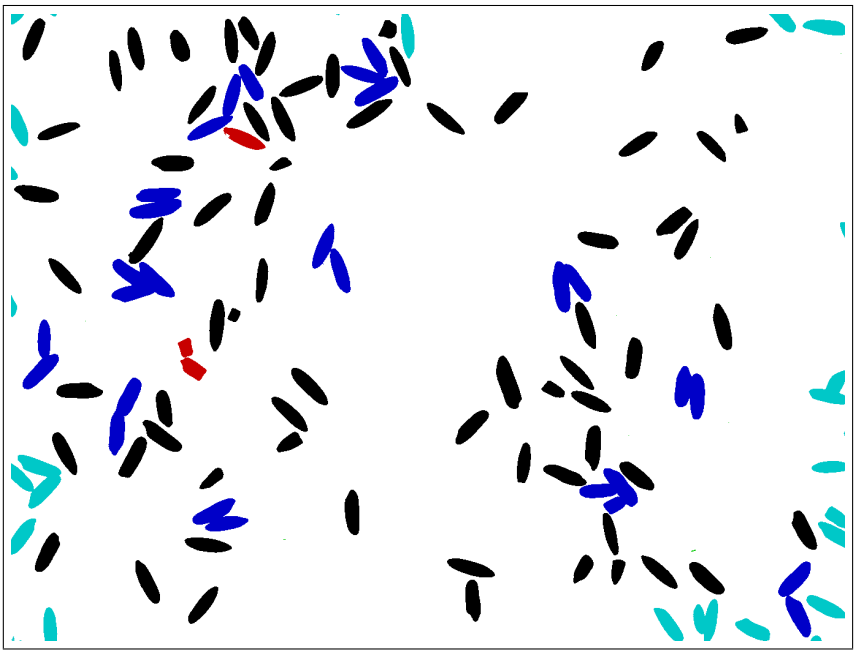

1.1.1 Grain measurement selection example.

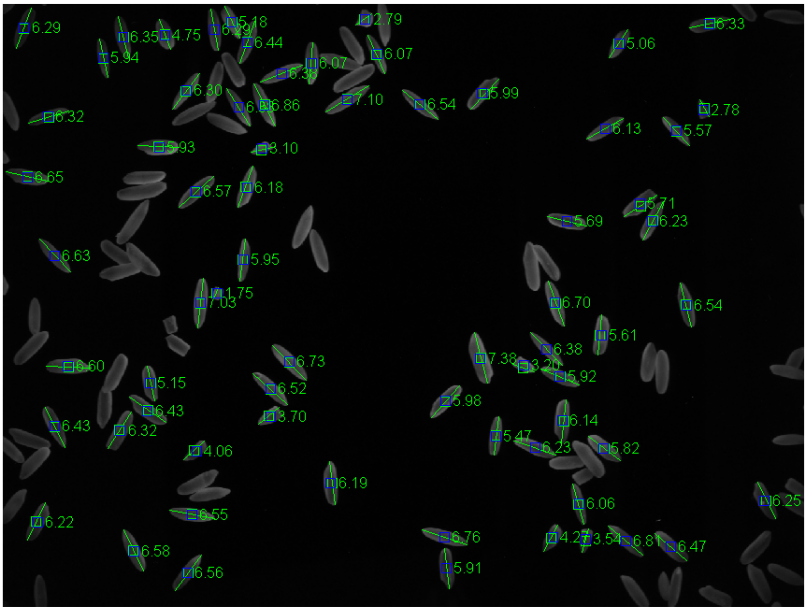

1.1.2 Length information back projected onto the suitable candidates only.

FIGURE 1.1: Example output images of grain selection and length measurement of Parboiled Long grain rice. The colour given to the rice objects indicate the status of the rice grain – black indicates a gain to be measured by the system. The back project of the estimated rice is represented by the green lines (quantised to the nearest pixel).

5. A novel robust K-Nearest Neighbours posterior class density model, used to classify the rice grains using shape information.

1.3 Outline of Thesis

This research survey is structured in seven chapters and a bibliography section detailed at the end of the document. Chapter 2 reviews related work in the field. Previous work was reviewed that comprises the outline of a computer vision inspection system for on-line measurement of broken rice. Chapter 3 presents a measurement system for the length measurement of rice grains *in stasis*. Experiments in this chapter are conducted on US Long rice. Chapter 4 presents a measurement system for a by-mass percentage of broken rice grains *in motion*. Experiments in this chapter are mainly conducted on a variety of rice types, including: US Long, Basmati, and Parboiled US Long rice. Chapter 5 explores classification using density estimation with shape features.

Initial experimentation is aimed at the general classification problem; three data-sets not associated with rice grains are used to verify the density estimators. The method is then applied to a data-set of US Long rice, the effectiveness is compared to the length definition method. Chapter 6 presents the experimental results of the overall measurement system, from the methodologies described in chapters 3, 4 and 5. Additional confirmation of results are obtained from the second prototype machine in Buhler Bangalore, India; the system continuously measures the broken rice percentage of Basmati and Sona Masoori rice varieties. Chapter 7 closes the thesis with a summary of the key findings and achievements, in addition to to suggestions for further research.

1.4 Chapter Summary

This chapter has introduced and motivated the research reported in this thesis. It included a brief discussion of the importance of visual information in the use of automatic inspection of organic material, and stressed the difficulty in reducing the bias error of measurements made and the need for an on-line and robust system. The reader was then given a breakdown of a number of key elements of this problem. Finally, an overview of the research in this thesis is presented; showing how it contributes towards solving the problem of on-line measurement of broken rice.

Chapter 2

Related Work

The first chapter discussed the problem of measuring the percentage of broken rice grains in a mill using machine vision. This chapter reviews previous research in the key stages of image analysis that has been identified. The first section of this chapter explores the measurement of broken rice percentage, and inspection of granular organic matter. The following sections explore work associated with the specific processing stages of interest that re involved in the context of accurate measurements of small objects from an image: with camera calibration; contour extraction; and finally the length measurement. The penultimate section reviews work on classification with shape features and posterior density estimates with K-Nearest Neighbour classifiers. A focus on the classification of plant species by the inspection of leaf samples was conducted. This allows the rigorous evaluation of the classifiers implemented with the use of a complex multi-class classification problem.

2.1 Automatic Inspection with Machine Vision

In the literature, there are a number of quality inspection systems for granular organic matter. However, no single approach has solved the problem of automatic on-line broken rice measurement. Previous work in this area (and also the area of milling quality) has been explored using image acquisition from flatbed scanners and static machine vision systems that use area cameras.

Francis Courtois *et al.* [13] has worked on one of the more recent publications, where a desktop PC and flatbed scanner is used to assess stress cracks in randomly disposed grains of rice. The authors report the cycle time to captured each image is 20 seconds (in the most optimistic cases of using faster scanners). The Watershed Transformation [20]

is used to identify the fissures in the rice grains (stress cracks). A number of geometric features were calculated, such as the perimeter, Feret's diameter, major and minor axis of fitted ellipsoid, and surface area. Some of these useful features are described in detail in section 2.4, which may be crucial for the accurate estimation of the rice grain length. The authors report they encounter a problem with the segmentation algorithm when there are many grains on the view, *i.e.* the segmentation ratio tends to drop when the amount of particles on the limited surface of the scanner glass is increased. They explain that the problem is caused by the increased probability of touching grains – an issue that will certainly arise in this application as well. The software algorithm appears to work quite well at measuring various broken percentages and fissure rates, with consistent measurement between repeated measurements, however the mean error appears large at times of up to 3 percent.

Ping Lin *et al.* [21] also developed a method, based on flatbed scanning and image analysis, to identify broken rice kernels. A velocity representation method was developed for pattern recognition based on the contour characteristics of the rice kernels. Image processing techniques were used to separate the rice grains from background pixels, and then preprocess the binary images in preparation for the velocity algorithm (a shape descriptor). In section 2.3 several methods for image segmentation are investigated, and later evaluated in this study. Additionally, a section on shape descriptors is explored in section 2.6.1. The authors claim high recognition rates between 96.7% and 98.73% of three varieties of rice using these methods. However, only relatively small samples of between 91 and 397 grains of rice (depending on the varieties tested) were used in the experiments that were conducted.

Jagdeep Aulakh *et al.* [22] attempts to measure the broken percentage of rice grains (in this paper described as the purity of hulled rice grain) with image processing techniques applied to images captured with a flatbed scanner. However, the authors do not provide a full evaluation of the problem, perhaps more specifically, the method is not automated (and not useful for this study). Another system for the separation of broken rice using flatbed scanners for image acquisition and the estimation of rice grain length, achieved a broken rice classification accuracy between 95.5 and 98.4%, depending on the rice variety (including white Basmati, white Jasmine, white Arborio and parboiled Loto) [23]. Also explored in this work is a classification solution using other morphological shape features of the rice, such as width, aspect ratio, and area. However, the classification accuracies were lower when compared to the length threshold method. The system can produce a result in roughly 3 minutes per sample (compared to about 30 minutes of manual analysis with a grain expert); however, the measurement is made on an unknown number of grains. It would seem apparent that flatbed scanning systems tend to be slow and

will not provide the platform to measure 10,000 grains within 10 minutes, as outlined in section 1.1.1.

B. K. Yadav *et al.* [24] use a CCD camera and desktop PC to automatically estimate the percentage of broken rice grains (also referred to as Head Rice Yield). The authors note that despite the extensive use of image analysis in manufacturing and medical industries, there are very few applications in grain-based industries. They also stress the importance of the the determination of milled rice quality to enable regular objective monitoring of milling operation, and as such allow the process to quickly react within to changes in material properties of the rice. The authors also hypothesed that the weight of individual grains, whether broken or head rice, is proportional to their relevant dimensional features; this information is useful for the later stages of the measurement system in this application – where a *by-count* percentage of broken kernels is converted to the industry standard *by-mass* definition, without access to the weight information of the rice kernels in-situ. A combined geometric feature, that the authors refer to as a characteristic dimension ratio, is used to identify broken grains from head rice form the respective length, perimeter and area measurements. A wide variety of rice grains were evaluated (ten types), however at disappointing numbers of samples grains (50 or less).

H. Aghayeghazvini *et al.* [25] use a high resolution CCD area camera (1944-by-2592 pixels) to image rice grains on a corrugated plate (for orientation), and a set of four circular 32 Watt fluorescent lamps. This illumination system was used to attempt to improve illumination evenly across the view, taking into account the camera was placed in the middle of the apparatus. The camera captures 8-bit monochromatic images, and an undisclosed method is used to extract the rice grains. The familiar length, perimeter and area measurements are estimated for each grain, and the classification of broken rice is determined from a linear regression approach of these three geometric features. The measurements were evaluated by comparing the estimated broken percentage with the ground-truth measured using a laboratory rice grader. The broken rice percentage showed a distinct power-law relationship with the characteristic dimension ratio defined in terms of length and area of head and broken rice kernels. A machine vision system for automatic inspection of broken corn kernels in motion has been previously prototyped [26], where motion blur was eliminated by the use of stroboscopic illumination. In this application a classification accuracy of 91% was achieved for detection of broken corn kernels, which is far from the target requirement of only 1% error outlined in chapter 1.

Another machine vision system was developed to inspect the internal damage of rough rice [27]. In this approach, a partial dark-field illumination set-up was used to highlight edges of the grain kernels, the following sub section briefly discusses the various illumination options available. The system was 91.5% accurate at this classification problem.

A similar system for broken corn kernel identification was designed using a cylindrical illumination method [28] with shape features and a neural network classifier. From these sources, it is increasingly understood that the lighting quality and suitability are crucial components for creating a robust vision inspection system. Four of the main illumination techniques consist of back lighting, full bright field (diffuse) lighting, partial bright-field (directional) lighting, and dark field lighting [29] [30]. The specifics of each technique may require different lighting, geometry and relative camera placement in order to achieve the desired effect. Back lighting generates immediate contrast as dark silhouettes appear against a bright background. It is noted that the advantages of back lighting are the low cost; ease of implementation and high contrast. However back lighting can produce fuzzy edges and physical placement of illumination behind the target object.

Full bright field lighting uses a large diffuser dome around the object to create relatively non-directional illumination. It is noted that the advantages of full bright field lighting are glare reduction on specular surfaces and ease of implementation. The disadvantages may include fuzzy edges and low contrast on unicolour parts of the target object. Additionally, a relatively large illumination source is required within close proximity to the object, to produce the desired effect. Partial bright field lighting is perhaps the most commonly used illumination technique (as it is most akin to everyday use). The illumination source is pointed towards the object, i.e. from the top, to create a good level of contrast. Some of the advantages of partial bright field lighting are the ease of implementation; good for casting shadows (if required) and may enhance topographical details. However, this technique is the most familiar with creating specular reflection from the object surfaces; and thus may create unwanted shadowing and also non-uniform illumination.

Dark field lighting is the least well known illumination technique. The illumination source is pointed towards the object at near right angle, such as 45°. Dark field lighting provides the highlighting of defects on the object surface, i.e. scratches and raised surface features, and can provide high contrast in certain applications. This is because very little of the background reflection is returned to the camera. However, a reduced amount of foreground reflection is returned to the camera and may not illuminate flat and smooth surfaces. In chapter 3, the lighting system of the proposed system is described – a dark field stroboscopic circular illumination source is used for the reasons of reduction in measurement error caused by motion blur, and edge highlighting.

B. J. Lloyd *et al.* [31] describes the evaluation of perhaps the closest resemblance to an automatic device for the measurement of broken grains. The authors test two systems: the GrainCheck machine vision system (Foss North America, Eden Prarie,

Minnesota, USA), and the GrainMan (Grain Machinery Manufacturing Corporation, Miami, Florida, USA) manual shaker. It is not disclosed how the machine vision commercial system performs it's broken measurement. The manual shaker table, however, mechanically sorts by the grains by length. This system underestimated the percentage of broken rice when compared to the industry standard broken measurement method for commercial milling. The vision system performed more accurately, with smaller error bars. Both methods require regular cleaning for measurement: a five minute cleaning procedure is required roughly every 10 measurements made, which is approximately based on 2,000 grains of rice per measurement.

2.2 Camera Calibration

There are two main factors which make it desirable to incorporate a correction component into the camera calibration method to compensate for optical distortion. A balance must be maintained between image contrast and optical distortion, based on the position of the camera to the target and the focal length of the optics. A lens with a shorter focal length will improve the contrast between foreground and background, but will incur a greater degree optical distortion. It is expected that any uncorrected lens distortion will bias the accuracy of a length measurement within an image. Additionally, there is a choice of cost vs. quality when selecting a suitable camera system for a machine vision system; if cost increases as some function of quality, and quality reduces lens distortion. Thus, having a software correction allows more flexibility in selecting a camera.

In the literature, there are many techniques for calibration of the camera in an image analysis system. The main concern is achieving a sufficiently high accuracy of length measurement of an object across the field of view of a chosen camera. One of the challenges is to compensate for the 'optical distortion' caused by lens aberrations, and 'geometric distortion' caused from the projection of a 3D object onto a 2D plane, *i.e.* a digital sensor. However, doing so with the aim of accuracy is another challenge within itself. Another vital task for some systems is to report all such length measurements in a real-world scale (millimetre units). Thus, in the situation where accurate length measurement is vital, some form of calibration will be required to tackle both of these tasks.

Radial distortion comes in two main patterns, barrel and pin-cushion. Barrel radial distortion, apparent when the radial coefficients are negative, has a decreasing effect on the image magnification as the distance is increased from the optical axis. Pin-cushion radial distortion has an increasing effect on the image magnification as the distance is increased from the optical axis. Tangential distortion is caused by the imperfect

centring of the lens components and other manufacturing defects in a compound lens. Figure 2.1 illustrates a set of 13 by 10 coordinates which have been distorted with the above patterns. In these examples, 13 points wide and 10 points high gives an aspect ratio which is a close approximation to the aspect ratio of the images captured from the camera system used. It was noticed that in this case of a 'wide' aspect image, the modelled lens distortion has a stronger effect in the horizontal case, compared to the vertical case.

In the optics literature, camera calibration has a specific meaning: the estimation of the various parameters used in the physical camera model. In many computer vision applications it is usually considered that a camera is already calibrated; which means that a model of the internal camera parameters is available and can be computed using a known calibration pattern such as a planar lattice of circles (or chess-board). One well used camera calibration technique is the one proposed by Tsai [32], where pinhole perspective projection is used to represent the camera model. Its implementation depends on 3D point coordinates corresponding to 2D pixels in the image, defined by the calibration pattern. It uses a two-stage technique to compute the position and orientation; then the internal parameters of the camera.

The pinhole camera model [33] is used as a first order approximation of a camera, where the camera aperture is described as a single point. The model creates a mapping from a point $(\mathbf{X}, \mathbf{Y}, \mathbf{Z})$ in a 3D scene to a point $(\mathbf{u}, \mathbf{v})$ in a 2D image plane using a perspective transformation, see figure 2.2. A non-linear term is then introduced to the model to define radial and tangential lens distortion.

The five intrinsic parameters of the linear model are the focal length, image format (horizontal and vertical pixel scale) and the coordinates of the principal point of the camera. These are represented in a 3 by 3 intrinsic matrix ($\mathcal{A}$). The extrinsic parameters denote the coordinate system from the 3D world to the 3D camera coordinates as a joint rotation-translation matrix. These are represented in a 3 by 4 extrinsic matrix ($[\mathcal{R}\,\mathcal{T}]$).

The pinhole model is:

$$s(\mathbf{u}, \mathbf{v}) = \mathcal{A}[\mathcal{R}\,\mathcal{T}](\mathbf{X}, \mathbf{Y}, \mathbf{Z}) \tag{2.1}$$

or:

$$\psi \begin{bmatrix} \mathbf{u} \\ \mathbf{v} \\ 1 \end{bmatrix} = \begin{bmatrix} F_{\mathbf{u}} & 0 & O_{\mathbf{u}} \\ 0 & F_{\mathbf{v}} & O_{\mathbf{v}} \\ 0 & 0 & 1 \end{bmatrix} \begin{bmatrix} \mathcal{R}_{11} & \mathcal{R}_{12} & \mathcal{R}_{13} & \mathcal{T}_1 \\ \mathcal{R}_{21} & \mathcal{R}_{22} & \mathcal{R}_{23} & \mathcal{T}_2 \\ \mathcal{R}_{31} & \mathcal{R}_{32} & \mathcal{R}_{33} & \mathcal{T}_3 \end{bmatrix} \begin{bmatrix} \mathbf{X} \\ \mathbf{Y} \\ \mathbf{Z} \\ 1 \end{bmatrix} \tag{2.2}$$

where ψ is a scale factor, $(\mathbf{u}, \mathbf{v})$ are the coordinates of a 2D point in the image space, $(\mathbf{X}, \mathbf{Y}, \mathbf{Z})$ are the coordinates of a 3D point in the world space, $(O_{\mathbf{u}}, O_{\mathbf{v}})$ is a principal

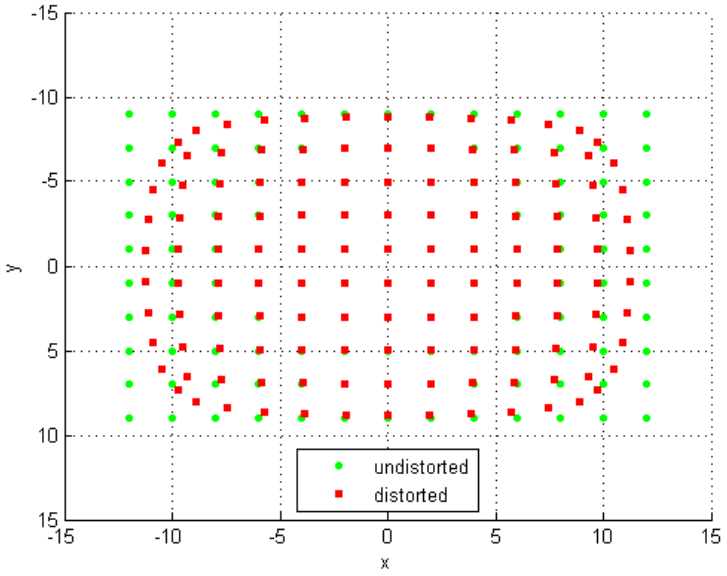

2.1.1 Barrel radial distortion.

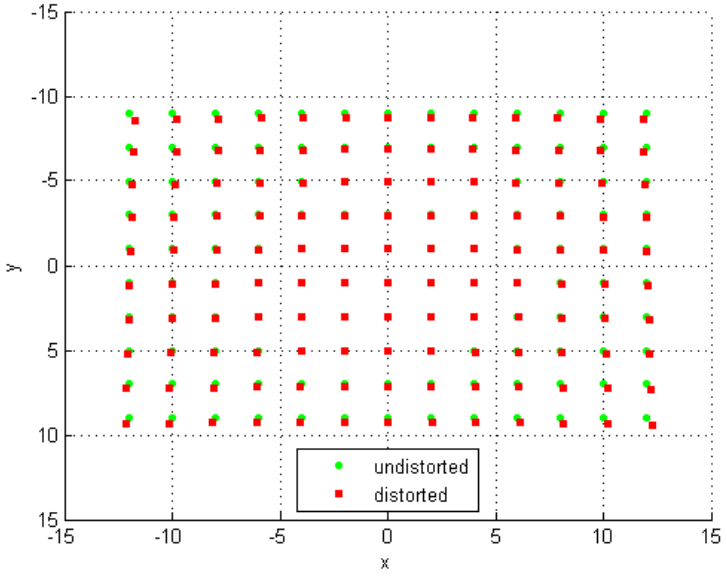

2.1.2 Tangential distortion.

FIGURE 2.1: Optical distortion using Brown's model, using a synthetic scale factor of 1 pixel per millimetre with no rotation or translation.

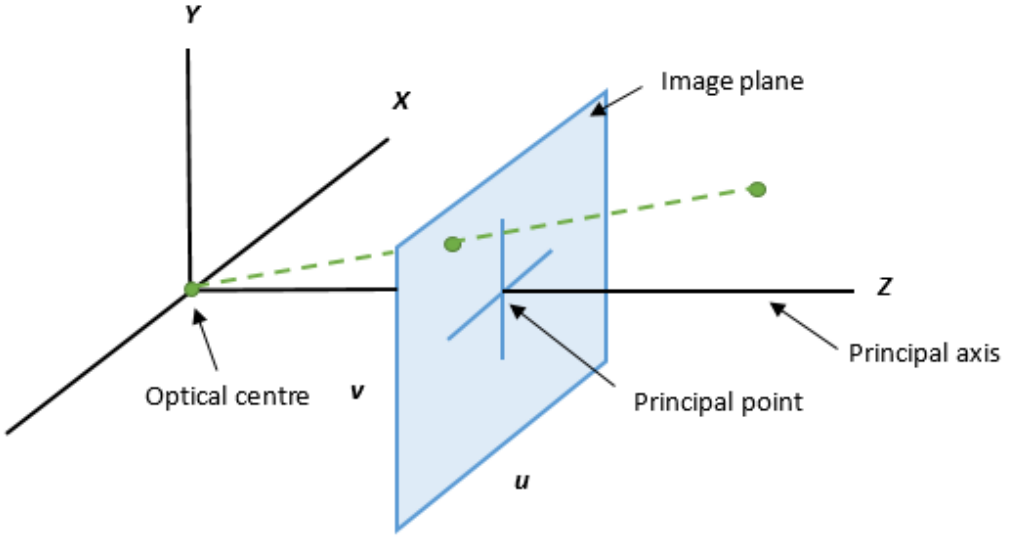

FIGURE 2.2: The geometry of the pinhole camera model. The green circles indicate a point in the real world and it's corresponding location in the image through a projection to the optical centre.

point which may usually be at the centre of the image and $(F_{\mathbf{u}}, F_{\mathbf{v}})$ are the focal lengthss in pixels.

The perspective transformation is equivalent to the following sequence of equations: firstly,

$$\begin{bmatrix} x \\ y \\ z \end{bmatrix} = \mathcal{R} \begin{bmatrix} \mathbf{X} \\ \mathbf{Y} \\ \mathbf{Z} \end{bmatrix} + \mathcal{T} \tag{2.3}$$

then, when $z \neq 0$, x' and y' are scaled co-ordinates in the camera frame:

$$x' = x/z \tag{2.4}$$
$$y' = y/z \tag{2.5}$$

finally, $\mathbf{u}$ and $\mathbf{v}$ are the image co-ordinates:

$$\mathbf{u} = F_{\mathbf{u}} x' + O_{\mathbf{u}} \tag{2.6}$$
$$\mathbf{v} = F_{\mathbf{v}} y' + O_{\mathbf{v}} \tag{2.7}$$

There are many models in the literature which represent various types of distortion caused by a lens. A particularly well known and useful model is Brown's distortion

model [34]; which is a physical model that compensates for both radial distortion caused by the curvature of a lens, and tangential distortion caused by misalignment of the physical elements within a lens. To model the lens distortion, the pinhole camera model in equation 2.3 is extended by introducing x'', y'' to represent the undistorted normalised camera co-ordinates, as a function of x', y':

$$x'' = x'(1 + \vartheta_1\mathcal{R}^2 + \vartheta_2\mathcal{R}^4 + \vartheta_3\mathcal{R}^6 \ldots) + 2\varphi_1 x'y' + \varphi_2(\mathcal{R}^2 + 2x'^2) \quad (2.8)$$

$$y'' = y'(1 + \vartheta_1\mathcal{R}^2 + \vartheta_2\mathcal{R}^4 + \vartheta_3\mathcal{R}^6 \ldots) + 2\varphi_2 x'y' + \varphi_1(\mathcal{R}^2 + 2y'^2) \quad (2.9)$$

where the radial distance $\mathcal{R}^2 = x'^2 + y'^2$, the radial distortion coefficients $\vartheta_1, \vartheta_2, \vartheta_3, \ldots$ form an infinite series, and φ_1, φ_2 are tangential distortion coefficients.

However, an empirical component is required in order to estimate all of the camera parameters as defined in Brown's physical lens distortion model. Heikkila [35] describes one technique: to use a full scale optimisation of all parameters, by minimising the total errors between the corrected image coordinates and synthetic coordinates projected by the forward camera model. This process requires that the distorted image coordinates are to be expressed in terms of their undistorted equivalents. For this to be realised, a backwards distortion model – an inverse problem – for which only an approximate solution is given.

It would normally be expected that such a solution is prone to instability, due to the small variations in point estimates becoming large errors in the correction via the inversion process. A least squares technique is used, as an optimal estimator, with the set of points $\mathcal{C}_i$ to find the solution; however, the distortion coefficients require a first approximation as they are not known. From the forward model, there is a close coupling between the distortion coefficients and the camera parameters; therefore, the estimation of the coefficients becomes unreliable without knowing the camera parameters.

Working from equation 2.8, the inverse model begins with $x'' = \frac{(\mathbf{u}-O_\mathbf{u})}{F_\mathbf{u}}$ and $y'' = \frac{(\mathbf{v}-O_\mathbf{v})}{F_\mathbf{v}}$. To estimate (x', y'), first initialise them as $x' \approx x''$ and $y' \approx y''$. Recursively, compute (x', y') by:

$$x' \leftarrow \frac{(x' - 2\varphi_1 x'y' + \varphi_2(\mathcal{R}^2 + 2x'^2))}{(1 + ((\vartheta_3\mathcal{R}^2 + \vartheta_2)\mathcal{R}^2 + \vartheta_1)\mathcal{R}^2)} \quad (2.10)$$

$$y' \leftarrow \frac{(y' - \varphi_1(\mathcal{R}^2 + 2y'^2) + 2\varphi_2 x'y')}{(1 + ((\vartheta_3\mathcal{R}^2 + \vartheta_2)\mathcal{R}^2 + \vartheta_1)\mathcal{R}^2)} \quad (2.11)$$

where, in practice, four iterations are sufficient to resolve strong lens distortions.

Alternative approaches are available, such as mathematically rigorous techniques, that

do not require a fixed calibration pattern. Such approaches are used during measurement stages, where the stage is used to calibrate itself. Forbes [36] discusses a general framework for self-calibration with different measurement examples. Such methods are generally useful in a situation with redundancy in the measurements made by an instrument, particularly where the instruments are so precise that there are no standard measurement grids of suitable accuracy with which to calibrate them.

This section has demonstrated problem and possible solutions for optical distortion removal and real world scale. Chapter 3 implements the calibration method using Brown's model (BDM) as described by Heikkila. Additionally, three novel and computationally efficient methods for correcting the distortions present in the lens of the imaging device was presented; these also allow the system to report any measurements or extracted features in real-world millimetre units.

2.3 Contour Extraction

There are a number of problems associated with extracting the edges of the rice grains from an image captured in a dusty environment. As one standard definition of a broken grain is determined by the length of that grain, the significance of the accuracy of the extracted contour was emphasised.

The contour information describes the perimeter of the 'connected presence' of the foreground objects. In the literature [37] there are various techniques that could be applied to extract the foreground contour of the rice grains. Three distinct groups contain different approaches to image segmentation: global knowledge, such as using a histogram of image features. Edge-based and region-based, where either may use local characteristics like brightness, texture, *etc*, to identify a closed boundary. This focused into global methods such as image thresholding and extend this to more local based methods. Edge detectors may have some use in this application as they tend to be very fast low-level algorithms. Region based methods tend to be complex iterative processes and are not suitable for an on-line application.

In a typical image analysis system, image segmentation (or binarisation) is performed to obtain the binary signal of the foreground objects. The input image commonly consists of concentrated objects on a uniform background, where in this case a simple global approach can be used to provide a complete contour extraction of the foreground objects from the background. It is assumed that the intended application will have no control over the feeding mechanism of the product. This limits the possibility of using prior knowledge of the background profile, for example using an empty image of the background to calibrate the contour extraction algorithm with a pre-calculated profile of the background.

For global thresholding, consider a grey scale image where $\mathcal{G}(\mathbf{u}, \mathbf{v}) \in [0, 255]$ is the pixel intensity at location $(\mathbf{u}, \mathbf{v})$. A global thresholding technique will compute a single global threshold t, used to compute a binary image $\mathcal{B}(\mathbf{u}, \mathbf{v})$, such that:

$$\text{if} \quad \mathcal{G}(\mathbf{u}, \mathbf{v}) \leq t \tag{2.12}$$

$$\text{then} \quad \mathcal{B}(\mathbf{u}, \mathbf{v}) = 0 \tag{2.13}$$

$$\text{else} \quad \mathcal{B}(\mathbf{u}, \mathbf{v}) = 255 \tag{2.14}$$

In the naive method (NaiveThresh), the global threshold value t is set as the mean grey level of the foreground and background classes. This approach easily segments an image which has a clear separation between the two classes, as represented by a bimodal histogram, depicted in figure 2.3.1. It is assumed that the intended application will have

a sufficient lighting setup to produce a foreground/background contrast ratio of at least 1.5.

A previous extensive comparison of image segmentation techniques by Trier & Taxt was conducted for the problem of document binarisation [38]; a domain with the major difficulty of non-uniform illumination across the field of view. They have shown that a global histogram thresholding technique (GlobalHist) by Otsu [39] out-performs other methods such as Kittler & Illingworth's [40] minimum error thresholding (MinErrorThresh). In addition, they find that the GlobalHist method had the fastest execution time out of all the methods they had tested. Niblack's [41] local threshold method (LocalVar) in addition to other local based methods tend to perform slower, due to the pixel-by-pixel level of detail. Trier & Taxt additionally concluded from their experiments that a modified LocalVar method that uses a post-processing step, by Yanowitz & Bruckstein [42], provided the best results outright in addition to being one of the fastest local based methods.

The GlobalHist method selects the threshold t that minimises the intra-class variance of the two classes of foreground and background, see figure 2.4. This is calculated for each possible threshold 1 to 256, and the threshold with the minimal variance is selected as the threshold t, such that:

$$\sigma_\omega^2(t) = \omega_1(t)\sigma_1^2(t) + \omega_2(t)\sigma_2^2(t) \tag{2.15}$$

where weights ω_i are the probabilities of the two classes separated by a threshold t, and σ_i^2 is the variance of these classes. Minimising the intra-class variance is the same as maximising inter-class variance, expressed as:

$$\sigma_b^2(t) = \sigma^2 - \sigma_\omega^2(t) = \omega_1(t)\omega_2(t)\left[\mu_1(t) - \mu_2(t)\right]^2 \tag{2.16}$$

where σ^2 is the variance of the global pixel intensities in the image, ω_i is in terms of class probabilities and μ_i as class means. These in turn can be updated iteratively with the following steps:

1. Compute histogram and probabilities of each intensity level.
2. Initialise $\omega_i(0)$ and $\mu_i(0)$.
3. Step through $t = 1 \ldots 256$. For each threshold, update ω_i and μ_i and compute $\sigma_b^2(t)$.
4. $t = \max(\sigma_b^2(t))$ will contain the selected threshold.

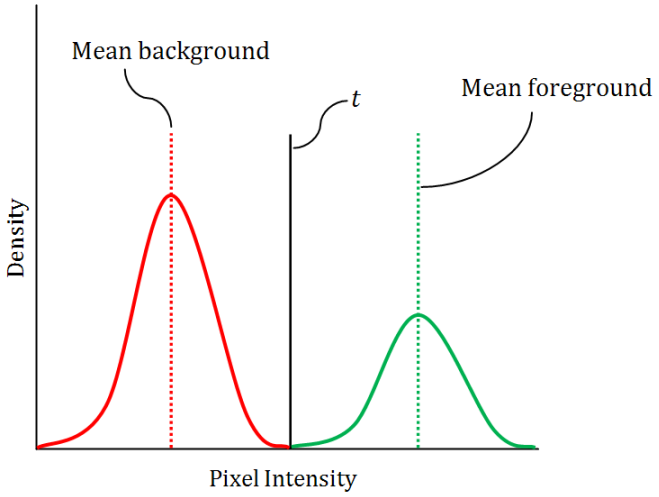

2.3.1 Pixel intensity histogram of an image where a naive global threshold value, t, is set to halfway between the mean foreground pixel and background pixel.

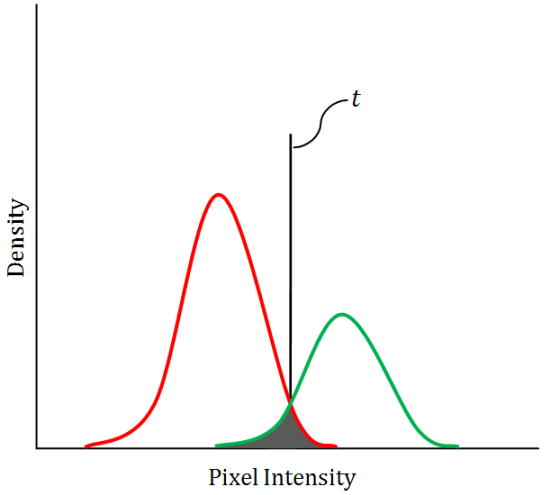

2.3.2 Global thresholding becomes problematic when illumination variation causes poor contrast. The selected threshold value causes incorrect segmentation of foreground pixels to the background class, shown as the dark shaded area.

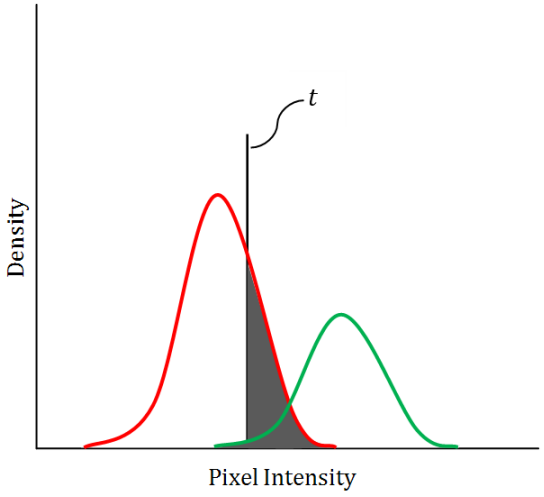

2.3.3 Example where the global threshold is incorrectly set.

FIGURE 2.3: Example image intensity histograms for image segmentation with global thresholding.

The GlobalHist method can optimise the global threshold selection; however, the inherent problem of misclassification from non-uniform illumination is still not settled, as shown in figure 2.3.2. Local thresholding methods attempt to overcome these problems by selecting a separate threshold value $t(\mathbf{u}, \mathbf{v})$ for each pixel $\mathcal{G}(\mathbf{u}, \mathbf{v})$. The LocalVar local based method calculates a threshold $t(\mathbf{u}, \mathbf{v})$ using second order statistics, such that:

$$t(\mathbf{u}, \mathbf{v}) = k\sigma(\mathbf{u}, \mathbf{v}) + \mu(\mathbf{u}, \mathbf{v}) \tag{2.17}$$

where $\mu(\mathbf{u}, \mathbf{v})$ is the local mean pixel intensity within window size b pixels from pixel $\mathcal{G}(\mathbf{u}, \mathbf{v})$, k is a constant (usually $k = -0.2$), and $\sigma(\mathbf{u}, \mathbf{v})$ is the local standard deviation pixel intensity within window size w from pixel $\mathcal{G}(\mathbf{u}, \mathbf{v})$.

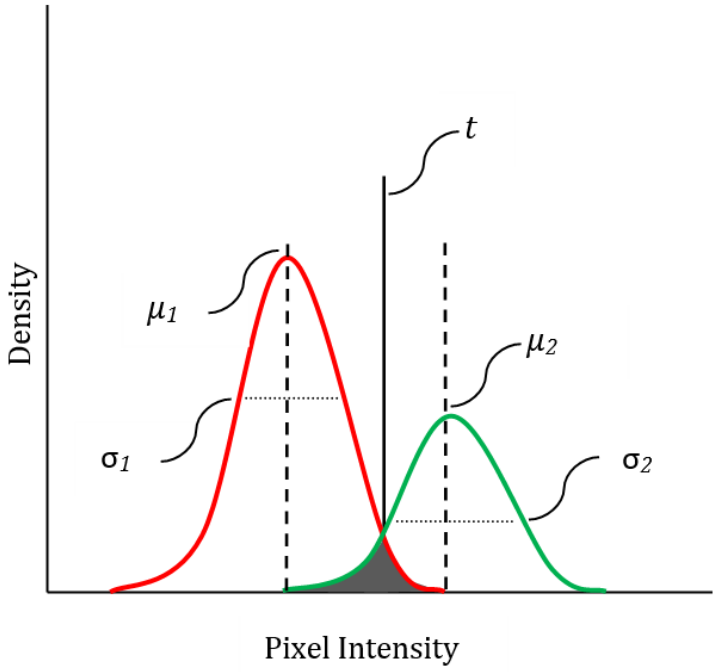

Figure 2.4: Global threshold selection from class means and variance.

Sezgin & Sankur [43] provide a full and comprehensive survey of image segmentation methods, however similarly to Trier & Taxt the main experiments are conducted for the purpose of document binarisation. The authors do additionally include experimentation for the purpose of non-destructive testing. The authors categorise and evaluate 40 thresholding methods where it is suggested the MinErrorThresh method ranked highest when considering 40 degraded document images according to average quality. In this evaluation, Sauvola's modified LocalVar method (LocalVarRatio) [44] ranked second. Additionally, the MinErrorThresh method ranked highest when considering 40 test images according to average quality; where the GlobalHist method ranked 6th.

The LocalVarRatio method calculates the threshold as:

$$t(\mathbf{u},\mathbf{v}) = \frac{k\sigma(\mathbf{u},\mathbf{v})}{128} + \mu(\mathbf{u},\mathbf{v}) \tag{2.18}$$

where $\mu(\mathbf{u},\mathbf{v})$ is the local mean pixel intensity within window size in w pixels from pixel $\mathcal{G}(\mathbf{u},\mathbf{v})$, γ is a constant (usually $\gamma = 3$), $\sigma(\mathbf{u},\mathbf{v})$ is the local standard deviation pixel intensity within window size w from pixel $\mathcal{G}(\mathbf{u},\mathbf{v})$.

A real time implementation of the LocalVarRatio method using the integral image has also been implemented [45]. The authors claim a ten-fold performance improvement in computation time, over the standard implementation, with the same segmentation performance. The authors note from their experiments that the LocalVarRatio method provides an improved segmentation performance over the GlobalHist method. In addition to the segmentation methods explored, we consider using low-level edge detectors in order to extract the contour information of objects. Edge detectors are typically fast and range from relatively simple first order convolution operations to more complex heuristic algorithms. Since it is expected that dark-field lighting setup to highlight the grain edges slightly, we test the popular edge detector methods in addition to the full segmentation methods previously discussed. Two edge detector methods that are particularly well-known and used are Canny's Edge Detector (EdgeCanny) [46] and the Laplacian of Gaussian (EdgeLoG) spatial filter [47]. Some fine tuning is possible with these two methods, in particular with the size and strength of the Gaussian smoothing filter.

Evaluation of the accuracy of the binary segmentation process has also been thoroughly explored. Sezgin & Sankur [43] describe several criteria used to evaluate segmentation performance, some of these focus on scoring the misclassification of pixels and others are based on penalising the segmentation for inaccurate edges or shape changes. For our data we will focus on using three Segmentation Performance metrics which are the following:

1. Misclassification Error (ME) [48], to highlight the percentage of misclassified pixels between extracted and ground-truth contours.

2. A simplified Edge Mismatch Error (SEME) [49], to rate the percentage of edge pixels matched from the extracted and ground-truth contours.

3. Modified Hausdorff Distance (MHD) [50], used to assess the shape similarity between extracted and ground-truth contours.

All three of these metrics require a ground-truth, that consists of a manually labelled binary image indicating the 'true' pixels of the input grains. All three metrics, after normalisations are applied, provide an error score between 0 and 1. Misclassification Error (ME) [48] highlights the percentage of incorrectly assigned pixels, for both background incorrectly classed as foreground and foreground incorrectly classed as background. The Misclassification Error is expressed as:

$$\text{ME} = 1 - \frac{|\mathcal{B}(\mathcal{B}=0) \cap G(G=0)| + |\mathcal{B}(\mathcal{B}=1) \cap G(G=1)|}{|G(G=1)| + |G(G=0)|} \tag{2.19}$$

where $\mathcal{B}(\mathcal{B}=0)$ and $\mathcal{B}(\mathcal{B}=1)$ are the background and foreground pixels in the binary image $\mathcal{B}(\mathbf{u},\mathbf{v})$; $G(G=0)$ and $G(G=1)$ are the background and foreground pixels in the ground-truth image $G_{\mathcal{B}}(\mathbf{u},\mathbf{v})$; and $|\ldots|$ is the cardinality of the set. A score of $\text{ME}=0$ indicates a perfect match between the ground-truth and segmented images and $\text{ME}=1$ indicates a complete misclassification.

Simplified Edge Mismatch Error (SEME) [49] is based on penalising discrepancies between the edge pixels from the binary image and ground-truth image. This may be useful when looking at the stability of the edge as the configuration is changed. The Simplified Edge Mismatch Error is expressed as:

$$\text{SEME} = 1 - \frac{|\mathcal{B}_e \cap G_e|}{|G_e|} \tag{2.20}$$

where $\mathcal{B}_e$ and G_e are the foreground *edge* pixels in the binary image and ground-truth image, respectively. A score of $\text{SEME}=0$ indicates a perfect match between the ground-truth and segmented edges, and $\text{SEME}=1$ indicates a complete mismatch of edge pixels.

Dubuisson *et al.* use a Modified Hausdorff Distance (MHD) [50], to measure the shape distortion between the binary image and ground-truth image. This is a more complex edge comparison than the SEME metric. This method works relatively well as it calculates the Euclidean distance between the two sets of finite points (binary image and ground-truth) and therefore compares the shape of the two objects. Given a set of points, we find the nearest point in the ground-truth target, and calculate the sum of the Euclidean distances between the matched points. The MHD metric has no upper bound, however we can produce a normalised score by dividing each MHD value by the maximum MHD value in the set. A score of $\text{MHD}=0$ indicates a perfect shape match between the ground-truth and segmented images, and $\text{MHD}=1$ indicates a completely distorted shape.

The contour extraction experiments are discussed in chapter 3. An inclusion of a wide selection of the various image segmentation and edge detector approaches and evaluate them using the contour accuracy metrics. Additionally, a description of a set of post segmentation filters was given; and that these would be required in order to extract a stable signal using these methods.

2.4 The Length of an Object from an Image

In the literature [51] [52] [53], the length of a region in an image is considered as part of a set of shape descriptors (also known as morphological parameters). Some geometrical descriptors are more commonly used for small particle measurement. The ellipse of inertia (PrincipalAxis) provides a robust measurement of the major axis of a grain, by fitting an ellipse around the centroid of the object which has the same first and second moments as the grain, see figure 2.5.1. The directions of maximum and minimum variance are the same as the orthogonal least squares best fit line and plane of the data. The sums of squares for that line and plane can be expressed in terms of the covariance matrix: the Eigen vector and Eigen value of the covariance matrix of the grain, gives the direction and lengths of the ellipse, respectively. The minimum and maximum of the direction, from the Eigen vector, indicate the angles of the minor and major axis. The major axis, ϕ, is the aim.

More flexibility in the measurement is given by measuring the longest parallel line projected onto the principal axis, at grain angle ϕ, as calculated from the ellipse of inertia. The ParallelPrincipalAxis length is expressed by first projecting each perimeter point onto the principal axis, such that:

$$\Lambda(\mathbf{u}, \mathbf{v}) = e(\mathbf{u}) \cos(\phi) + e(\mathbf{v}) \sin(\phi); \tag{2.21}$$

Then, calculate the maximum Euclidean distance between any two of the projected points:

$$\text{ParallelPrincipalAxis} = \max(\Lambda(\mathbf{u}, \mathbf{v})) - \min(\Lambda(\mathbf{u}, \mathbf{v})); \tag{2.22}$$

Two additional methods to measure the length are explored. The approach for either is to measure the maximum Euclidean distance between the perimeter pixels, see figure 2.6. The first method allows any two perimeter points belonging to the grain, known as the Longest Chord (LongestChord). The second restricts the perimeter pixel pairing to only measure the longest chord that passes through the object centroid, referred to as Longest Centroid Chord (LongestCentroidChord).

The last approach of measuring length uses the enclosing space around the grain as the measurement input. A Bounding Box (BoundingBox) describes the minimum enclosing rectangle of the points $e(\mathbf{u}, \mathbf{v})$, where the minimum of a measurement such as area or perimeter is used. The calculation is simple when the rectangle is parallel to the coordinate axes, the bottom left and top right corners of the rectangle would be identified as $\min(e(\mathbf{u}, \mathbf{v}))$ and $\max(e(\mathbf{u}, \mathbf{v}))$, respectively. A length measurement is the longest distance between any of the box edges, though inaccuracies are induced if the object angle is different to the coordinate axis.

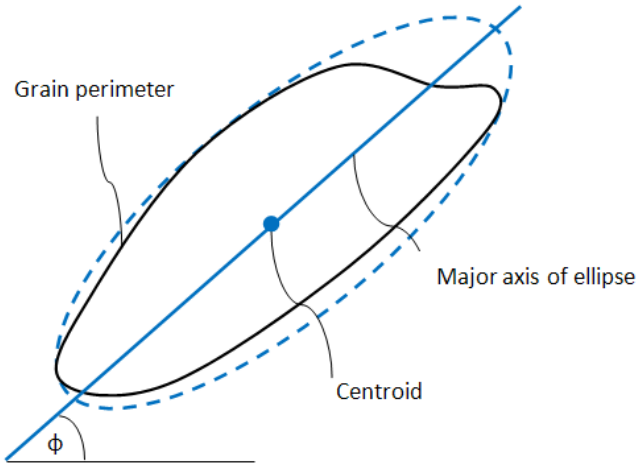

2.5.1 Ellipse of Inertia, which is the ellipse with the same second central moment as the grain.

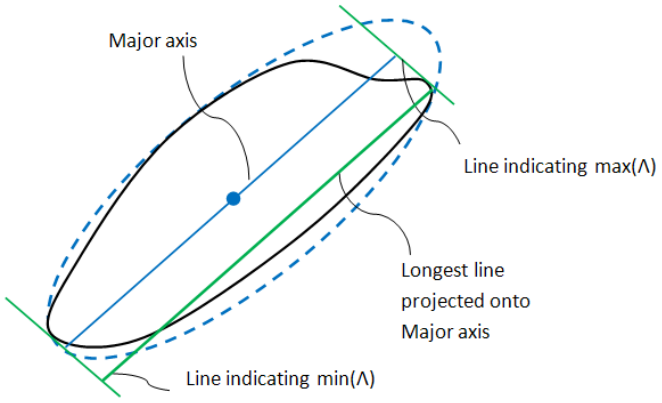

2.5.2 Calculating the length as the longest projected line about the major axis of the ellipse.

FIGURE 2.5: Length measurement of a grain based on the Ellipse of Inertia.

The difficult problem arises when trying to minimise the bounding rectangle when taking into consideration the orientation of the rectangle, thus the Minimum Bounding Box (MINIMUMBOUNDINGBOX) defines this length, shown in 2.7. The problem is described similarly to rotating callipers (ROTATINGCALIPERS) algorithm (also refereed as the Feret's diameter). The approach is to mimic the process of clamping the parallel jaws of a Vernier caliper around two opposing ends of the object. Toussaint [54, 55] shows that for the convex polygon, a linear time algorithm for the minimum area enclosing rectangle is known. It is based on the observation that a side of a minimum area enclosing box must be collinear with a side of the convex polygon.

The implemented length definitions and associated experiments are further discussed in

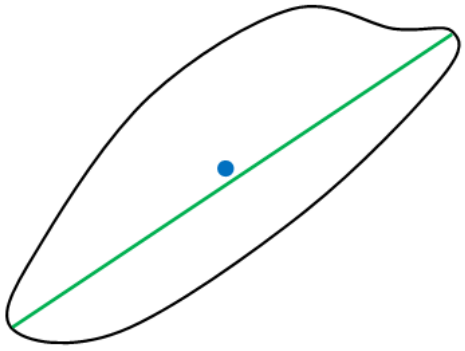

2.6.1 Longest chord from any two perimeter pixels

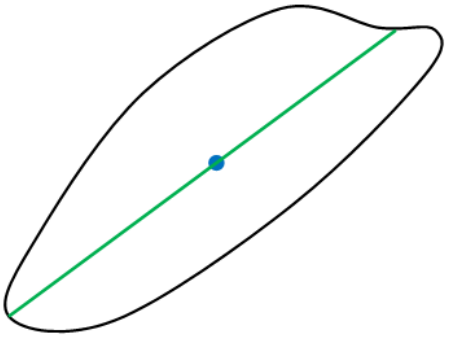

2.6.2 Longest chord passing through the object centroid

FIGURE 2.6: Chords between a grain's perimeter pixels.

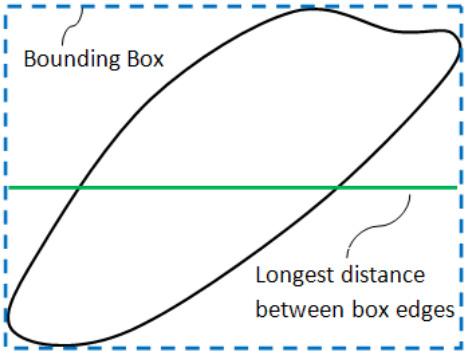

2.7.1 Bounding Box of the grain.

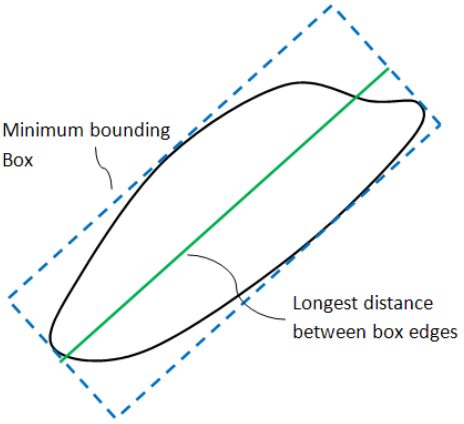

2.7.2 Minimum Bounding Box of the grain, where the rectangle orientation is optimised to minimise the area of perimeter of the rectangle.

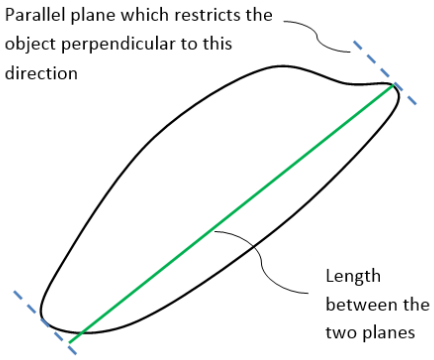

2.7.3 Rotating calipers length (also known as the Feret's Diameter), where the movement of the object is restricted along the direction orthogonal to parallel planes across the perimeter of the object.)

FIGURE 2.7: More length definitions.

chapter 3. The experiments are described to report the accuracy of these length definitions with respect to a sample of head and broken rice. The error of the length estimates are derived from ground-truth measurements made by hand with Vernier callipers.

2.5 Bias due to Finite Measurement Aperture & Touching Objects

Consider that a grain is only determined to be broken from the measured length of the grain. In this case, the accuracy of length measurement is directly connected to the classification error of broken rice grains. Given that the measurement apparatus has no control over the feed, and thus the objects may be touching one another when imaged. The touching objects in the image would appear occluded and have no complete contour to which an accurate length measurement can be estimated. In the literature, rejecting occluded particles from the window edge is a known problem [56] [51]. Given a finite measurement window that samples from a larger field of view, a decision is made to reject particles touching the edge. The occluded shape may not contain enough useful information to create a further decision on that particle. Given various sizes of particles, a bias effect is expected due to the higher probability that a larger particle will touch the measurement edge. The Miles-Lantuejoul [57] (ML) measurement can be used as an estimation of the conditional likelihood of a grain being of a certain length given it is not occluded.

Consider the shortest side of a measurement frame w and the longest diameter of the particle, then ML is as follows:

$$\mathrm{ML} = \frac{(w-l)^2}{w^2} = \left(1 - \frac{l}{w}\right)^2 \tag{2.23}$$

However, it is expected that in this application there are two sources of touching bias: one caused from the window edge, and the other from the rice grains touching one another. Two approaches are considered to resolve these bias errors. The first approach is to employ object separation techniques to allow the individual grains in each clump of touching grains to be measured independently. Previous work in this area has been explored with regard to granular organic matter, such as rice grains and wheat kernels [58–63]. However, the accuracy of current separation techniques may introduce a new source of bias error in the measurement of broken rice. In some cases, successful separation may not alter the general shape description of an object that was previously touching; although, an accurate length measurement inferred from a separated object may be biased (shorter).

The second option is to only measure rice grains that are single, and ignore touching grains. Given the limitation that only 'wholly visible' grains are measured, a correction for the bias error that is introduced into the measurement of broken rice. Given the knowledge that there may be a bias error introduced form the probabilities of touching given length, in chapter 4 a corrective approach is derived from Bayes Theorem to

estimate the bias error. An empirical observation of the behavior and probabilities of grains touching grains and grains touching the window edge. This is somewhat complex, as there is a requirement to maintain a high accuracy of manual labelling to provide a useful estimation of the bias errors, i.e it is very resource-intensive to provide an accurate ground-truth of the data. However, it is claimed to provide an upper-bound to the estimated bias error.

2.6 Shape Classification with Density Estimation Methods

We have briefly explored the literature with broken rice measurement in this chapter. Some work has used shape descriptors of the rice kernels for classification. However, we have also indicated the need for a robust and unbiased estimate of the proportion of broken grains. In order to fully demonstrate the accuracy of classification in a probabilistic approach, we focus this area into a multi-class classification of plant species using image processing techniques. Plant species are not only vast in number, but also in their use; estimates of the number of species of flowering plants range from 220,000 [64] to 420,000 [65]. Automatic recognition of plants is useful for a variety of industries such as foodstuff and medicine [66], reduction of chemical wastage during crop spraying [67, 68], and also for species identification and preservation [69].

Plant taxonomy suggests that a species can be successfully inferred from the leaves; the leaves are more readily available, easily found, and collected than other parts of the plant. The literature suggests a variety of work has been documented in the machine vision field using data-sets of leaves and image processing techniques. Mobile applications for identifying plant species using automatic visual recognition have now been developed, such as the Leafsnap system that identifies tree species in the Northeastern United States [70]. The following sections explore the work related to feature extraction for leaves, and then classification with density estimates.

2.6.1 Shape Features

Various different shape extraction techniques have been applied to leaves. J.-X. Du *et al.* [66] explore leaf classification with a data-set of 20 species of leaf and 20 samples of each. Fifteen shape feature descriptors were calculated per sample and used to classify the plant species automatically; these consist of eight conventional digital morphological shape features: aspect ratio, rectangularity, area ratio of convex hull, perimeter ratio of convex hull, sphericity, circularity, eccentricity, and form factor; the remaining set of seven features are a group of improved geometrical moments [71]. Three classifiers were tested: Nearest Neighbour (NN) [72], K-NN [73] and move-median hyper-sphere classifier [74]. The classification accuracy is shown to be the highest with the NN classifier, with 93% accuracy using half of the data as training and the remaining half as query data. The K-NN (with $K = 4$) and move-median hyper-sphere classifiers were 92% and 91% accurate, respectively.

Contrary to this approach, Z. Wang, *et al.*,[75] explores the classification of leaf species using a single relatively complex feature: the centroid contour distance curve (CCDC).

The object eccentricity is also used as a rejection criterion to reduce computation time. These features are scale, translation, and rotation invariant (after the appropriate normalisations are applied). The starting point of the matching algorithm is determined using a morphological thinning of the shape (skeleton). A distance function is then computed at each starting point mapped from the remaining skeleton onto the original shape edge: the best result is selected and proposed for matching.

Y. Shen *et al.* [76] also used the CCDC. Their approach gives a precision rate of 72%, given this many sample points. A direct comparison is made to the method suggest by A. Hong *et al.* [69], who uses the CCDC curve in addition to an angle code histogram of the shape's contour. A dissimilarity measure is given by combining a weighted summation of the two features. It is noted on a data-set of flower images that a recall rate of 56% is achieved using these shape features, compared to a set of colour features which archives 67% (both over a set of 80 images). A combination of shape and colour gives a recall rate of 80% over 80 images.

The CCDC shape descriptor is defined as the following. Let $(\mathbf{u}_i, \mathbf{v}_i) \ldots, (\mathbf{u}_n, \mathbf{v}_n)$ be the set of points about the contour of a shape where n is the maximum number of perimeter points, see figure 2.8. An ordering function is required to create a chain of connectivity of the perimeter pixels, since the signal will only retain the pertinent the pertinent shape information by tracing the contour in a contiguous fashion. The CCDC shape descriptor is described with the following equation:

$$\bar{\mathbf{u}} = \frac{\sum_{i=1}^{n} \mathbf{u}_i}{n} \tag{2.24}$$

$$\bar{\mathbf{v}} = \frac{\sum_{i=1}^{n} \mathbf{v}_i}{n} \tag{2.25}$$

$$\mathrm{CCDC}_i = \sqrt{(\mathbf{u}_i - \bar{\mathbf{u}})^2 + (\mathbf{v}_i - \bar{\mathbf{v}})^2} \tag{2.26}$$

where $(\bar{\mathbf{u}}, \bar{\mathbf{v}})$ is the centroid position of the shape. Depending on the size and complexity of the leaf, n may naturally vary; therefore, to ensure uniformity of the number of elements a point reduction step is computed with linear interpolation.

The CCDC in this form is given about an arbitrary starting point; whichever point happens to be at index $i = 1$. Therefore, it is necessary to order the signature with a suitable and repeatable starting point. The alignment method used was based on the principal axis of the shape (the 2nd moment of inertia). The perimeter of the shape is projected onto the principal axis and the two points at either end are matched to two perimeter pixels. Out of these two pixels, one is selected to be the starting point based on which is furthest of the two from the centroid. This signature is translation invariant,

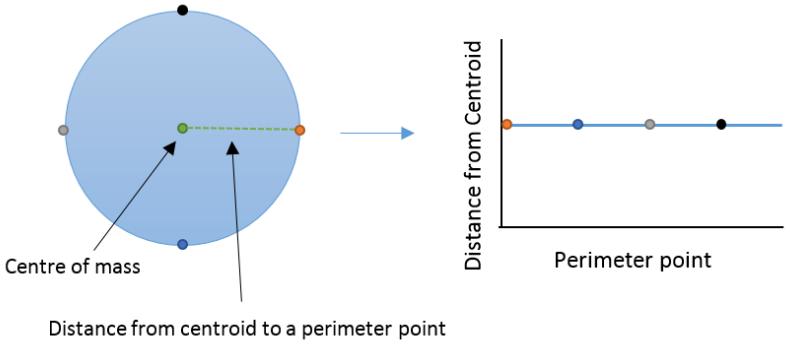

2.8.1 Example CCDC of a circle.

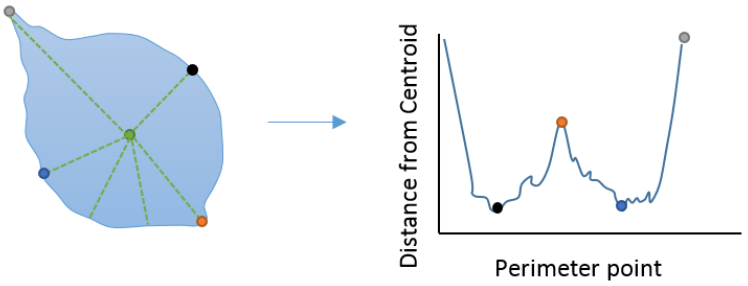

2.8.2 Example CCDC of a leaf shape.

FIGURE 2.8: Illustration of the CCDC shape descriptor.

due to the distance metric taken from the centroid. For scale invariance the signature is normalised, such that:

$$\mathrm{CCDC}_i = \frac{\mathrm{CCDC}_i}{\sum_{i=1}^{n} \mathrm{CCDC}_i} \tag{2.27}$$

Additionally, Ping Lin *et al.* use the velocity representation (VEL) of the contour, which is given as the first derivative of the CCDC descriptor [21]. The authors conduct experiments from relatively small samples of three rice varieties of rice (between 91 and 158). The reported classification accuracies were: 96.7% for Thailand rice, 98.73% for Pearl rice, and 97.14% for Changlixiang rice.

T. Nam *et al.* [77] uses a modified Minimum Perimeter Polygons shape feature. Enhancements include a form of non-maxima suppression in order to speed up computation by reducing the number of feature points. A Dynamic matching algorithm is used to classify the queried sample. A Nearest Neighbour algorithm was also tested, however the authors considered the computation time too costly. The results show the precision and recall performance of the retrieval method to be the best out of those tested, which includes: Fourier descriptors, chain code histogram [78] and invariant moments.

A. El-ghazal *et al.* [79] uses Fourier Descriptors for automatic classification. The Farthest point distance is a novel shape signature which is compared to eight popular signatures (each is a 1D function representation the 2D area or boundary). These are the radial distance, chord length distance, angular function, triangular function, triangular centroid area, triangular area representation, complex co-ordinates, polar co-ordinates and angular radial co-ordinates. The Discrete Fourier Transform is used to reduce the matching cost of the shape signatures. A high performance or recall rate is noted due to the signature tending to capture corner information of the objects. J. C. Neto *et al.* [67] uses a rotation normalised chain coded elliptic Fourier function based on the leaf boundary. Principal component analysis was used to select the Fourier coefficients with the best discriminatory power. Finally, discriminant analysis was used to develop the species identification models. A mean classification rate of 89.4% was recorded using this method on specific samples of plant leaves.

Other shape descriptors in the literature are the directional fragment histogram [80]; edge orientation histogram, or otherwise known as the curvature histogram (CH) [78]; shape context descriptor [81]; and the curvature scale space descriptor [82]. T. F. Cootes [83] has an extensive set of works pertaining to active shape models. M. Persson *et al.* [68] and H. T. Sogaard [84] both implemented active shape models for weed and crop identification. A classification rate of 85% to 92% was reported, depending on the data-set used. However, it is noted that active shape models are computationally expensive and may not be suited for real-time applications.

In chapter 5, we implement the CCDC shape descriptor (labelled as SHA) for the identification of plant species using images of leaves. For rice grains, we additionally use the CH descriptor and the VEL method. A texture (TEX) and margin feature (MAR) are also extracted and used, for the classification of plant species from images of leaves; these are both described in the following two sections.

2.6.2 Texture Features

A number of both traditional and novel texture analysis techniques have been applied to leaves. Backes *et al.* have applied multi-scale fractal dimensions [85] and deterministic tourist walks [86] to plant species identification by leaf texture, although their experiments involved very limited data-sets which makes them hard to evaluate. Casanova *et al.* [87] used an array of Gabor filters on a larger data-set, calculating the energy for the response of each filter applied, and achieved reasonable results, whilst Liu *et al.* have presented a method based on wavelet transforms and support vector machines [88].

Cope *et al.* [89] achieved an 85% identification rate on 32 species of a single plant species using the co-occurrences of different scale Gabor filters [90]. For each leaf image, 1024 small windows from the surface of the leaf are randomly selected. Then, For each window, 20 features based on the responses from different filters applied to all the pixels in the window. The filters used are a rotationally invariant version of the Gabor filter:

$$g(\mathbf{u}, \mathbf{v}) = \exp \frac{\sqrt{x^2 + y^2}^2}{2\sigma^2} \cos \frac{2\pi\sqrt{x^2 + y^2}}{\lambda} \tag{2.28}$$

where σ is the standard deviation, and λ is the wavelength, set to be $\lambda = 3\sigma$. Five different scale filters are used, each produced by varying the σ parameter.

Each filter is convolved with the window, and four features are then calculated for that filter for the window, such that:

$$\text{Average positive value} = \sum_{\substack{(i,j)\in window \\ s_j \geq 0}} \frac{f_{ij}}{w} \tag{2.29}$$

$$\text{Average negative value} = \sum_{\substack{(i,j)\in window \\ s_j \leq 0}} \frac{f_{ij}}{w} \tag{2.30}$$

$$\text{Energy} = \sum_{(i,j)\in window} \frac{{f_{ij}}^2}{w} \tag{2.31}$$

$$\text{Entropy} = -\sum_{(i,j)\in window} \frac{|f_{ij}|}{w} \log \frac{|f_{ij}|}{w} \tag{2.32}$$

where *window* is the current window, f_{ij} is the response for the current filter at pixel (i, j), and w is the size of the window.

Whilst these studies were all performed on texture windows acquired using traditional imaging techniques, Ramos [91] used images acquired using a scanning electron microscope, and Backes [92] used magnified cross-sections of the leaf surface epidermis. While these provide interesting results, such images are not available on a large scale.

2.6.2.1 Margin Features

Although the leaf margin is of great importance to botanists, there has been surprisingly little work towards its automated analysis. This may be due to the fact that not all plant species leaves feature teeth, although in these cases classification could still be aided by quantitative descriptors of the margin, which in many of these cases are still not entirely smooth. Another reason could be the difficulty in successfully acquiring meaningful measurements, particularly if it is assumed that these descriptors should match those

currently used by botanists. McLellan and Endler [93] used a single value measure of margin roughness, calculated by summing the angles between the lines connecting adjacent points around the contour. This was then combined with a selection of single-parameter shape descriptors.

Cope *et al.* [94, 95] create a leaf margin descriptor by creating a histogram feature vector that comprises the Histogram of Gradient Intensity method [96]. A median filter is applied to the binary leaf image to acquire a smoothed version of the leaf's shape. From this, m evenly spaced points are calculated, encompassing the entire outline. The sub-pixel point at which this line intersects the original leaf's outline is then found. The distance between this point and the current point is then calculated, and these distances for all the points in the smoothed outline are combined in order to produce a margin signature, $\mathbf{s} = \langle s_1, ..., s_m \rangle$, see figure 2.9.

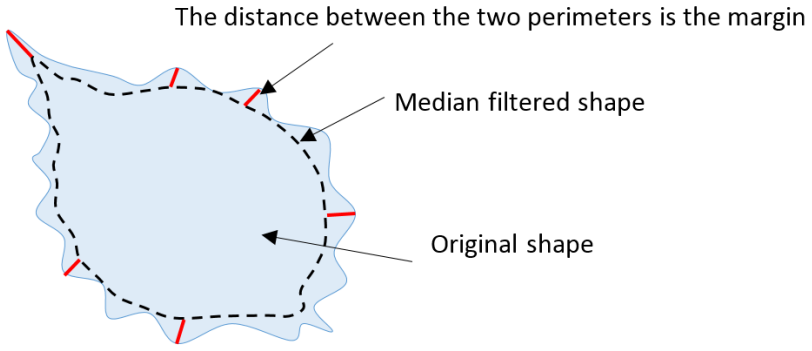

FIGURE 2.9: Illustration of the fine scale margin of an object.

The extracted margin is partitioned into n overlapping windows, $\mathbf{x} = \langle x_1, ..., x_n \rangle$, of equal size and spacing (in this case $n = \frac{m}{8}$ and the window size used is $\frac{m}{128}$). For each point within a window, x_i, 3 values are calculated:

1. Magnitude: This is the signed distance between the smoothed margin point and its corresponding point in the original margin, where the sign is determined by whether the original margin point lines are inside or outside of the smoothed margin.

2. Gradient: The signed difference between the current point in the margin signature and the next point.

3. Curvature: The angle at the current point between the previous point and the next point.

For each of these, two features are then calculated for the window, producing a 6-feature descriptor for each window:

$$\text{Average positive value} = \sum_{\substack{s_j \in x_i \\ s_j \geq 0}} \frac{s_j}{w} \tag{2.33}$$

$$\text{Average negative value} = \sum_{\substack{s_j \in x_i \\ s_j \leq 0}} \frac{s_j}{w} \tag{2.34}$$

where x_i is the current window, s_j is the value at a point within the signature, and w is the size of the window.

2.6.3 Classifiers & Posterior Estimates

The K-Nearest Neighbour (K-NN) classifier is a fundamental tool for pattern analysis, providing a straightforward means of estimating which class a previously unseen sample vector belongs to, given a finite training set. It naturally generalises to problems with multiple classes; for a 'test' set of unseen vectors, the resulting precision and recall statistics provide an insight into the separability of the problem. Moreover, its performance can be improved using metric learning approaches [97], and accelerated with enhanced implementations [98].

The standard K-NN classifier requires a single parameter, K, to select the K nearest elements in the training set: the single most popular class label in this subset is output as the *discrete* estimate. There are some possible variations of a K-NN system in the type of distance measure used and in the tie-break mechanism. With increasing size of training set, the accuracy of the K-NN discrete estimate tends towards the lowest possible – the Bayes error rate – if K can be increased along with the training set size, or twice this rate otherwise [99]. However, the focus of the current work is with small training set sizes: the objective is to use the limited data available as efficiently as possible. A probabilistic estimate of class label is not part of the standard output of the K-NN. However, the standard method [100] is to base the estimate on the proportion of the K neighbours in each class. It can be shown that this will, again in the case of large training set size, provide estimates that converge on the Bayes estimates of the p.d.f.s for each class label. A useful development [101] is to allocate a weight to each member of the training set, and then optimise these weights to maximise the likelihood of this training data.

For discrete estimates, the evaluation of a classifier's performance is straightforward: precision and recall can be combined into a single 'mean accuracy' characteristic. The most appropriate evaluation of probabilistic estimates is to report the mean log likelihood

of the unseen test data: this is maximised when the Bayes estimate of the p.d.f. is used, and in general its expectation will differ by the Kullback-Leibler divergence from the p.d.f. Most importantly, probabilistic estimates from different sources can be combined together much more effectively than discrete estimates. If the sources are conditionally independent then this is a straightforward multiplication: this enables evidence to be combined with prior probabilities, or the separate available channels of evidence to be combined together.

Let the training set of n vectors, $\mathcal{Y}$, be denoted by $\mathbf{y_1}, \ldots, \mathbf{y_n}$ and the test set $\mathcal{X}$ is formed by m vectors $\mathbf{x_1}, \ldots, \mathbf{x_m}$. Both sets are labelled using $y_1, \ldots, y_n$ and $x_1, \ldots, x_m$, respectively, where each label corresponds to one of the C discrete classes (or categories) $1, \ldots, C$. For convenience, an identity operator $\mathbf{I}(\cdot)$ is defined to obtain a vector's label, *i.e.* $\mathbf{I}(\mathbf{x_i}) \equiv \mathbf{x_i}$, and in particular $p(\mathbf{I}(\mathbf{x_i})=\mathbf{j}) \equiv \mathbf{p}(\mathbf{x_i}=\mathbf{j})$. Formally, the objective is to calculate the estimator $\hat{p}(\cdot)$ to be as close as possible to the Bayes estimate $p^*(x_i=j)$; in other words the probability that a given test vector has label j, where $1 \leq j \leq C$. This can be factored into a likelihood term and a prior probability that sample i is of label j:

$$\underbrace{\hat{p}\big(x_i=j\big)}_{\text{posterior}} = \underbrace{\hat{L}\big(x_i=j \,\big|\, \mathbf{x_i}, \mathcal{Y}\big)}_{\text{likelihood}} \underbrace{\mathcal{P}(x_i=j)}_{\text{prior}} \tag{2.35}$$

Typically, for experimental purposes, the prior terms are often all set to be equal; though naturally, in practical applications they may have specific values determined by the circumstances. The posterior estimator is an estimate of the unknown, optimal, Bayes estimate $p^*(\cdot)$. By assuming an exhaustive and exclusive labelling, both $\hat{p}(\cdot)$ and $p^*(\cdot)$ will sum to unity over the C classes. Additionally, the Bayes estimate $p^*(\cdot)$ is optimal in the sense that it minimises the posterior expected loss over the unseen test set $\mathbf{x_i}$, across all possible estimates $\hat{p}$.

The appropriate evaluation measure for any given estimate, is the Kullback-Leibler divergence $D(p^*(\cdot), \hat{p}(\cdot))$. However, since in general $p^*(\cdot)$ is unknown, one way to report the accuracy of a particular estimator $\hat{p}_\alpha$ is by evaluating its mean log posterior LP_α, using a sufficiently large unseen test set $\mathcal{X}$:

$$\mathrm{LP}_\alpha = \sum_{i=1}^{m} \log \hat{p}_\alpha\big(\mathbf{I}(\mathbf{x_i})=\mathbf{x_i}\big) \tag{2.36}$$

This expression quantifies the extent to which this estimator 'picked the right horse to win the race', *i.e.* the value of $\hat{p}(\mathbf{x})_\mathbf{i}$ for the correct label x_i . This quantity is maximised for the Bayes estimator p^*, and it can be used to compare the relative accuracies of any two methods α and β, with estimators $\hat{p}_\alpha$ and $\hat{p}_\beta$. One aspect of this metric is that it

diverges to $-\infty$ if $\exists i : \hat{p}\big(\mathbf{I}(\mathbf{x_i}) = \mathbf{x_i}\big) = \mathbf{0}$. As a consequence, the estimator fails to assign a finite probability to an event that did indeed transpire. To address this problem, an estimator should assign finite probabilities to all possible label assignments.

Alternatively, the accuracy of the estimates can be evaluated by combining evidence from S multiple sources; in other words, the set of training sets $\{\mathcal{Y}_1, \ldots, \mathcal{Y}_S\}$, where the vectors in each set have their own associated feature space. If these sources are independent, then the combined estimate $\hat{\mathbf{p}}(\cdot)$, using these estimators for these features is:

$$\hat{\mathbf{p}}(\mathbf{x_i} = \mathbf{j}|\mathcal{Y}_\mathbf{1} \ldots \mathcal{Y}_\mathbf{S}) = \frac{\prod_{\mathbf{s=1}}^{\mathbf{S}} \hat{\mathbf{p}}(\mathbf{x_i^s} = \mathbf{j}|\mathcal{Y}_\mathbf{s})}{\sum_{\mathbf{c=1}}^{\mathbf{C}} \prod_{\mathbf{s=1}}^{\mathbf{S}} \hat{\mathbf{p}}(\mathbf{x_i^s} = \mathbf{c}|\mathcal{Y}_\mathbf{s})} \tag{2.37}$$

The standard approach is to define a proportional estimator [100], $\hat{p}_{\text{PROP}}(\cdot)$, as follows. For any given input vector $\mathbf{x_i}$, the subset of K nearest training set neighbours is ordered according to their ascending distance to the considered sample $\mathbf{y_1^i}, \ldots, \mathbf{y_k^i}, \ldots, \mathbf{y_K^i}$, whereas $K_i(j)$ denotes the number in this set that is of category j. (The superscript i denotes that the order of the indices $1, \ldots, K$ is determined by the test vector $\mathbf{x_i}$). Then, an estimate $\hat{p}'$ of the probability that $\mathbf{x_i}$ belongs to category j, is constructed proportionally to $\frac{K_i(j)}{K}$. It is shown that in the case of large training set size, equation 2.38 converges to the definition of probability density. Figure 2.10 illustrates the PROP estimator and the Bayes Risk.

Furthermore, the estimator is not very efficient at making use of the available information. For instance, it assigns zero probability to those outcomes for $\mathbf{x_i}$ lacking any 'precedent' in the training set; *i.e.* for which, among the K members of the training set nearest to $\mathbf{x_i}$, none have a matching category, so $K_i(j) = 0$. To overcome this problem, a constant proportion of the probability mass, Ω, is allocated to account for this chance of 'model failure', shared out equally among the C classes:

$$\hat{p}_{\text{PROP}}(x_i = j) = \frac{(1 - \Omega)K_i(j)}{K} + \frac{\Omega}{C} \tag{2.38}$$

A similar approach is integrated into all types of estimator investigated here. While it is possible to optimise the value assigned to Ω, it would take very large, stationary datasets to get any meaningful results, since it is effectively insurance against rare outcomes. Atiya [101] generalises this idea by proposing the assignment of an unconstrained weight w_k to each member of the training set $\mathbf{y_k}$, using a sigmoid function to transform this into g_k, which always lies in the unit interval. As a result, an estimate is given by the

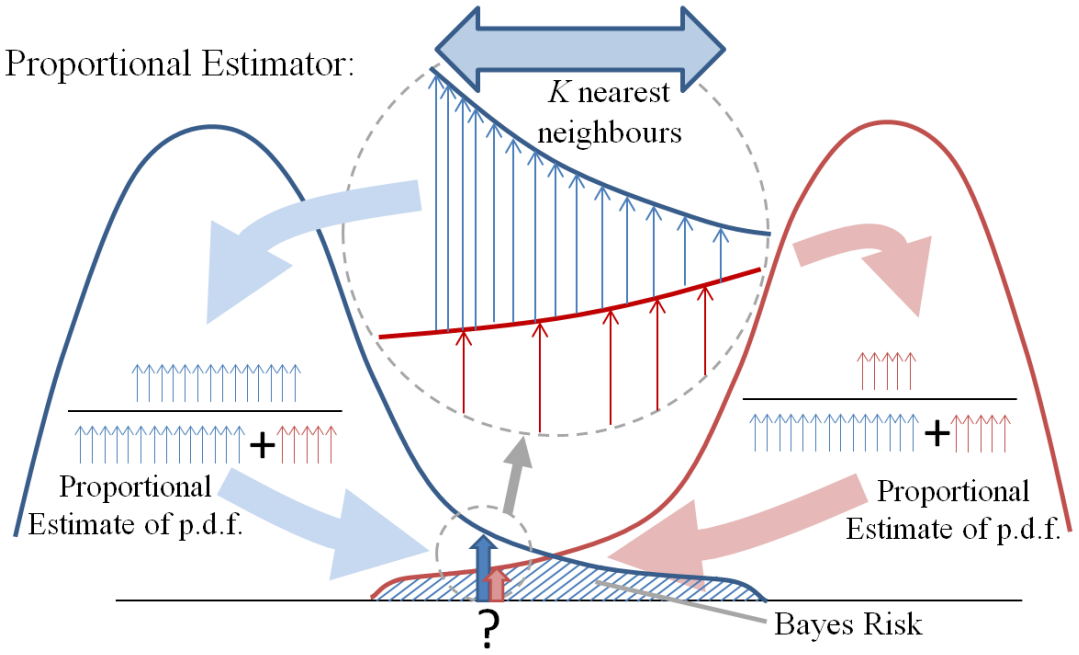

FIGURE 2.10: Supposing estimates of posterior probability density functions for two classes are required: the PROP estimator uses the proportion of the K neighbours found to have that class label in each case. As the overall density (number) of available neighbours increases, this estimate will converge on the true p.d.f. However, it makes inefficient use of the available information. Also shown is the 'Bayes Risk'; which is the expectation of minimum risk due to some inevitable errors.

following equation:

$$\hat{p}_{\text{WPROP}}(x_i = j) = \frac{(1-\Omega)K_i(j)}{K} \sum_{k=1}^{K} g_k \delta(y_k = j) + \frac{\Omega}{C} \tag{2.39}$$

where the $\delta(\cdot)$ picks out only those neighbours of category j, and Ω is once again the term to guard against model failure. The key advantage is that, within the training set, the set of unconstrained weights $\{w_k\}$ can be optimised to maximise the likelihood of the training set given this estimator: the cost function can be shown to be convex with the appropriate stationary point. Thanks to this, the efficient search approach by gradient-ascent is applied to find the optimal set of weights.

The Parzen windows algorithm is regarded as a generalisation of the K-NN techniques, however assigning a weighting function from a Gaussian kernel (which requires optimisation) [102, 103]. Parzen windows has no implementation of a training phase; however, the query phase remains quite slow due to the lack of sparseness. Similar to the K-NN classifier, asymptotical convergence is expected on the performance of Parzen windows [104]; although there are no such guarantees exist for finite sample sizes. There are

also other approaches to density estimation: parametric methods such as expectation-maximization of Gaussian mixture models [105], and non-parametric kernel-based methods [106, 107] that generalise the histogram-based accumulation of samples. In chapter 5 of this research survey, we implement both the PROP and WPROP methods for density estimation from a K-NN classifier. In addition, a set of novel approaches are described to define a series of estimators based on tabulation of prior statistics.

2.7 Chapter Conclusion

Automatic on-line measurement of broken rice is a difficult problem that is not fully explored in the literature. Implementations for static measurement have been documented using flat-bed scanning equipment with varying levels of success. Other systems have been developed for an on-line implementation; where several key advancements have been made: in the selection of partial-dark field illumination for highlighting of the object edges; other systems use stroboscopic illumination to remove the issues associated with motion blur from moving objects captured from area cameras. These key aspects are employed in the measurement system developed throughout this thesis.

Camera calibration poses an important and fundamental task of removing optical distortion from the image. The pinhole model and the extension for modelling the distortions caused by the curvature of the lens, in an area camera, have both been described. The extraction of the foreground object contour is also a core component of image processing systems. There are numerous methods for image segmentation and edge detection that we can use as part of the contour extraction process. Chapter 3 contains the implementations of an existing method in addition to three novel calibration techniques specifically designed for this type of accurate measurement system. Additionally, we also describe the contour extract techniques and length definitions and the associated evaluation methods. In particular, a novel approach is considered to create a hybrid between local and global thresholding.

An existing technique was found to model the bias within a finite measurement aperture. However, when measurements are made for moving particles such as rice grains, there is an additional error from the objects touching each other. Accurate contour information from touching grains of rice can not be simply inferred. In chapter 4, we explore a technique to correct for the bias errors associated with touching objects. Smaller objects are less likely to be touching, and as smaller objects are more likely to be broken then the broken percentage measurement of the input sample would be incorrect.

The last portion of literature that we have explored pertains to the identification of plant leaves using shape features and pattern recognition classifiers. We emphasise that plant species classification allows a suitable level of complexity for multi-class classification, and also the potential difficulties when working with low samples of training data. A set of shape, interior texture, and fine-scale margin features are described for leaf images. We also note the robustness and straightforward approach of combing density estimates computed from separate features within a probabilistic classification framework. Therefore, we focus on two standard approaches that estimate the class posterior using the K-Nearest Neighbours method. Chapter 5 discusses the framework for identification of plant species with leaves. In addition, we describe a set of novel methods for posterior probability estimation using tabulated sets of statistics.

Chapter 3

Static Measurement of Rice Length

In the previous chapter we discussed the existing research related to the measurement of broken rice, and the key stages of building a complete on-line computer vision system. In this chapter, we present a system for the accurate length measurement of static rice grains on a glass plane. Rice grains that are manually placed in the viewing area of this system must not be touching one another.

The first section in this chapter discusses the overall problem of the measurement system. Following from this, the first section of work beings with the methods and evaluation of camera calibration for optical distortion correction and real-world unit conversion. A description is given of how to select a suitable operating point between optical distortion and contrast caused from selecting different optical lenses; in particular, a selection needs to be made between 8, 16, and 24 mm focal length lenses. Section 3.2 contains a body of work that estimates the uncertainty in the length measurement caused by the quantisation effect of the area camera. Section 3.3 explores the selection of the most suitable contour extraction algorithm, used to remove variation in the foreground signal caused by different configurations of the optical system. Section 3.4 defines the experiments that measure the accuracy of the various length descriptions of imaged static rice grains. A data-set consisting of US Long rice is used to evaluate the accuracies of each length definition that is tested. Both broken and head rice samples are tested to evaluate the length measurement errors from the static measurement apparatus. The final section concludes the chapter with the significant findings.

3.0.1 Outline of the Problem

It was previously indicated that rice millers have the needs for a low-cost, low-maintenance, robust and unbiased, on-line measurement of broken rice percentage. The goal of this research is to work towards such an on-line measurement system. Computer vision provides an alternative for automated and non-destructive technique to accomplish these requirements. Such an inspection system based on image analysis and processing has a variety of applications in the food industry [108]. However, applying these techniques to a granular food product contains a number of specific problems to overcome.

Firstly, measurements made on images of rice introduce new sources of error such as optical distortion from the camera lens, and the consistency of the rice edge signal, *i.e.* the segmentation of the foreground pixels from the background. In addition to the removal of distortion, there is the necessity to convert from pixels to real-world measurement units for the use of length measurement, *i.e.* from image co-ordinates to millimetres. The target objects are physically small, such that the resolution of the imaging device needs to be sufficient to prevent quantisation from biasing the measurements made. Secondly, a direct problem with working with rice is the presence of rice dust in the product stream.

To keep the sensor low-cost, and food safe, the machine would need to be self-cleaning without many mechanical moving parts (that may damage the product or interrupt the efficiency of the mill, or introduce new costs with wear and tear and cleaning). Image analysis of moving rice on a viewing area, such as a glass chute, would provide a low-cost sensor that is self cleaning; the downward flow of rice on the glass chute would continuously clean the glass itself. Thirdly, the definition of a broken rice grain from an image produces a set of errors associated with the subjectivity of the definition and the ground-truth. For example, the by-length criteria for a broken grain can be implemented, but this would rely heavily on the accuracy of a length measurement of a rice grain from the image. Additionally, the accuracy of the rice grain contour would be pertinent to the shape feature descriptors of the rice, when used as an additional classification criteria to length.

Additionally, a bias effect is expected when measuring from a sample of grains assumed to be 'single'. In reality, the free flowing rice grains can and will touch each other and thus parts of rice grains may be occluded within the image. There is also a bias error related to measuring particles within a finite aperture. In both cases of edge effects and occlusion, larger objects are more likely to be 'touching', than smaller objects. Therefore, any measurement made on the sample of rice grains assuming the grains were single, *i.e.* not touching, would be biased. Finally, the industry standard measurement for broken

percentage of rice is a by-mass unit, not a by-count one. It is generally accepted that the errors for a by-mass unit are approximately half that of a by-count unit. The automatic system using an imaging source would not have access to the weight information of the rice grains, and would need to be able to convert to a by-mass percentage of broken rice on-the-fly.

Figure 3.1 shows how the *general* problem, of enabling a computer vision based system to measure the percentage of broken rice grains, can be divided into three main stages. The first stage consists of camera calibration: a one-time set-up of the measurement system. This process describes the one-time task of calibrating the measurement tool for removal of optical distortion and conversion to real world units. A calibration look-up table is created once, then subsequently used during the measurement stages of the system. The second stage is single grain contour extraction, which is part of the measurement pipeline. The aim is to extract a calibrated and corrected (distortion free) contour of every singulated rice grain from the input image. The processes in this stage consists of rice contour extraction, which describes the segmentation of foreground from background pixels (and selection of the perimeter edge of the rice grains); and then single grain contour calibration, which applies the distortion correction model to the single rice grains (and converts the data to real-world units).

The final stage of the processing pipeline extracts key measurements about the singulated grains of rice. The aim here is to infer information about the rice grain, and then estimate the required measurement of the rice (such as the percentage of broken rice). The processes in this stage can consist of a length based approach, which is discussed extensively over the following chapters of this thesis. The solution can then be extended by allowing the inclusion of shape based feature extraction and classification, *e.g.* suitable pattern recognition methods with shape features extracted from the rice grain contour can be used to identify broken rice. Given the requirements of high-speed computation (for real time measurement), the classification process can be cascaded: such that only a selection of marginal broken grains would be further classified by shape. In the subsequent chapters, this processing pipeline will be further extended and described, to assist in clearly defining the system as it progresses through static measurement, to rice in motion, to on-line.

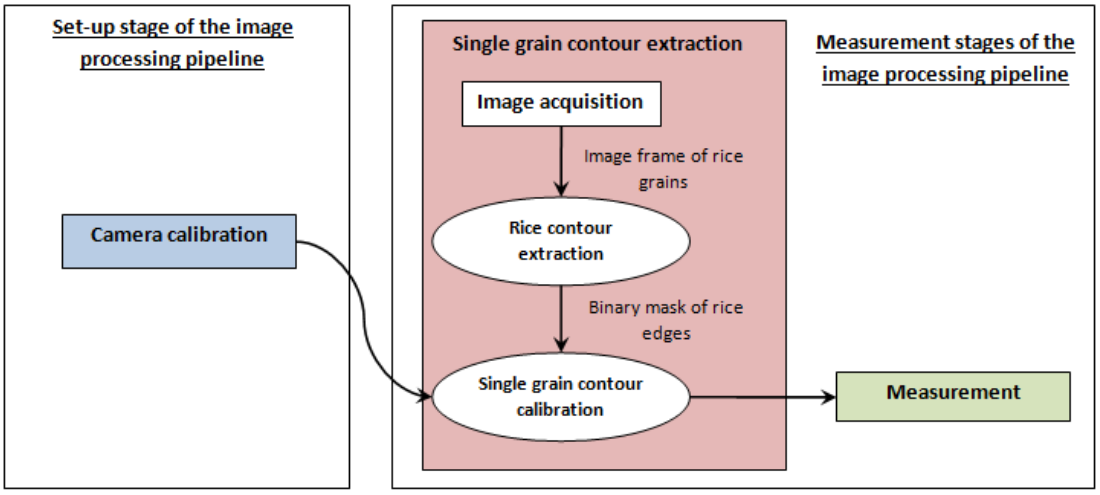

FIGURE 3.1: Overview of the general problem of enabling a computer to measure rice grains from an image captured with an area camera.

The operating point for the static rice measurement apparatus consists of a partial dark field lighting set-up. The illumination system has been configured to use stroboscopic dark field illumination, with a red coloured LED ring light. It is expected that a stroboscopic illumination source removes the 'ghosting' effect that may be seen at short exposure times, *i.e.* the illumination is switched off when the camera chip is being read after the frame has been captured. This effect will be highly desired when the system is modified to capture rice that is moving, to aid in the reduction of the negative effects of motion blur. The initial optical set-up is illustrated in figure 3.2. The imaging device used, is a 1.4 Megapixel CCD Ultra Compact Camera (GC1350, Prosilica, Canada), that has a spatial resolution of 1360-by-1024 pixels capturing at 20 frames-per-second, progressive scan CCD with square pixels, and Gigabit Ethernet interface. Three lenses were tested with the system: 8 mm, 16 mm, and 24 mm Compact Fixed Focal Length Lenses (Edmund Optics, UK); fitted with a C-mount to the camera.

An overview of the image processing pipeline of the rice in stasis apparatus is shown in figure 3.3. First, the camera calibration look-up table is created. Then, the measurement stages consist of the following processes: single grain contour extraction, and single grain contour calibration. Finally, the length measurement per calibrated grain contour is processed.

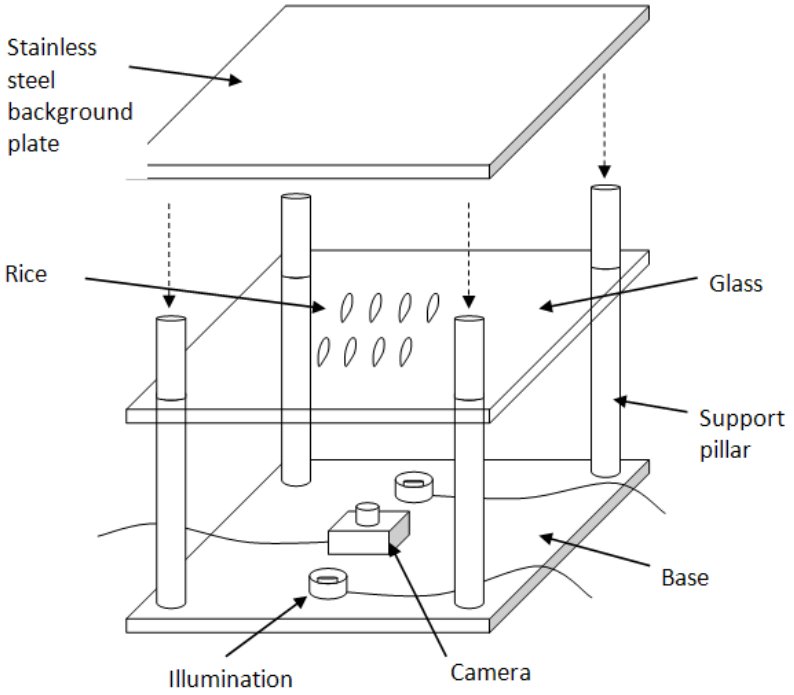

3.2.1 Concept sketch.

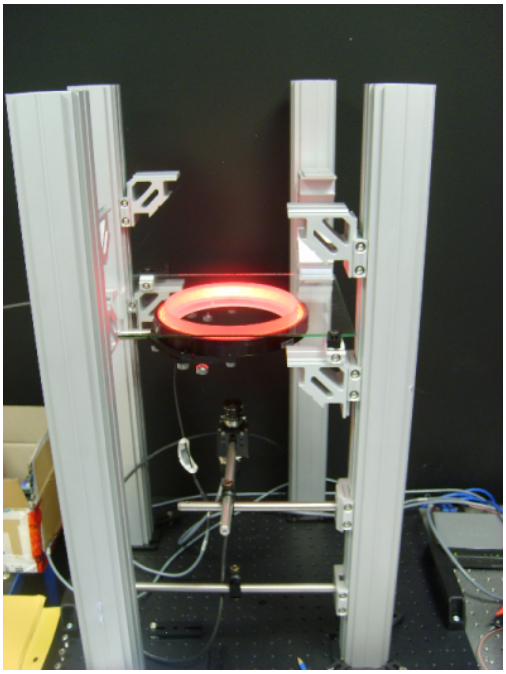

3.2.2 Photograph of the prototype hardware in the laboratory.

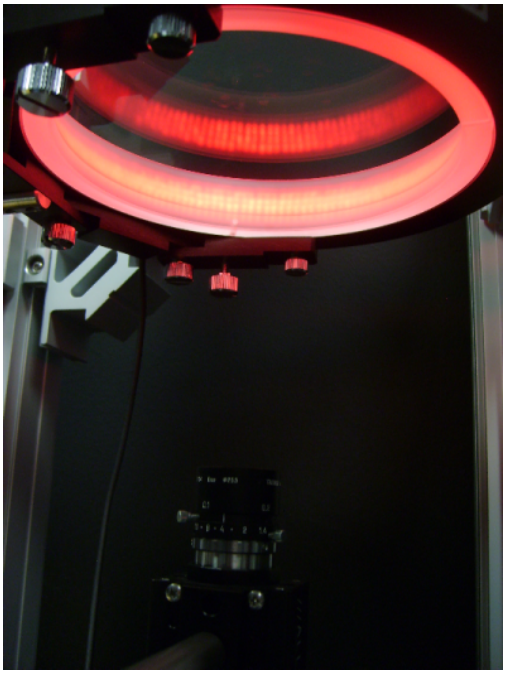

3.2.3 Photograph of the red LED ring light illumination.

FIGURE 3.2: Concept and prototype rice in stasis measurement apparatus.

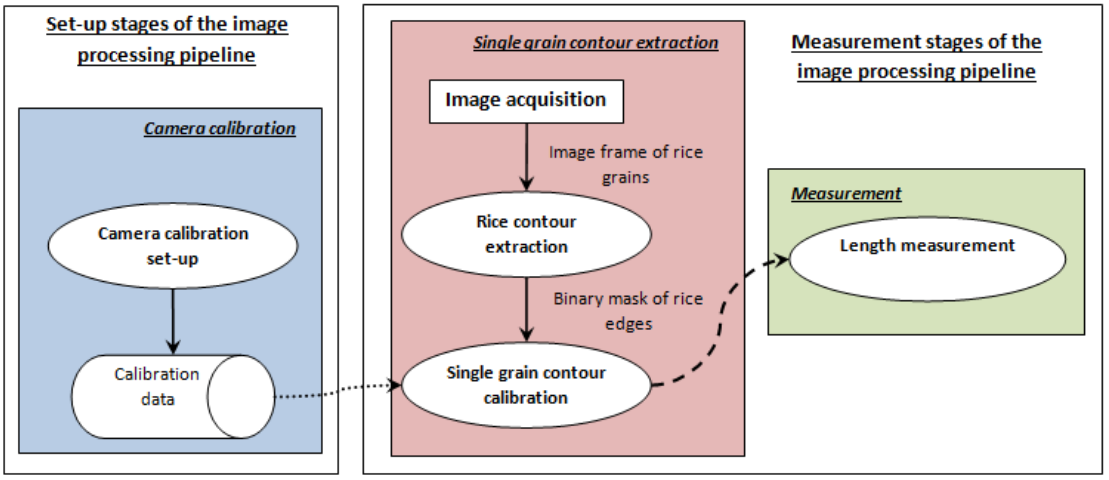

FIGURE 3.3: Overview of the problem of enabling a computer to measure the length of rice kernels.

3.1 Camera Calibration for Optical Distortion Correction and Real-World Units

Considering our specific application is a measurement system of the length of rice grains, a suitable algorithm is needed to limit the variation of the measurement caused by lens distortion. An example target may be a maximum of 0.05 mm variation across the view of the image when measuring the length between two points 6 mm apart, which is the average length of a white short rice kernel (a 0.83% error). The proposed camera calibration method will use a single image of a calibration pattern, used by the routine to create the correction model. A calibration target is a common requirement for many calibration solutions. When required, the correction model is subsequently used to estimate the corrected real-world length between any pair of pixel coordinates from within the image. The objects to be measured are assumed to lie on a plane, approximately perpendicular to the optic axis of the camera.

We hypothesise that there is a suitable operating point between the optical distortion from a given lens and the foreground to background contrast ratio. Therefore, an investigation is conducted with the potential optical set-up for the static measurement process by testing three camera lenses of focal lengths of 8 mm, 16 mm and 25 mm. The aim is to remove the optical distortion and provide a clear contrast between the foreground and the background, *i.e.* it is hypothesised that a ratio of foreground to background of at least 1.5 would be sufficient. It is expected that some residual optical distortion is virtually unavoidable with short focal length lenses, although as the focal length increases the optical distortion decreases. Additionally, the contrast of the foreground and background pixels is reduced when the distance between the lens and the target in the viewing plane is lengthened. The four tested calibration methods in this study consist of the following:

1. Full Calibration with Brown's Distortion Model (BDM), which is a physical lens model that compensates for both radial and tangential lens distortion.

2. Lattice of Scale Estimates (LSE), a novel first order calibration method to estimate any non-specific local distortion in the lens.

3. Smoothed Lattice of Scale Estimates(SLSE), where an appropriate smoothing model is applied to the Lattice to further reduce the correction error.

4. Parametric Regression Model (PRM), where the fitting of a polynomial surface from real-world to image coordinates provide a global mapping of the distortion.

In section 3.1.1 we describe the calibration pattern in full detail. The following three sections explain the novel LSE, SLSE, and PRM camera calibration methods. Section 3.1.5 defines the evaluation method for selecting a calibration routine that performs to our requirements.

3.1.1 Calibration Pattern

All lens distortion correction models implemented in this investigation use a calibration pattern, that usually consists of a fixed pattern which may be available on different media, which we refer to as the calibration target [35], see figure 3.4 for an example. It is assumed that a complete matrix of points from the pattern are visible within the viewing plane of the camera. Therefore, the number of circles within each row and column will be consistent, although there may be more columns than rows and vice versa (based on the aspect ratio of the camera). Additionally, a further assumption that the optical distortion is not so gross as to disrupt the correspondence, *i.e.* no extreme 'fish-eye' optical distortion is present.

The selected calibration target that for use in this project is a Fixed Frequency Grid Distortion Target (C/N: 58508, purchased from Edmund Industrial Optics, UK). The target contains an accurately printed pattern onto a white polyester film, called Mylar. The chosen pattern is a lattice of 75 by 75 circles of 1 mm diameter, with a 2 mm pitch from centre to centre. The certificate of accuracy of the Mylar target reports that the pattern is accurate to within ±35 microns corner to corner. This accuracy was confirmed by Max Levy Autograph Incorporated in Philadelphia, Pennsylvania, USA; where the measurement was made on an optical comparator from Optek, Texas, US, with periodic back calibration against a measured glass scale. Additionally, the circle size of which is accurate to ±13 microns and circle to circle spacing accurate to ±5 microns.

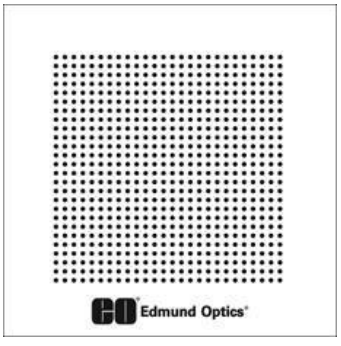

FIGURE 3.4: Example calibration target (Edmund Industrial Optics, UK.)

Given a 16 mm camera lens, the target would be placed on a glass viewing plane approximately 30 cm away. The illumination system with red LEDs is positioned below

the glass plane. The images of the target are processed in order to extract the binary signal of foreground and background pixels. Extraction of the circles from the image is a straightforward task, due to the uniform white background contrasting with the black circles on the target, as explained in section 2.3. A dust filter is then applied to remove any object in the image with less than 65 pixels, in addition to disregarding any objects with pixels touching the border of the image frame.

Each circle in the image is reduced to a single coordinate, referred to as the control point. If there are n_{ROW} rows and n_{COL} columns visible, with no missing elements, then there are $\{c_1, \ldots, c_i, \ldots, c_n\}$ control points where $n = n_{\text{COL}} n_{\text{ROW}}$. The control point coordinate for each circle is estimated as the centre of mass of the connected pixels of the circle, *i.e.* the mean coordinate of all the pixel coordinates from within the circle.

Each circle centre from $\{\mathcal{C}_i\}$ has two sets of coordinates. The first set of coordinates, $(\mathbf{u}_i, \mathbf{v}_i)$, are the estimated centre of mass of these circles in the distorted image. Figure 3.5 contains an example input image of the calibration target, from three different focal length lenses, with a back projection of the estimated centre of mass for each circle. The second set of coordinates, $(\mathbf{X}_i, \mathbf{Y}_i, \mathbf{Z}_i)$, are created to be the corresponding ground-truth points, in the world coordinate system, of the circle centres $(\mathbf{u}_i, \mathbf{v}_i)$. The real-world points are assumed to lie on an 'exact' lattice with a spacing of 2 millimetres, given the high accuracy printing of the Mylar target.

3.1.2 Lattice of Scale Estimates

The first novel method introduced in this thesis is this Lattice of Scale Estimates calibration method is not based on a physical model and thus does not directly estimate specific lens distortion. Rather, we aim to create a first order mapping of the set of points $\{\mathcal{C}_i\}$. The set of image points $(\mathbf{u}_i, \mathbf{v}_i)$ and world coordinate points $(\mathbf{X}_i, \mathbf{Y}_i, \mathbf{Z}_i)$ are used to make local estimates of the scaling between any two adjacent (or nearby) points; essentially 'snapping' any given image points to the nearest pattern points and providing the estimate of scale from the calibration grid.

Consider that g and h are two points of interest anywhere in the two dimensional image, *i.e.* any pair of pixel coordinate in the image that is of interest such as the ends of a rice grain, and $||g - h||$ is the Euclidean distance between these two points. The length $\hat{l}$, in millimetres, is:

$$\hat{l} = ||g - h||\, \psi \tag{3.1}$$

where ψ is a global scaling factor (the ratio of mm to pixels).

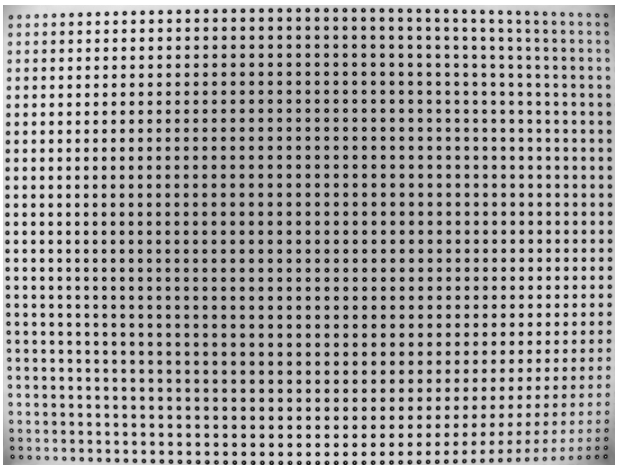

3.5.1 8 mm

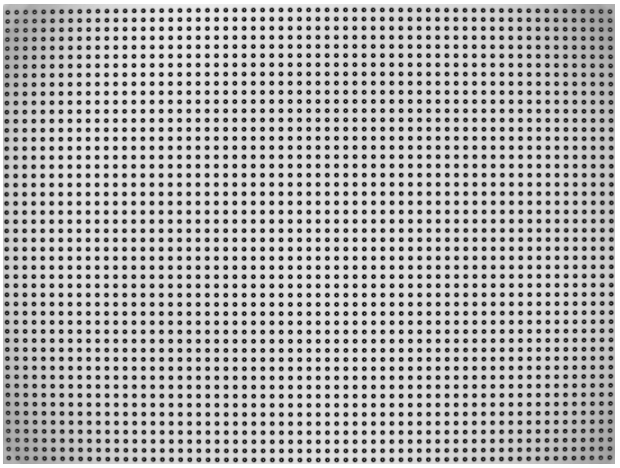

3.5.2 16 mm

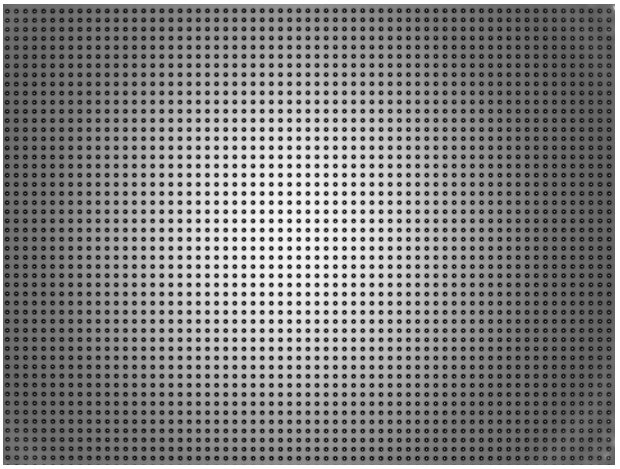

3.5.3 25 mm

FIGURE 3.5: Sample image of the calibration target from three different focal length lenses. The white dots represent a back projection of the extracted centroid of each circle. From the three different lenses, the relative levels of optical distortion are visible, where the most distortion is visible using 8 mm lens, then the 16 mm lens, and finally the lowest level of distortion with the 25 mm lens.

The length $\hat{l}$, in its current form, may be inaccurate due to the distortion from the lens (as one would expect). We intend to incorporate an estimated local correction factor within the global scaling factor ψ. From the set of distorted image points $(\mathbf{u}_i, \mathbf{v}_i)$, we select the nearest control point, $\mathcal{C}_g$, to point g. The selection can be completed by iteratively searching for the minimum Euclidean distance between all other points to g, *i.e.* $\mathcal{C}_g$ is the index i of $\min(||g - \{\mathcal{C}_i\}||)$.

The point $\mathcal{C}_g$ has both image coordinates $\mathcal{C}(\mathbf{u}_g, \mathbf{v}_g)$ and real-world coordinates $\mathcal{C}(\mathbf{X}_g, \mathbf{Y}_g, \mathbf{Z}_g)$. Similarly, the nearest control point $\mathcal{C}_h$ to point h must be selected in the same way as for $\mathcal{C}_g$. The estimated global scaling and local correction factor between these points is given as:

$$\psi = \frac{||\mathcal{C}(\mathbf{X}_g, \mathbf{Y}_g, \mathbf{Z}_g) - \mathcal{C}(\mathbf{X}_h, \mathbf{Y}_h, \mathbf{Z}_h)||}{||\mathcal{C}(\mathbf{u}_g, \mathbf{v}_g) - \mathcal{C}(\mathbf{u}_h, \mathbf{v}_h)||} \tag{3.2}$$

Given that the process approximates the scale factor between the *nearest* grid points to the query points, we expect a margin of error in the solution. The components of this process are illustrated in figure 3.6.

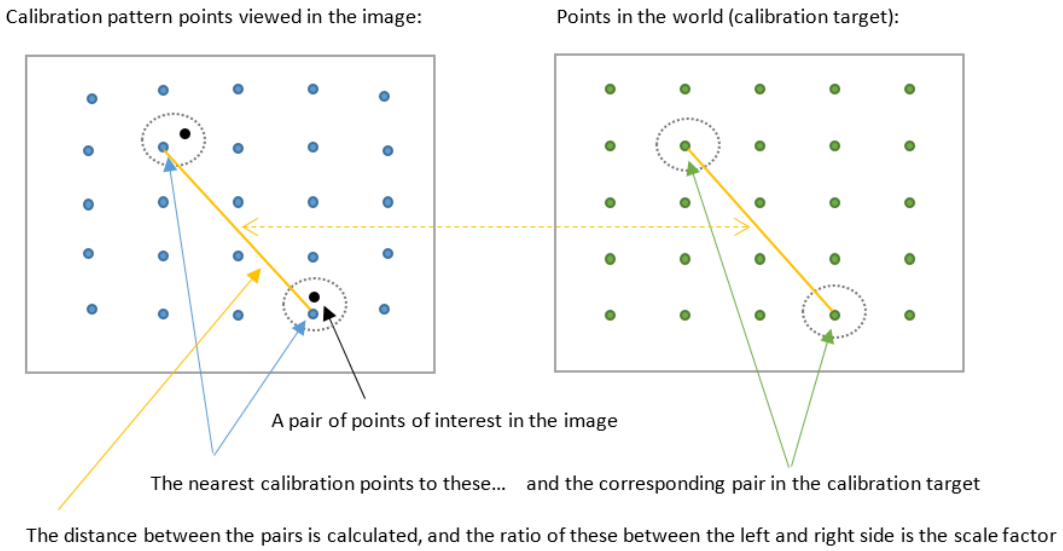

FIGURE 3.6: Estimating the scale and correction factor between two points in the image. The grid on the left hand side represents the imaged calibration pattern. The grid on the right hand side represents the real-world pattern. The estimates scale factor is the ratio of the two yellow lines, between the two point of interest g and h (black circles).

A diagnostic visualisation tool of the distortion can be created as 3D surface plots of a set of scale factors calculated between the lattice of circle points in the calibration pattern. We calculate a set of scale factors in two directions, horizontal and vertical, between all points in the pattern. Example completed lattices of scale estimates are shown in figure 3.7. From these diagnostic images, the error caused by the quantisation of point-pairs is

clearly visible; however, the slow trend of lens distortion is also visible. We observe that the distortion appears to differ in severity between horizontal and vertical directions.

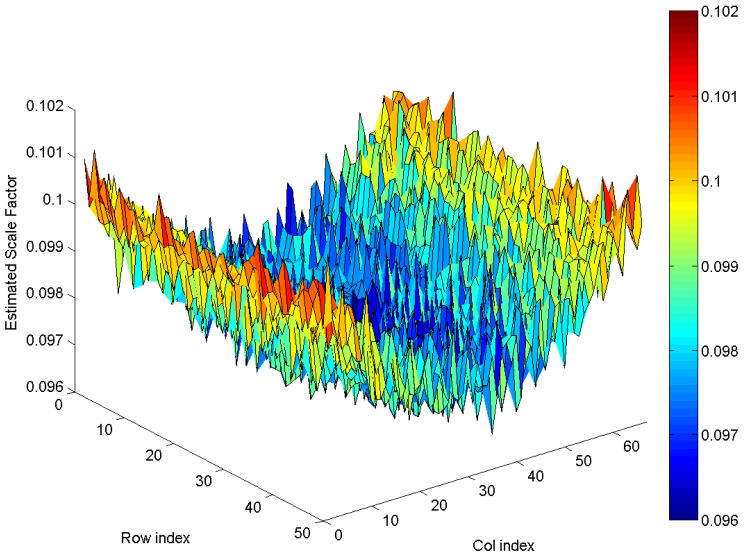

3.7.1 Analysis between horizontal points.

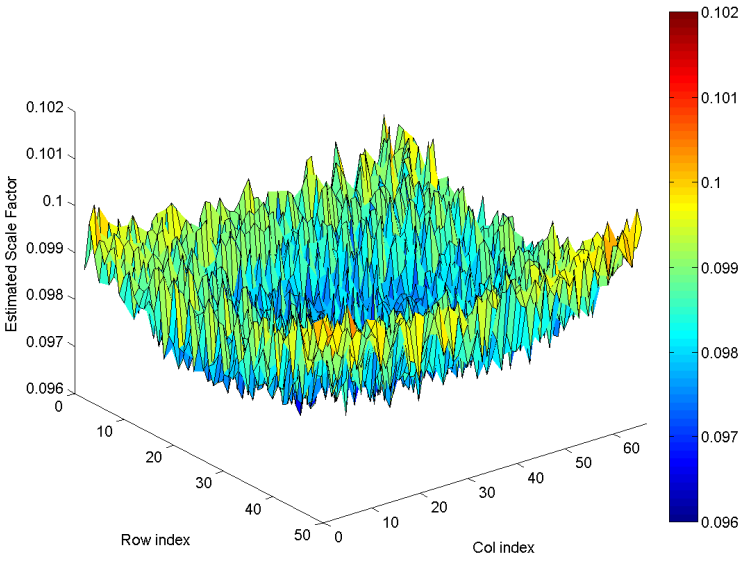

3.7.2 Analysis between vertical points.

FIGURE 3.7: Visualisation aids that illustrate the LSE novel scale factor estimates. The change in scale factor is apparent across the entire view. In addition to the error of these estimates are evident, produced by the error from the centroid estimations of the circles in the image.

3.1.3 Smoothed Lattice of Scale Estimates

This method applies a smoothing model to the LSE method in section 3.1.2, to attempt to reduce the variance of the correction (see figure 3.7. The aim is to provide a smooth signal which has any high spatial frequency variations removed, leaving only the low spatial frequency trend. The proposed method for smoothing the lattice of scale estimates is a rotationally symmetric Gaussian low-pass filter [109] [37] of a fixed kernel size and strength (modelled by the standard deviation of the elements in the filter). The filter is applied to the scale factors using convolution and not applied to the image pixels themselves.

When the kernel is positioned in the matrix of scale factor estimates, some array values may be out of bounds. A smaller/modified kernel is used in these situations, so as to not include any influence of the null elements. Intuitively we would expect a small filter size is sufficient to reduce short-term variations, such as 7-by-7 kernel size. For on-the-fly calculation of the scale factor, the Gaussian filter can be used to smooth a small window of the scale factors that surround the nearest points to g and h. Two smoothed lattices of scale estimates are illustrated as surface plots in figure 3.8. The same method for creating these visualisations of the scale factors were used as the LSE method, shown in figure 3.7.

3.1.4 Parametric Regression Model

The second novel method for addressing camera distortion is the Parametric Regression Model, where a piecewise cubic interpolation with nonlinear least squares regression [37, 110] is used to estimate a global mapping from the set of points $\{\mathcal{C}_i\}$ from the set of image pairs $\{\mathbf{u}_i, \mathbf{v}_i\}$, and world coordinate pairs $(\mathbf{X}_i, \mathbf{Y}_i, \mathbf{Z}_i)$. We would expect a similar effectiveness of this model compared to the SLSE method, as they are both based directly on a fitting of the control points. Two slopes are created by mapping the set of image coordinates to the world coordinates $\mathbf{X}_i$ against $\mathbf{u}_i, \mathbf{v}_i$ and $\mathbf{Y}_i$ against $\mathbf{u}_i, \mathbf{v}_i$. Two functions, $\mathbf{X}_i = f(\mathbf{u}_i, \mathbf{v}_i)$ and $\mathbf{Y}_i = g(\mathbf{u}_i, \mathbf{v}_i)$, will fit the polynomial model to these two surfaces using a non-linear least squares method. Linear regression is not used due to the curvature of the distortion. A 3rd degree polynomial was found to create a suitable mapping of the distortion; in this case the function to arrive at the corrected $\mathbf{X}$ coordinate $\mathbf{X}'$ is:

$$\mathbf{X}' = x_{00} + x_{10}\mathbf{u} + x_{01}\mathbf{v} + x_{20}\mathbf{u}^2 + x_{11}uv + x_{02}\mathbf{v}^2 + x_{30}\mathbf{u}^3 + x_{21}\mathbf{u}^2\mathbf{v} + x_{12}\mathbf{u}\mathbf{v}^2 + x_{03}\mathbf{v}^3 \quad (3.3)$$

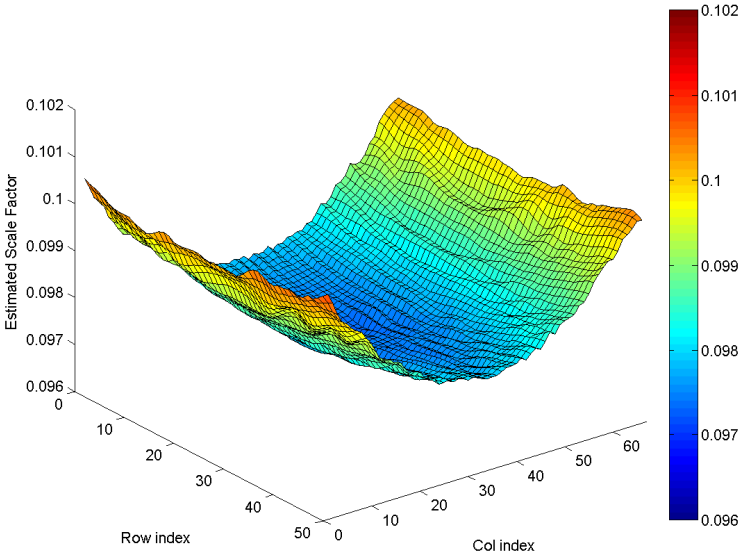

3.8.1 Analysis between horizontal points.

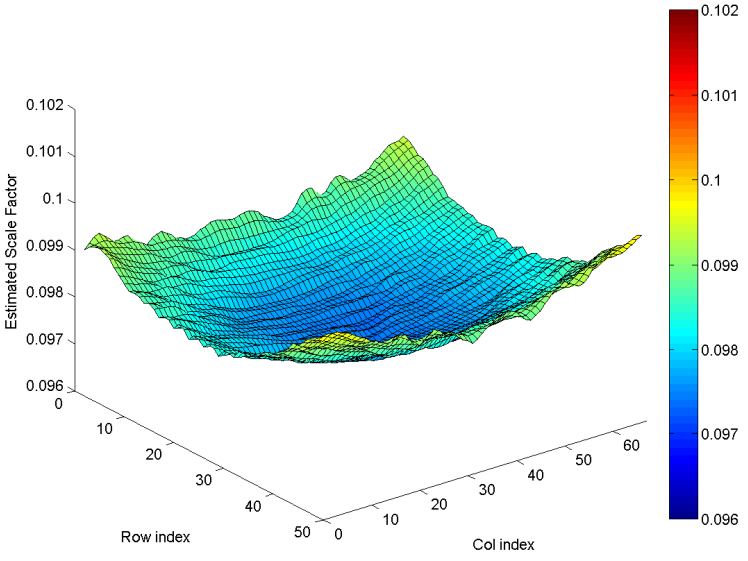

3.8.2 Analysis between vertical points.

FIGURE 3.8: Visualisation aids that illustrate SLSE scale factor estimates with a Gaussian filter size of 5-by-5 and strength of 2. The majority of local variations in the error are effectively removed by the approach, compared to the scale estimated shown in figure 3.7.

where $x_{00}, x_{10}, x_{01}, x_{20}, x_{11}, x_{02}, x_{30}, x_{21}, x_{12}, x_{03}$ are the estimated coefficients of the surface fit $\mathbf{X}_i = f(\mathbf{u}_i, \mathbf{v}_i)$. Similarly the function to arrive at the corrected $\mathbf{Y}$ coordinate $\mathbf{Y}'$ is:

$$\mathbf{Y}' = y_{00} + y_{10}\mathbf{u} + y_{01}\mathbf{v} + y_{20}\mathbf{u}^2 + y_{11}\mathbf{uv} + y_{02}\mathbf{v}^2 + y_{30}\mathbf{u}^3 + y_{21}\mathbf{u}^2\mathbf{v} + y_{12}\mathbf{uv}^2 + y_{03}\mathbf{v}^3 \quad (3.4)$$

where $y_{00}, y_{10}, y_{01}, y_{20}, y_{11}, y_{02}, y_{30}, y_{21}, y_{12}, y_{03}$ are the estimated coefficients of the surface fit $\mathbf{Y}_i = g(\mathbf{u}_i, \mathbf{v}_i)$.

3.1.5 Performance Evaluation

An initial insight into determining a suitable performance metric for the calibration method is to use the calibration target itself as ground-truth information. We could examine the rows or columns of the measured distances between the circles in the pattern for both the horizontal and vertical directions. We would expect that an increased parabolic shape indicates a stronger distortion. It is hypothesised that there is an additional error term added by the estimation of the control point centroid. We expect that the impact of this error is reduced in inverse proportion to the distance, as the gap between the two points being measured is increased. Consider the combined variance of the error, σ_E^2, is a function of $(\sigma_{\delta c}, \sigma_{\delta d})$, where $\sigma_{\delta c}$ is the variance of the error of the estimated control point and $\sigma_{\delta d}$ is the error from the distortion. Thus,

$$\sigma_E^2 = \sqrt{\sigma_{\delta c}^2 + \sigma_{\delta d}^2} \quad (3.5)$$

We then expect that the error increases linearly over distance:

$$\sigma_{\delta d} = \sigma_{\delta m} \cdot G_d \quad (3.6)$$

where $\sigma_{\delta m}$ is the error per millimetre, and G_d is the distance between the two control points i and j.

The first figure of merit is the statistical standard deviation of all the Euclidean distances between adjacent control points in the calibration pattern, *i.e.* orthogonal to the lattice, denoted as ε_σ. If the circles on the printed calibration target are 2 mm apart with little error (see section 3.1.1), then: $\varepsilon_\sigma \approx 0$. The same measurement from the circles in the captured image before and after calibration will highlight the variation across the view. Both horizontal and vertical pairing of consecutive circles are considered together to create a single measurement.

For the uncalibrated image an estimated scale factor $\psi = \frac{d_\mu}{G_d}$ is used to make the image pixel distances comparable with the calibrated millimetre distances, where G_d is

the ground-truth distance between the measured control points (2 mm) and d_μ is the arithmetic mean of the Euclidean distances between consecutive points on the lattice. A histogram of the distances between consecutive points can be produced as a diagnostic tool. The mean distance of all horizontal distances between consecutive points can be calculated for each column to show a trend of the apparent distortion across the width of the image. Likewise, the mean distance of all vertical consecutive points can be calculated for each row to show a trend across the height of the image.

The second figure of merit estimates the absolute error across the view, *i.e.* the level of nonuniform error caused by the lens. The mean error is defined as $\varepsilon_\mu = |d_\mu - G_d|$. We would be reasonably confident of accurately estimating the distortion if the distribution of errors are Gaussian. This metric is particular useful in our situation, since our final goal of measurement percentage of broken rice in this chapter depends on the length measurement of objects in the image view. Experiments 3.1, 3.2 and 3.3 are conducted to evaluate the novel and existing correction methods using these figures of merit.

Experiment 3.1. We observe the error over various distances between pairs of control points, to ascertain a suitable operation point for useful analysis of the calibration correction methods. A sweep of distances from 2 mm to 30 mm was computed using the correction model from the full BDM calibration method. For this experiment, only the 16 mm lens was calibrated and tested. A distance of 2 mm equates to consecutive control points, 4 mm equates to one control point between the pairs, 12 mm equates to 5 points between the pairs, *etc.* Figure 3.9 shows the results of the error measurement as a function of the distance between the measurement points.

In this particular experiment, we isolate the error by applying correction onto the same control points which were used to create the calibration model. The gradient of the curve indicates the distortion error. Consider a perfect correction was obtained, we would expect that the offset of the curve where it intersects at zero, represents the error of the centroid estimation and that this would be the same before and after calibration. We observe there is a trade off between reducing the proportion of error from the estimation of the centroid. Thus, the spacing between control point pairs has been fixed to 12 mm. A common and useful analysis measurement method in engineering is to use 2σ to represent the error (at 95% of the population of data), so the reported 12 mm error would be equivalent to the 2σ of a 6 mm distance.

Experiment 3.2. Two calibration figures of merit are calculated from a series of images from the static measurement apparatus. The calibration target is observed four times, where a 90° rotation of the target is made between each image. In addition, a

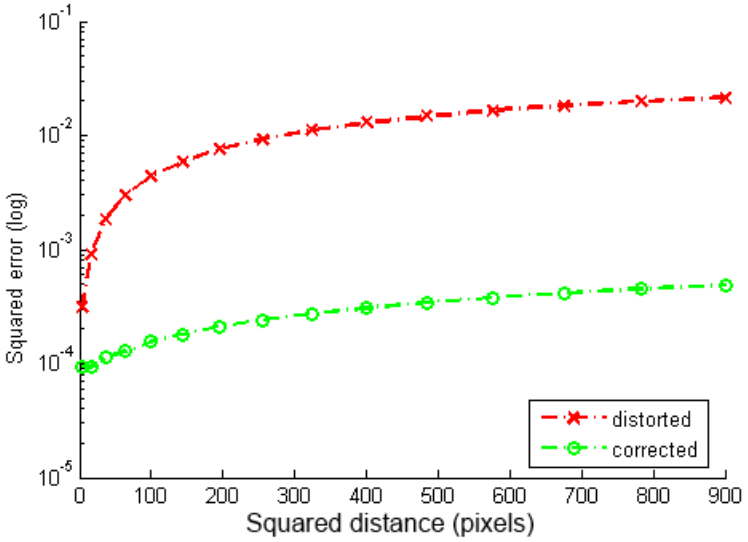

FIGURE 3.9: The measurement error (in pixels) based on the distance between control points of the calibration pattern, using the BDM correction model. The gradient of the curve for uncorrected (distorted) data indicates the relative error at different distances between the measurement points.

series of four images are captured where a 45° rotation of the target was made between each image; to highlight any error from diagonal measurements made from the system. The performance metrics are computed for each image, using the 12 mm distance as the ground-truth (selected from Experiment 3.1), and presented as an average of the four results.

Table 3.3 contains the calibration accuracy results, where a scale factor of 12 pixels per millimetre is used for the UNCALIBRATED case (for comparative purposes, see Experiment 3.1). The mean error should be carefully considered in the UNCALIBRATED case, because of the estimated scale factor used. We observe that all tested calibration methods reduced the error of distances between control points 12 mm apart from an estimated 0.7%, in the uncalibrated case to, at most 0.1%. For the mean error, all methods produced a reduction from 1.8% to 0.02%. Both of these errors surpass the target of 0.83% error. We remain confident with the results, as indicated by the Gaussian shaped distribution of a population of 6,000 measured distances, see the diagnostic plots in appendix A. It is recommended not to use the full calibration method with Brown's model as the selected calibration method, considering that the reported absolute error was worse in all tests as well as the increased design complexity. Additionally, the diagnostic plots indicate some form of distortion remains, indicated by the slope in figure A.1.3.

The best noted performance for distortion removal is either the PRM Regression method or the SLSE method, both providing the most reduction to the error. The recommended calibration method is PRM with 3 degrees of freedom which offers a flexible distortion

Direction	Method	Mean (mm)	ε_σ (microns)	ε_μ (microns)
90°	UNCALIBRATED	12.2	78.3	213.4
	BDM	12.0	13.9	2.8
	LSE	12.0	14.0	1.6
	SLSE	12.0	11.3	1.0
	PRM	12.0	10.2	1.7
45°	UNCALIBRATED	17.3	116.0	308.8
	BDM	17.0	17.8	3.9
	LSE	17.0	14.9	2.3
	SLSE	17.0	12.4	1.5
	PRM	17.0	11.1	2.5

TABLE 3.1: Results of the calibration methods, expressed as the mean error between a set of points 12 mm apart. The UNCALIBRATED results are estimated by converting the pixel error to millimetres with a global scale factor of 12 pixels per millimetre.

removal technique in addition to having the advantage of being less complicated. This method additionally offers a suitable scaling factor strategy to estimate the pixel to millimetre conversion, shown by the low absolute errors of 1.7microns; although the SLSE method have the lowest mean error of 1.0 microns.

Experiment 3.3. The relative levels of optical distortion from various lenses can be observed from images captured from the camera system. Figure 3.5 contains the back projection of the calibration pattern from the system using an 8, 16, and 24 mm lens. The changes in the contrast across the view in these specific images highlight the variation in the foreground only (as the Mylar target is obscuring the background). The outcome of this experiment is the selection of an optical set-up consisting of a lens with a suitable focal length and distance from the target viewing plane. The selection of the lens is then fixed for all subsequent investigations. This is done to reduce the complexity of the experimentation process as the optical set-up is tightly coupled with the camera calibration and contour extraction method.

Table 3.2 contains the calibration results per lens type tested in the system. The selected camera calibration methods have provided a similar performance for the 16 mm lens compared to those reported from experiment 3.2. However, slight improvements have been noted, from 11.3 to 10.8 microns standard deviation and 1 to 0.4 microns error, in the case of the SLSE method; from 10.2 to 10 microns standard deviation and 1.7 to 1.1 microns error in the case of the PRM method.

The camera calibration methods reduced the deviation of distances between control points 12 mm apart from 0.7% to less than 0.09%, and the error reduced from 1.9%

to 0.01%. For the 25 mm lens, a drastically reduced distortion is noted in the uncalibrated image, having only approximately one third of the distortion when looking at the standard deviation of the error compared to the 16 mm lens. The camera calibration methods reduced the error of distances between control points 12 mm apart from 0.2% to less than 0.1%. For the error, a reduction from 1.4% to 0.01%. For the 8 mm lens an increased distortion is noted in the uncalibrated image, having approximately three times the distortion compared to the 16 mm lens.

Lens	Method	Mean (mm)	ε_σ (microns)	ε_μ (microns)
8 mm	UNCALIBRATED	12.2	249.6	203.8
	SLSE	12.0	13.4	1.0
	PRM	12.0	16.1	2.9
16 mm	UNCALIBRATED	12.2	80.8	225.0
	SLSE	12.0	10.8	0.4
	PRM	12.0	10.0	1.1
25 mm	UNCALIBRATED	12.2	24.7	165.1
	SLSE	12.0	10.5	0.9
	PRM	12.0	9.9	0.7

TABLE 3.2: Distortion correction performance using each of the three available lenses.

We observe that both PRM and SLSE calibration methods are effective for the removal of optical distortion and calibrating measured distances into millimetres for all three tested focal lengths. However, the 8 mm lens results show a slight decrease in performance as the variation in the measured area is reported higher than the other two lenses, at roughly three times the level of error. We suggest the 16 mm lens be used as a suitable operating point for the measurement apparatus.

3.2 Estimation of Error from Image Quantisation

An estimate of the number of repeated measurements of a rice grain would be required in order to achieve a suitable level of variance in the error of the measured length. Pixel quantisation is an effect of both the intensity resolution as well as the spatial resolution of the imaging chip within a digital camera, and so one would expect a baseline error in the length measurement that is attributed to pixel quantisation during image acquisition [111]. In section 3.2.1 a set of theorems are proposed to simulate the quantisation error on a length measurement.

Let us consider that the length measurement of a rice grain is the Euclidean distance between the two end pixels of the contour of the grain. We calculate the expectation of error in the length measurement due to the effects of pixel quantisation as the standard deviation of the distribution of errors from the two end pixels, using two models. The first represents a vertical grain, and the second represents a grain at any given angle. The variance of the errors from these three models are described in section 3.2.2. Section 3.2.3 gives an error prediction; we also conduct trials on the three simulated quantisation models.

3.2.1 Quantisation Model

Three models are discussed, increasing in complexity. The first is a simple model considering pixel quantisation in one dimension: a vertical grain. The second and third models consider the 2D case where the grain may fall at any angle. These two models only differ on where we place our assumption of uniform distribution of the angles involved.

3.2.1.1 Vertical

Consider a grid that represents the quantisation of the world into pixel units. We create a simple model of this quantisation by considering the pair of end pixels belonging to a vertical grain. We use y to represent the vertical coverage of presence within one of the end pixels, assuming a uniform probability density function of the coverage within this pixel. See figure 3.10 for an example of the pixel quantisation of the edge of a grain. Please note that for illustration purposes, the quantised edge is set to the edge of the pixel, not the centre. However in reality the quantised edge would be the centre of the pixel. In practical terms however there is no erroneous effect in our model as the size of the pixel remains the same.

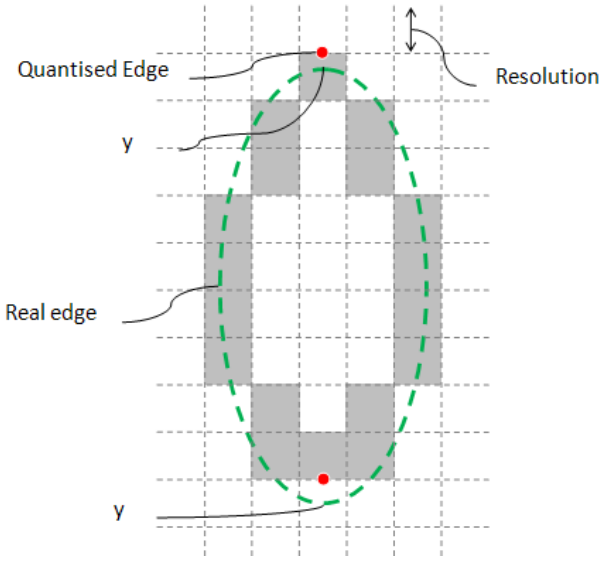

3.10.1 Example quantisation of the edge of a vertical grain.

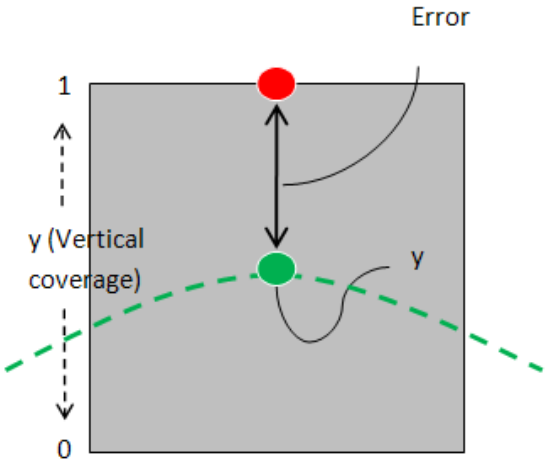

3.10.2 Close up of end y.

FIGURE 3.10: A simple model of the quantisation error, with respect to grain length. The red circles represent the quantised point of the rice grain (green dashed ellipse). In this example the quantised point is tired to the edge of the grid, not the centre, for illustrative purposes only – in practice, the centre of the grid co-ordinate is used.

Working with the first of the end pixels, we expect that as the coverage y tends towards 0.5, the error is at its highest. The estimated error is:

$$\text{if} \quad y < \tfrac{1}{2} \tag{3.7}$$

$$\text{then} \quad \varepsilon(y) = -y \tag{3.8}$$

$$\text{else} \quad \varepsilon(y) = 1 - y \tag{3.9}$$

See figure 3.11 for a plot of the estimated error.

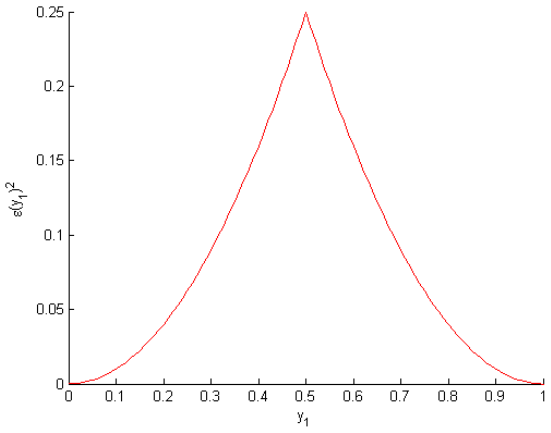

FIGURE 3.11: Estimated error for the vertical quantisation model, where $\varepsilon(y)^2$ is shown against y.

3.2.1.2 Any Angle: Assumed Uniform Distribution of θ

This model extends the vertical grain case in section 3.2.1.1 to allow us to define the expectation of quantisation error in the length measurement at any grain orientation, see figure 3.12.1.

We aim to calculate the error in the quantisation of the pixel as a function $\varepsilon(x, y, \theta)$, where x is the horizontal coverage of the pixel, y is the vertical coverage, and θ is the angle between the grain orientation and the quantised point. This is illustrated in figure 3.12.3. A set of local terms of the pixel: Δ_x represents the difference between the real edge x and the quantised edge, and Δ_y represents the difference between y and the quantised edge; illustrated in figure 3.12.2. The distance of the error is given as: $d = \sqrt{\Delta_x^2 + \Delta_y^2}$.

A scaling factor, $\cos(\theta)$, of the distance of the error is used to account for the cases where the grain orientation is in an opposing direction to the that of the quantisation

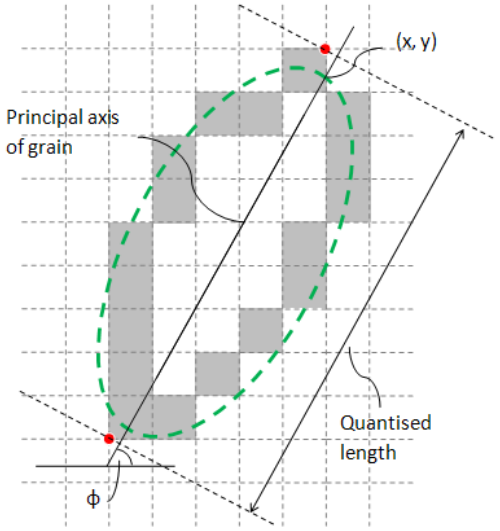

3.12.1 Example quantisation of the edge of a grain at an angle.

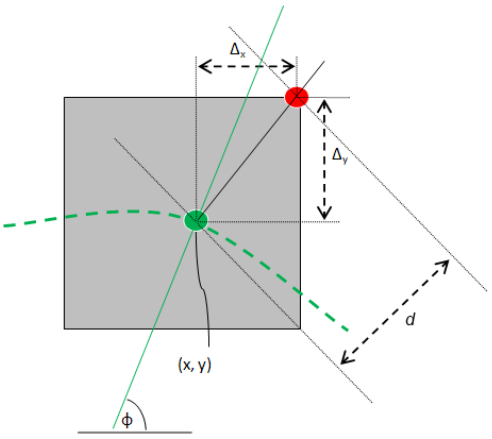

3.12.2 Close up of end (x, y) of a grain at angle ϕ where Δ_x and Δ_y is shown.

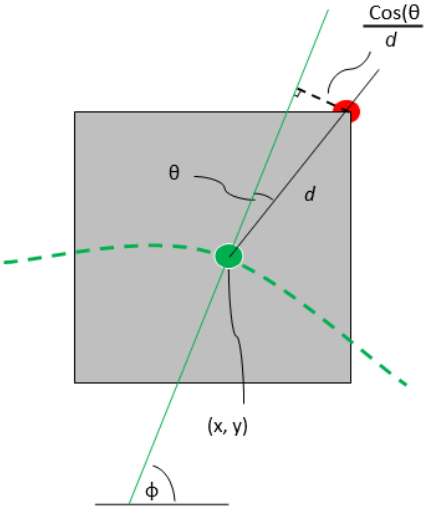

3.12.3 Close up of end (x, y) of a grain at angle ϕ where angle θ and line $\cos(\theta)$ are shown.

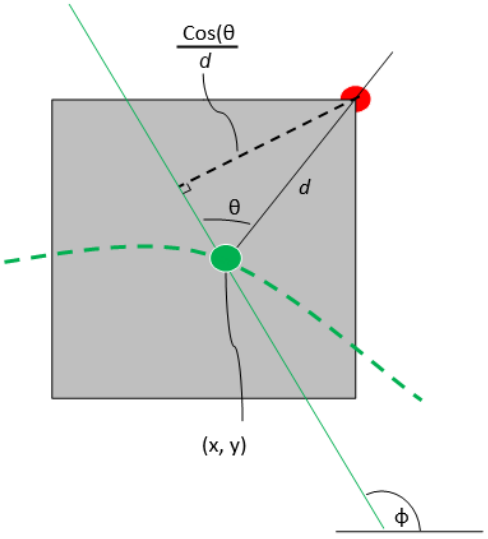

3.12.4 Consider the grain from Fig. 3.12.3 falls at an opposite angle ϕ, but the same position in the quantisation grid. The error d would not have the same effect as in the previous example, as the length of the grain at this angle is in the opposite direction as the error d. We observe that the line $\cos(\theta)$ is effected by the angle and can be used as a scaling factor of the error based on the angle of θ.

FIGURE 3.12: A more complex model of the quantisation error with respect to grain length, where the grain orientation is taken into account.

error, see figure 3.12.4. The error at one end of the pixel is given by:

$$\varepsilon(x, y, \theta) = \sqrt{\Delta_x^2 + \Delta_y^2} \cdot \cos(\theta) \tag{3.10}$$

3.2.1.3 Any Angle: Assumed Uniform Distribution of ϕ

This model extends the case in section 3.2.1.2 to allow us to define the expectation of quantisation error in the length measurement at any grain orientation without an assumption of the angle θ having a uniform distribution, but rather the grain orientation ϕ which we consider has a true uniform distribution. We aim to calculate the error in the quantisation of the pixel as a function $\varepsilon(x, y, \phi)$ where x is the horizontal coverage of the pixel, y is the vertical coverage and ϕ is the angle of the grain. Δ_x and Δ_y represent the difference between the real edge x and the quantised edge; and y and the quantised edge. The distance of the error remains as $d = \sqrt{\Delta_x^2 + \Delta_y^2}$. As $\theta = \phi - \psi$, $\cos(\theta) = \cos(\phi - \psi) = \cos(\phi)\cos(\psi) + \sin(\phi)\sin(\psi)$, see figure 3.13.

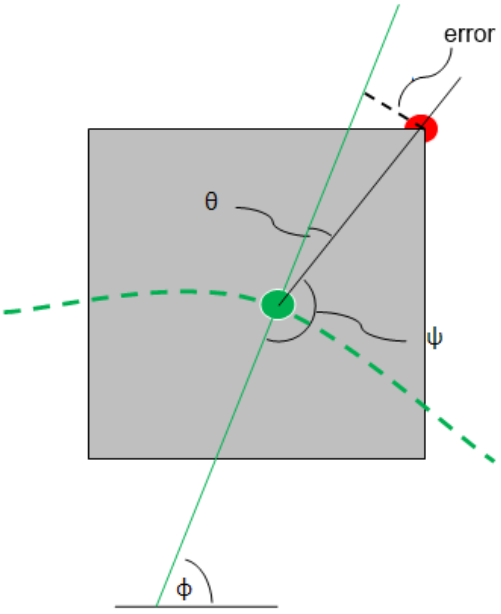

FIGURE 3.13: Following the example from figure 3.12.1, a pixel end (x, y) of a grain at angle ϕ.

The error at one end of the pixel is given by:

$$\varepsilon(x, y, \phi) = \sqrt{\Delta_x^2 + \Delta_y^2}\,[\cos(\phi)\cos(\psi) + \sin(\phi)\sin(\psi)] \tag{3.11}$$

3.2.2 Estimate of the Variance from Image Quantisation

In this section, we describe three experiments to calculate the variance of the errors using the three models discussed in section 3.2.1. Theorem 3.1 estimates the quantisation error using the vertical length measurement model; theorem 3.2 estimates the error using a uniform distribution of θ; the final model is used in theorem 3.3, where we estimate the quantisation error using grains at any angle ϕ.

Theorem 3.1. The variance of the errors from a length measurement between two pixels is given by:

$$\mathrm{Var}(\varepsilon(l)) = E[\varepsilon(l)^2] - (E[\varepsilon(l)])^2 \tag{3.12}$$

where $\varepsilon(l) = 2 \cdot \varepsilon(y)$. Consequently, the squared error is given by $\varepsilon(l)^2 = (2 \cdot \varepsilon(y)^2 + \varepsilon(y)^2) + (2\varepsilon(y)\varepsilon(y))$. The expected value of the errors from a length is $E[\varepsilon(l)] = E[\varepsilon(y)] + E[\varepsilon(y)]$. As y is assumed to have a uniform distribution, we are expecting that the coverage within the two pixels will move together as the quantisation grid moves. In this case there is no bias, *i.e.* an assumption of general symmetry. Therefore, $E[\varepsilon(l)] = 0$.

The expected value of squared errors from a length measurement is $E[\varepsilon(l)^2] = E[\varepsilon(y)^2] + E[\varepsilon(y)^2] + E[2\varepsilon(y)\varepsilon(y)]$. As with the above assumption of general symmetry, $E[2\varepsilon(y)\varepsilon(y)] = 0$. Finally, as there are two points to a length measurement, we multiply the error by 2 as we assume the error is the same amount for each end. Therefore, equation 3.12 becomes:

$$\mathrm{Var}(\varepsilon(l)) = 2E[\varepsilon(y)^2] \tag{3.13}$$

We calculate the expected value of the distribution of errors for a single position. We consider for the distribution of y, the interval $[0, \frac{1}{2}]$ is the same as the interval $[\frac{1}{2}, 1]$. Therefore,

$$E[\varepsilon(y)^2] = 2\int_{y=0}^{\frac{1}{2}} \varepsilon(y)^2 dy \tag{3.14}$$

which is solved to $E[\varepsilon(y)^2] = 2\frac{1}{24} = \frac{1}{12}$.

As we are assuming the same pdf for both end pixels of y, $E[\varepsilon(y)^2] = E[\varepsilon(y)^2] = \frac{1}{12}$. Therefore, $\mathrm{Var}(\varepsilon(l)) = \frac{1}{12} + \frac{1}{12} = \frac{1}{6}$. The standard deviation is given by $\sigma = \sqrt{\mathrm{Var}(\varepsilon(l))} = \frac{1}{\sqrt{6}} = 0.4082$ pixels.

Theorem 3.2. The variance of the distribution of errors of a length measurement at any angle is given by $\mathrm{Var}(\varepsilon(\vec{l})) = E[\varepsilon(\vec{l})^2] = 2 \cdot E[\varepsilon(x, y, \theta)^2]$.

The expected value of $\varepsilon(x, y, \theta)$ is:

$$E[\varepsilon(x, y, \theta)] = \frac{1}{2\pi} \int_{\theta=0}^{2\pi} \int_{x=-\frac{1}{2}}^{\frac{1}{2}} \int_{y=-\frac{1}{2}}^{\frac{1}{2}} \sqrt{x^2 + y^2} \cdot \cos(\theta) \cdot dx \cdot dy \cdot d\theta \tag{3.15}$$

as (x, y) are assumed to have uniform distributions, we are expecting that the coverage within the two pixels will move together as the quantisation grid moves. Therefore, $E[\varepsilon(x, y, \theta)] = 0$.

Consequently, the expected value of the squared error is:

$$E[\varepsilon(x, y, \theta)^2] = \frac{1}{2\pi} \int_{\theta=0}^{2\pi} \int_{x=-\frac{1}{2}}^{\frac{1}{2}} \int_{y=-\frac{1}{2}}^{\frac{1}{2}} (x^2 + y^2) \cdot \cos^2(\theta) \cdot dx \cdot dy \cdot d\theta \tag{3.16}$$

To solve equation 3.16 we can calculate for one direction, say x, and double the result, as both dimensions belong to a square pixel:

$$E[\varepsilon(x, y, \theta)^2] = \frac{1}{2\pi} \int_{\theta=0}^{2\pi} \int_{x=-\frac{1}{2}}^{\frac{1}{2}} x^2 \cos^2(\theta) \cdot dx \cdot d\theta \tag{3.17}$$

so:

$$E[\varepsilon(x, y, \theta)^2] = \frac{1}{2\pi} \int_{\theta=0}^{2\pi} \left[\frac{1}{3}x^3\right]_{x=-\frac{1}{2}}^{\frac{1}{2}} \cos^2(\theta) \cdot d\theta \tag{3.18}$$

where $\left[\frac{1}{3}x^3\right]_{x=-\frac{1}{2}}^{\frac{1}{2}} = \frac{1}{12}$.

Therefore:

$$E[\varepsilon(x, y, \theta)^2] = \frac{1}{2\pi} \cdot \frac{1}{12} \int_{\theta=0}^{2\pi} \cos^2(\theta) \cdot d\theta \tag{3.19}$$

Lastly, $\int_{\theta=0}^{2\pi} \cos^2(\theta) \cdot d\theta = \pi$. The expected value of the squared error for a position at any angle is: $E[\varepsilon(x, y, \theta)^2] = 2(\frac{1}{24\pi})\pi = \frac{1}{12}$.

Thus, $\mathrm{Var}(\varepsilon(\vec{l})) = 2 \cdot \frac{1}{12} = \frac{1}{6}$. The standard deviation of the error is $\sigma = \sqrt{\mathrm{Var}(\varepsilon(\vec{l}))} = \frac{1}{\sqrt{6}} = 0.4082$ pixels. This is the same as the vertical grain simulation in theorem 3.1.

Theorem 3.3. The variance of the distribution of errors of a length measurement at any angle is given by $\mathrm{Var}(\varepsilon(\vec{l})) = E[\varepsilon(\vec{l})^2] = 2 \cdot E[\varepsilon(x, y, \phi)^2]$.

The expected value of $\varepsilon(x, y, \phi)$ is:

$$E[\varepsilon(x, y, \phi)] = \frac{1}{2\pi} \int_{\phi=0}^{2\pi} \int_{x=-\frac{1}{2}}^{\frac{1}{2}} \int_{y=-\frac{1}{2}}^{\frac{1}{2}} \Delta_x \cos(\phi) + \Delta_y \sin(\phi) \cdot dx \cdot dy \cdot d\phi \tag{3.20}$$

As (x, y) are assumed to have uniform distributions, we are expecting that the coverage within the two pixels will move together as the quantisation grid moves. Therefore, $E[\varepsilon(x, y, \phi)] = 0$.

Consequently, the expected value of the squared error is:

$$E[\varepsilon(x,y,\phi)^2] = \frac{1}{2\pi}\int_{\phi=0}^{2\pi}\int_{x=-\frac{1}{2}}^{\frac{1}{2}}\int_{y=-\frac{1}{2}}^{\frac{1}{2}}(\Delta_x^2\cos^2(\phi))+(\Delta_y^2\sin^2(\phi))+(2\Delta_x\Delta_y\cos(\phi)\sin(\phi))\cdot dx\cdot dy\cdot d\phi \tag{3.21}$$

Solving equation 3.21 gives:

$$E[\varepsilon(x,y,\phi)^2] = \frac{1}{2\pi}\cdot\left[(\frac{1}{12}\pi)+(\frac{1}{12}\pi)+0 = \frac{1}{12}\right] \tag{3.22}$$

The expected value of the squared error for a length at any angle is: $\mathrm{Var}(\varepsilon(\vec{l})) = 2\cdot\frac{1}{12} = \frac{1}{6}$. The standard deviation of the error is $\sigma = \sqrt{\mathrm{Var}(\varepsilon(\vec{l}))} = \frac{1}{\sqrt{6}} = 0.4082$ pixels. This is observed to be the same for all three models we have created.

3.2.3 Uncertainty Prediction of Quantisation Error

In this section, we describe two experiments to quantify the level of uncertainty. First, experiment 3.4 estimates the uncertainty by using the previously calculated variance of quantisation error; then experiment 3.5 estimates the uncertainty from simulation trials of the quantisation model.

Experiment 3.4. The standard error of a sample of measurements, *i.e.* the measure of uncertainty, is defined as $\mathrm{SE}_\varepsilon = \frac{\sigma}{\sqrt{n}}$ where n is the number of measurements in the sample. We use the variance in error, estimated from theorems 3.1 to 3.3 to calculate the standard error. As the data are normally distributed the upper and lower confidence limits can be derived from the standard error of the sample. The confidence limits for a 99.7% (3σ) confidence interval is expressed as $\mu + (\mathrm{SE}_\varepsilon \cdot 3)$ and $\mu - (\mathrm{SE}_\varepsilon \cdot 3)$ for the upper and lower limits, respectively, where μ is the arithmetic mean of the sample.

Table 3.3 contains a series of standard errors, using $\sigma = 0.4082$ pixels (calculated from the three models of quantisation error). Table 3.4 contains the confidence limits for various intervals. We expect that a suitable level of variance in the error of the measured length is achieved with 5 measurements of a grain; this means that with 99.7% confidence (three standard deviations), the error would lie within ± 0.046 mm.

n	1	2	3	4	5	10	20	50	100	200
SE_ε	0.41	0.29	0.24	0.20	0.18	0.13	0.09	0.06	0.04	0.03

TABLE 3.3: Estimated standard error of image quantisation, in pixels, for various sample sizes, where $\sigma = 0.4082$.

Interval		n=1	2	3	4	5	10	20	50	100	200
68.30%	(1σ)	0.41	0.29	0.24	0.20	0.18	0.13	0.09	0.06	0.04	0.03
81.80%	(1.5σ)	0.61	0.43	0.35	0.31	0.27	0.19	0.14	0.09	0.06	0.04
95.00%	(1.96σ)	0.80	0.57	0.46	0.40	0.36	0.25	0.18	0.11	0.08	0.06
95.40%	(2σ)	0.82	0.58	0.47	0.41	0.37	0.26	0.18	0.12	0.08	0.06
99.00%	(2.576σ)	1.05	0.74	0.61	0.53	0.47	0.33	0.24	0.15	0.11	0.07
99.70%	(3σ)	1.22	0.87	0.71	0.61	0.55	0.39	0.27	0.17	0.12	0.09

TABLE 3.4: Estimated confidence limits of quantisation, in pixels, for various intervals.

Experiment 3.5. A set of trials were conducted using the simulated models of image quantisation. A series of length measurements are made for each of a set of ellipses (representing rice grains) between a minimum and maximum length. The grains are drawn onto a quantised grid of a fixed scale factor, and the length error is recorded. A series of 1,000 measurements were made for each of 1,000 artificial grains of length between 6 and 10 mm. The simulated scale factor was set to 10 pixels per 1 mm.

Table 3.5 contains a series of results for various grain orientation ranges. We observe no change in the error given the grain orientation, of ± 0.041 mm for each catchment range including any orientation.

ϕ range	Mean	ε_σ	Skewness	Kurtosis
Fixed 90°	0	0.041	-0.013	2.377
Fixed 45°	0	0.041	-0.017	2.984
Random from $0 - 360°$	0	0.041	-0.005	2.560

TABLE 3.5: Distribution of errors for three ranges of grain orientation, ϕ, in mm, over a set of 1 million measurements.

3.3 Rice Contour Extraction

The contour extraction process is required to prepare the image for detection of objects (rice grains). The input for this process is a single monochrome image of rice grains captured from the sensor, and the output is a binary image (where a zero-value represents the background pixels, and a one-value represents the presence of the foreground object). In this image, each contour describes the outline of either a single grain, or of a group of two or more touching grains. The grain must not be touching the edge of the image. The first step in this process is image segmentation, which is the transformation of the original image into the binary image. The perimeter of connected presence is calculated from a binary image and that returns a perimeter map. A pixel belongs to the perimeter of an object if that pixel is nonzero and is connected to at least one zero-valued pixel. In the 2D case, the search window uses a connectivity of 4 pixels for horizontal and vertical directions only. Additionally, an 8-connected neighbourhood can be used to include the diagonal directions.

We expect that an inaccurate or noisy contour of an object will bias any length measurement made from that contour. Thus, we require the contour of an object to be invariant to factors such as contrast changes between the foreground and background. Such changes may be observed across both the width and height of the viewing plane. Additionally, contrast changes can occur over time, where the background quality may degrade as various levels of dust can accumulate on the surface of the background. However, there is a possibility that the flow of rice can 'self-clean' the viewing plane and/or background plate. The initial candidate list of image segmentation techniques that are included in this research survey consist of these existing methods:

1. NaiveThresh baseline histogram method.
2. GlobalHist histogram method.
3. MinErrorThresh minimum error threshold.
4. LocalVar local adaptive thresholding.
5. LocalVarRatio local adaptive thresholding.
6. EdgeLoG spatial filter for edge detection.
7. EdgeCanny edge detector.

A novel modification is considered. The GlobalHist method along with other global based approaches may not overcome misclassification due to non-uniform illumination.

An attempt to reduce the impact of the global illumination footprint on local sections of the image can be made by dividing the image into subsections. A sub set of 'global' statistics can then be made for each tile of the grey level image. This is further discussed in section 3.3.1. Section 3.3.2 contains both the requirement and solution for a set of post segmentation filters for the removal of unwanted artifacts in the binary image. Section 3.3.3 defines the evaluation method for selecting the contour extraction method that provides the most stable contour of a rice grain in two situations: given various levels of rice dust interference, and position of the rice grain in the viewing area.

3.3.1 Local Analysis via a Tiling Strategy

It is proposed that global thresholding with the GlobalHist method is applied to smaller independent parts of the image, to create a more localised version, labelled as HybridHist. It is proposed that this is achieved by dividing the input image into tiles, and a separate GlobalHist based histogram threshold selection is applied to each. The combined result is achieved by connecting the individually segmented tiles back together.

However, a specific tile where there are no foreground objects will cause spurious segmentation. This is because the global statistics of a single tile caused a misrepresentation of foreground objects. The result of the segmentation method would always result in a false partition. A filter must be applied to improve the robustness of this approach. This filter selects a tile that has fewer than two distinct peaks. This selected tile is then segmented to contain no foreground pixels. One remaining observation can be made on this method however. Due to the tiling of the grey level image, a hard line of disparity between adjoining tile thresholds can be observed. If an object were to cross over the carving lines, then artifacts may appear between objects due to the different threshold values. A modification can be made to reduce the above observed effect by applying a smoothing filter, such as Gaussian low pass filter, on the threshold values prior to thresholding. The smoothing function creates an interpolation between the hard values, that reduces the undesirable effect. This method is labelled as SmoothHybridHist.

An inherent problem with a global based thresholding is the lack of consideration for the scenario when no actual foreground object is in the image. This effect produces a large misclassification error, see figure 3.14. The scenario is that global statistics are computed on an image or tile which has no foreground objects in view. The global method will use these statistics and incorrectly select a threshold value, thus producing a misclassification where some or most of the background pixels will be assigned as foreground pixels. The two main methods where we observe this are with the GlobalHist method, and the hybrid HybridHist method analysis using image tiling.

3.14.1 Input image with no foreground object.

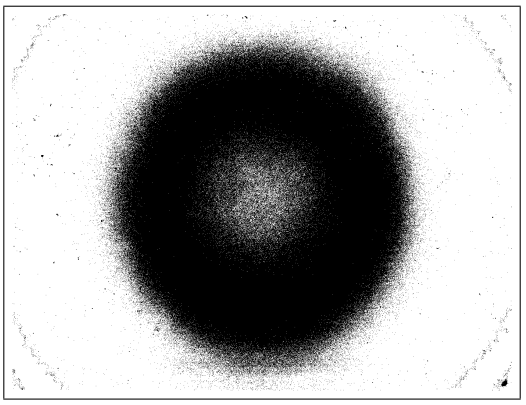

3.14.2 Binary image using GLOBALHIST. A spurious signal is indicated by the black pixels (foreground presence).

3.14.3 The peak detection filter applied before GLOBALHIST.

FIGURE 3.14: A problematic example for global thresholding, where the image contains no foreground presence. In the binary images of these examples, white indicates a background pixel.

A method is created to recognise the scenario of an 'empty' image or tile. We expect to have two peaks in the pixel intensity histogram, therefore a straightforward peak detection approach can be used (we have not search for an alternative). However there may be more robust search tools, such as K-means clustering. The peak detection algorithm is a search for the local maxima, described in the following steps:

1. Compute the normalised pixel intensity histogram of the image or tile.
2. Smooth the histogram with a moving mean filter [37] to sufficiently indicate distinct peaks, such as a $\left[\frac{1}{3}\frac{1}{3}\frac{1}{3}\right]$ kernel which slides over the histogram values and records the mean intensity in a new smoothed histogram $\mathcal{H}$.
3. Scan the smoothed histogram bins from left to right, *i.e.* $\mathcal{H}(i) : i = 1, 2, \ldots n$ where n is the number of bins. A peak is found if $\mathcal{H}(i) > \eta$ and $\mathcal{H}(i) > \mathcal{H}(i+1)$ and $\mathcal{H}(i) > \mathcal{H}(i-1)$, where η is a constant representing the minimum allowed

value for a peak. This means a peak is found when the value to the right is lower than the current value (indicating a descent); stop searching if a peak was found.

4. Scan the bins from right to left. A peak is found if $\mathcal{H}(i) > \eta$ and $\mathcal{H}(i) > \mathcal{H}(i-1)$, *i.e.* the value to the left is lower than the current value; stop searching if a peak was found.

The peak detection algorithm therefore returns the number of peaks as: 0, 1 or 2; in addition to the bin locations. The accompanying filter can intercept the image or tile and force all pixels within to be false (background) if there are fewer than 2 peaks, *i.e.* the filter is used as a decision process to remove a tile based on whether it contains no foreground pixels. For fine tuning of the η parameter, we examine a few scenarios. Consider a single tile of the image divided into 8-by-8 tiles, at 170-by-128 pixels; and a $\frac{1}{7}$ fragment of a grain would have an estimated 200 pixel footprint. If this fragment was present in a tile with no other objects, then $\frac{140}{21760}100 = 0.92\%$, which is greater then $\eta = 0.01\%$. A value of $\eta = 0.2\%$ should be sufficient to detect a 50 pixel mass, such as a $\frac{1}{7}$ fragment of a grain captured partially in the corner of a tile, *i.e.* the fragment happens to be positioned in the corners of four adjacent tiles, see figure 3.15.

3.3.2 Post Contour Extraction Filters

Special scenarios can occur with images of rice grains in free flow, after image segmentation has been performed. These consist of the following:

1. Rice dust particles; an average grain of head rice contains a connected set of roughly 1400 pixels, a quarter grain would be 350 pixels; it is possible that any object with fewer than 150 pixels should be classed as dust.

2. Clumps of touching grains, due to the occlusion of the rice edges.

3. Grains touching the viewing plane border; The camera field of view does not fully captured the entire glass chute, this means that some rice grains could be partially visible in the captured image. These incomplete grains are therefore ignored, and not used for measurement of broken rice as the length can not be accurately obtained (missing pixels).

4. The scenario where the sensor is capturing images where there are no rice grains present in the viewing plane.

5. All space in the view is filled with grains; this would be an unlikely occurrence given the assumption that the feed level is sparse.

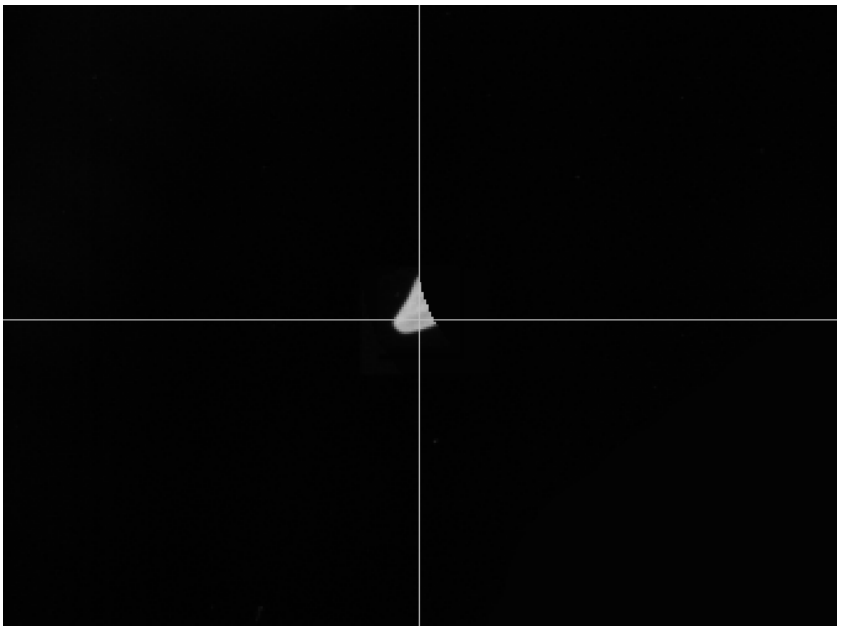

3.15.1 Worst case scenario of a single $\frac{1}{7}$ fragment of a grain spread over 4 tiles.

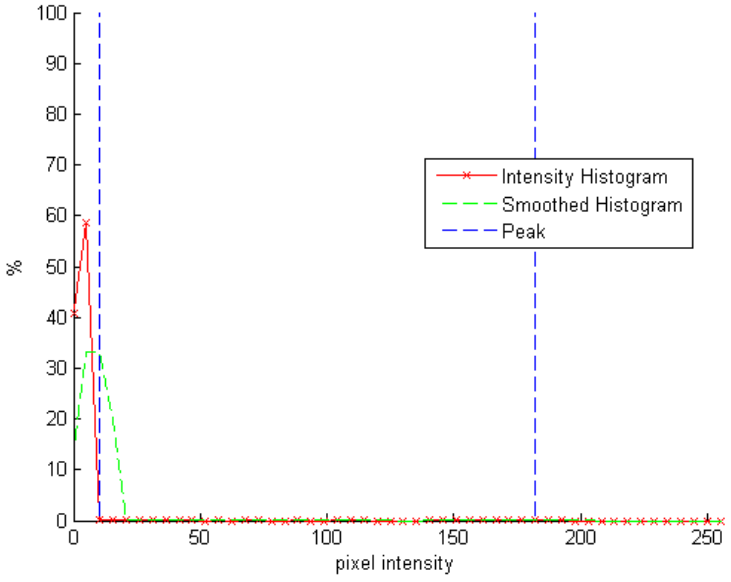

3.15.2 Consider one of the four tiles, two peaks were found with $\eta = 0.02\%$.

FIGURE 3.15: Peak detection with further tiling examples, such as an inadvertently sub sampled broken grain.

The following list of image processing filters are always applied to every input frame, in cascading order, to remove the previously noted issues:

1. Morphological fill: This filter is applied to remove any holes in the foreground of the segmented image. A hole is defined as a set of background pixels that cannot be 'reached' by filling in the background from the edge of the image.

2. Eight-wise object connectivity: The standard 8-direction connectivity rule is applied to the binary image. This allows all adjacent 'on' pixels to be considered for connectivity to an object. The result is a 'label map' image that identifies each connected object in the image with a unique index per object. From this image, the next set of filters are applied.

3. Dust filter: For the removal of objects smaller than broken grains. This avoids dust being counted as broken rice. Currently, an object is considered to be dust if it contains less than 100 touching pixels, defined simply as a less then a tenth of a grain of rice (industry standard definition) converted to pixels from the scale factor of the image to world.

4. Clump filter: For the removal of large groups of grains. Since we only measure single grains, this cleans the image to provide faster computational performance for single grain detection. Currently, an object is considered to be a clump if it contains more than 2,500 connected pixels. However, this will not remove all clumps, and pairs of grains may remain. This area is defined simply as any value greater than two grains of rice converted to pixels from the scale factor of the image to world.

5. Edge-touching filter: For the removal of any connected foreground pixels that are touching the edge of the image.

3.3.3 Performance Evaluation

Two experiments were conducted for evaluating the image segmentation methods used for contour extraction of the rice grains. Experiment 3.6 evaluates the foreground and background contrast variation; experiment 3.7 evaluates the position variation of objects across the viewing plane. Additionally, we include a set of test images, for each method, in appendix C.

During experimentation with the HybridHist and SmoothHybridHist methods, the input image is divided into equally sized rectangular tiles and each tile is separately segmented using an GlobalHist based histogram threshold selection method. For the 1360-by-1024

pixel resolution image, an 8-by-8 tiling is used, such that each tiled image is 170-by-128 pixels. This value was fixed with internal experimentation, too many tiles and the method becomes too localised, therefore 8-by-8 tiling would be the maximum. To prevent a step-change in the threshold used for adjacent tiles, the SmoothHybridHist method uses a Gaussian low pass smoothing filter with a 7-by-7 kernel and $\sigma = 2$. Lastly, we use 8-wise as a preferred option for pixel connectivity, as discussed in section 3.3.

Three segmentation performance scores from the literature (ME, SEME, and MHD) are used to provide an indication of how well the segmentation algorithms are performing, as previously introduced in section 2.3. The contour stability is represented by the overall contour error over all optical configurations. Given a grain of rice captured from each of a series of configurations, each of the three segmentation performance metrics is recorded for the grain. A set of configurations could refer to either changing the background plate or changing the position of the grain on the viewing plane. To reduce errors caused by image quantisation, a particular grain is observed multiple times.

Experiment 3.6. For the first experiment, we evaluate the contour extraction accuracy depending on variation in the contrast between foreground and background. The rice grains are placed within the centre of the viewing plane of the camera to reduce additional errors associated from position changes. The position of the grains of rice on the viewing plane remain the same throughout the changing of the background plates, to reduce measurement errors from positional sources. The three levels of background quality tested in this experiment are designed to simulate variation in the foreground and background contrast cased by rice dust in-the-field: a flat metal plate with a dark matt Teflon coating, represents the standard background level; a flat Teflon plate with one layer of rice dust (affixed with spray mount); lastly, a flat Teflon plate with two layers of rice dust. Figure 3.16 contains an example comparison image of each.

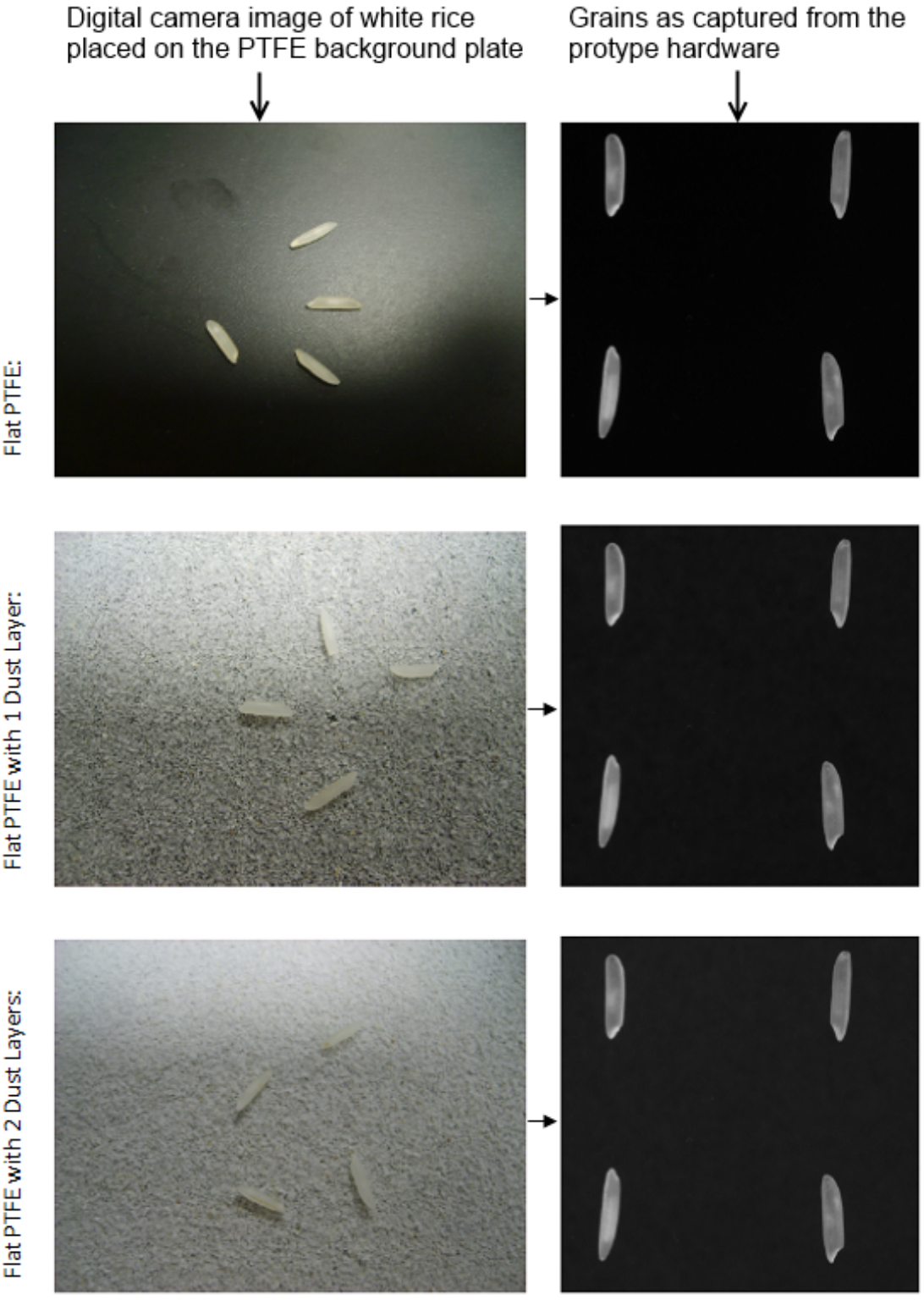

FIGURE 3.16: Comparison of white US Long samples on the three different background plates. The plain black background Teflon coated plate is the simplest problem; then, one and two layers of rice dust were fixed onto the background plates using spray mount. The images on the left were captured from a digital camera in the middle of a normally lit room (think of non specialised piece of hardware), the images on the right hand side are captured from the prototype sensor (fully configured). The illumination variation and contrast changes are noticeably reduced by the specially configured hardware.

An initial analysis of the data can be computed by calculating the mean grey level pixel intensities for the two segmented classes, of foreground and background (post contour extraction). The ratio of foreground to background indicates the variation in signal caused by the different levels of background quality, see table 3.6. Our initial expectation of 1.5-to-1 foreground to background has been surpassed at all the three tested levels of background quality.

Background	Mean Foreground Intensity	Mean Background Intensity	Ratio
Teflon Flat	112	3	33.7
Teflon 1x Dust	117	17	6.9
Teflon 2x Dust	119	24	4.9

TABLE 3.6: Foreground to Background signal ratio as the background quality changes from a solid black Teflon plate, to Teflon plates coated with one and two layers of rice dust.

The following experimental results consists of 9 examples of US Long rice grains captured in 20 separate images for each grain. The results are presented in table 3.7. We observe that all methods except MINERRORTHRESH, LOCALVAR and LOCALVARRATIO perform relatively well across all the figures of merit. As for overall performance, SMOOTHHYBRIDHIST gives the lowest mean segmentation errors. A set of output rice grain contours from each method are shown in appendix B.

Method	ME	SEME	MHD
NAIVETHRESH	0.007	0.076	0.022
GLOBALHIST	0.007	0.072	0.021
MINERRORTHRESH	0.064	0.709	0.570
HYBRIDHIST	0.006	0.065	0.016
SMOOTHHYBRIDHIST	**0.001**	**0.009**	**0.001**
LOCALVAR	0.307	0.371	0.041
LOCALVARRATIO	0.270	0.913	0.949
EDGELOG	0.013	0.132	0.059
EDGECANNY	0.027	0.300	0.127

TABLE 3.7: Stability evaluation of the contour extraction methods with variation in contrast in the image. These three performance metrics were previously introduced in chapter 2.

Experiment 3.7. The second experiment evaluates the contour extraction accuracy depending on the position of the grain on the viewing plane. The background plate and illumination is fixed to reduce additional errors associated from foreground and background variation. The positional changes in this experiment are designed to simulate any remaining uncertainties in the measurement which are a direct effect of the grain's

position in the view being changed, such as any residual geometric distortion, or illumination variation across the view. Figure 3.17 illustrates an example series of grains captured as the positions are changed.

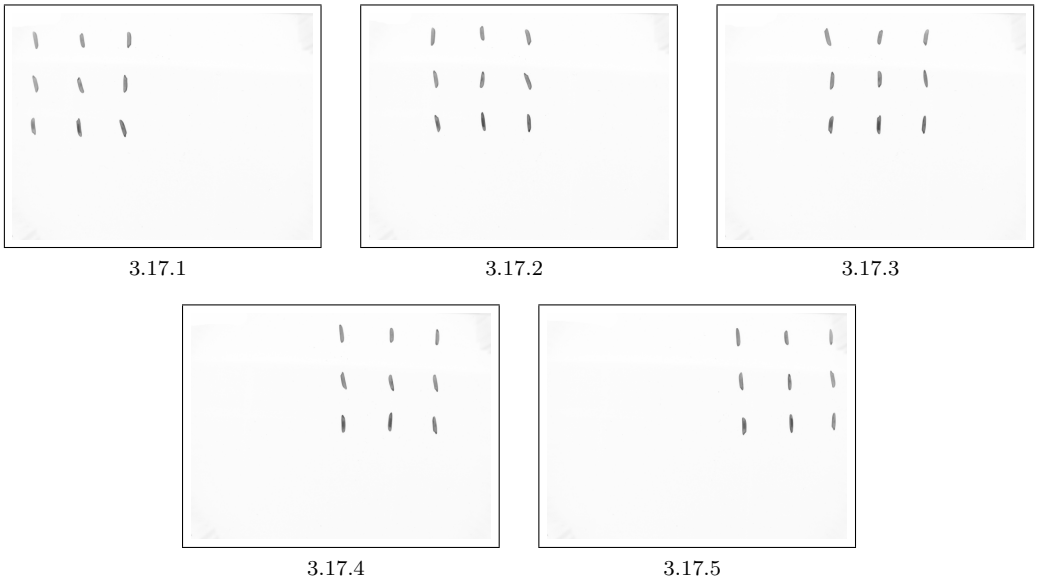

3.17.1 3.17.2 3.17.3

3.17.4 3.17.5

FIGURE 3.17: Figures 3.17.1 to 3.17.4 are examples of captured images (negatives) of US Long samples in different position configurations across the view. The same grains are kept in the same local formation in order to maintain correspondence with respect to the manually labelled ground-truth.

The following experimental results for position variation, consists of 9 examples of US Long rice captured over a series of 10 images of each grain, are presented in table 3.8. We observe that there is less contour stability than as seen with contrast changes in experiment 3.6. Most of the tested algorithms have stable contours as the position in the view changes, with the outright best being the novel SMOOTHHYBRIDHIST method, which has the with the lowest error on all three segmentation error metrics.

Method	ME	SEME	MHD
NAIVETHRESH	0.013	0.111	0.024
GLOBALHIST	0.010	0.096	0.019
MINERRORTHRESH	0.094	0.892	0.951
HYBRIDHIST	0.006	0.061	0.011
SMOOTHHYBRIDHIST	**0.002**	**0.014**	**0.002**
LOCALVAR	0.013	0.126	0.039
LOCALVARRATIO	0.091	0.872	0.895
EDGELOG	0.015	0.132	0.033
EDGECANNY	0.034	0.334	0.181

TABLE 3.8: Stability evaluation of the contour extraction methods with variation in position across the view. These three performance metrics were previously introduced in chapter 2.

Due to the requirement of fast computation times, the mean contour extraction computation times were monitored and are shown in table 3.9. These include the filter stages and contour extraction using each segmentation algorithm.

Contour Extraction Method	Mean Processing Time (ms)
NaiveThresh	1513
GlobalHist	375
MinErrorThresh	407
HybridHist	406
SmoothHybridHist	469
LocalVar	555
LocalVarRatio	443
EdgeLoG	676
EdgeCanny	1122

Table 3.9: Mean contour extraction computation time per image.

From experiment 3.6, we observe that the initial analysis of the background to foreground ratio of 33:1, with a flat black Teflon plate. In the worst case of two layers of dust glued onto the plate, the ratio was approximately 5:1; both ratios are above our system requirement of 1.5:1. With the SmoothHybridHist method we observe little variation in either configuration change. For all three tested segmentation performance metrics for misclassified pixels, edge mismatch or shape comparison. We observe that errors caused by position provide a greater risk of contour stability than contrast variation does. Therefore post geometric distortion removal, we estimate that position variation still contains the highest remaining error, which we would attribute to illumination variation across the view.

3.4 Definition of Rice Length

For consideration of the accuracy of length, we include a candidate list of length definitions, as previously discussed in chapter 2; these consist of the following:

1. Principal Axis length of the Ellipse of Inertia (PrincipalAxis).
2. Parallel Principal Axis (ParallelPrincipalAxis).
3. Longest Chord (LongestChord).
4. Longest Centroid Chord (LongestCentroidChord).
5. Rotating Callipers length (RotatingCalipers).
6. Bounding Box length (BoundingBox).
7. Minimum Bounding Box (MinimumBoundingBox).

Section 3.4.1 discusses the performance evaluation experiments for quantifying the accuracy of each length definition.

3.4.1 Performance Evaluation

Two experiments were conducted for evaluating the measurement accuracy of rice grain length. Experiment 3.8 evaluates the length measurement of head rice; experiment 3.9 evaluates the length measurement of broken rice.

Given a grain of rice captured from a series of images, the length in millimetres is measured using each proposed length measurement method. The length measurement incorporates the use of the selected camera calibration method in order to remove geometric lens distortion and calibrate the measurement into millimetres. A ground-truth length of each rice grain is measured and recorded with digital Vernier callipers. The errors in the measurement associated with quantisation are avoided by calculating the mean grain length over the set of multiple images of that grain. Multiple observations of relatively few labelled grains is a more efficient way to measure the accuracy of a given operating point, compared to relatively many grains (of unknown length). The uncertainty is defined as the mean and variance of the errors of the length measurements made by the system.

Experiment 3.8 We monitor the measured grain length from the seven methods that have been previously described in section 2.4. A data-set was captured with the apparatus, consisting of a set of 10 images of rice grains each containing the same 24 hand measured broken grains in slightly difference positions. The rice grains are roughly positioned in a 4 by 6 grid within the viewing area, see figure 3.18.

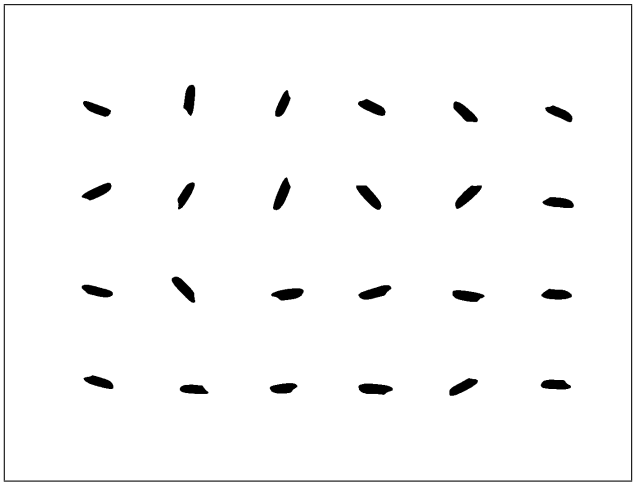

3.18.1 Head rice.

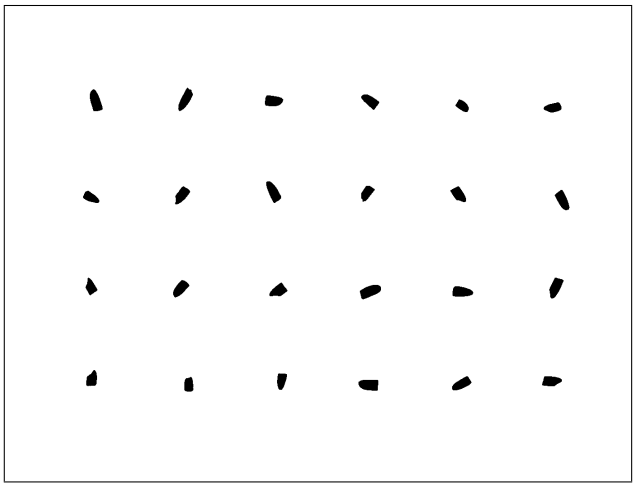

3.18.2 Broken rice.

FIGURE 3.18: Example data-set image for head and broken US Long rice. For each image, image segmentation and post-processing filters were applied. Broken rice grains were also measured and evaluated, to give an indication if the system performed with different error rates caused by the changes in rice shape from complete to broken grains.

The results of length measurement accuracy, with head rice, is reported in table 3.10. Additionally, we include a set of test images, for each method, in appendix C. From measuring head rice, SMOOTHHYBRIDHIST image segmentation gives consistently lower mean errors than the standard global GLOBALHIST method. The mean error appears to be roughly equivalent to the previously estimated quantisation error of 0.041 mm. The

ParallelPrincipalAxis method and the Longest chord are almost identical when measuring head rice, with 0.046 mm deviation in the error (at the same amount of error cause from pixel quantisation). The MinimumBoundingBox method performed unexpectedly poorly compared to the ParallelPrincipalAxis and RotatingCalipers methods; however, one possible explanation is that the reported errors refer to the ground-truth made from caliper measurements, which can sometimes be very different to a box shaped enclosure (due to the 'biting' point angles of the measurement jaws).

Contour Method	Length Definition	Mean Length (mm)	ε_σ	ε_μ (mm)
GlobalHist	PrincipalAxis	6.551	0.089	-0.260
	ParallelPrincipalAxis	6.758	**0.036**	**-0.053**
	LongestChord	6.758	**0.036**	**-0.053**
	LongestCentroidChord	6.480	0.095	-0.331
	RotatingCalipers	6.758	**0.036**	**-0.053**
	BoundingBox	6.274	0.564	-0.537
	MinimumBoundingBox	6.358	0.496	-0.453
SmoothHybridHist	PrincipalAxis	6.567	0.095	-0.245
	ParallelPrincipalAxis	6.774	**0.046**	**-0.038**
	LongestChord	6.774	**0.046**	**-0.037**
	LongestCentroidChord	6.499	0.090	-0.312
	RotatingCalipers	6.774	**0.046**	**-0.037**
	BoundingBox	6.285	0.568	-0.526
	MinimumBoundingBox	6.378	0.476	-0.434

Table 3.10: Error in length measurement for each definition applied to head rice, captured using the 8 mm lens. The mean error is given as the reported length minus the ground-truth length.

Experiment 3.9 This experiment is conducted identically to experiment 3.8. However, the measured rice grains are broken (instead of head rice). The results of length measurement accuracy, with broken rice, is reported in table 3.11. We observe a change in the relative performance of the length definitions, compared to the head rice samples from experiment 3.8. When measuring the length of broken grains, the best performing methods for reducing the mean length error are the BoundingBox and Rotating BoundingBox, which conversely gave the worst results with head rice. If we consider the mean error from both sets of grains then the ParallelPrincipalAxis measurement still has the lowest mean error at 0.06 mm, compared to -0.2 mm mean error for both BoundingBox and Rotating BoundingBox methods. We observe that the LongestChord and RotatingCalipers methods both give similar mean errors when compared to the ParallelPrincipalAxis method. Finally, we report the mean computation time per grain length measurement in table 3.12. We observe the ParallelPrincipalAxis length definition is, on average, computed the fastest out of the set of methods.

Contour Method	Length Definition	Mean Length	ε_σ	ε_μ (mm)
GlobalHist	PrincipalAxis	3.824	0.106	-0.142
	ParallelPrincipalAxis	4.103	0.054	0.137
	LongestChord	4.124	**0.043**	0.158
	LongestCentroidChord	3.802	0.066	-0.164
	RotatingCalipers	4.124	**0.043**	0.158
	BoundingBox	4.002	0.182	0.036
	MinimumBoundingBox	3.957	0.157	**-0.009**
SmoothHybridHist	PrincipalAxis	3.844	0.117	-0.122
	ParallelPrincipalAxis	4.129	0.067	0.163
	LongestChord	4.149	**0.055**	0.183
	LongestCentroidChord	3.831	0.075	-0.135
	RotatingCalipers	4.149	**0.056**	0.183
	BoundingBox	4.025	0.189	0.059
	MinimumBoundingBox	3.985	0.150	**0.019**

Table 3.11: Error in length measurement for each definition applied to broken rice, captured using the 8 mm lens.

Length Definition	Mean Processing Time (μs)
PrincipalAxis	329
ParallelPrincipalAxis	27
LongestChord	73
LongestCentroidChord	78
RotatingCalipers	101
BoundingBox	23
MinimumBoundingBox	25

Table 3.12: Mean length measurement computation time per grain kernel.

It is recommended, out of the tested methods, that the ParallelPrincipalAxis length as the length measurement of choice. Despite the mean error ranging from -0.053 to 0.163 mm from head to broken grains, the mean error of 0.06 mm and mean error of 0.057 mm are lower than the remaining measurement methods. Suitable alternatives are the LongestChord and RotatingCalipers methods; both of these provide similar errors in length measurement, however contain more significant computational requirements than the ParallelPrincipalAxis length. This is further emphasised by the increased average computation times from both these methods compared to ParallelPrincipalAxis.

3.5 Chapter Conclusion

This chapter has presented a new approach that combines various components for accurately measuring the length of rice grains that sit on a glass plane. A series of existing

and novel methods comprise the following processes: camera calibration; contour extraction and a series of post segmentation filters; and an extensive compliment of length definitions that could describe the length of the rice grains.

For each component of the system, we have described a set of evaluation methods by which the optimal configuration may be identified and selected. Through experimentation, we identify the most appropriate components that comprise a complete image processing pipeline. From experiment 3.1, we determine that 12 mm is ideal for the spacing between control point pairs for evaluating the distortion levels from the camera lens; this is equivalent to measuring the length between 6 consecutive circles on the calibration pattern. Experiment 3.2 is conducted to estimate the effectiveness of the distortion removal techniques. It can be inferred that the best performance for distortion removal is from the PRM (Parametric Regression Model) method, providing the most reduction to the mean error of ± 10.2 microns over the range of 12 mm test distances. The recommended calibration method is PRM with 3 degrees of freedom which offers a flexible distortion removal technique in addition to having a straightforward implementation. This method additionally offers a suitable scaling factor strategy to estimate the pixel to millimetre conversion, shown by the comparatively low absolute errors obtained after calibration. Experiment 3.3 demonstrates that the PRM and SLSE (Smoothed Lattice of Scale Estimates) calibration methods are effective for the removal of optical distortion for all three tested focal lengths. The results evaluating the 8 mm lens show a slight decrease in performance, at roughly three times the level of residual calibration errors; however, with improved relative performance in foreground and background contrast levels. Therefore, we suggest the 8 mm lens be used as a suitable operating point for the measurement apparatus.

From theorems 3.1, 3.2, and 3.3 (using increasing complexities of quantisation error model) we observe the same estimate of mean quantisation error to be 0.41 pixels, when measuring the length of rice grains in the image. Experiment 3.4 shows that given a grain of rice was measured five times, we estimate that at the 99.7% confidence level we would expect an uncertainty of ± 0.55 pixels; ± 0.39 pixels for 10 measurements; and ± 0.27 pixels for 20 measurements. If the optics system is configured to approximately 12 pixels per millimetre, this length error equates to 0.046 mm (for 5 grains), which for the purposes of static grain measurement is sufficient. From experiment 3.5, the uncertainty in length measurement due to image quantisation is ± 0.041 mm. This represents the 'lower bound' on overall system accuracy, assuming everything is working perfectly. This error is estimated from theoretical analysis, simulated models and experimental trials.

In experiment 3.6 we evaluated the contour extraction of rice grains, as the contrast configuration was altered by reducing the background quality, *i.e.* 'adding rice dust'.

Similarly, in experiment 3.7 we evaluated the contour extraction as the rice moved position across the viewing area, *i.e.* picking up on errors from residual geometric distortion as well as illumination variation across the view. We conclude the outright best contour extraction method is the SmoothHybridHist method, which is the novel technique of using a local tiling strategy with the GlobalHist method, and then combining the thresholds values using a Gaussian smoothing filter. From experiments 3.8 and 3.9, we are able to select a method which provides the most accurate length estimation compared to hand measured lengths with the Vernier calliper. From measuring the length of head rice, we find that the SmoothHybridHist image segmentation method gives consistently lower mean errors than the standard global GlobalHist method, in the case of ParallelPrincipalAxis length measurement there was 0.015 millimetres lower mean error. However, regarding broken grains: a 0.026 mm increase in mean error; we observe that the errors are below the quantisation error, which we expect to be 0.041 mm. We would recommend, out of the tested methods, that the ParallelPrincipalAxis length as the length measurement of choice.

In summary, we recommended a static measurement system working with the PRM calibration routine; 8 mm lens; SmoothHybridHist contour extraction method, with the peak detection correction; and the ParallelPrincipalAxis length definition. The overall system accuracy, with these components, is evaluated in chapter 6.

Chapter 4

On-Line Measurement of Broken Rice Percentage with Length

In the previous chapter we presented a system for the accurate length measurement of static and singulated rice grains. In this chapter, we extend the method to allow the measurement of the percentage of broken rice grains during mid-flow. The rice in motion measurement apparatus enables the bulk-flow of rice grains with the use of a mechanical feeding mechanism and a sloped glass plane. The expected flow speed of the rice grains on the glass plane is, at most, 1 metre per second. We expect that there are six possible sources of mean error for the measurement of rice in motion: the misclassification error from selecting single grains, the biased probability of seeing shorter grains, tumbling grains, and residual mean errors from geometric distortion and from non-uniform contrast across the view.

For all of the experiments discussed in this chapter, the brightness setting of the ring light system was fixed to maximum. The lighting system is expected to be strobing with the LED driver over-loaded. When using the strobing mode, by default, the duty-cycle of the LED ring light is not used to maximum capacity; therefore the the LED ring light can be over-driven until the duty-cycle remains roughly the same as a static light source. The over-drive on the RIM kit was set to 700% input level of the current rating. However, we would not expect an effective seven fold increase in background to foreground contrast (due to diminishing returns). Figure 4.1 contains an outline and two images of the prototype measurement apparatus.

Geometric distortion errors and non-uniform illumination were addressed in chapter 3. Tumbling grains are a by-product of the feeding mechanism of the first prototype motion measurement apparatus, and can cause a new mean error where grains appear shorter than they are (discussed later). Motion blur does not require a corrective approach

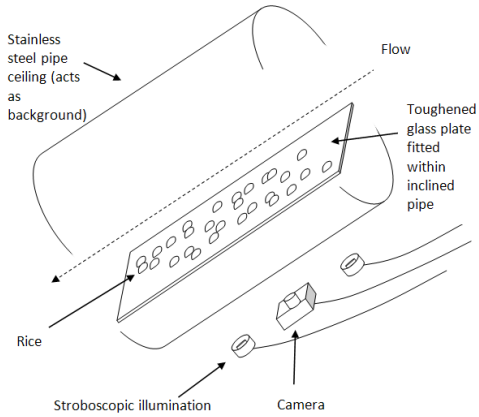

4.1.1 Concept sketch.

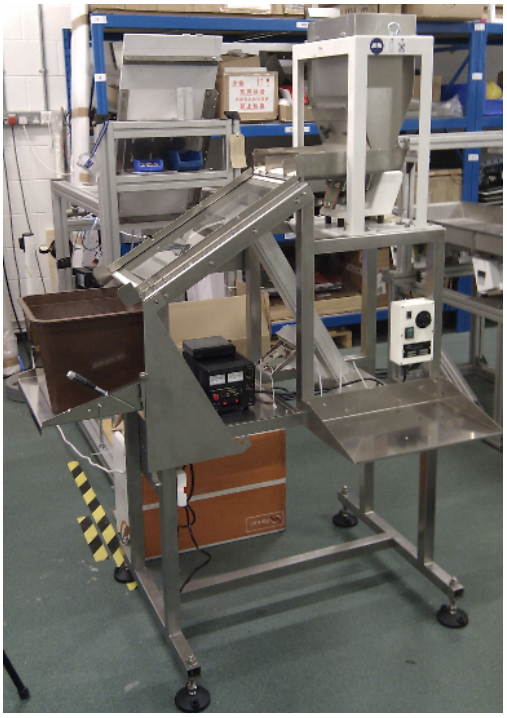

4.1.2 Photograph of the prototype hardware in the laboratory (no camera installed).

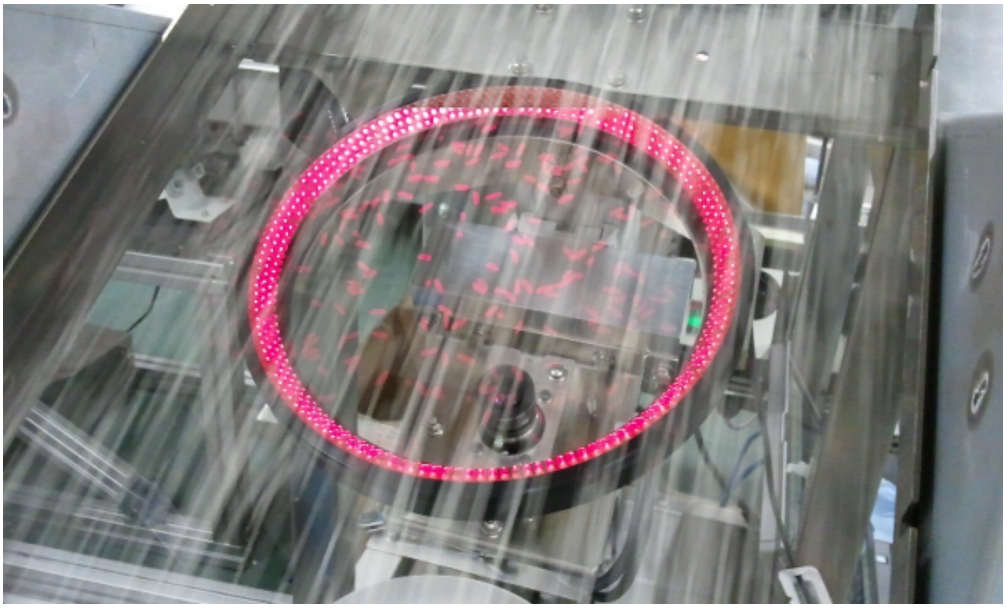

4.1.3 Photograph of a top down view of rice during mid-flow capture. The red illuminated grains from within the stroboscopic LED illumination field appear frozen, whereas the remaining grains appear in motion due to the different shutter speed of the digital camera.

FIGURE 4.1: Concept and prototype of the rice in motion measurement apparatus.

given the illumination system is stroboscopic, due to reduced errors [26]. The remaining issues are addressed in the image processing pipeline of the rice in motion measurement apparatus, shown in figure 4.2.

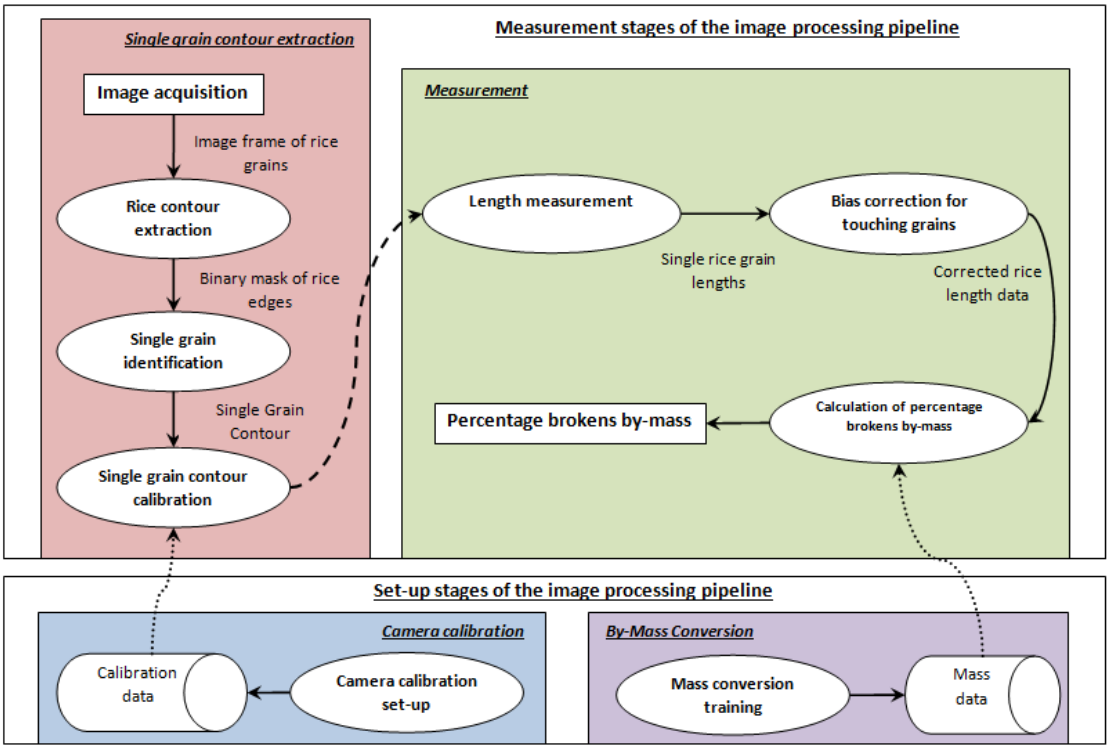

FIGURE 4.2: Overview of how to enable a computer to measure the percentage of broken rice grains in motion, using a length measurement decision criterion.

The single grain contour extraction stage is the first of the measurement pipeline. The aim is to extract a calibrated and corrected (distortion free) contour of every singulated rice grain from the input image. The processes in this stage consists of rice contour extraction, which describes the segmentation of foreground from background pixels (and selection of the perimeter edge of the rice grains); single grain identification, which rejects touching grains (grain-to-grain as well as grain-to-edge touching); and then single grain contour calibration, which applies the lens distortion correction model to the singulated rice grains.

The measurement processes takes place within the second stage of the measurement pipeline. The aim here is to infer information about the rice grain, given the extract contour from a single grain, and estimate the percentage of broken rice (by-mass). This process consists of a length measurement from the calibrated contour data of single grains; bias correction for touching grains, which tackles the problem of assuming all grains are single when we have rejected touching grains; and finally, calculation of percentage of broken rice by-mass, which applies a conversion factor to the by-count measurement of the percentage of broken rice.

In the first section of this chapter we define the percentage of broken rice by-count from a population of measured rice grain lengths; we also discuss the expected sampling consistency of measurements of percentage of broken rice grains. Section 4.2 describes the process of single rice grain detection using simple morphological features. Section 4.4 explores the correction factor required for removing the error from the biased probability making it more likely to see shorter grains of rice. Section 4.3 discusses the possible mean errors associated with tumbling grains, *i.e.* a grain that may spiral or spin in addition to bumping into other grains. Section 4.5 contains the necessary steps to perform a conversion from a by-count to a by-mass estimation of broken rice percentage. In the final section, we conclude the chapter with the important findings.

4.1 Percentage of Broken Rice By-Count

The percentage of broken rice is defined by the one of the industry standards, consisting of the length rule: a broken grain is less than three quarters of the average length of the head rice kernel for that variety (a fixed value). The rice in motion measurement apparatus measures the length of a population of rice grains over a series of images. One way of estimating the percentage of broken rice is to apply the threshold criterion to the length distribution of the measured grains. Let $p(l|v)$ be the distribution of single grain lengths in mm, *i.e.* the probability of grain lengths given that they are visible. This is considered what we measure from what we 'see' in a standard captured data stream of rice grains during bulk flow (given that the touching grains are ignored and the single grains are measured). The length distribution of all the rice grains in the image, touching and single, would be represented by $p(l)$.

A correction model is applied to estimate $p(l)$ from $p(l|v)$, this is further discussed in section 4.4. For the moment, assume that $p(l) \approx p(l|v)$. The area under the curve $p(l)$ is normalised to 1, such that:

$$p(l) = \frac{p(l)}{\int p(l)dl} \tag{4.1}$$

Let B_τ be the measurement of the proportion of broken grains. The percentage of broken rice is given by splitting the distribution of lengths into broken grain and head rice classes, with a single length threshold τ, see figure 4.3. The area under the curve for each class is the respective proportion of broken and head rice (as the curve has already been normalised).

Thus, B_τ is given as the area between the interval $p(0 < l < \tau)$:

$$B_\tau = \int_{l=0}^{\tau} p(l)dl \tag{4.2}$$

where τ is the length threshold set given the rice variety *e.g.* set to $\tau = \frac{3}{4}\mu$, where μ is the mean grain length of that variety of rice.

A relatively good approximation of the consistency of the percentage of broken rice measurement is derived from binomial sampling [112], given by the formula: $\sigma = 2\sqrt{\frac{B_\tau(100-B_\tau)}{n}}$. Where, B_τ is the contamination level and n is the sample size. An estimation within a 95% statistical confidence level is assumed. Relevant information from the hand measured sample can be used in the above formula; we evaluate some useful parameters in experiment 4.1.

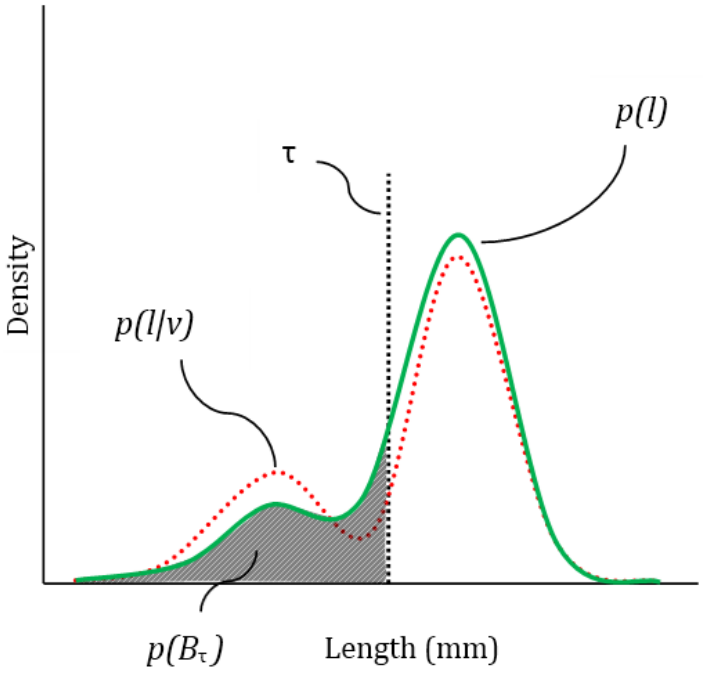

FIGURE 4.3: The percentage of broken rice, defined by a single grain length threshold τ, is given as the area under the normalised distribution of grain lengths $p(l)$, between the interval of $p(0 < l < \tau)$. It is the distribution $p(l|v)$ that is observed by the measurement system, which in general, may differ from $p(l)$.

Experiment 4.1. The estimation of the 95% confidence level sampling consistency of broken rice is evaluated using the above model. Table 4.1 contains a set of estimations of the standard deviation of errors, ε_σ. It is recommended that a minimum of 2,000 grains should be measured when sampling rice; we would thus expect an improvement in the consistency of the ground-truth percentage of broken rice, to $\pm 1.34\%$ and $\pm 1.79\%$ for 10 and 20% input contamination of broken rice, respectively.

Contamination %	Sample Size	ε_σ
10	1000	1.8974
	2,000	1.3416
	2,500	1.2000
	5,000	0.8485
	10,000	0.6000
	25,000	0.3795
	50,000	0.2683
15	1,000	2.2583
	2,000	1.5969
	2,500	1.4283
	5,000	1.0100
	10,000	0.7141
	25,000	0.4517
	50,000	0.3194
20	1,000	2.5298
	2,000	1.7889
	2,500	1.6000
	5,000	1.1314
	10,000	0.8000
	25,000	0.5060
	50,000	0.3578

TABLE 4.1: Percentage of broken rice measurement consistency tables with 95% confidence, for various numbers of samples and contamination percentages.

4.2 Single Grain Identification

Single rice grain detection is an important component of the image processing pipeline for broken rice grain measurement; the assumption is made that only single rice grains will be measured by the system. Therefore, not only is the accuracy of 'singles' algorithm important, but obtaining a method that works across different varieties of rice grains with preferably no additional parameter changes (given there are approximately 40,000 varieties of rice worldwide [113]).

The industrial sponsor has shared the Length-Width-Corner (LWC) method for single grain detection. The LWC algorithm is applied to the input binary image to remove contours that comprise two or more grains. The algorithm takes its name from the three parameters consisting of: length threshold, width threshold, and corner threshold. Clumps are identified if any of these parameters are exceeded by the appropriate measurements of the contour in the image.

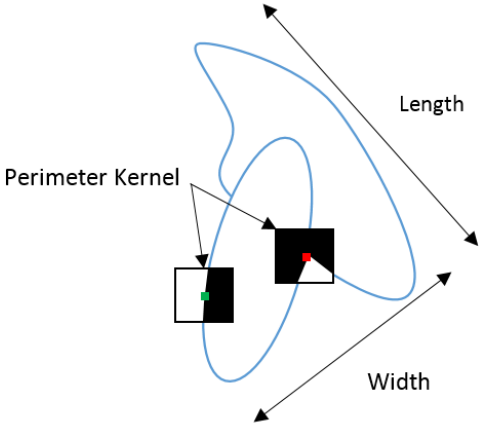

4.4.1

FIGURE 4.4: Illustration of the LWC single grain detector. In this example two touching grains are visible, the length and width of the footprint are readily computed, if these exceed the parameter thresholds then a touching grain is detected. A third component checks to see if any 'corners' are detected: defined as a moving kernel that has an area percentage greater than the allowed threshold. In this example the red square indicates the perimeter pixel of the grains where a corner was detected, at a threshold of over 75% coverage of the kernel. The green square is a perimeter pixel that is not a corner.

The optimised parameters are sought in order to have a variety independent solution for detecting single grains. At this stage only a rough estimate of length and width of the clumps are required to detect the single grains, therefore the same length method is used but without calibration and optical distortion removal. If either the object's length or width exceed the relevant thresholds, then that object is labelled as a clump. In the case of the corner threshold, a sliding 7-by-7 pixel window moves around the perimeter of the

group of pixels for an object. If at any point the coverage in the window (percentage of presence pixels) exceeds the corner angle threshold, then a 'corner' has been found. Given one or more corners in an object, then that object is labelled as a clump.

In section 4.2.1, we describe an experiment to estimate the acceptable accuracy levels of single rice detection (that could be used for broken rice measurement). In order to estimate the accuracy of the LWC algorithm a sweep of the three parameters is performed, further discussed in section 4.2.2. A wider sweep of the parameters will determine if a single combination can be used to accurately separate single grains from all tested varieties of rice.

4.2.1 Estimation of Acceptable Accuracy of Singles Detection

In experiment 4.2, an estimation of the acceptable accuracy of singles detection is derived with respect to the effect on the mean error of broken rice measurement. We model the estimate of the percentage broken rice, given an accuracy level of single detection. The following notation be used:

- Let B be the true contamination percentage of broken grains in a sample of rice.
- Let P be the percentage of single grains that are to be queried by the system. These grains do not include obvious clumps (which are pre-filtered before the singles detection process).
- Let Δ_P be the change in the percentage singles P. This represents an estimated upper bound error of singles detection.

The observed estimate of the broken rice percentage is then defined as the following:

$$\hat{B} = \frac{PB}{(100 - B)P + (PB)} \tag{4.3}$$

The adjusted estimate, that takes into account the error in singles detection, is given as:

$$\hat{B}' = \frac{PB}{(100 - B)(P + \Delta_P) + PB} \tag{4.4}$$

The mean error in the broken rice measurement caused by singles detection is given as $\hat{B}' - \hat{B}$.

Experiment 4.2. The estimation of the bias in broken rice measurement caused by misclassification of single rice is evaluated using the above model. Given 10% broken

rice, $P = 95$ and a range of Δ_P values, a set of the estimated errors on broken rice measurement is shown in table 4.2. These results indicate that with a value of 1% error in singles detection, we expect a mean error of -0.09% on the measurement of broken rice, which suggests that a significant error in single grain detection has a minimal effect the broken percentage.

Error in Singles Detection (%)	Error in % Broken Measurement
1.0	-0.09
2.0	-0.19
3.0	-0.28
4.0	-0.37
5.0	-0.45
6.0	-0.54
7.0	-0.62
8.0	-0.70
9.0	-0.79
10.0	-0.87

TABLE 4.2: Estimated mean error on broken rice measurement given an expected error in singles detection accuracy.

4.2.2 Accuracy of Singles Detection

We can observe how much the broken rice percentage alters as a function of the the singles detection accuracy, by monitoring the difference between maximum and minimum of the broken rice percentage scores over a sweep of the relevant parameters, *i.e.* the range of the percentage broken rice over a sweep of the algorithm parameters. The accuracy of the algorithm is measured by cross validation with a labelled ground-truth. In order to ground-truth the data for the accuracy experiments, the binary images of the single grains and clumps were manually sorted into their respective categories (single or clump). Three varieties of rice are tested; these consist of a large sample of images of roughly 12,500 grains each of US Long, Basmati, and Parboiled US Long. The three data-sets were extracted from previously captured data of rice during mid-flow with the rice in motion measurement apparatus. Figures 4.5 and 4.6 contain sample images of both single and clump classes. Obvious clumps are automatically disregarded in the system, defined as a very large area of connected pixels (it must contain at least three rice grains). The data-set contained several regions for which the class was unknown, of roughly 50 samples per rice type; these were extracted and disregarded. Figure 4.7 contains a sample of these regions.

The mean accuracy definition, ACC, is generally calculated as $(1 - (\frac{\text{FP}+\text{FN}}{n}))$, where FP is the number of false positives (grains incorrectly classed as single), FN is the number

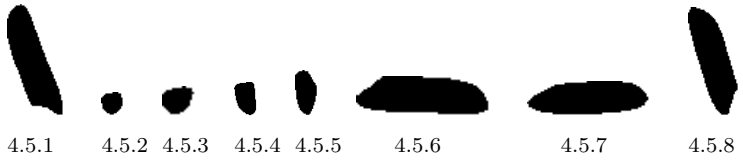

FIGURE 4.5: A sample of 'single' Basmati rice grains.

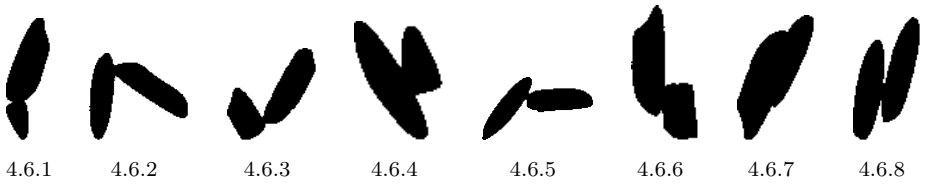

FIGURE 4.6: Sample 'clumps' of Basmati rice grains.

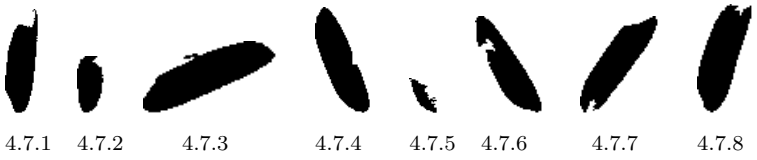

FIGURE 4.7: Samples of disregarded Basmati rice grains not used in the experiments.

of false negatives (grains incorrectly classed as clumps) and n is the total number of images analysed. In order to estimate the accuracy of the LWC algorithm, a sweep of the three parameters was performed in experiment 4.3. Then, experiment 4.4 determines if a single set of parameters for the algorithm can be used to accurately separate single grains from all tested varieties of rice, *i.e.* a variety independent algorithm.

Experiment 4.3. The accuracy of the LWC algorithm was estimated over a sweep of the three available parameters. Table 4.3 contains these results. Figure 4.8 contains three surface plots of the variety dependent parameter sweeps for each variety of rice. Figure 4.9 contains three surface plots of the variety dependent parameter sweeps. The LWC algorithm does not appear to be sensitive over the 7-by-7-by-7 parameter sweep, where the range of broken rice percentage is 0.09%. For both US Long and Basmati rice, a range of 0.06% is observed. The LWC algorithm is shown to have a high accuracy of $> 99.8\%$ over a reasonable range of parameters. However the Basmati rice required a starting point of the length parameter to be ˜30 pixels greater than US Long and Parboiled US Long. We observe that the corner threshold parameter of 75% was optimal irrespective of rice variety.

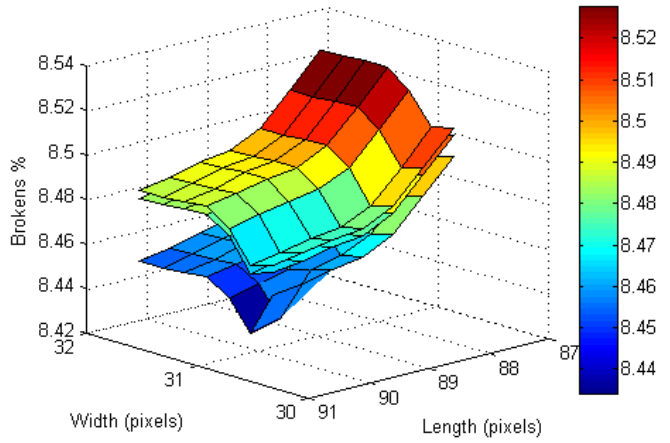

4.8.1 US Long

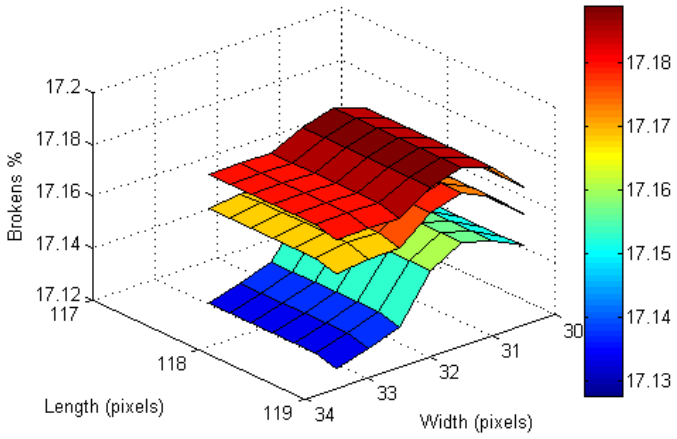

4.8.2 Basmati

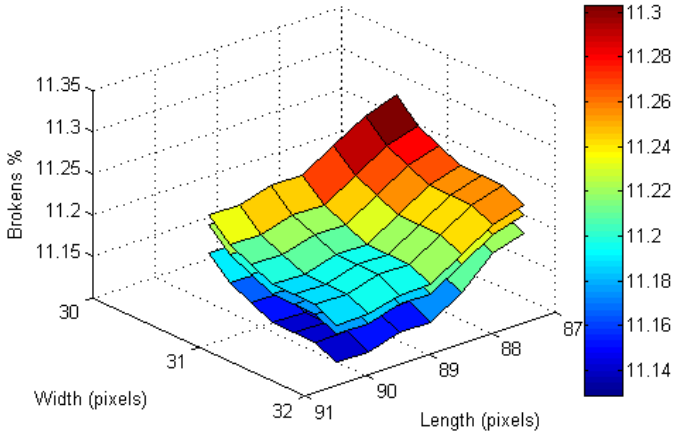

4.8.3 Parboiled US Long

FIGURE 4.8: Percentage broken rice from a sweep of variety dependent LWC parameters. In each surface plot, three layers are given representing Corner thresholds 72, 75 and 78 (the lowest, middle point and highest corner threshold values that were tested).

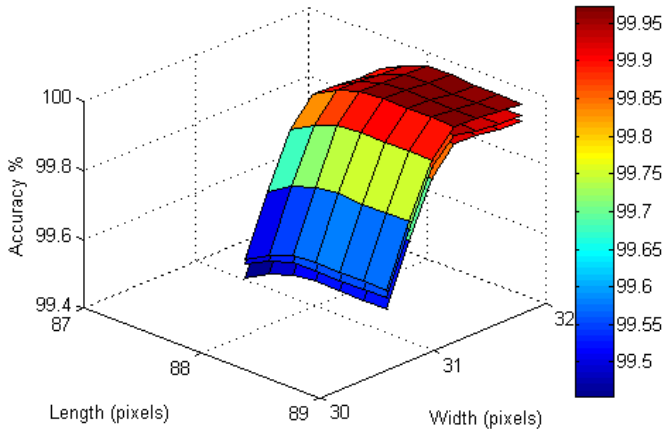

4.9.1 US Long

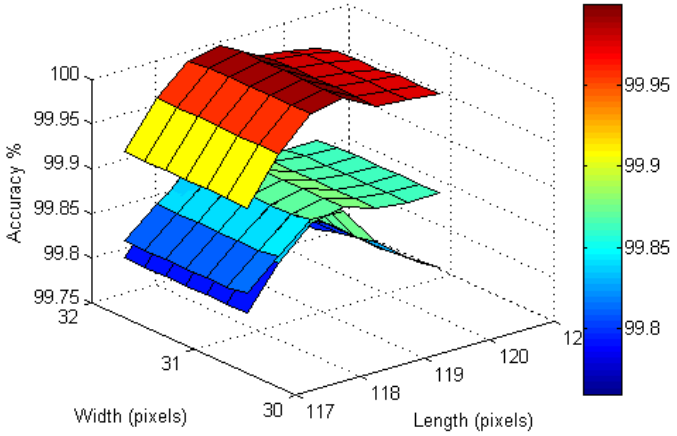

4.9.2 Basmati

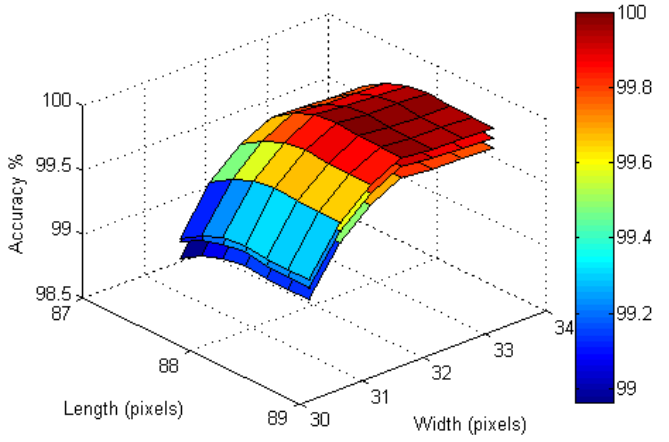

4.9.3 Parboiled US Long

FIGURE 4.9: Accuracy over a sweep of the parameters with the LWC algorithm. In each surface plot, three layers are given. These represent the lowest, middle point and highest corner threshold values that were evaluated during the parameter sweep.

Rice Type	Range (%)	Accuracy (%)	Best LWC Parameters (pixels)
US Long	0.09	99.97	(90, 33, 75)
Basmati	0.06	100	(120, 33, 75)
Parboiled US Long	0.06	100	(90, 33, 75)

TABLE 4.3: Singles detection performance using variety dependent parameters. The range is calculated over a large sweep of the parameter combinations. The Best LWC Parameters are shown, for the highest performing set with regards to detection accuracy.

Experiment 4.4. In this experiment we determine if a single set of parameters for the algorithm can be used to accurately separate single grains from all tested varieties of rice. The parameters of the algorithm are incremented in step sizes of 3 pixels, for a large range of values of each. The accuracy results with the wide sweep of the LWC algorithm are shown in figure 4.10, using a fixed value 75% (reported in experiment 4.3 to be the optimal corner threshold). In this case, the minimum accuracy across the three varieties are shown and the optimal parameters are selected as the maximum of these. A sample of false positives and false negative are shown in figures 4.11 and 4.12, respectively. In addition, we report that the method processes ˜12,500 grains in 2.1 minutes (for singles detection only).

We have determined that, the optimised parameters for variety independent detection of single grains are: length: 8.2 mm, width: 2.7 mm and Corner threshold: 75% (converted to millimetres from the calibration algorithm using a length of 99 pixels, and a width of 33 pixels). The optimal parameter selection provides 99.93% accuracy. From experiment 4.2, we estimate that 1% error in singles detection would give a mean error of -0.09% on the measurement of broken rice. The single detection algorithm would therefore be well within these errors.

Rice Type	Accuracy (%)
US Long	99.96
Basmati	99.93
Parboiled US Long	99.93

TABLE 4.4: Results of parameter free singles detection performance, tested on three varieties of rice.

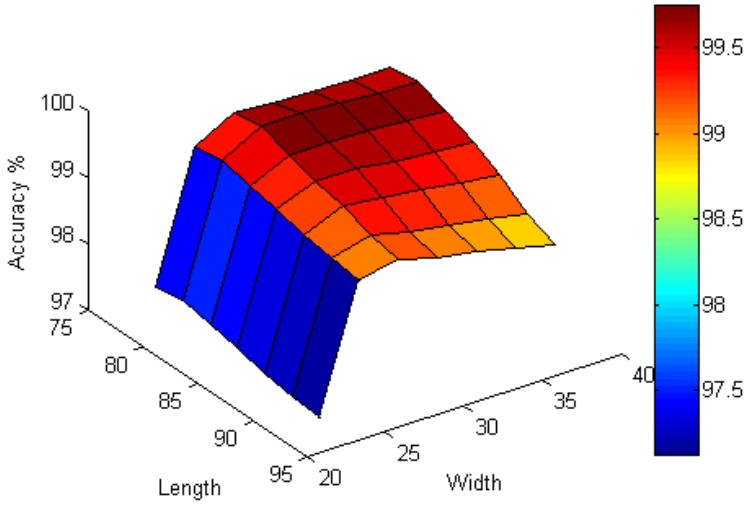

4.10.1

FIGURE 4.10: Accuracy over a wide sweep of the length and width parameters using the LWC algorithm. The corner threshold was set to 75 (the optimal value). The minimum accuracy percentage across the three varieties are shown in the surface plot. The optimal parameters are selected as the maximum of these accuracy values.

4.11.1 4.11.2 4.11.3 4.11.4

FIGURE 4.11: Sample of false positives (Basmati).

4.12.1 4.12.2 4.12.3 4.12.4 4.12.5

FIGURE 4.12: Sample of false negatives (Basmati).

4.3 Error from Tumbling Grains

The 2D nature of the optical and processing pipeline renders the apparatus unable to notice whether a grain is tumbling or not. The observed silhouette of the rice grain may be severely foreshortened, due to the smaller observed footprint, see figure 4.13. We report that the first prototype hardware produces a tumbling grain rate of 2%, as indicated by the mechanical engineers from the industrial sponsor. The industrial sponsor has independently worked on reducing the tumbling grain percentage, and would expect no significant level of tumbling grains in the second prototype of the rice in motion measurement apparatus, further discussed in experiment 6.3 from chapter 6. We have devised three experiments to identify the impact on the measurement of broken rice; this is useful to help evaluate any results that we obtain with the first prototype. Experiment 4.5 models the foreshortening effect from three shapes. Experiment 4.6 estimates the effect of the distortion from tumbling grains from a Monte Carlo simulation. Finally, experiment 4.7 is conducted using a sample of 100% head rice.

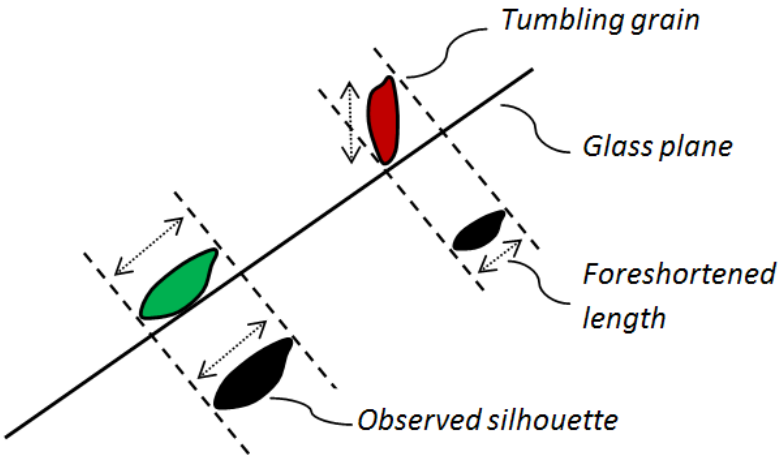

FIGURE 4.13: Illustration of the foreshortened appearance, to a camera below the glass plane, of the observed grain length given a grain was tumbling away from the glass.

Experiment 4.5. An estimation of the contour foreshortening is made by modelling three shapes. These consist of a line, ellipse and rectangle. A simulation trial of each shape is conducted using a range of uniformly random length and orientation (angle of the shape from the simulated flat plane). A suitably large trial of measurements is conducted. This consists of 50,000 length values at each orientation between 0° (flat) and 90° (maximum tumble) from the horizontal glass plane. We observe, from modelling a line, that a tumbling grain of 11° may give a significant impact on the observed length, with a mean length error of −0.1 mm, see figure 4.14. The results of the elliptical

shape, considered the closest shape of the three tested to a rice grain, suggests a similar relationship to the simple line. However, we see that a significant error in length of −0.1 mm, is now apparent with a grain orientation of 17°, see 4.14.

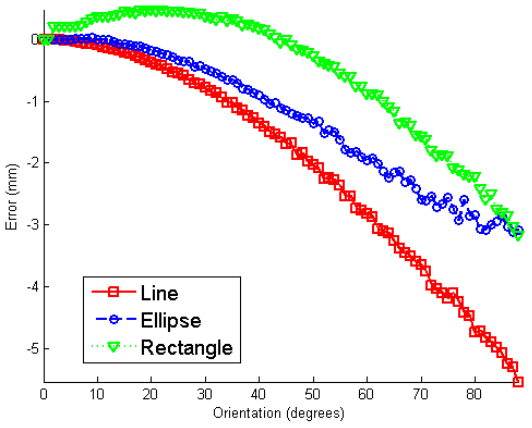

4.14.1 Foreshortened observed length, using shapes from 0 to 90° orientation.

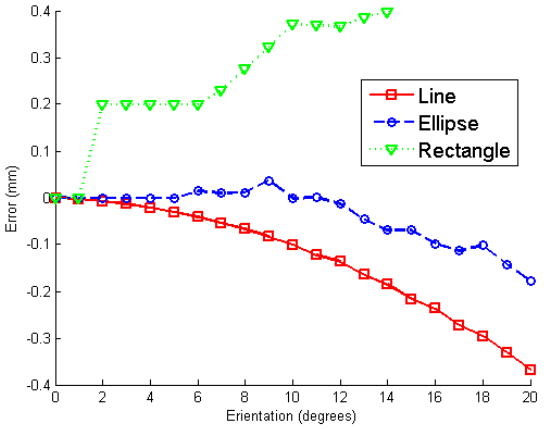

4.14.2 Close up of 0 to 20°. Quantisation error is expected for simulations of both the ellipse and rectangle shapes.

FIGURE 4.14: Estimated mean error of the observed length from tumbling grains. Three simulation trials were conducted using lines, ellipses and rectangles.

Experiment 4.6. An estimation of the effect of the distortion from tumbling grains is made using a Monte Carlo simulation. We create a Gaussian distribution of 1 million grain lengths, with a mean length of 6.369 mm and standard deviation of 0.56 mm; *e.g.* a tumbling rate of 2% would indicate that 20,000 grains would be distorted due to tumbling. Thus, 20,000 uniformly randomly selected grains are picked and assigned a uniformly random angle of tumbling. Each of the tumbling grains are distorted by the length error as estimated in experiment 4.5, shown from the ellipse curve in figure 4.14.

The simulated mean error due to the effect of contour foreshortening of tumbling grains is shown in table 4.5. Various tumbling grain rates were calculated, see figure 4.15. We observe that a 2% tumbling rate gives an estimated length error of −0.025 mm due to the foreshortening effect. An equivalent of 1% broken rice would be observed due to the same 2% tumbling rate; considered to be a significant error in broken measurement caused from one source. If the tumbling rate is reduced to the system requirement rate of 0.1% (section 1.1.1), the estimated mean error would be −0.001 mm; consequently the error on broken rice measurement would drop from 1% to an estimated 0.2%. A 10% tumbling rate signifies a considerable error on mean length, greater than 0.1 mm. However, we consider than the percentage broken rice is far more distorted as a result of increased tumbling grains.

Tumbling %	Mean Length (mm)	Distorted Length (mm)	Error (mm)	Broken %
0.0	6.369	6.369	0.000	0.2
0.1	6.369	6.367	-0.001	0.2
0.5	6.369	6.362	-0.006	0.4
1.0	6.369	6.356	-0.012	0.6
2.0	6.369	6.344	-0.025	1.0
5.0	6.369	6.306	-0.063	2.2
10.0	6.369	6.243	-0.125	4.2
20.0	6.369	6.118	-0.250	8.3

TABLE 4.5: Estimated mean error, from simulation trials, due to the foreshortening effect from tumbling grains.

Experiment 4.7. This experiment estimates the effect of tumbling grains from samples of 100% head rice (US Long and Parboiled US Long varieties). We hypothesise that a population of only head rice would appear to contain some broken grains if fed with a system that produces the tumbling effect. A ground-truth length measurement is made with Vernier callipers from a hand picked sample of approximately 20 grains, and the broken percentage is calculated from manually finding any accidental broken rice in the sample of head rice. Then, the percentage of broken rice is measured from the rice in motion apparatus, from approximately 20,000 grains. When compared to the hand measurements, the observed error would indicate the error caused by tumbling grains.

The ground-truth measurements of the experiment are shown in table 4.6, and the measurements from the system are reported in table 4.7. We observe from US Long grain samples, an average mean error of 0.47% caused by tumbling rice grains. The Parboiled US Long samples contained more breakage, however the corresponding mean error was disproportionately larger than the standard rice, with an mean error on broken rice measurement of 1.89%. The average error from all samples, 1.18%, is approximately

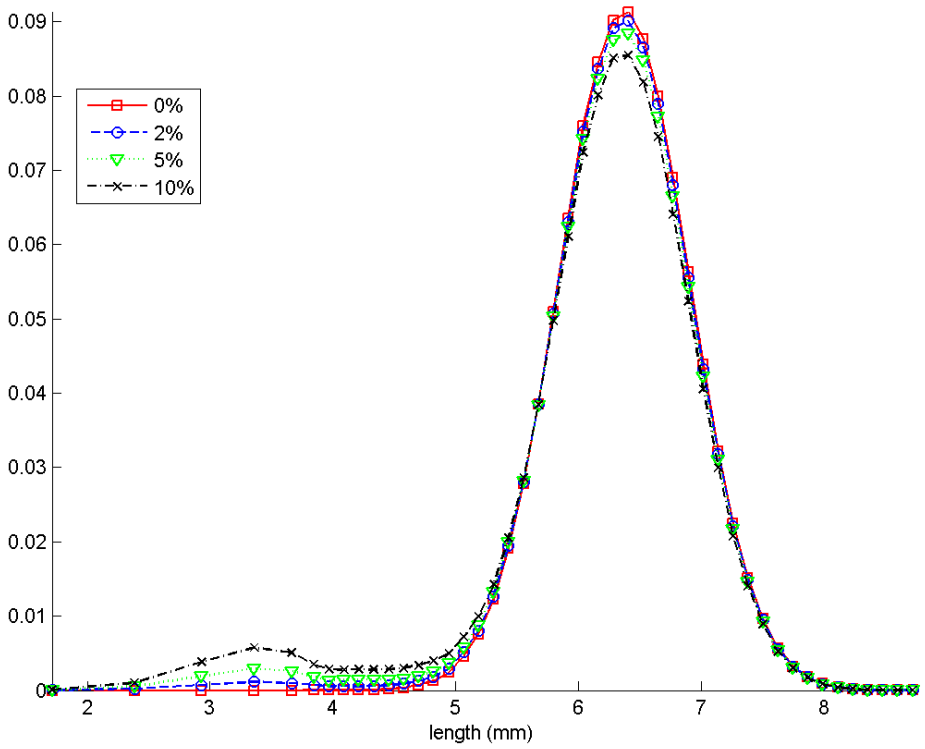

FIGURE 4.15: Simulated distributions of grain lengths with various tumbling rate percentages. The distortion for the selected tumbling grains was as calculated from figure 4.13. We can observe there may be little change in the mean length as the tumbling percentage increases. However, the area under the curves alter more drastically. This may indicate a much larger problem for estimation of the broken rice percentage.

the same as modelled in experiment 4.6, where we estimate a 1% error in broken rice percentage due to 2% tumbling grains.

Head Rice Type	Mean Length	Median Length	Broken %
US Long	6.71	6.75	0.17
Parboiled US Long	6.79	6.8	0.31

TABLE 4.6: Ground-truth broken rice percentage measured by Vernier calliper; only samples from a batch of head rice were selected. The mean and median length are calculated from a 20 grain sample hand measured with Vernier callipers.

Head Rice Type	Mean Length	ε_σ	Median	Broken %	ε_μ %
US Long	6.59	0.48	6.63	0.62	0.45
Parboiled US Long	6.67	0.58	6.74	2.12	1.81

TABLE 4.7: Broken rice percentage measured from the bulk-flow of only head rice. This set of results should be directly comparable to the ground-truth count in table 4.6.

4.4 Error from Touching Grains

There are two conditions where a grain is not measured by the apparatus: whether a grain is touching the border of the viewing window, and if that grain touches another grain. Any grain that has a partial or occluded contour is therefore ignored. Thus, a complete profile of a singulated grain is considered to be suitably visible. In both cases, intuitively, it is expected that there is an additional bias effect making it more likely to measure a broken or small grain. However, the flow of rice is complex and other factors may negate such this bias, *e.g.* the relative window size, and the throughput.

Continuing from the notation in section 4.1: Let $p(l|v)$ be the conditional probability of having a grain length given the grain is visible. This is considered what we measure from what we 'see' in a standard captured data stream of rice grains during bulk flow (given that the touching grains are ignored and the single grains are measured). The classification of broken rice as estimated from an observed subset $p(l|v)$ is $\hat{B}_\tau$. In this case, the information is partitioned with a bias effect on the probability of seeing a grain due to its length, and $\hat{B}_\tau$ would thus be a biased estimation of the broken rice. The mean error be the difference between the subset observed classification of broken rice and the input level, given as $\hat{B}_\tau - B_\tau$. A shift in the mean error of -0.05 and $+0.05$ indicates a 5% underestimation and a 5% overestimation of broken rice, respectively. The mean error is illustrated in figure 4.16.

In section 4.4.1, we estimate the biased effect on the visibility of a grain, due to its length. Section 4.4.2 contains the correction model that we have derived from Bayes Theorem of conditional probabilities.

4.4.1 Estimation from Empirical Observation

In this section, we estimate the broken rice percentage error due to the biased effect on the probability of seeing a grain due to its length. The estimation is made given the knowledge of the lengths of all grains of rice in a population, regardless of whether they touch other grains or the window edge. Given that there are two independent conditions of a grain being single or touching and a grain being complete or occluded, we can anticipate that a grain can meet one four combinations of those conditions, see figure 4.17.

A special rule is used for a touching grain that is connected to the window edge by proxy, *i.e.* when a grain is connected to the edge because it is touching a grain that is occluded. In this case, although the entire connected footprint of both grains is considered as occluded, we determine that the individual grain in question would not be

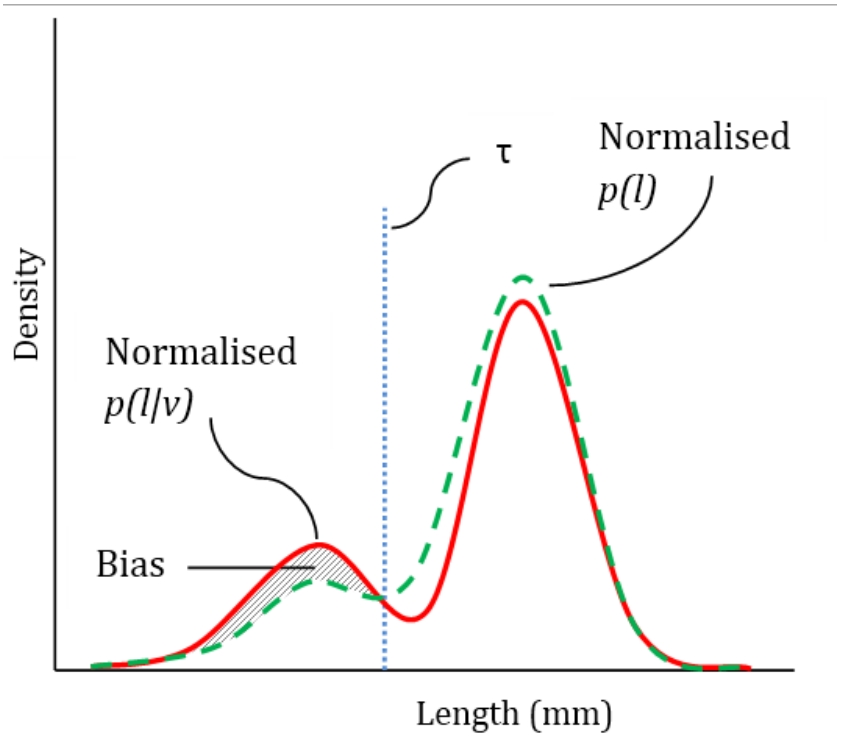

FIGURE 4.16: The mean error in broken rice percentage due to the biased effect of seeing a grain due to its length; the mean error is shown as the area of the shaded part in the diagram.

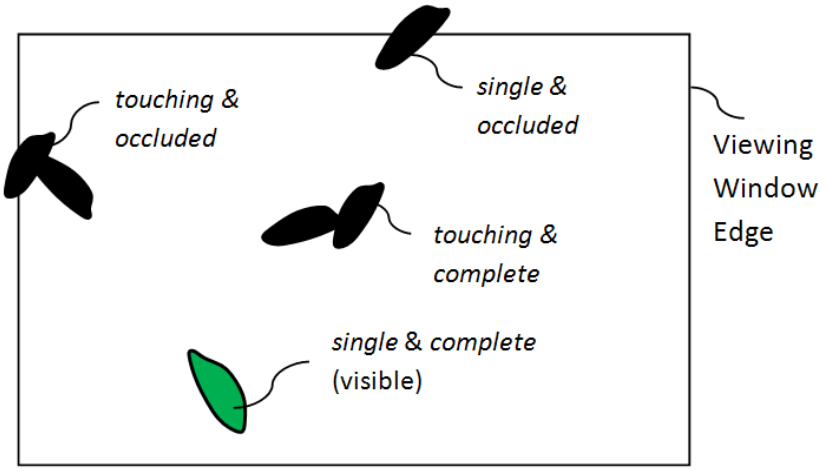

FIGURE 4.17: The four pairs of conditions for a grain of rice. A grain is only considered visible when it is both single (s) and complete (c). Thus, a grain is invisible given it is either touching ($\bar{s}$) or occluded ($\bar{c}$).

occluded given if it was separated from the touching neighbour. The following notation is used:

- Let $p(s)$ be the marginal probability that a grain is single, *i.e.* the probability that any randomly selected grain is not touching another grain where no other information is known other than the percentage coverage of the grains in the window. Let $p(\bar{s})$ be the marginal probability that a grain is touching, *i.e.* not single.
- Let $p(c)$ be the marginal probability that a grain is complete, *i.e.* the probability that any randomly selected grain is not touching or occluded by the viewing window edge. Intuitively, both $p(s)$ and $p(c)$ are considered as independent conditions. Let $p(\bar{c})$ be the marginal probability that a grain is occluded, *i.e.* not complete.
- Let $p(v)$ be the marginal probability that a grain is visible, *i.e.* the joint probability of the grain being single and complete: $p(v) = p(s, c)$.
- Let $p(v|l)$ be the conditional likelihood of a visible grain given a length. We expect a bias effect on the likelihood of a grain being visible given a length, as smaller objects will tend to have less chance of touching another grain or the viewing edge.

We expect that $p(s)$ is dependent on the coverage of the product flow; as the condition is considered true when a grain is touching another grain. Given that there are more grains on the viewing area we would expect more touching grains. With regards to $p(c)$ and the relationship to the coverage, we expect little to no change in the chance of a grain touching the edge given change in throughput. This is because the window edge is of a fixed size and position, hence a limited 'area of connectivity' to grains. Thus, a change in coverage would make no change to this area. As such, we expect little change to the chance of a grain touching the edge as the coverage is increased.

The four distributions $p(l|s, c)$, $p(l|s, \bar{c})$, $p(l|\bar{s}, c)$ and $p(l|\bar{s}, \bar{c})$ when combined, equate to $p(l)$. The conditional likelihood that we want to estimate is the probability of a grain being visible given its length, $p(v|l)$, where $p(v) \equiv p(s, c)$. In experiment 4.8 we estimate the bias due to touching grains by manually labelling data, and aggregating the lengths into the four described distributions.

Experiment 4.8. In this experiment, we estimate the bias on broken rice percentage caused by only measuring grains that do not touch the window edge or other grains. We empirically observe the behaviors of touching grains from manually labelled data captured from a Buhler Sortex Z-Series optical sorting machine. The optical set-up of the Z-series differs to the rice in motion measurement apparatus in three main ways:

1. The chute is three times as wide (300 mm).
2. The camera is line-scan, with approximately one third the resolution (at 0.3 mm per pixel).
3. The input product is moving faster than the 1 metre per second.

The expected operating point of the rice in motion measurement apparatus is roughly 250 kg/h. Therefore, two data-sets were prepared, one at 250 kg/h and the other at 650 kg/h; the respective mean coverage is approximately 4.2% and 10%, and the total number of available frames is 600 and 285, respectively. However, not all frames were processed during extraction and labelling of the grains. A sample frame, considered as a 1024-by-1024 pixel window, is shown in figure 4.18.

The semi-automated data-set preparation method to obtain the four distributions involves the following four main steps:

1. For complete grains: A sub-window is cut from each frame, of raw input data, with 50 pixels from the each edge (top, bottom, left and right). All grains touching the 'inner-edge' or outside the 'inner-window' are discarded. Automatic singles detection, using the LWC method from section 4.2, is used on the sub-windows to separate the single and touching grains. The grain thumbnails (small images of presence) are extracted and sorted into appropriate labelled folders. These lengths of these grains will give the distributions of $p(l|s,c)$ and $p(l|\bar{s},c)$ for single and touching grains, respectively.
2. For occluded grains: The same inner-edge of 50 pixels from the each edge is highlighted in the raw input data. Any grain in the image not touching the inner-edge is discarded. Automatic singles detection is used to separate the single and touching grains. The grain thumbnails are extracted and sorted into appropriate labelled folders. These lengths of these grains will give the distributions of $p(l|s,\bar{c})$ and $p(l|\bar{s},\bar{c})$ for single and touching grains, respectively.
3. The extracted thumbnails from the singles detector are then manually corrected.
4. Manual cuts are made to the images of the touching grains that have not been automatically separated; A cut is when the user uses image editing software to re-colour the connecting pixels of touching grains as the background colour.
5. The length of each grain under each of the four conditions is measured; the ensemble statistics are recorded.

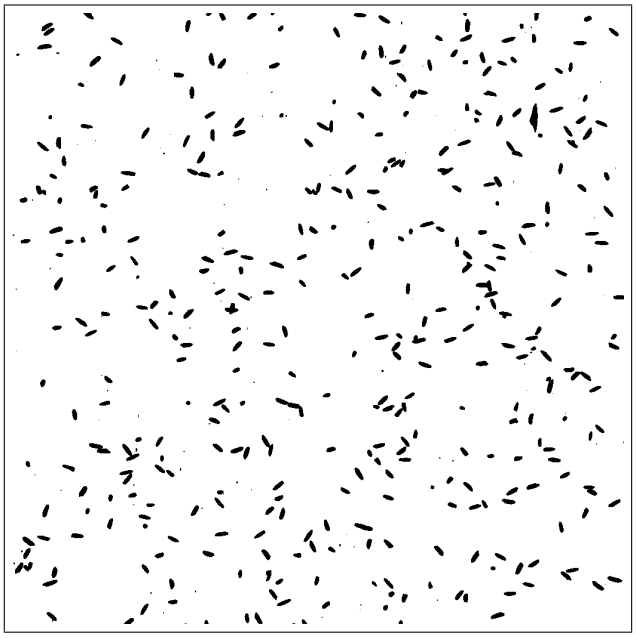

4.18.1 250 kg/h throughput (4.2% coverage).

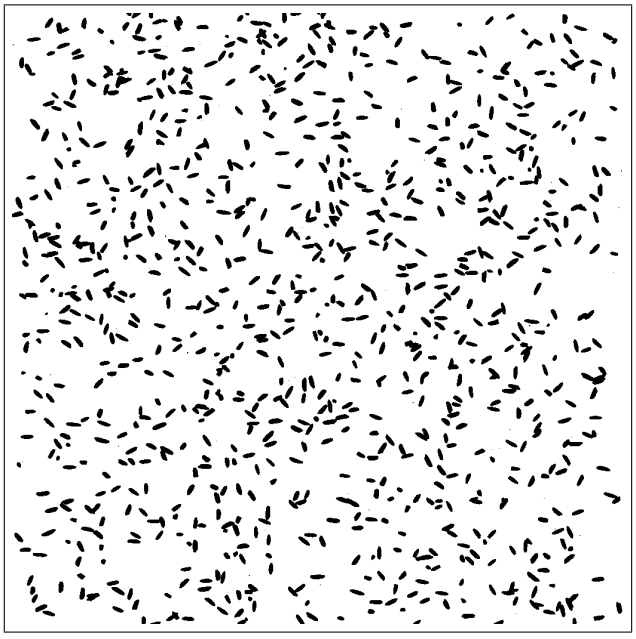

4.18.2 650 kg/h throughput (10% coverage).

FIGURE 4.18: Sample frames of raw input data from Z-Series optical sorter.

The number of grains in the data-set is approximately 20,000 and 10,000 at 250 kg/h and 650 kg/h, respectively; the actual broken rice contamination is unknown. Given the low resolution of the data, we would be cautious of the results based on measured length. Therefore, a coarse quantisation would be required in order to produce any useful distributions of grain length. Figure 4.19 shows the extracted length distributions from the Z-Series data-set. The measured broken rice percentage due to the probability of seeing a grain due to its length is noticeable when monitoring the distributions $p(l)$ and $p(l|v)$.

We report the results in table 4.8. The difference in the percentage of broken rice B_τ and the observed percentage of broken rice $\hat{B}_\tau$ are significantly different: a mean error of 1.9% and 4.4% indicates an overestimation of the percentage of broken rice, at 250 and 650 kg/h, respectively. From this experiment, we proceed to correct for this mean error in the measurement of broken rice in section 4.4.2.

Throughput (kg/h)	B_τ	$\hat{B}_\tau$	ε_μ
250	20.6	22.5	1.9
650	19.0	23.5	4.5

TABLE 4.8: Percentage of broken rice from all rice grains in the Z-Series data-set, B_τ, is compared to the observed percentage, $\hat{B}_\tau$, from only the visible grains. For this experiment, $\tau = 5$ mm.

4.4.2 Correction Model

A corrective approach is derived from Bayesian statistics to estimate the mean error due to the biased effect on the probability of seeing a grain due to its length. Such an approach is useful for an online implementation, as the input-data constantly changes over time. We apply a correction factor to the grain lengths data and mass data, before the measurement is completed. This correction is required, because the measurement is made given the lack of knowledge of the lengths and masses of all grains of rice in a population, only the knowledge of the single grains is known.

An expression is derived using Bayes Theorem of conditional probabilities allowing the estimation of the bias on broken rice measurement using only the observed lengths of grains that are visible, and the estimated biased effect on the visibility of a grain due to its length. Following from the notation given in section 4.1: let $p(v|l)$ be the conditional likelihood of a visible grain given a length. We expect a bias effect on the likelihood of a grain being visible given a length, as smaller objects will tend to have less chance of touching another grain or the viewing edge. Additionally, let $p(s|l)$ and $p(c|l)$ be the respective conditional probabilities of being single or complete, given a length.

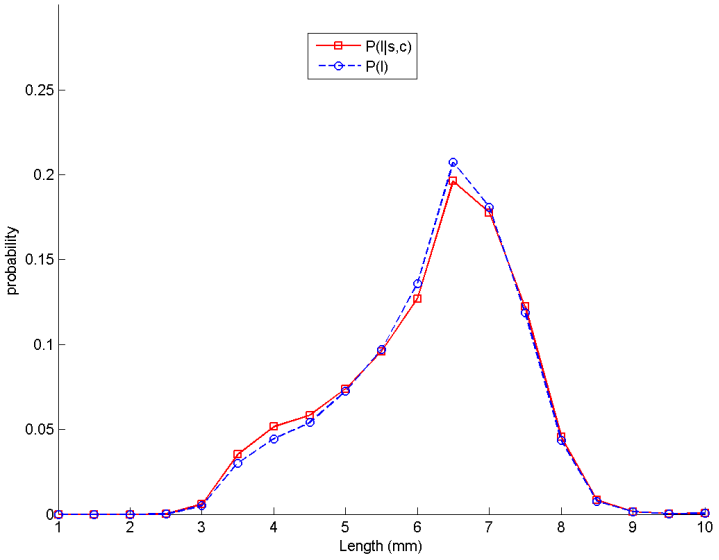

4.19.1 The $p(l)$ and $p(l|v)$ distributions at 250 kg/h throughput.

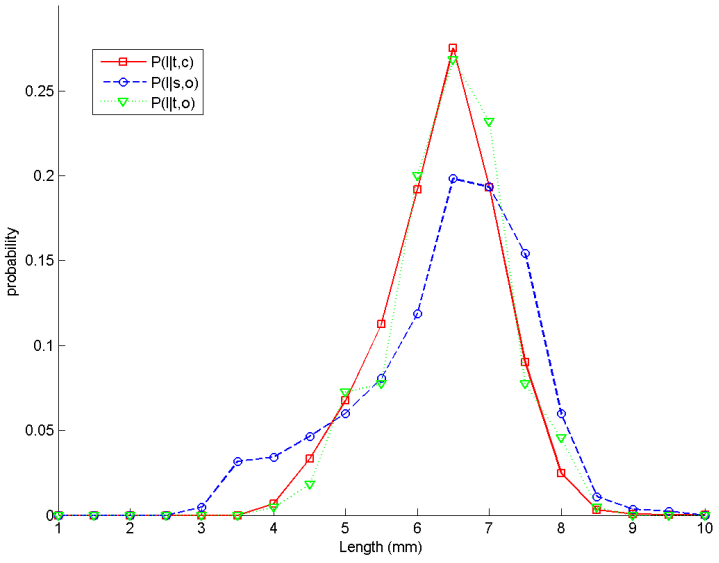

4.19.2 The equivalent $p(l|s,\bar{c})$, $p(l|\bar{s},c)$ and $p(l|\bar{s},\bar{c})$ distributions.

FIGURE 4.19: The extracted length distributions from the Z-Series data-set.

From Bayes Theorem of conditional probabilities:

$$p(l, v) = p(l|v)p(v) = p(v|l)p(l) \tag{4.5}$$

By rearranging the above equation, we can estimate the length distribution $p(l)$ as:

$$p(l) = \frac{p(l|v)p(v)}{p(v|l)} \tag{4.6}$$

The unknown constant $p(v)$ is used as a scaling factor to normalise the area under $p(l)$ to 1. Therefore, we can remove it from the equation to evaluate a proportionally equivalent $p(l)$, given as:

$$p(l_1) \propto \frac{p(l|v)}{p(v|l)} \tag{4.7}$$

From $p(l_1)$ we can estimate the scaling factor and thus the normalised $p(l)$, such that:

$$p(v) = \frac{1}{\int p(l_1)dl} \tag{4.8}$$

where $\int p(l_1)dl$ is the area under $p(l_1)$.

Thus, the estimated length distribution $p(l)$ is then given as:

$$p(l) = p(l_1)p(v) \tag{4.9}$$

$$= p(l_1)\frac{1}{\int p(l_1)dl} \tag{4.10}$$

A linear fit of the $p(v|l)$ distribution is produced from the sampled statistics of visible grains $p(l|s, c)$, the observed $p(l)$ distribution and $p(v)$, such that (by rearranging Bayes Theorem of conditional probabilities):

$$p(v|l) = \frac{p(l|v)p(v)}{p(l)} \tag{4.11}$$

In experiment 4.9, we estimate $p(v|l)$ from manually labelled data.

Experiment 4.9. We estimate the $p(l)$ and $p(l|v)$ distributions of length using the manual labelled Z-Series data-set from experiment 4.8. From these, we can infer the $p(v|l)$ distribution.

These distributions are shown in figure 4.20. We report the results of the correction model in table 4.9. We observe an overestimation of the percentage of broken rice, indicated by a mean error of 1.2% and 2.3% for 250 and 650 kg/h, respectively (using a broken threshold of $\tau = 5$ mm). Given these corrected estimates using the probabilities

of seeing a grain, we see there is a significant reduction in the overestimation of the percentage of broken rice. Comparing the results to those from experiment 4.8, we infer there is a reduction in the mean error of 0.7% and 2.2%, for 250 and 650 kg/h throughput, respectively. Further experimentation is conducted in chapter 6, where we compare the measurement of broken rice with and without the corrective approach.

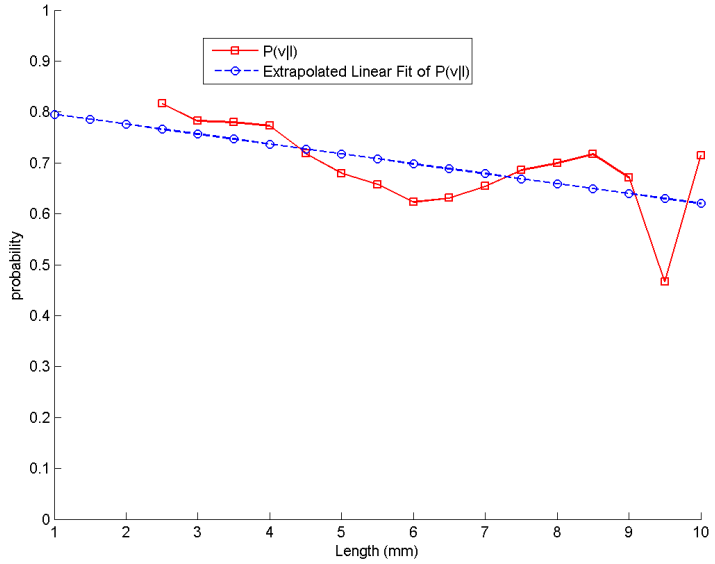

4.20.1 Extrapolated Linear Fit of $p(v|l)$ for 250 kg/h throughput.

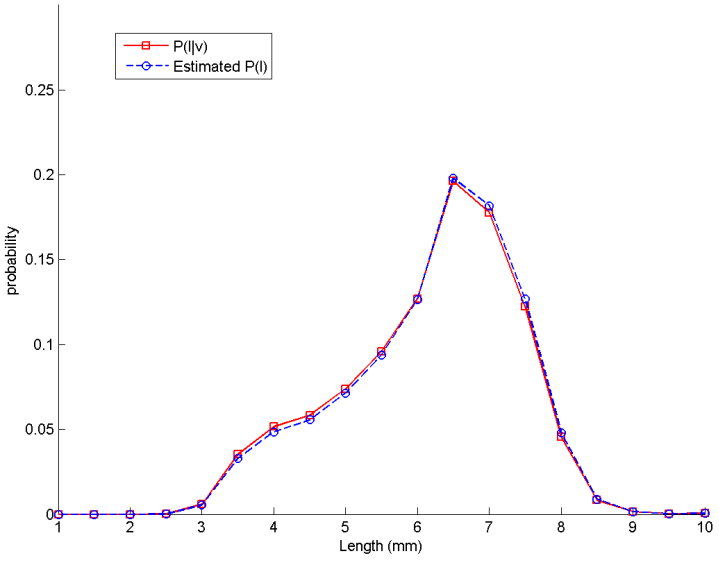

4.20.2 Estimation of $p(l)$ for 250 kg/h throughput.

FIGURE 4.20: The estimated length distribution, calculated from the linear fit of $p(v|l)$; and the measured grains $p(l|v)$ from the Z-Series data.

Throughput (kg/h)	τ	B_τ (from est. $p(l)$)	$\hat{B}_\tau$	ε_μ
250	5.0	21.3	22.5	1.2
650	5.0	21.2	23.5	2.3

TABLE 4.9: Error corrected broken rice percentage as calculated from the estimated $p(l)$; using the observed grain lengths $p(l|v)$ from the Z-Series data in experiment 4.8. We observe lower mean error that the uncorrected broken percentage estimates from table 4.8.

4.5 Conversion to Percentage Broken Rice By-Mass

The percentage of broken rice, defined by the industry standard length rule, is a *by-mass* estimation. Currently a *by-count* estimate in calculated from the rice in motion measurement apparatus. In order to convert from one measurement to the other, we first estimate the mass M of a rice grain as a function of measured area A of a rice grain. The mass estimation process takes an input vector of the grain areas in mm^2 and outputs a vector of masses of grains in milligrams. Given n number of observations of A and M the problem is considered as fitting the data to a straight line given by the expression:

$$M = (aA + b) + \varepsilon \tag{4.12}$$

where a and b are the parameters of the model, ε is the error of the model. This problem is then empirically solved with linear regression with two degrees of freedom [114].

To obtain an estimate of A from a rice grain, consider an object in the image having n number of pixels and having a set of pixel coordinates $P(\mathbf{u}, \mathbf{v})$. In this specific case the width or height of any pixel is given by the distance between that pixels coordinate and its nearest pixel neighbour. We could consider two possible neighbour pixels to $P(\mathbf{u}, \mathbf{v})$. The first is the neighbour pixel to the right of each pixel of the object, $q_h = P(\mathbf{u}+1, \mathbf{v})$. The second is the neighbour pixel below each pixel of the object, $q_v = P(\mathbf{u}, \mathbf{v}+1)$.

The horizontal pixel length d_g is the corrected distance in mm from the calibration routine, given the two points P_g and q_g. The vertical pixel length d_h is the corrected distance from the calibration routine, given the two points P_h to q_h. The calibrated area of an object in mm^2 is defined as:

$$A = \sum_{i=1}^{n} d_g d_h \tag{4.13}$$

Two experiments are conducted to evaluate the suitability of the conversion model from area to mass of broken rice. Experiment 4.10 evaluates the above model and estimates the parameters for a mixture of rice varieties; ideally, in the final system we require a conversion model that is variety independent. Therefore, for experiment 4.11, we use the combined parameters of the available rice types; and then evaluate the effectiveness of the general model for conversion of area to mass.

Experiment 4.10. The evaluation of the presented by-mass conversion method is straightforward. Assistance was given from the industrial sponsor with the collecting

and analysis of these results[1]. Rice grains samples from Basmati, TNDLX, Kranti, BPT and ASD16 were selected. The mass and area of each grain is measured to create the training data: the mass is measured using an electronic balance with an accuracy of ±0.00001 grams; the area is measured from images of rice grains captured with the static rice apparatus. The area of 80 grains in total are estimated (45 broken grains and 35 whole grains). The training data with total of 400 measurements is used to train the conversion model.

The parameters of the linear regression model for each rice variety and all grains are shown in table 4.10 along with the co-efficient of regression (r^2). By separating all the grains into whole and broken grains the parameters are different especially for whole grains. The model parameters for broken grains are: $a = 1.8804$ and $b = -2.3564$ with $r^2 = 0.9191$; for head rice they are: $a = 2.1805$ and $b = -6.4688$ with $r^2 = 0.8762$.

Rice	Parameter	Basmati	TNDLX	Kranti	BPT	ASD16	All
Broken	a	0.5983	0.6531	0.4661	0.5904	0.5733	1.8804
	b	-1.3134	-0.7918	-2.1035	-1.1256	-1.3357	-2.3564
	r^2	0.9470	0.9708	0.9573	0.9488	0.9554	0.9191
Head	a	0.4525	0.4787	0.3690	0.5262	0.2970	2.1805
	b	6.6085	2.1737	-0.2733	1.4278	4.7812	-6.4688
	r^2	0.4489	0.5102	0.6586	0.6090	0.3384	0.8762
Both	a	1.7218	1.3818	1.8613	1.3535	1.7030	1.8065
	b	-2.0296	-0.3456	-0.9328	-0.0330	-1.4807	-2.2819
	r^2	0.9534	0.9622	0.9361	0.9512	0.9713	0.9267

TABLE 4.10: Mass conversion parameters for a selection of rice varieties, split into broken, head rice, and both broken and head rice samples. The All column indicates a population of rice grains mixed from all samples was used.

Experiment 4.11. Using both the general parameters from experiment 4.10, the conversion model was created and evaluated. All varieties of rice grain were combined to create the data-set in this experiment; similarly, we use the combined parameters to build the conversion model. The error is calculated as the difference in the estimated percentage of broken rice by-mass and the ground-truth, sorted and measured by hand with digital calipers and weighing scales.

The results of the variety specific conversion method for estimating the percentage broken by mass are shown in table 4.11. We observe that the general model gives a suitably low mean error of 0.98%. We conclude there is no significant difference between the actual and estimated percentage of broken rice by-mass, at the 5% significance level of a two tailed t-test.

[1]Many thanks to Bismillah Kani for the work conducted with data-set preparation and evaluation

Head Mass (g)	Broken Mass (g)	Broken %	Estimated %	ε_μ %
1.35	0.98	42.16	42.41	-0.25
	0.37	21.58	20.45	1.13
	0.52	27.62	27.55	0.07
1.63	0.96	37.07	36.17	0.90
	0.25	13.42	12.89	0.53
	0.54	25.02	24.12	0.90
1.23	0.91	42.47	39.88	2.59
	0.22	15.44	13.91	1.53
	0.18	13.00	11.63	1.38
Mean				**0.98**

TABLE 4.11: Results of the general linear regression mass conversion model.

4.6 Chapter Conclusion

In this chapter we have extended the approach for measurement of grain length as discussed in chapter 2. An additional set of components are explored to enable the system to accurately measuring the percentage of broken rice grains in motion. These consist of: the standard definition of broken rice and a discussion on sampling consistency; the process of single grain identification using the length-width-corner algorithm; an exploration into the errors caused by tumbling grains, and touching grains (which requires an appropriate correction model); lastly, the conversion method from by-count to by-mass percentage broken rice. We have described a set of evaluation methods for which to overcome or correct the errors associated with measuring rice grains during mid-flow. From this analysis, we identify the suitability of the described methods tested during this project. From experiment 4.1, we would recommend that a minimum of 2,000 grains should be measured when sampling rice grains; where we would thus expect the consistency of the ground-truth percentage of broken rice to fall within $\pm 1.34\%$ and $\pm 1.79\%$ for 10 and 20% input contamination of broken rice, respectively.

From experiment 4.2, we estimate that 1% error in singles detection would give a mean error of -0.09% on the measurement of broken rice. In experiment 4.3, we determine that in the case of US Long rice, a change of broken rice percentage up to 0.1% is observed given a ± 3 value sweep of the three parameters for the LWC singles detection algorithm. The range of error appears to be less severe for Basmati rice. Given the flexibility for fine tuning of the parameters (variety dependent), the method gave accuracy percentages from 99.97% to 100% for US Long to Basmati rice. From experiment 4.4, we have determined that the optimised parameters for variety independent detection of single grains are: length: 8.2 mm, width: 2.7 mm and Corner threshold: 75%; this optimal parameter selection provides 99.93% accuracy in single rice detection. The single

detection algorithm is well within 1% error; therefore, we expect an error of much less than -0.09% in the percentage of broken rice.

Experiment 4.5 indicates the simulated mean error due to the effect of contour foreshortening of tumbling grains. We estimate that a tumbling grain with an orientation of 17° provides a significant distortion to the length of a grain, by -0.1 mm. Using the data from this experiment, we conduct a series of Monte Carlo simulations in experiment 4.6. We observe that a 2% tumbling rate gives an estimated length error of -0.025 mm due to the foreshortening effect. An equivalent of 1% broken rice would be observed due to the same 2% tumbling rate; this would be a substantial error in broken measurement caused from one source. If the tumbling rate is reduced to the target rate of 0.1%, the estimated mean error would be -0.001 mm; consequently the mean error on broken rice measurement would drop from 1% to an estimated 0.2%. From experiment 4.7, we observe from US Long grain samples, an average mean error of 0.47% caused by tumbling rice grains. The Parboiled US Long samples contained more accidental breakage, however the corresponding mean error was disproportionately larger than the standard rice, with an average error on broken rice measurement of 1.89%. The average errors from all samples, 1.18%, is approximately the same as modelled in experiment 4.6, where we estimate a 1% error in broken rice percentage due to 2% tumbling grains.

From experiment 4.8, we estimate the bias effect of grain of rice being seen, by the system, due to its length. It can be inferred that the difference in the overall percentage of broken rice B_τ and the observed percentage of broken rice $\hat{B}_\tau$ is significant. We estimate, from a sample of 10,000 rice grains, an error of 1.9% at an equivalent throughput of the rice in motion measurement apparatus (250 kg/h). This indicates an overestimation of the percentage of broken rice that is beyond the acceptable requirements of the system. We then derived an expression, using Bayes Theorem, for the relevant conditional probabilities to estimate a correction factor to provide the broken rice percentage; this approach requires a pre-calculated conditional probability distribution of seeing a grain due to its length. In experiment 4.9 the approach was evaluated using the conditional probability distribution of seeing a grain due to its length from 4.8. Given these corrected estimates using the probabilities of seeing a grain, it can be inferred that there is a significant reduction in the overestimation of the percentage of broken rice. Comparing the results to those from experiment 4.8, there is a reduction in the mean error of 0.7% and 2.2%, for 250 and 650 kg/h throughput, respectively. Further experimentation is conducted in chapter 6, where a comparison is made of the measurement of broken rice with and without the corrective approach.

In experiment 4.10, we calculate the parameters of a model for estimating the mass of a rice grain from its area. We evaluate a set of parameters for a selection of rice

varieties, and produce an aggregate solution to be used as a general conversion model; *i.e.* a variety-independent solution. In experiment 4.11, we observe that the general model gives a suitably low average error of 0.98% for the estimation of the mass of a grain given its area. Therefore, we conclude there is no significant difference between the actual and estimated percentage of broken rice by-mass.

In summary, we provide a series of methods that create the processing pipeline for a working measurement system for rice in motion. In chapter 6, we conduct an extensive set of experiments to evaluate the overall system accuracy of broken percentage measurement using the rice in motion measurement apparatus.

Chapter 5

Density Estimation Classification with Shape Features

In the previous chapter we explained how the static rice measurement apparatus and algorithm was extended to allow the analysis of rice grains in motion. The presented methods were shown to allow the by-mass measurement of the percentage of broken rice using the standard length threshold criterion for the classification of broken or head rice. In this chapter, we explore the possibility of using shape information to further improve the classification of broken rice. For the standard definition of a broken rice, the probability that a grain is broken is entirely dependent on the estimated length of the rice grain; any associated errors in that single length measurement may bias the estimate of the proportion of broken grains. However, other features can be taken into consideration that may not have the same bias effects. The requirements for a real-time system limit the types of features that could be implemented, such that we can only work on the binary information from post-segmentation. This however does allow the extraction of shape information that may or may not encompass the length of the grain. We explore K-NN density estimation techniques, for the purpose of obtaining a more accurate probabilistic estimate that a grain is broken.

In order to demonstrate the effectiveness of the existing and novel techniques, we apply the classification method to a variety of data-sets that comprise of multiple classes. In these domains, a variety of feature modalities are available, in particular with regards to the classification of leaf species with the availability of not only shape, but colour and texture. Therefore, the main body of this chapter pertains to working towards the unbiased class estimate from a range of features inputs. The strength of probabilistic classification is demonstrated by the straightforward integration of the sets of probabilities calculated independently from each feature vector. To facilitate the on-line

measurement of broken rice, we would recommend that the classifiers are cascaded: first by length, and then marginal rice grains are classified using shape. An overview of a proposed image processing pipeline for this approach is shown in figure 5.1.

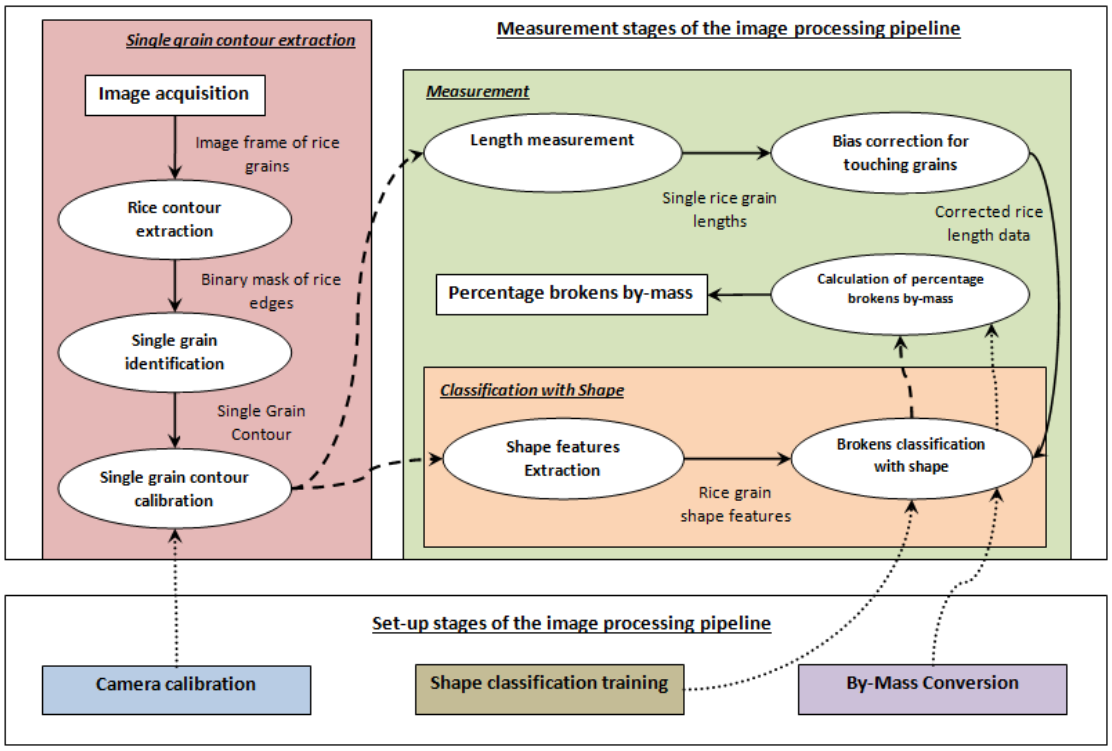

FIGURE 5.1: Overview of how to enable a computer to measure the percentage of broken rice grains with both length and shape information.

Section 5.1 describes the novel work to define a series of estimators based on tabulation of prior statistics. Two public data-sets are used to evaluate the methods, in addition to a new data-set of one-hundred varieties of leaves. Section 5.2 applies the presented approach using a data-set of 25,000 manually labelled Sona Masoori rice grains. The last section of the chapter concludes with the main points.

5.1 Probabilistic Framework for K-NN Classification

Two methods for probabilistic classification from a K-NN classifier are tested: these include the standard [100] and the recent extension [101]. A novel approach is proposed, which has the dual advantages of a fast, non-iterative implementation, and also providing significantly more accurate estimates than the state-of-the-art, over a range of test sets. Within the framework, the K-NN classifier is used to provide statistics about its expected performance within the training set, which are then used to provide estimates for the unseen test set process.

To construct an accurate estimate of the posterior probability of class membership, given a K-NN classifier, it is proposed to investigate various definitions of tables that can be used to accumulate statistics from the training set. These tables can be combined and used to record the varying degrees of certainty that have been encountered across the sections of the input space. Hence, for an unseen test vector, its relation to its nearest neighbors in the training set can be used to identify similar sections of the input space, and simply look up the probability that has been measured from the cross-validated statistics. Figure 5.2 illustrates the proposed framework.

To tabulate these statistics from the training set, a 'leave-one-out' cross validation is applied. This means that features are extracted and accumulated, leaving out a single member of the training set. These features are used to predict the label of the left-out sample: the result is stored as a prior statistic. This process is repeated a number of times, to assemble a table of the prediction performance, conditioned upon the different values that the extracted features can assume. In general, discrete features were chosen, in preference to continuous ones: this allows a tabulation as opposed to a regression. An important design decision is the number of possible feature values, *i.e.* the number of elements in the conditional tables: a fine-grained model can provide more detail, while a course-grained model allows more statistics to accumulate per element which provides more reliable predictions.

We propose to use four different features of the training set to generate the prior statistics: VotingSplit table, Rank table, Distance feature, and ConfMat (confusion matrix). These are presented in the subsequent sections (5.1.1 to 5.1.4), following the notation from section 2.6.3. These tables are then combined together in various ways to generate several estimators that can be evaluated on test sets alongside the Prop and Wprop methods. The methods for combining the tables are described in section 5.1.5.

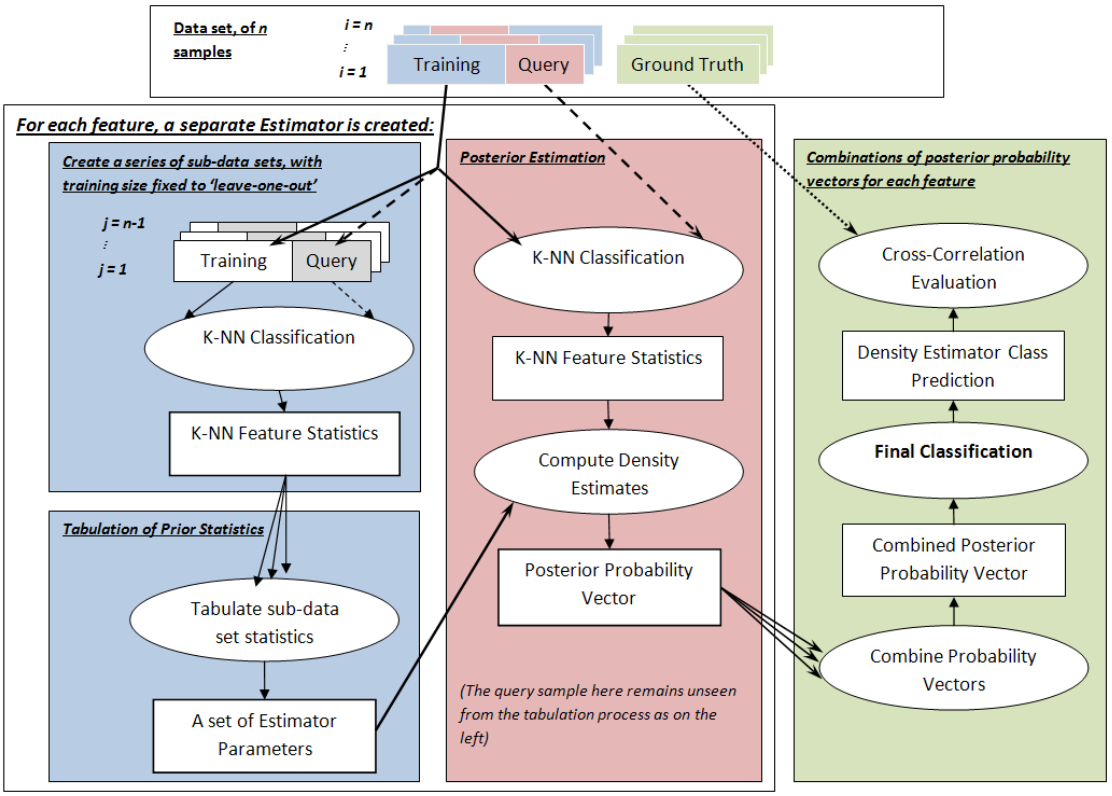

FIGURE 5.2: The proposed novel density estimator framework using tabulated statistics calculated from an internal data-set. A posterior estimate for the unseen query sample can then be calculated using the prior estimates. The evaluation method is also illustrated, whereby each probabilistic estimate per feature can be combined to produce various class predictions. The selected classifier features used to build the estimator, in addition to the test sample feature combinations, can thus be evaluated like-for-like, (allowing a selection of the preferred classification solution).

5.1.1 The VotingSplit Table

It is hypothesised that the *degree of agreement* between the K nearest neighbors to $\mathbf{x_i}$ provides a useful indication about the certainty of the classification result. Intuitively, a unanimous verdict from the K nearest neighbors is a more certain result, than some equivocation between two or more labels. This degree of agreement can be simply modelled by a histogram with K bins: each element K of the histogram is used for those cases in the training set in which K of the nearest neighbors have the same label as the predicted result. The histogram is used to accumulate and then calculate the proportion of these cases in which the predicted result is correct. This is achieved using the 'leave-one-out' methodology to fabricate a sub-set of test cases from within the training set, in each case omitting it from the list of neighbors used to determine its result. An example of the accumulation of the VOTINGSPLIT table, in addition to the remaining three features, is shown in figure 5.3.

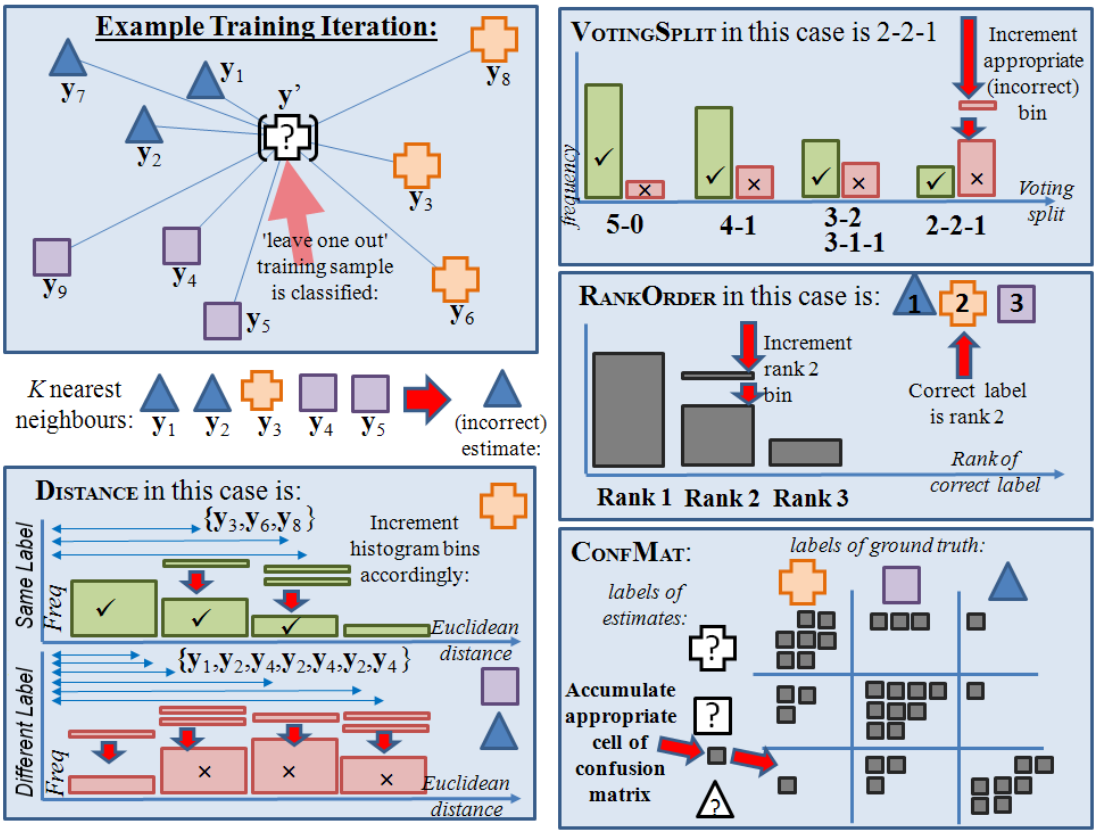

FIGURE 5.3: An example iteration of the accumulation of the tabulated statistics: VOTINGSPLIT, RANK, DISTANCE, and CONFMAT features. These features would eventually be tabulated over all of the training iterations, using each training sample as a new leave-one-out test sample.

5.1.2 The Rank Order of Correct Labels

Another perspective on the performance of the classifier is to rank the distinct labels of the nearest neighbors, by distance, and to assess the relative frequency with which the correct label is present at each of these ranks. Thus, in a specific example, if the labels of the 6 nearest neighbors were, in order, $\{a, c, c, b, a, d\}$, the ordered set of distinct labels would be $\{a, c, b, d\}$, the duplicates having been removed. Following a similar 'leave-one-out' methodology to that presented in section 5.1.1, the rank of the correct label is used to increment the respective element of a histogram. After all members of the training set have been tested in this way, this histogram is normalised to provide an indication of relative frequency.

5.1.3 Conditional Dependence on Distance

The accumulation of statistics to measure the recorded (Euclidean) distance between samples that are either the same label or different labels, is well established in the

literature [115]. In this context, the set $|\mathbf{y}' - \mathbf{y_k}|$ denote the distances between the cross-validation probe $\mathbf{y}'$ and its K nearest neighbors $\mathbf{y_k}$. The distances are quantised into the histogram bins; for those distances for which the neighbour and the probe have the same label, *i.e.* $y' = y_k$, histogram $\mathcal{H}_1$ is incremented. Otherwise, histogram $\mathcal{H}_2$ is incremented. To obtain a probability that is conditioned upon a given quantised distance (and histogram bin) W, the histograms are normalised to their respective priors.

5.1.4 The ConfMat Confusion Matrix

The ConfMat confusion matrix can be incremented using the class label from the K-NN classifier. Each column of the matrix represents the instances in a predicted class, while each row represents the instances in an actual class. The frequency with which, over the training set, category j_1 is classified as category j_2. This can also be generalized, to accumulate probability mass rather than discrete classification results.

5.1.5 Combination of Tables

The following novel estimators are created by combining some of the feature tables previously described:

1. The Distance+VotingSplit estimator: This combined table uses the Distance feature from the K-NN framework in addition to additional granularity of splitting the information into the additional categories of the VotingSplit table.

2. The Rank+VotingSplit matrix estimator: Similar to the above method, however instead uses the Rank table separated further by including an extra dimension of the VotingSplit table.

3. The ConfMat+Rank estimator: Whereby probability mass is accumulated into the confusion matrix instead of +1 values. In this case, the probability mass is estimated by building the Rank table and using the associated value for the current sample as a prior estimate of the probability mass. This new table is then used in the same way as the standard ConfMat table.

4. The ConfMat+Rank+VotingSplit estimator: Similar to the above method, however instead uses the additional information from the combined Rank+VotingSplit table to estimate the probability mass which, again, in turn is accumulated into the ConfMat matrix instead of +1 values.

5.1.6 Experimental Evaluation

The following novel estimators are implemented: DISTANCE+VOTINGSPLIT, CONFMAT, RANK, RANK+VOTINGSPLIT, CONFMAT+RANK and CONFMAT+RANK+VOTINGSPLIT combinations of tabulated statistics (section 5.1). Additionally, the two standard methods PROP, WPROP are tested. The eight estimators are evaluated using unseen test sets. Results are accumulated using ten-fold evaluation (for Iris and Wheat data-sets) and ten-fold evaluation of the leaves data-set. In each of these iterations, the estimator is rebuilt completely, thus ensuring that a sample used as a test vector in one iteration, can be used as a training vector in another iteration, without compromising the integrity of the experiments. In all cases there are an equal number of samples used from each class, effectively setting the priors to be equal. The performance results reported consist of the mean log posterior (LP), *i.e.* expected log likelihood, of the density estimates; and the mean classification accuracy (ACC) of the estimators. For the results concerning the Leaf data-set, we report the accuracy in terms of the mean precision (PRE) and mean recall (REC), due to the number of classes and complexity of the data-set.

For each estimator, the number of separate features to be included in the classification can be varied. Each feature has its own separate K-NN system that is trained on the respective training data. There are two, three and four separate K-NN systems created, for the Iris, Leaves and Wheat data-sets; the Leaves features are multivariate (64-elements each); the Iris and Wheat features are univariate. In the current investigation, the K-NN system is configured with a Euclidean distance measure and the first-nearest neighbour is used as the tie-break mechanism. Additionally, the 'model failure' value of $\Omega = 0.01$ is used for all experiments, *i.e.* 1% of the probability mass is reassigned to all classes thus removing zero valued elements.

In each case, the evaluation reports two measures of performance: the log posterior of the probabilistic estimate, and the accuracy of the final discrete estimate. The main objective of the experiments is to understand which of the available estimators provides the most accurate classification results. Subsequently, the performance as a function of training size is investigated, using the high-dimensional (Leaves) data-set.

In experiment 5.1, two public benchmark data-sets are employed to validate the performance of considered methods: iris flower and wheat seed kernel. The experimental design restricts the processing of these data-sets to a single variable per K-NN classifier, to examine the efficacy with which the probabilistic estimates from each classifier can be combined. Then, for experiment 5.2, the one-hundred species leaves data-set is evaluated; which is a challenging classification problem due to major/minor species of plant leaves.

Experiment 5.1. In this experiment, we evaluate the set of density estimators with the two publicly available data-sets: the iris flowers and the wheat seed kernels. Fisher's iris data [104, 116] is a well known data-set in the pattern recognition literature. It consists of 50 samples from 3 varieties of Iris plant. The features of the iris data consist of four scalar values; these refer to the length and width of the petal (PL and PW), and the length and width of the sepal (SL and SW). Guvenir et al, [117], use the iris data-set (amongst others) to validate the performance of their own weighted K-NN classifier. In the case of $K = 3$, using a ten-fold cross-validation, the mean classification accuracy was reported to be 90.7% for the standard classifier definition. The authors report an accuracy of 94% using their weighted K-NN metric (with the same $K = 3$ parameter). We create four separate feature vectors per iris sample, which relate to each of the petal and sepal dimensions (rather than use all values in one feature vector). Another publicly available data-set consists of seven attributes of wheat seed kernels [118]. The data-set consists of 70 samples from 3 different varieties of wheat. The attributes refer to the area (AR), perimeter (PE), compactness (CO), length of kernel (LK), width of kernel (WK), asymmetry coefficient (AS) and length of kernel groove (LKG). The authors report a mean classification accuracy of 92% using a clustering algorithm technique. Similarly to the Iris data-set, we create separate feature vectors using each of these attributes within the test framework.

For both data-sets, we report the mean classification accuracy over with the ten-fold cross validation methodology. The experimental results using the iris flower data-set is shown in table 5.1. All described density estimation methods were tested in this case with $K = 3$. No significant differences were observed when experiments were conducted with $K = 5$ and $K = 7$. The results using the wheat seeds data-set is shown in table 5.2. Some minor differences were noted when experimenting with $K = 5$ and $K = 7$; however, we include results using $K = 3$. For both cases, results of three different feature combinations are shown for comparative purposes.

The Prop and Wprop estimators perform similarly with respect to mean classification accuracy over the ten-fold cross-validation. Using the iris flower data-set, a 96% mean accuracy with the PW feature alone and 90% with all four of the PL+PW+SL+SW features. With regards to the expected log likelihood using the PW feature alone: -0.165 to -0.103 for Prop and Wprop, respectively. For all estimators the single PW feature worked better than any combination of the PL, PW, SL, and SW features. Comparatively, Guvenir et al [117] reported an accuracy of 94% using their proposed weighted K-NN metric using all four values. All of the tested estimators performed less than this, however the Rank+VotingSplit method was closest with 93.33% mean accuracy using the four features.

Similarly to the iris flower data-set, the results with wheat seeds show that many of the features combined together from the seven available did not give the optimal solution. Generally, the framework worked optimally with the AR, AS, and LKG features. We observe that of all estimators, the ConfMat+Rank method performs the strongest with a mean classification accuracy of 92.38% and expected log likelihood of -0.152, using the combination of AR+AS+LKG features. Comparatively, Charytanowicz et al [118] reported a mean classification accuracy of 92% using a proposed clustering algorithm on the same data-set using all seven features. The Rank+VotingSplit estimator performed next best with 90.48% mean accuracy and mean log posterior of -1.159 (also using the AR+AS+LKG features).

Estimator	Features	LP	Acc
Prop	PW	-0.165	96.00
	PL+PW	-0.064	94.67
	PL+PW+SL+SW	-0.113	90.00
Wprop	PW	-0.103	96.00
	PL+PW	-0.061	95.33
	PL+PW+SL+SW	-0.115	90.67
Distance+ VotingSplit	PW	-0.967	28.67
	PL+PW	-0.345	24.67
	PL+PW+SL+SW	-0.387	25.33
ConfMat	PW	-0.093	96.00
	PL+PW	-0.302	92.67
	PL+PW+SL+SW	-0.349	92.67
Rank	PW	-0.077	96.00
	PL+PW	-0.267	96.00
	PL+PW+SL+SW	-0.313	90.67
Rank+ VotingSplit	PW	-0.088	94.00
	PL+PW	-0.221	95.33
	PL+PW+SL+SW	-0.263	93.33
ConfMat+Rank	PW	-0.072	96.00
	PL+PW	-0.071	96.00
	PL+PW+SL+SW	-0.211	92.67
ConfMat+Rank+ VotingSplit	PW	-0.074	96.00
	PL+PW	-0.204	96.00
	PL+PW+SL+SW	-0.245	92.00

Table 5.1: Results of density estimation classification using the iris flower data-set.

Estimator	Features	LP	Acc
Prop	AR+AS+LKG	-0.182	88.10
	PE+WK+AS+LKG	-0.133	88.57
	AR+PE+CO+LK+AS+LKG	-0.137	88.57
Wprop	AR+AS+LKG	-0.171	87.62
	PE+WK+AS+LKG	-0.134	88.57
	AR+PE+CO+LK+AS+LKG	-0.169	87.62
Distance+	AR+AS+LKG	-0.177	78.57
VotingSplit	PE+WK+AS+LKG	-0.192	81.43
	AR+PE+CO+LK+AS+LKG	-0.162	86.19
ConfMat	AR+AS+LKG	-0.172	86.67
	PE+WK+AS+LKG	-0.163	88.57
	AR+PE+CO+LK+AS+LKG	-0.183	89.05
Rank	AR+AS+LKG	-0.163	90.48
	PE+WK+AS+LKG	-0.154	88.57
	AR+PE+CO+LK+AS+LKG	-0.184	88.10
Rank+	AR+AS+LKG	-0.159	90.48
VotingSplit	PE+WK+AS+LKG	-0.148	87.14
	AR+PE+CO+LK+AS+LKG	-0.181	87.14
ConfMat+Rank	AR+AS+LKG	-0.152	92.38
	PE+WK+AS+LKG	-0.143	90.00
	AR+PE+CO+LK+AS+LKG	-0.183	89.52
ConfMat+Rank+	AR+AS+LKG	-0.151	90.00
VotingSplit	PE+WK+AS+LKG	-0.143	87.14
	AR+PE+CO+LK+AS+LKG	-0.185	87.62

Table 5.2: Results of density estimation classification using the wheat seed data-set.

Experiment 5.2. The leaves data-set comprises one-hundred species of leaf; for each species, there are sixteen distinct samples, photographed as a colour image on a white background. A small sample of these species is shown in figure 5.4, and a sample of all 100 is available in appendix D. The data-set inherently consists of having a wide set of classes with a low number of samples. Additionally, many sub species resemble the appearance of other major species, as well as many sub species with a major species can resemble a radically different appearance. As such, this data-set provides the main classification challenge from the three data-sets described in this chapter. From each leaf sample, three distinct features were extracted: a Centroid Contour Distance Curve shape signature (Sha), an interior texture feature histogram (Tex), and a fine-scale margin feature histogram (Mar). Each feature is represented by a 64-element vector.

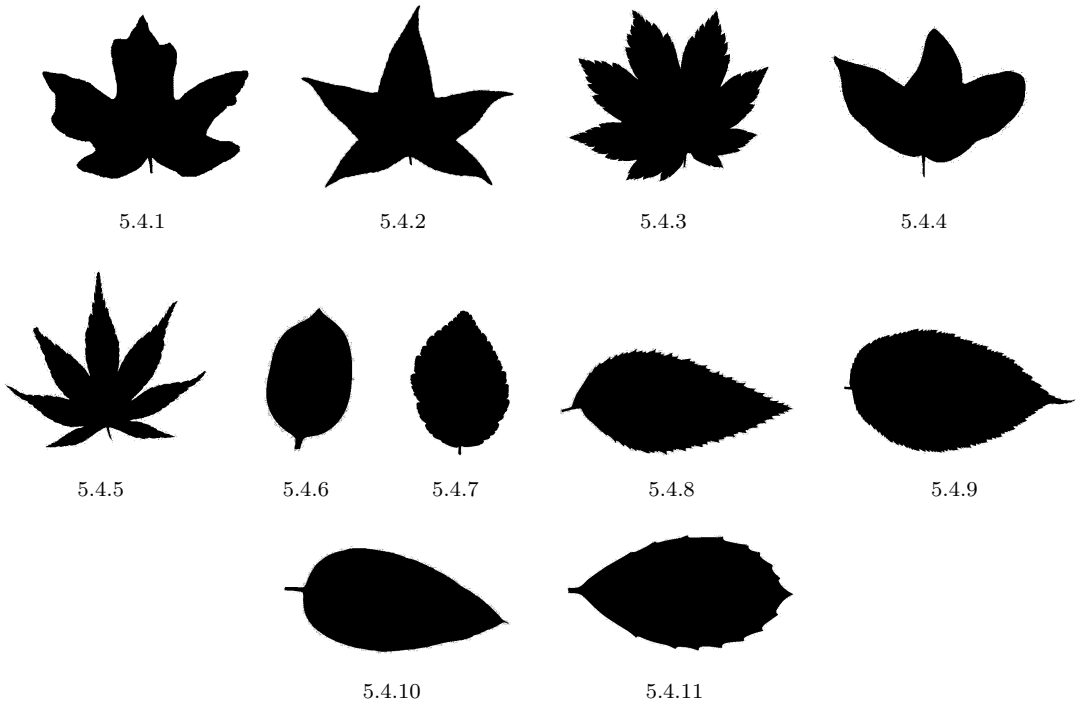

Figure 5.4: A binary image example of a small variety of plant species that are part of the challenging one-hundred leaves data-set: 5.4.1 Acer Campestre. 5.4.2 Liquidambar Styraciflua. 5.4.3 Acer Circinatum. 5.4.4 Acer Mono. 5.4.5 Acer Palmatum. 5.4.6 Ilex Cornuta. 5.4.7 Alnus Rubra. 5.4.8 Alnus Sieboldiana. 5.4.9 Betula Austrosinensis. 5.4.10 Eucalyptus Urnigera. 5.4.11 Ilex Aquifolium.

The experimental results using the plant leaves data-set is shown in table 5.3. All described density estimation methods were tested in this case with $K = 3$ and $K = 5$. The results shown consist of the combined Sha+Tex+Mar classified features (unanimously, the best feature combination across all estimators for the leaves data-set). We report the mean precision (Pre) and mean recall (Rec) metrics in order to provide more detail

on the performance of the estimators using this more complex data-set. In this study, the vector sizes for each feature are fixed to 64-elements.

The most complex data-set, consisting of the plant leaves, has further supported the performance of the Rank+VotingSplit estimator. The mean classification precision and recall for the ten-fold evaluation was 99.42% and 99.38%, respectively; with an expected log likelihood of -0.17 (using $K = 5$). Comparatively, the Prop and Wprop methods performed well with a mean precision and recall of 98.3% and 98.19%, respectively; the expected log likelihood for these methods was -0.569 and -0.368, respectively. The parameter selection from $K = 3$ to $K = 5$ had shown a 1.38% and 1.5% boost in classification accuracy, for both the Prop and Wprop methods. However the Rank+VotingSplit method worked consistently across the two tested K values. The remaining estimator methods performed with varying success, most notably the ConfMat based methods worked worse for the plant leaves data-set.

We report the average experiment time taken to classify one trial of the one-hundred species leaves data-set, *i.e.* the average time to compute one-fold of 100 test samples using 1500 training samples. One trial comprises of building a separate K-NN density estimator for *each* feature vector *i.e.* the classification timings noted here indicate timing of the entire experiment using all features. Our implementation of the Prop estimator had completed this task in 21.8 seconds, whereas the Wprop estimator was completed in 31.7 seconds. The Distance+VotingSplit estimator performs slowest with 41 seconds processing time, and the remaining estimators all completed within 33 seconds.

Estimator	K	LP	Pre	Rec
Prop	3	-0.814	96.98	96.81
	5	-0.569	98.33	98.19
Wprop	3	-0.554	96.87	96.69
	5	-0.368	98.31	98.19
Distance+	3	-0.394	97.88	97.75
VotingSplit	5	-0.282	97.97	97.81
ConfMat	3	-0.327	92.96	92.25
	5	-0.251	91.22	90.13
Rank	3	-0.263	99.31	99.25
	5	-0.202	99.36	99.31
Rank+VotingSplit	3	-0.221	99.42	99.38
	5	**-0.170**	**99.42**	**99.38**
ConfMat+Rank	3	-0.197	97.88	97.69
	5	**-0.155**	97.31	97.19
ConfMat+Rank+	3	-0.189	94.75	94.56
VotingSplit	5	**-0.158**	92.29	91.81

Table 5.3: Results of density estimation classification using the leaves data-set, and the Sha+Tex+Mar features combination.

Experiment 5.3. The classification accuracy is then reported as a function of training size, in addition to the mean log posterior metric. We evaluate the performance of the PROP, WPROP, and RANK+VOTINGSPLIT; all selected from the relative performances observed from experiment 5.2.

The respective results are shown in figure 5.5. As a function of the training set size, the discrete classification performance is readily interpreted: at low values of available samples, and especially for low values of K (number of nearest neighbours), the RANK+VOTINGSPLIT estimator provides significantly better performance. However, the mean log likelihood of the test samples is not so straightforward: when $K = 3$, this estimator's performance increased with the training set size, yet when $K = 5$ the converse relationship was observed. Further investigation is necessary: one hypothesis is that the latter model is too complex (and so overtraining may occur).

Thus, the effectiveness of the framework is shown when combining the probabilistic estimates from individually processed features. For the leaves data set, the optimal configuration used all available features; however, this may not always be the case as shown with the iris flower and wheat seeds data sets. It has been shown to be effective in the particular task of classification with low training samples and a relatively large variety of categories.

There are several avenues of future work. For leaf recognition, it will be useful to validate the framework with noisy and missing data, e.g. missing parts of the sample leaf or focus errors. More generally, there are other areas of probabilistic estimation for which the proposed framework may be useful, e.g. correct estimation of face or vehicle registration plate details apparently permit a similar analysis. The evaluation of probability density will extend to check that kernel-based methods and Parzen windows do not offer any advantage under these conditions. Finally, it will be useful to investigate the extent to which properties of the training set statistics can predict the out-of-sample performance on the test set, to enable the most appropriate combination of tabulated data to be automatically selected and used.

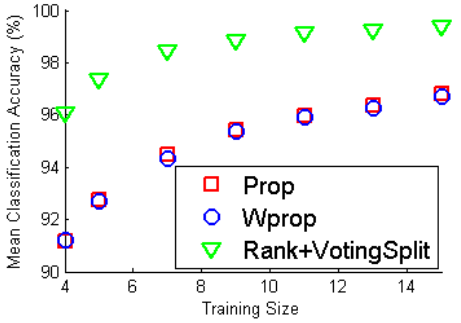

5.5.1 Mean classification accuracy with $K = 3$.

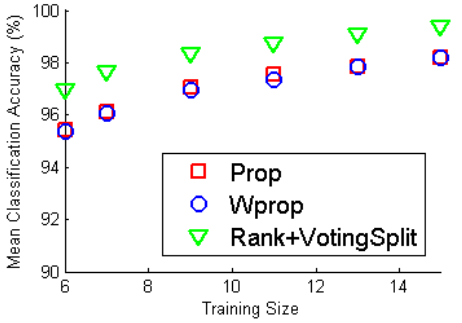

5.5.2 Mean classification accuracy with $K = 5$.

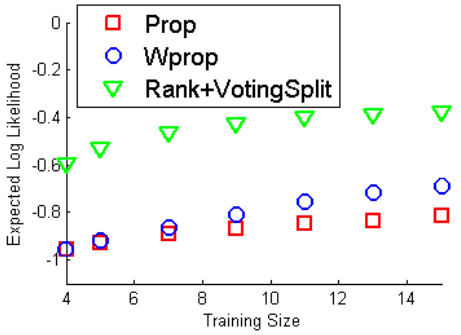

5.5.3 Mean posterior log with $K = 3$.

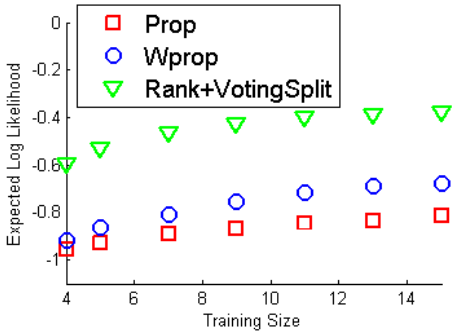

5.5.4 Mean posterior log with $K = 5$.

FIGURE 5.5: Density estimator performance as a function of training size, using the leaves data-set. The training size indicates the number of samples *per class*, that comprise of the complete training set.

5.2 Classification of Broken Rice with Shape

The estimation of percentage broken rice by shape is subjective and not straightforward. We identify the broken grain first by length, then any marginal grains are classed subjectively by the shape: defined by having sharp edges. Given this approach, we devise two experiments with rice grains that use this definition of broken. In experiment 5.4 we manually label a large data-set of rice grains from two independent sources; into broken and head rice classes. We then estimate the mean error in broken percentage given this subjective definition of a broken grain by shape. Experiment 5.5 selects a large number of grains from the *mutually* labelled set from experiment 5.4; then evaluates the automatic classification of broken and head rice classes using posterior estimates from the methods described in this chapter and a set of three specific shape features.

Experiment 5.4. The rice data-set in this experiment consists of 25,000 images of Sona Masoori rice grains, as imaged by the rice in motion measurement apparatus. The ground-truth percentage of broken rice was calculated from the original samples fed into the measurement apparatus; this was measured, from a sample of 2,500 rice grains, to be 24.48% by-count and 11.51% by-mass (using the length definition of broken rice). The sampling consistency formula from section 4.1, indicates an expected sampling error of $\pm 1.6\%$ in the by-count measurement of broken rice percentage; we expect half of this value, $\pm 0.8\%$, represents the sampling error for a by-mass measurement of broken rice percentage.

We exclusively refer to a shape based definition of broken rice. Two individuals have hand labelled the set of 25,000 rice grain images, by image, into broken and head rice categories; the broken grain is identified by the appearance of sharp edges. Figures 5.6 and 5.7 contains a random sample of 20 head rice grains for each set of manual labels. Similarly, figures 5.8 and 5.9 contain samples from the head rice class labels.

From set 1, the percentage of broken rice is 25.77% by-count; compared to set 2 which we report 26.72% broken rice. The difference between the these ground-truth values of broken rice for the same set of grains may be significant, indicated by the difference of 1%; however, this remains lower than the estimated $\pm 1.6\%$ sampling error.

A separate data-set, set 3, of rice grain images is created from the two manually labelled sets: by selecting all labels that are mutually agreed upon from both sets. This removes, to some degree, the labelling error from subjective opinion of a broken grain of rice. We report that there were 321 samples that were not mutually labelled as either broken or head rice; consequently, we report the ground-truth broken percentage by-count is now 26.03% (using a shape definition of broken rice).

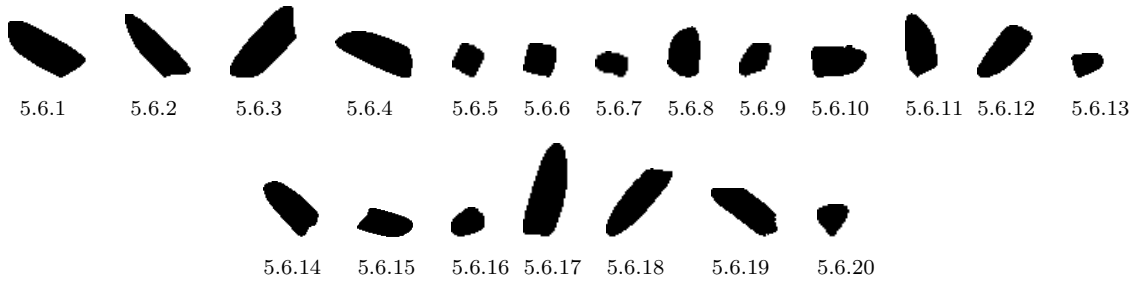

FIGURE 5.6: A sample of labelled broken Sona Masoori rice grains from the first set.

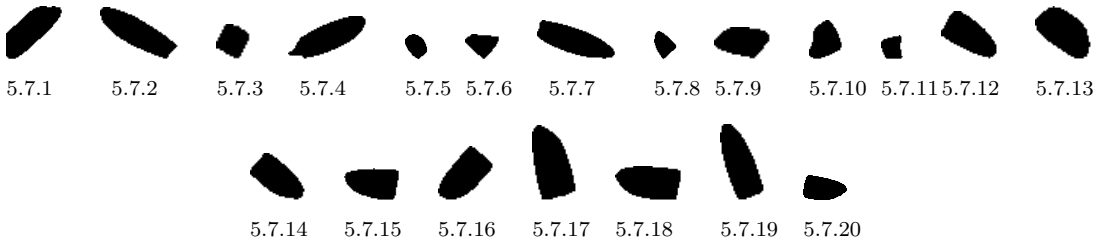

FIGURE 5.7: A sample of broken Sona Masoori rice grains from the second set, manually labelled by a different individual.

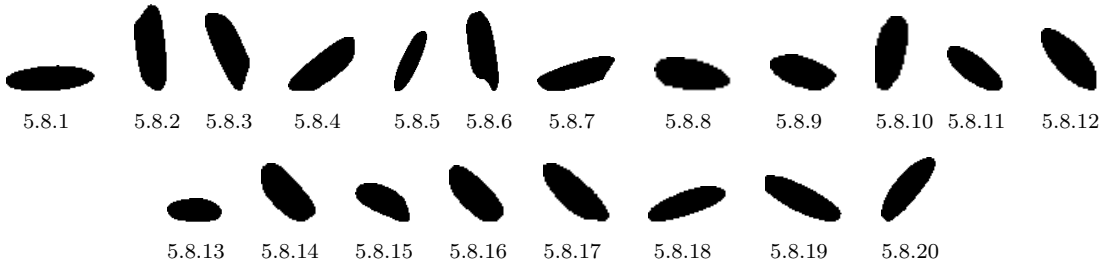

FIGURE 5.8: A sample of manually labelled Sona Masoori head rice from the first set.

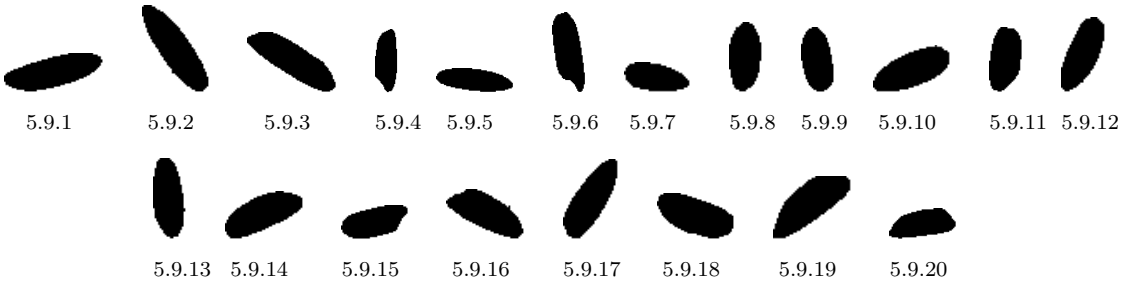

FIGURE 5.9: A sample of Sona Masoori head rice from the second set, manually labelled by a different individual.

Experiment 5.5. To determine the classification accuracy of broken rice with shape, we randomly select 3,000 samples each of broken and head rice (from the mutually agreed labels within the population of 25,000 grains from experiment 5.4). From each rice grain sample in the new 6,000 grains data-set, three distinct features were extracted: a centroid contour distance curve shape signature (CCDC), a curvature histogram (CH), and the velocity shape representation (VEL) (as previously discussed in chapter 2). Each feature is represented by a 16 element vector. The K-NN estimators tested in this experiment consist of the PROP, WPROP, RANK, and RANK+VOTINGSPLIT methods.

Table 5.4 contains the results of the 6,000 grain data-set, using the ten-fold cross evaluation method similar to experiments 5.1 and 5.2. We observe that the PROP estimator works outright best over the ten-fold evaluation, with -0.037 mean posterior log, 97.70% mean precision, and 97.74% mean recall. However each of the other tested estimators all provided mean precision and recall rates of above 97.20% using the CCDC+CH+VEL combined features. It is expected that the PROP posterior estimate to be closer to the Bayes estimate as the training size tends towards infinity, hence the relative improved performance.

Estimator	Features	LP	Pre	Rec
Prop	CCDC	-0.088	97.20	97.26
	CH	-0.095	96.55	96.56
	VEL	-0.130	90.25	91.81
	CCDC+CH	-0.044	97.15	97.16
	CCDC+CH	-0.053	97.35	97.45
	CH+VEL	-0.052	97.20	97.25
	CCDC+CH+VEL	**-0.037**	**97.70**	97.74
Wprop	CCDC	-0.072	97.20	97.26
	CH	-0.079	96.45	96.46
	VEL	-0.121	90.30	91.84
	CCDC+CH	*-0.043*	97.15	97.16
	CCDC+CH	-0.051	96.80	96.97
	CH+VEL	-0.048	96.55	96.68
	CCDC+CH+VEL	**-0.045**	**97.65**	97.70
Rank	CCDC	-0.067	97.20	97.26
	CH	-0.074	96.55	96.56
	VEL	-0.127	90.25	91.81
	CCDC+CH	**-0.051**	**97.20**	97.26
	CCDC+CH	-0.053	97.20	97.26
	CH+VEL	-0.051	96.55	96.56
	CCDC+CH+VEL	-0.068	97.65	97.70
Rank+	CCDC	-0.062	96.70	96.72
VotingSplit	CH	-0.070	95.55	95.55
	VEL	-0.125	90.00	91.31
	CCDC+CH	-0.050	97.10	97.11
	CCDC+CH	-0.051	97.10	97.19
	CH+VEL	-0.049	96.85	96.92
	CCDC+CH+VEL	**-0.048**	**97.20**	97.25

Table 5.4: Results of density estimation classification using the 6,000 grain Sona Masoori data-set.

5.3 Chapter Conclusion

In this chapter we have described a novel set of K-NN density estimators using tabulated prior statistics. Two public data-sets were used to compare the novel methods with the state-of-the-art. In addition, a new data-set of one hundred plant species was used for the purpose of species identification using the shape, texture and fine scale margin features from images of leaves. We highlight that specific combinations of the novel estimators produce more accurate density estimations than the other methods, when considering the complex multi-class data-set with few sample numbers.

From experiment 5.1, we infer that the state-of-the-art PROP and WPROP estimators perform similarly with respect to mean classification accuracy, over the ten-fold cross-validation. In addition, we report comparative results with methods in the literature that are tested on these data-sets, although they are not specifically density estimator methods. Using the iris flower data-set, a 96% mean accuracy with the PW feature alone and 90% with all four of the PL+PW+SL+SW features; compared to a method that performs with 94% accuracy. With regards to the expected log likelihood using the PW feature alone: -0.165 to -0.103 for PROP and WPROP, respectively. All of the tested estimators performed less accurately than this, however the RANK+VOTINGSPLIT method was closest with 93.33% mean accuracy using the four features. Similarly to the iris flower data-set, the results with wheat seeds show that many of the features combined together from the seven available did not give the optimal solution. Generally, the framework worked optimally with the AR, AS, and LKG features. We observe that of all estimators, the CONFMAT+RANK method performs the strongest with a mean classification accuracy of 92.38% and expected log likelihood of -0.152, using the combination of AR+AS+LKG features. Comparatively, Charytanowicz *et al.* [118] reported a mean classification accuracy of 92% using a proposed clustering algorithm on the same data-set using all seven features. The RANK+VOTINGSPLIT estimator performed next best with 90.48% mean accuracy and mean log posterior of -1.159 (also using the AR+AS+LKG features).

From experiment 5.2, we evaluated the classification performance of the most complex data-set consisting of the plant leaves. We observe, from this experiment, a high performance of the RANK+VOTINGSPLIT estimator; the mean classification precision and recall was reported to be 99.42% and 99.38%, respectively; with an expected log likelihood of -0.17. Comparatively, the PROP and WPROP methods performed well with a mean precision and recall of 98.3% and 98.19%, respectively; the expected log likelihood for these methods was low in comparison to the novel estimator, with values of -0.569 and -0.368, respectively.

In experiment 5.3, we evaluate the classification performance of the density estimators as a function of the training set size. The discrete classification performance is readily interpreted: at low values of available samples, and especially for low values of K (number of nearest neighbours), the RANK+VOTINGSPLIT estimator provides significantly better performance. Thus, the effectiveness of the framework is shown when combining the probabilistic estimates from individually processed features. It has been shown to be effective in the particular task of classification with low training samples and a relatively large variety of categories; however, the standard approach seems to work best with problems having a relatively low number of classes or large numbers of training samples.

We then define the broken grain by its shape in experiment 5.4; a large set of 25,000 grains were manually labelled by two independent sources. We infer that the difference between the these ground-truth values of broken rice for the same set of grains may be significant, indicated by the 1% change; however, this remains lower than the estimated $\pm 1.6\%$ sampling error that we expect. Experiment 5.5 evaluates the density estimators on a large sample of Sona Masoori rice, with respect to the classification accuracy of identifying broken rice grains. A set of 6,000 grains (half broken, half head rice) was randomly extracted from a mutual set of the two labels of 25,000 grains previously used in experiment 5.4. The PROP estimator worked outright best, with -0.037 mean posterior log, 97.70% mean precision, and 97.74% mean recall. However each of the other tested estimators all provided mean precision and recall rates of above 97.20% using the CCDC+CH+VEL combined features. It is expected that the PROP posterior estimate to be closer to the Bayes estimate as the training size tends towards infinity, hence the relative improved performance. We infer that the mean classification accuracy (97.70%) is comparable to those reported in the literature, in chapter 2, of between 90 and 98.4% accuracy with different systems and varieties of rice. However, we evaluate the tested methods in this chapter over a 10-fold evaluation of 6,000 rice grains, compared to much smaller samples in the literature.

Chapter 6

Experimental Results of the Rice in Motion Measurement System

This chapter presents the experimental results obtained from the implementation of the different methods described in the previous chapters. Also, a brief discussion of these results is included with the aim of giving the reader details of the accuracy and robustness of each method. In section 6.1 of this chapter we describe the experimental results regarding the rice in *motion* measurement apparatus, comprising of the most suitable components that were explored and evaluated in chapters 3 and 4. The final section concludes the chapter with the most important details from our experiments.

6.1 Experimental Results of Rice-in-Motion Measurement System

In this section we describe a series of three experiments, for the purpose of estimating the accuracy of the most suitable components, for broken rice analysis, that comprise of the rice in motion measurement system. In experiment 6.1, we estimate the uncertainty of the measurement of broken rice percentage from the system thus far (by-count). Three rice varieties are tested: US Long, Parboiled US Long, and Basmati. Experiment 6.2 investigates the repeatability of the measurement of percentage broken rice, tested with US Long grain rice. For both these experiments, the by-count estimation of broken rice is reported. Lastly, experiment 6.3 describes the experiments conducted for continuous broken rice measurement by-mass of two varieties of rice over a one hour period; the by-mass estimation is reported in this experiment.

Experiment 6.1. This experiment is conducted to estimate the mean error on the measured percentage of broken grains during mid-flow. A 100 gram sample of grains is measured using a broken rice shaker, which consists of a lattice of sharp edged holes of fixed diameter; there are roughly 2,500 grains per 100 g. The shaker used was designed to filter grains of rice with a length of 4.8 mm. A sample of 100 randomly selected grains is selected and measured on the static measurement apparatus; a corresponding hand measured length is made via the digital Vernier calliper, as further ground-truth information. The bulk feeding system of the rice in motion measurement apparatus was used to supply a continuous sample of rice, until 25,000 single grains were measured; approximately 500 frames are imaged per sample of rice. Figure 6.1 and 6.2 show a pair of diagnostic images for US Long and Basmati rice grains; The first image frame shows post image segmentation labelling, and the second is the input image with back projection of the length measurement.

Table 6.1 contains the ground-truth percentage broken rice, calculated using a shaker device designed to separate grains less than or equals to 4.8 mm. Table 6.2 contains the static rice measurement apparatus measurements of a corresponding 20 grain sample. In addition a 100 grain sample was measured to provide a better mean measurement of the population. The results from the rice in motion apparatus are available in table 6.3. For US Long rice, we observe a mean error of 1.91%. A similar case is observed for Parboiled US Long and Basmati rice with 2.51% and 1.2% mean error, respectively. These mean errors are unexpectedly overestimated, as we consider that tumbling grains would produce an underestimation effect on the observed samples.

Rice Type	Mean Length	Median Length	Broken %
US Long	6.08	6.32	10.61
Parboiled US Long	6.16	6.22	11.43
Basmati	5.42	5.99	21.06

TABLE 6.1: Broken rice percentage measured by hand from 100 gram samples of three varieties of rice (each 100 g sample contains roughly 2,500 grains). The three-quarter broken rice threshold was 4.8 mm. The mean and median length was calculated from a 20 grain sample hand measured with Vernier callipers.

Rice Type	Mean Length, from 20	Median	Mean from 100	Median
US Long	6.07	6.29	5.87	6.13
Parboiled US	6.21	6.02	6.28	6.22
Basmati	5.51	6.22	5.6	6.39

TABLE 6.2: Ground-truth measurements of US Long grain rice, from 20 and 100 random grains placed on the static rice measurement apparatus. The 20 grain sample contains correspondence with the hand measured length in table 6.1.

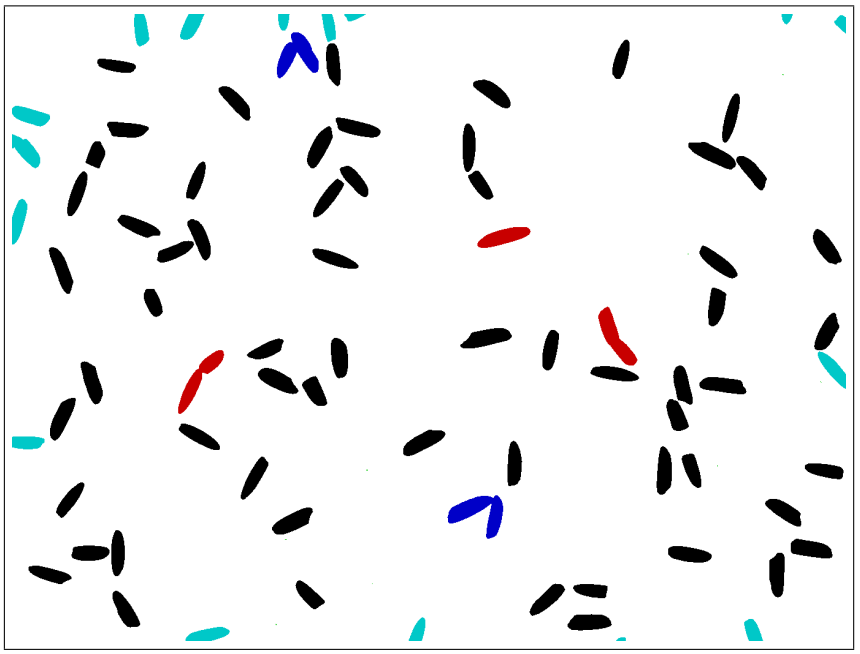

6.1.1 Grain measurement selection example.

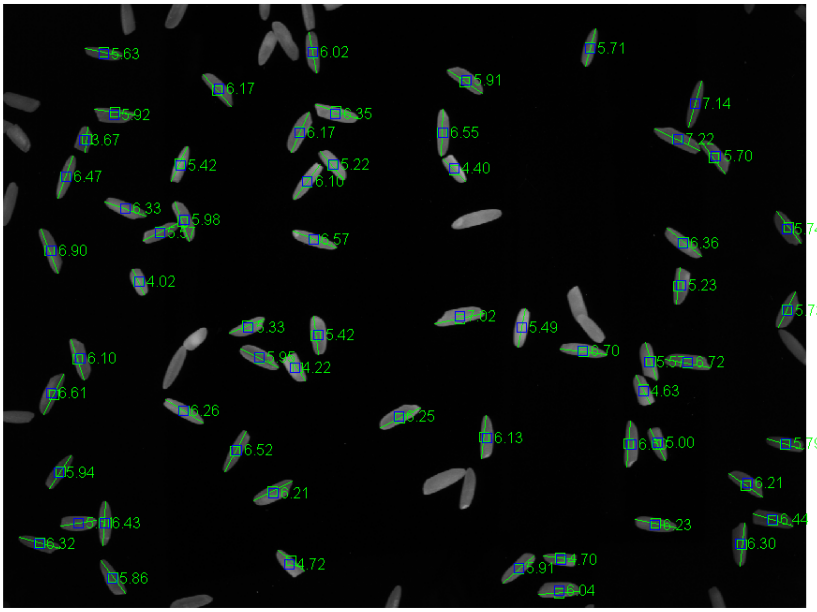

6.1.2 Length information back projected onto the suitable candidates only.

FIGURE 6.1: Example output images of grain selection and length measurement of US Long grain rice. The colour given to the rice objects indicate the status of the connected pixels they are assigned to: black indicates a gain to be measured, everything else is ignored; dark blue is a clump; red is a grain touching a grain; light blue indicates a grain touching the image edge (directly or by-proxy). The back projection of the estimated length is represented by the green lines (quantised to the nearest pixel).

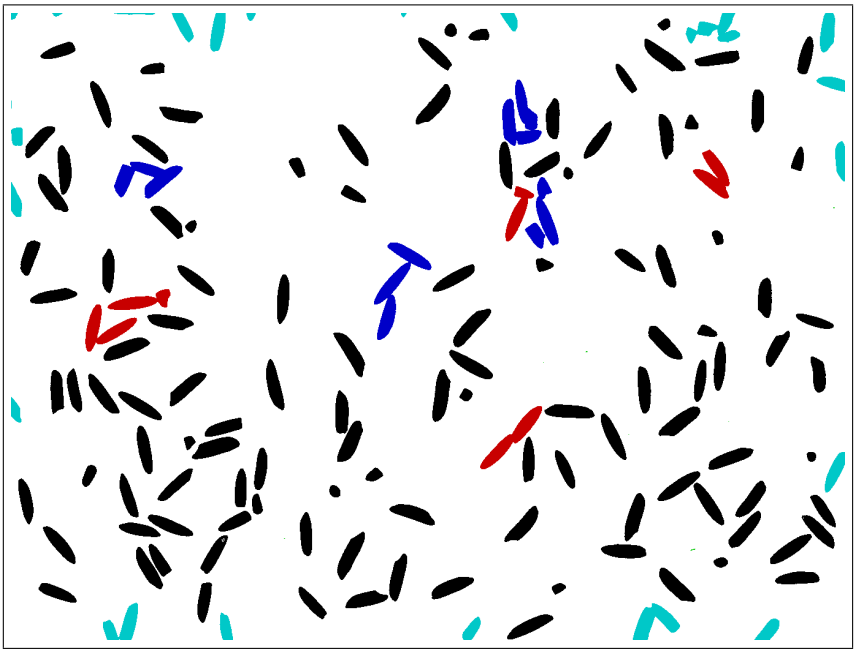

6.2.1 Grain measurement selection.

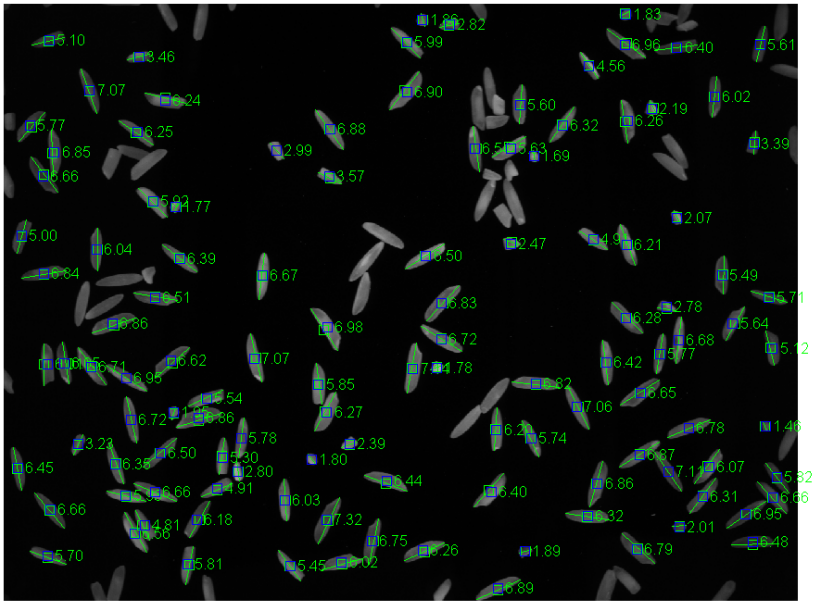

6.2.2 Back projection of length in milimetres.

FIGURE 6.2: Example output images of grain selection and length measurement of Basmati rice.

Rice Type	Mean Length	Corrected Mean	Broken %	Corrected Broken %
US Long	5.87	5.91	9.82	8.70
Parboiled US	5.88	5.94	13.94	12.19
Basmati	5.66	5.78	22.26	19.27

TABLE 6.3: Broken rice percentage measured from bulk-flow of three varieties of rice, captured from the rice in motion measurement apparatus.

Experiment 6.2. The consistency of broken rice percentage by-count was evaluated in this experiment, using a sample of US Long rice captured from the rice in motion measurement apparatus. The total population, of roughly 22,500, rice grains is divided into groups of 2,500 grains. The mean and median length of each group is recorded, see figure 6.3.1. In addition the percentage of broken rice is calculated at the 4.8 mm threshold, see figure 6.3.2.

The results are shown in table 6.4. Here the standard error is calculated as SE = $\frac{\sigma}{\sqrt{n}}$ where n is the number of samples (in this case 9 sets of 2,500 grains). We report, at the 95% confidence level, a deviation in error of ±0.4644% in the by-count measurement of broken rice percentage. For an equivalent by-mass estimation, we would expect half of this error.

Measurement	ε_σ	Standard Error	95% Confidence Level
Mean Length (mm)	0.02	0.0070	0.014
Median Length (mm)	0.01	0.0026	0.005
Broken %	0.7	0.2322	0.464

TABLE 6.4: Sampling consistency of mean length, median length and percentage of broken rice for US Long grain, measured with the rice in motion measurement apparatus. This error calculation denotes the standard deviation of the set of 9 groups of grains.

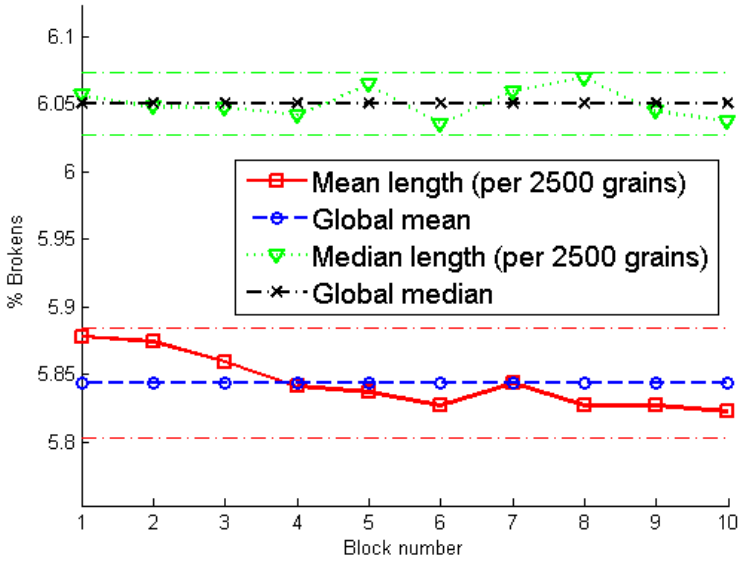

6.3.1 Consistency of mean and median length per group of 2,500 grains.

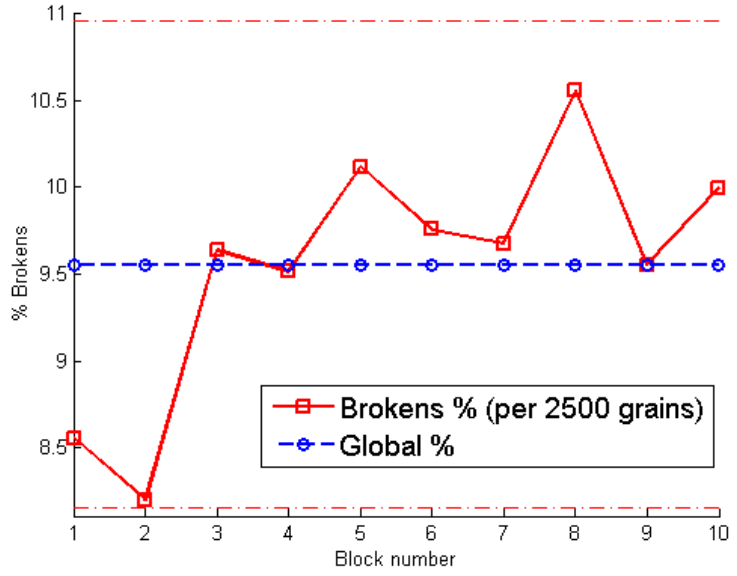

6.3.2 Consistency of percentage of broken rice.

FIGURE 6.3: Sampling consistency of US Long grain rice measured with the motion measurement apparatus. Groups of 2,500 grains of rice were measured and the results recorded for each one; consisting of the mean length, median length, and percentage of broken rice per group. The dashed lines indicate two standard deviations of the error.

Experiment 6.3. The continuous measurements from the prototype apparatus were performed by the industrial sponsor in Bangalore, India. With permission, we describe the experiment that was conducted. A second prototype of the rice in motion measurement apparatus was built by mechanical engineers from the sponsor. This version of the hardware has been confirmed to have no significant level of tumbling grains, and a highly optimised optical set-up. The experiment highlights two new components: that the system is continuously reporting measurements, and that the by-mass percentage broken rice is estimated by the system; previously experiments 6.1 and 6.2 reported the by-count percentage of broken rice.

Continuous measurements of the percentage of broken rice *by-mass* are conducted over a one hour period. At a regular time interval, of roughly 5 minutes, a batch of 500 images are captured by the prototype rice in motion measurement apparatus. This number of frames is sufficient to allow the machine to measure the length of approximately 25,000 single grains of rice. A manual sample of rice is also collected at this time. An example of an input frame of Sona Masoori rice is shown in figure 6.4.

The set of 12 batches of manual and machine measured rice samples were processed, and the consistency of the measurements can be reported. Table 6.5 contains the continuous measurement results of the experiment using Basmati rice grains; likewise, table 6.6 shows results with Sona Masoori long grain rice. Figures 6.5 and 6.6 show the percentage broken measurement for the same two data-sets.

The mean error of broken rice estimation without correction factor applied is 0.12%, and with correction factor applied is -0.57%, on the data samples of Basmati rice. We observe the application of the correction factor appears to bias the broken measurement. A similar occurrence is observed with the Sona Masoori data samples: the mean error without a correction factor applied is 0.70%, and with correction factor applied is -1.38%. Given the choice of whether to apply the bias correction model, we claim that both with and without correction produces a consistent measurement of percentage broken rice by-mass, using length alone. In addition, the average complete measurement time of roughly 25,000 rice grains is reported to be under 5 minutes.

6.2 Chapter Conclusion

This chapter has explored the uncertainty in the measurement of the percentage broken rice; the measurement is estimated from moving rice grains via the rice in motion apparatus comprising of the components described in the previous chapters.

6.4.1 Input grey-scale frame of dust mixed with rice.

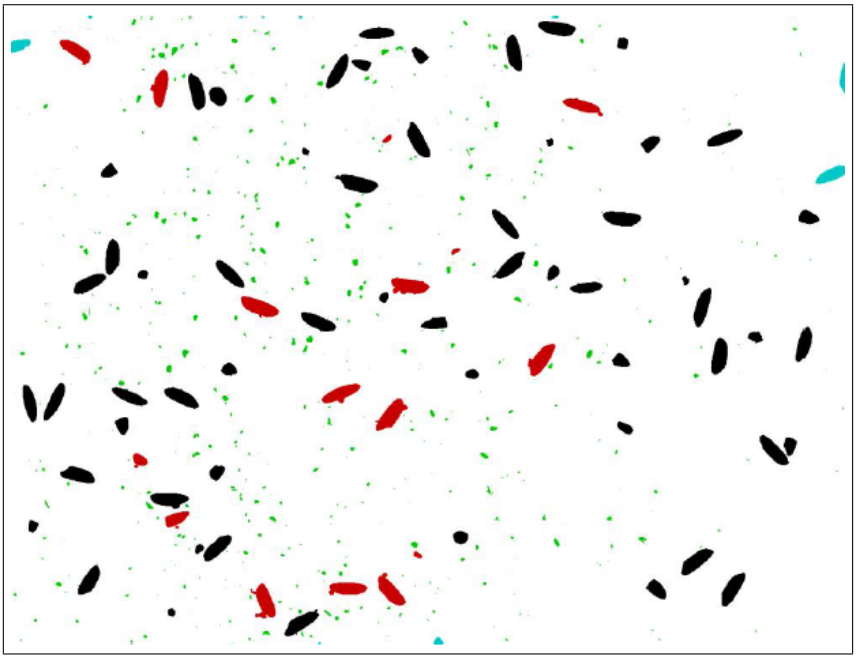

6.4.2 Back projection of extracted foreground signal, in black.

FIGURE 6.4: A sample frame of Sona Masoori rice, as captured from the rice in motion apparatus.

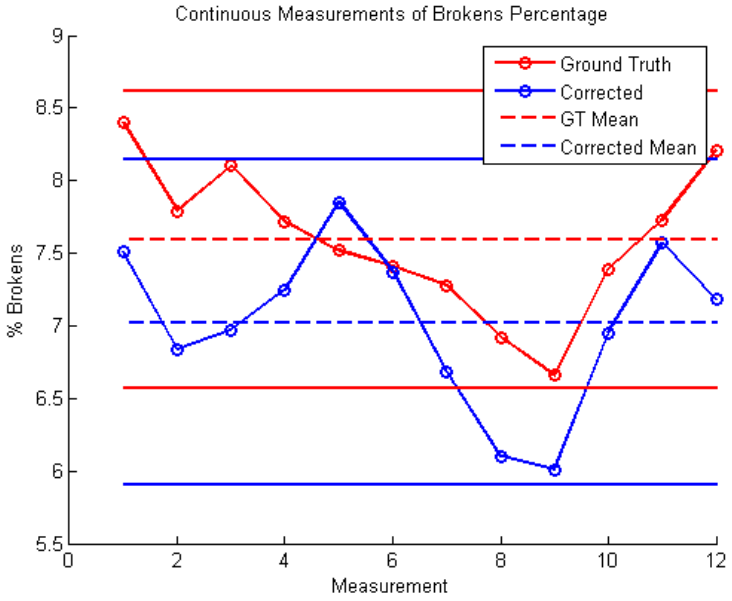

6.5.1

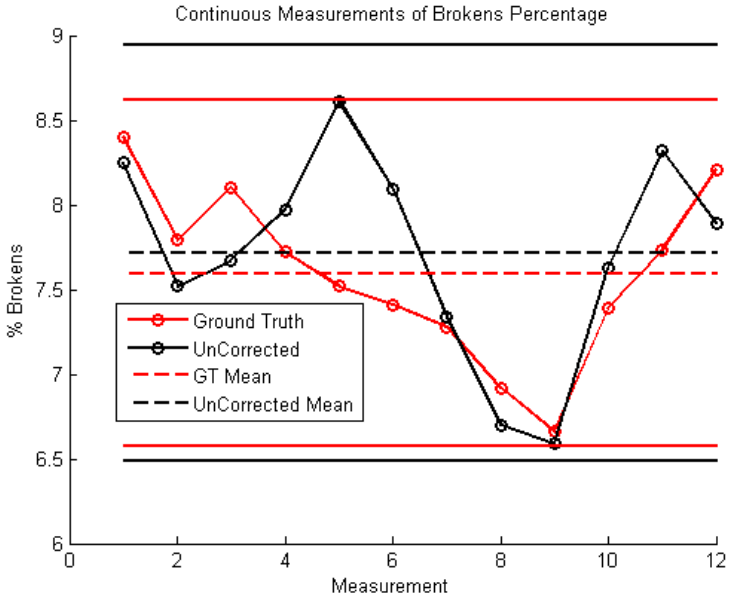

6.5.2

FIGURE 6.5: Continuous broken percentage measurement of Basmati rice, using the rice in motion apparatus prototype in Bangalore, India.

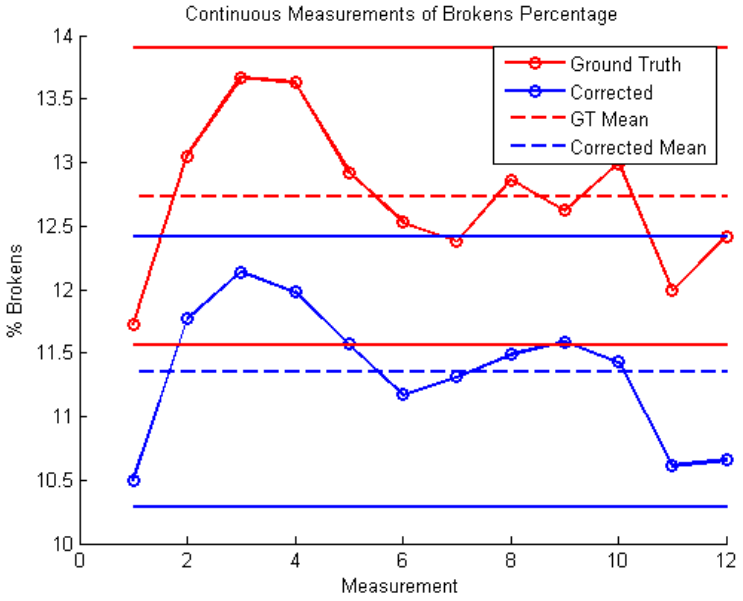

6.6.1

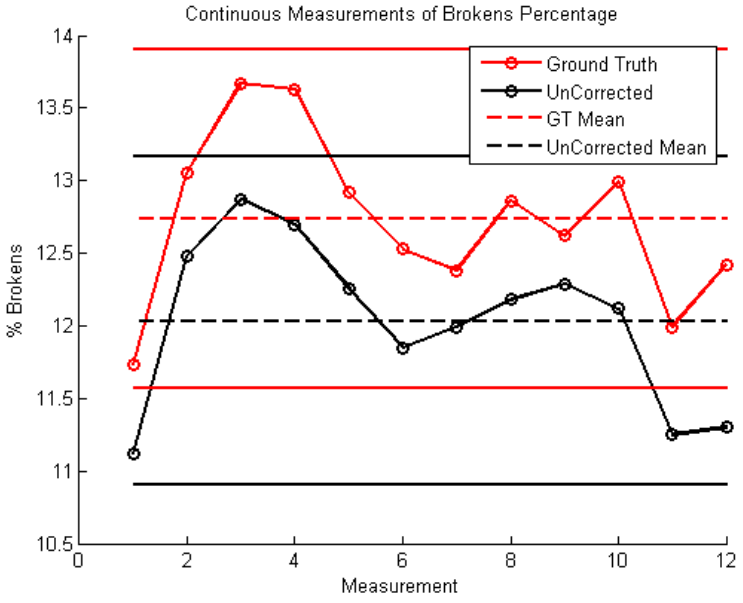

6.6.2

FIGURE 6.6: Continuous broken percentage measurements of Sona Masoori, in a similar experiment to the one conducted using Basmati rice.

Batch	Estimated Broken %	ε_σ	Uncorrected Broken %	Uncorrected ε_σ
1	7.51	-0.89	8.25	-0.15
2	6.84	-0.95	7.52	-0.27
3	6.97	-1.13	7.67	-0.43
4	7.25	-0.47	7.97	0.25
5	7.85	0.33	8.61	1.09
6	7.37	-0.04	8.09	0.68
7	6.68	-0.60	7.34	0.06
8	6.10	-0.82	6.7	-0.22
9	6.01	-0.65	6.59	-0.07
10	6.95	-0.44	7.63	0.24
11	7.57	-0.16	8.32	0.59
12	7.18	-1.03	7.89	-0.32
Mean		**-0.57**		**0.12**

TABLE 6.5: Continuous broken percentage measurements of Basmati, using the rice in motion apparatus, from 12 samples measured over a one hour period of bulk flow. The mean error is given as the reported length minus the ground-truth length.

Batch	Estimated Broken %	ε_σ	Uncorrected Broken %	Uncorrected ε_σ
1	10.50	-1.23	11.12	-0.61
2	11.77	-1.28	12.48	-0.57
3	12.14	-1.53	12.87	-0.80
4	11.98	-1.65	12.7	-0.93
5	11.57	-1.35	12.26	-0.66
6	11.17	-1.36	11.85	-0.68
7	11.31	-1.07	11.99	-0.39
8	11.49	-1.37	12.18	-0.68
9	11.59	-1.03	12.29	-0.33
10	11.43	-1.56	12.12	-0.87
11	10.61	-1.38	11.25	-0.74
12	10.66	-1.76	11.3	-1.12
Mean		**-1.38**		**-0.70**

TABLE 6.6: Continuous broken percentage measurements of Sona Masoori, in a similar experiment to the one conducted using Basmati rice.

We estimated the uncertainty in the by-count measurement in experiment 6.1. A large sample of 25,000 rice grains of three varieties was included in the evaluation. For US Long rice, we observed a mean error of 1.91%. A similar case is observed for Parboiled US Long and Basmati rice with 2.51% and 1.2% mean error, respectively. For equivalent by-mass estimations, we would expect half of these errors. However, these mean errors were unexpectedly overestimated, as we consider that tumbling grains would produce an underestimation effect on the observed samples (not an overestimation). From experiment 6.2 we reported, at the 95% confidence level, an error of ±0.46% in the consistency of the by-count measurement of broken rice percentage; for an equivalent

by-mass estimation, we would expect half of this error.

In experiment 6.3 a large continuous measurement trial was conducted using two varieties of rice. We observed a mean error of broken rice estimation without correction factor applied is 0.12%, and with correction factor applied is -0.57%, on the data samples of Basmati rice. The application of a correction factor was to accommodate for mean error in the selection rice grains that are measured (experiment 4.8); however, we now observe the correction factor produces a worse estimate of the percentage of broken rice. A similar occurrence is observed with the Sona Masoori data samples: the mean error without a correction factor applied is 0.70%, and with correction factor applied is -1.38%. Given the choice of whether to apply the bias correction model, we observe that both with and without correction produces a consistent measurement of percentage broken rice by-mass. In addition, the measurement time based on 25,000 rice grains is reported to be under 5 minutes; we infer this is suitable for continuous measurements in an on-line environment.

The stable and continuous operations of the prototype rice in motion measurement apparatus has been demonstrated. The rice in motion measurement apparatus estimated the percentage or broken rice from a set of 12 samples at a regular time interval of approximately five minutes; furthermore, two varieties of rice were evaluated (Basmati and Sona Masoori). From the analysis of the mean error and the maximum mean error, we conclude that the reported accuracy of the broken rice percentage by-mass from the measurement system are clearly suitable to be used for regular monitoring and better control of rice milling operations.

Chapter 7

Conclusion

This thesis has worked towards an on-line computer vision system for the measurement of broken rice grain percentage, using the length and shape information extracted from area camera images. This task was divided into three following sub-problems:

1. The measurement of rice length, *in stasis*.
2. The on-line measurement of percentage broken rice by length, *in motion*.
3. The inclusion of shape features as an additional classification criterion to length.

A system has been presented to each of these rice measurement problems, and form a complete on-line visual inspection apparatus for the measurement of broken rice grains. The objectives were reached by the inclusion of existing and novel methods to create and define the image processing pipeline of the machine vision system. This chapter presents the conclusions of this work.

Due to the confidential agreements made at the start of this project, publication of sensitive and potentially valuable materials has not been possible. The sponsor has begun internal preparations to eventually produce a patent on the measurement system; for which the author is included as a co-inventor of the apparatus. However, due to the work in chapter 5 being generalised and evaluated on public data-sets, a publication has been accepted based on some of the work in this research survey:

Charles Mallah, James Cope, and James Orwell. Plant leaf classification using probabilistic integration of shape, texture and margin features. *Signal Processing, Pattern Recognition and Applications*, 2013.

Section 7.1 summarises the main body of work from the chapters in this thesis. In section 7.2 the prominent achievements of this research are described, including a brief

description of the experiments conducted during this term. In the final section a set of suggestions are made of how the research may continue.

7.1 Chapter Summaries

Chapter 1 opened with an introductory discussion to motivate and contextualise the research. A case was presented for the requirements for a robust measurement system for granular particles, and then discuss the general problem of how to create a machine vision system to measure rice grains. This encompasses the basic requirement to obtain a contour of single rice grains, that is not distorted from the curvature of the lens. The highlighted requirements indluce the necessity for high-speed computation of the algorithm, to facilitate on-line measurement on a single workstation. In addition, the problem is broken into three main bodies of work: the measurement of static rice grain length, the measurement of broken rice in motion using length, and then with the inclusion of shape features.

In chapter 2, related work in the measurement of broken rice was approached. The problem has not been entirely solved for on-line continuous measurement. Various works that emphasise the importance of hardware selection for the task, as well as a range of image processing techniques that are relevant to the problem. Some techniques were based on the standard length definition of percentage broken rice, and other previous work used shape information. In addition to rice, the classification of plant species from images of leaves was part of the investigation; a problem that usually encompass large numbers of classes and few data samples. The case was stated that multiple features can potentially be collected for these classification problems, and a straightforward and robust approach is to combine density estimates from separate classifiers. The standard method of density estimation with the K-Nearest Neighbour classifier is discussed, in addition to the recent extension.

The first body of work was presented in chapter 3. A system was described for the accurate measurement of static rice grain length, on a glass viewing area. The system was built around a stroboscopic illumination ring of red LED lights, and a high-spatial resolution monochromatic camera. The image processing pipeline was discussed and the subsequent components were described and evaluated. A wide range of existing methods and novel ideas were explored, with the aim of reducing the mean error in the length measurement. A series of experiments from 3.1 through to 3.9 were devised to evaluate the various components related to static measurement. The processing pipeline for static measurement consists of: camera calibration, contour extraction, and estimation of absolute length. A set of novel calibration routines and modifications to two image

segmentation methods was introduced. The related experiments are described in table 7.1.

Experiment	Aim	Outcome
3.1 to 3.5	Estimate the errors on length measurements caused by pixel quantisation.	At the 99.7% confidence level, a ±0.041 mm error is expected; estimated from theoretical analysis, simulated models and experimental trials.
3.6, 3.7	Selection of a contour extraction method for rice grains that provides the most stable signal given changes in position and illumination.	The SmoothHybridHist method, which is the novel technique of using a local tiling strategy with the GlobalHist method, and then combining the thresholds values using a Gaussian smoothing filter.
3.8, 3.9	Selection of a length definition which provides the most accurate length estimation compared to hand measurements with the Vernier calliper.	The ParallelPrincipalAxis length measurement, due to simplicity and estimated errors below that of image quantisation.

Table 7.1: Summary of the experiments described in chapter 3.

The second body of work, in chapter 4, extends these principals. A presentation was included, consisting of additional components that allow the length measurement system to be expanded for the purpose of accurately estimating the percentage of broken rice in motion (within 1% mean error). A set of new problems are addressed: selecting single grains for measurement, the bias from touching grains, the possibility of motion blur, the foreshortening effect of tumbling rice, and the definition and conversion of broken percentage by-mass. The methodology exclusively assumes that a relatively sparse feed of rice grains is imaged by the device, however only single rice grains are included in the measurement. A series of experiments from 4.1 through to 4.11 were devised to evaluate these new sources of bias as well as evaluating the required components to enable a robust measurement of moving rice; these are described in table 7.2.

The third body of work is discussed in chapter 5 focused on the combination of different features, such as various shape descriptors, in a probabilistic framework. Several novel density estimators that work with the K-Nearest Neighbour methodology are proposed. These consist of a set of tabulated statistics that are pre-computed using sub-sets of the training data; different statistics can be produced and combined in various ways. The set of novel and standard density estimators are tested using several data-sets, including a complex multi-class data-set of leaf images. It was shown that more accurate density estimations are produced by certain combinations of the novel tabulated statistics; in

Experiment	Aim	Outcome
4.1	To estimate the number of grains to measure for useful analysis of broken rice percentage.	A minimum of 2,000 grains should be measured when sampling rice: measurement uncertainty of $\pm 1.34\%$ and $\pm 1.79\%$ for 10 and 20% input contamination of broken rice, respectively.
4.2 to 4.4	An optional set of parameters for the LWC single rice detection method.	Variety independent parameters: length: 8.2 mm, width: 2.7 mm and Corner threshold: 75%, providing 99.93% accuracy in single rice detection, with a projected mean error of less than -0.09% in broken rice measurement.
4.5 to 4.7	To quantify the mean error on broken rice measurement due to the effect of tumbling grains.	From Monte Carlo simulations, a 2% tumbling rate gives an estimated length error of -0.025 mm due to the foreshortening effect. The average error estimated from samples of rice was 1.18% (approximately the same as modelled in the simulation experiment.)
4.8	To estimate the bias effect of grain being seen, by the system, due to its length	A significant error of 1.9% at 250 kg/h was estimated from 10,000 rice grains.
4.9	Evaluate the proposed correction factor derived from Bayes Theorem of conditional probabilities.	A significant reduction in the overestimation of the percentage of broken rice of 0.7% at the 250 kg/h throughput.
4.10, 4.11	Develop a general conversion model to estimate the mass of a rice grain from the area.	A general set of parameters was modelled, and the average mean error of the conversion method was suitably low at 0.98%; this was statistically insignificant at the 95% confidence level.

TABLE 7.2: Summary of the experiments described in chapter 4.

particular the novel methods work well with reduced training samples. Lastly, the classification accuracy of various shape features is evaluated on a large data-set of broken and head rice grains. Experiments from 5.1 through to 5.5 were devised to evaluate the performance of the standard and novel density estimators, using a variety of data-sets, described in table 7.3.

Experiment	Aim	Outcome
5.1	Evaluate the classification accuracy of the set of density estimator methods (novel and standard) on publicly available data-sets.	The PROP and novel density estimators perform comparatively well with the methods in the literature that evaluate the iris flower and wheat seed univariate data-sets.
5.2	Evaluate the classification performance of the most complex data-set consisting of the 100 species of plant leaves (with low training samples)	A high performance of the novel RANK+VOTINGSPLIT estimator was observed; the mean classification precision and recall was reported to be 99.42% and 99.38%, respectively; with an expected log likelihood of -0.17.
5.3	Further investigate the best noted density estimator methods with respect to performance as a function of training sample size.	At low values of available samples, and especially for low values of K (number of nearest neighbours), the RANK+VOTINGSPLIT estimator provides consistent improved performance than the standard approaches at all tested training sizes.
5.4	Estimate the error of broken rice percentage given the subjectivity of shape.	The difference between two independent labelled data-sets indicated a 1% change in the percentage of broken rice (from 25,000 Sona Masoori grains); however, this remains lower than the estimated $\pm$1.6% sampling error.
5.5	Evaluate the performance of the density estimators with respect to identifying broken grains of rice using shape features.	The PROP estimator worked best, with -0.037 mean posterior log, 97.70% mean precision, and 97.74% mean recall. However each of the other tested estimators all provided mean precision and recall rates of above 97.20% using the CCDC+CH+VEL combined features on the data-set of 6,000 Sona Masoori grains (half broken, half head rice).

TABLE 7.3: Summary of the experiments described in chapter 5.

In chapter 6, a series of experiments were described for the evaluation of the proposed measurement system built from the methods described in the three previous chapters. The rice in motion measurement apparatus is extensively evaluated from experiments 6.1 through to 6.3, described in table 7.4.

Experiment	Aim	Outcome
6.1	Estimate the uncertainty in the by-count measurement of percentage broken rice using the first prototype of the rice in motion apparatus.	From a large sample of 25,000 rice grains each of three varieties of rice, a mean error of 1.91%, 2.51% and 1.2% was observed, for US Long, Parboiled US Long and Basmati, respectively.
6.2	Quantify the consistency of the by-count measurement of broken rice percentage.	At the 95% confidence level, a error of ±0.4644%, estimated from a sample of 22,250 US Long grains.
6.3	Estimate the uncertainty in the by-mass percentage of broken rice, in a continuous measurement trial, using the second prototype of the rice in motion apparatus.	Evaluation of a series of 12 measurements of 25,000 rice grains each of two varieties of rice. Observations were made of a mean error of broken rice estimation without correction factor applied is 0.12%, and with correction factor applied is -0.57%, on the data samples of Basmati rice. A similar occurrence is observed with the Sona Masoori data samples: the mean error without a correction factor applied is 0.70%, and with correction factor applied is -1.38%.

TABLE 7.4: Summary of the experiments described in chapter 6.

7.2 Achievements

This research survey has outlined the image processing steps that comprise a complete on-line measurement system for the inspection of rice grains. The proposed systems incorporate many techniques to provide the complete methodology, however several achievements were made during the scope of the project.

A set of fast and accurate calibration procedures were created for the removal of optical lens distortion in chapter 3. The proposed systems were accurate enough for the measurement of small objects in the view of an area camera, and for the conversion to real world units. The distortions present would cause significant error if not corrected, however the corrective approach using the full camera model was not sufficient to correct for this.

A novel tiled image segmentation approach was proposed in chapter 3, to improve the stability of the rice grain contour that is extracted from the monochromatic area camera image. The method successfully encompasses the global statistic in a local approach, allowing more sensitivity to local variation in the image, compared to global thresholding techniques. This is required, as the variation in the contour of small objects such as rice grains can severely effect the measurements made. A post-extraction filter is applied to each tiled window to detect the presence of foreground objects, as the standard method does not cope with an image that contains no foreground signal. Other local based methods tend to be computationally expensive

A corrective approach was described in chapter 4, derived from Bayes Theorem, for the removal of mean errors caused by finite aperture size and the biased probabilities of viewing objects dependent on their size. Using the relevant conditional probabilities, empirically observed, the corrective model was demonstrated to reduce the mean error of the rice broken percentage, estimated from large samples of rice grains.

A set of novel robust K-Nearest Neighbours posterior class density models were developed and thoroughly evaluated in chapter 5. A set of possible statistics is presented, that are tabulated from prior observation. The combination of these features allows a new set of density estimations, based on the K-NN method, to be created. It was demonstrated that the method works particularly well in situations with large numbers of classes and low training samples: in the case with the complex one hundred plant species data-set, both situations are present.

The continuous and consistent on-line measurement of the by-mass percentage of broken rice was demonstrated in chapter 6. The results obtained from the experimental apparatus and prototype device indicate that it is feasible to obtain on-line measurements that

are well within the required tolerance. This would enable such a device to be deployed in a number of important industrial applications.

7.3 Further Work

In this thesis, solutions to the problems of on-line measurement of broken rice grain percentage were presented. Whilst the three systems presented address particular issues that arise with accurate measurements of small scale objects using an area camera, further work is required to reduce the errors associated with some of these components. A system that reduces these mean errors would be an even more valuable tool for the on-line measurement of broken rice.

The bias correction model, presented in chapter 4, attempts to remove the problems associated with measuring single rice grains; all touching grains are ignored by the system, therefore the bias is introduced. A mechanical change to the feeding system could separate rice grains, and reduce this effect; or, one could employ object separation techniques to perform this with image processing; additionally, an improved correction model could be established, perhaps by taking the throughput of the flow into account, to correct for the overcompensation caused by the proposed one in this thesis.

The classification of broken rice using shape features, presented in chapter 5, attempts to use a framework to produce the probability that a grain is broken. It is indicated that the high accuracy rates of various data-sets, including rice grains. However, there are many other shape features that could be implemented such as invariant moments, Fourier descriptors, and wavelets.

More interesting than refinements to the systems presented here, are the potential applications of this work; measurement systems for other varieties of granular organic matter could be designed using the image processing pipeline, components and principles outlined in this research survey.

Appendix A

Camera Calibration Diagnostic Plots

Figures A.1 to A.4 contain diagnostic plots for each of the BDM, LSE, SLSE, and PRM calibration methods, respectively. These examples show the correction performed on the 8 mm lens. The relative levels of distortion removal are demonstrated with the various diagnostic plots.

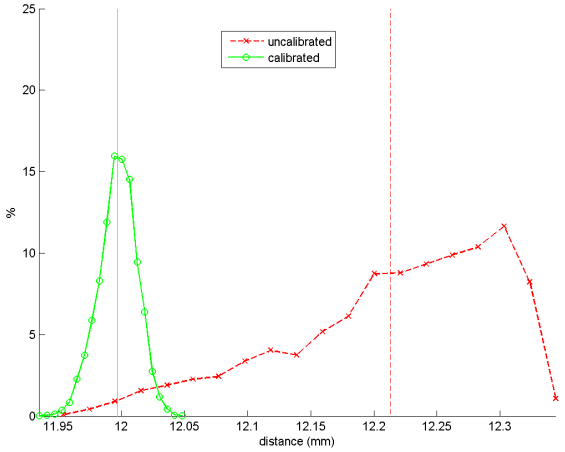

A.1.1 Histogram of distance between pairs of control points

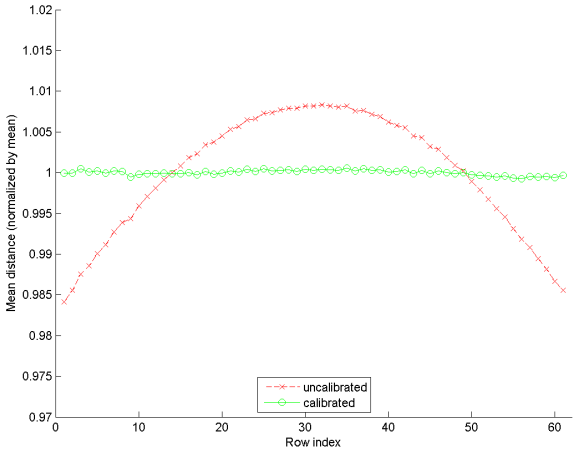

A.1.2 Normalised mean distance between horizontal pairs of control points per column

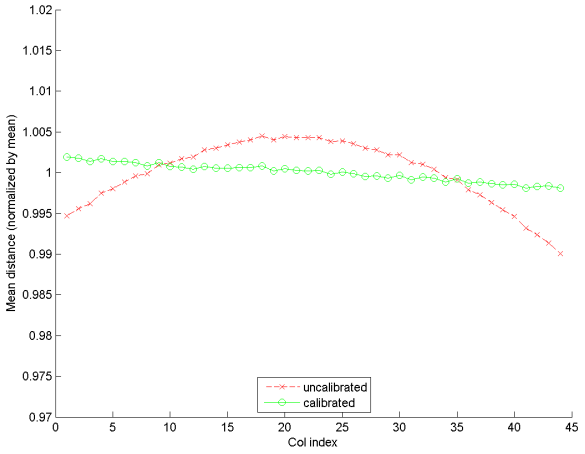

A.1.3 Normalised mean distance between vertical pairs of control points per row

FIGURE A.1: Diagnostic plots for camera calibration with BDM.

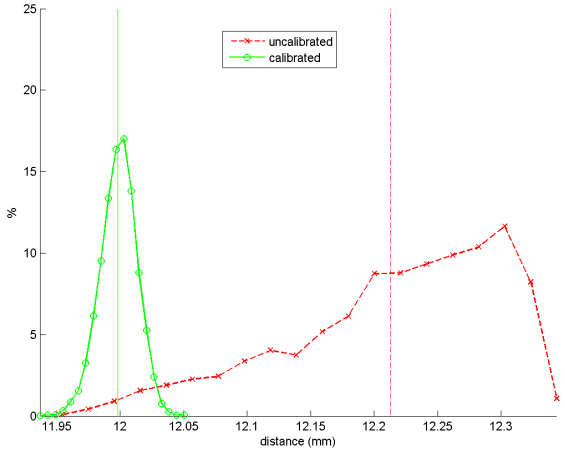

A.2.1 Histogram of distance between pairs of control points

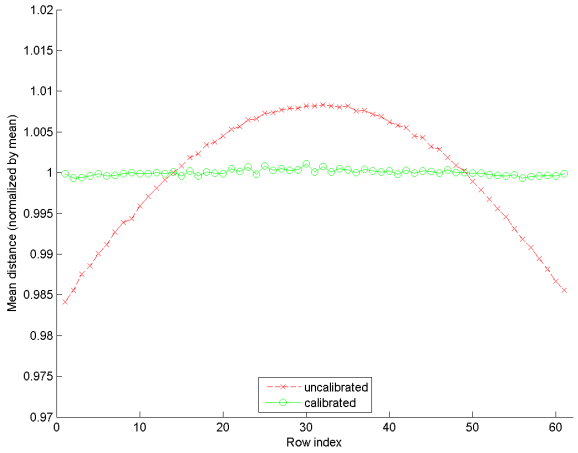

A.2.2 Normalised mean distance between horizontal pairs of control points per column

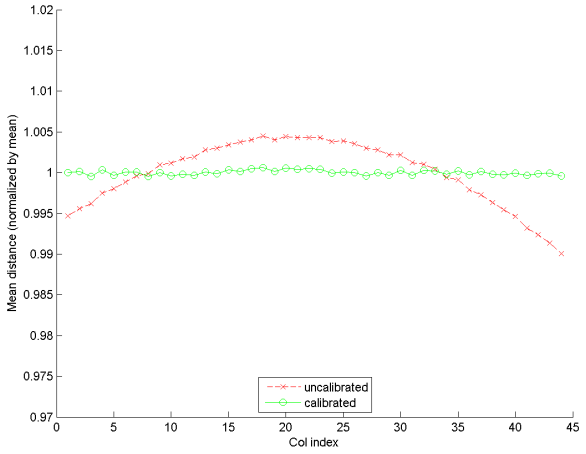

A.2.3 Normalised mean distance between vertical pairs of control points per row

FIGURE A.2: Diagnostic plots for camera calibration with LSE.

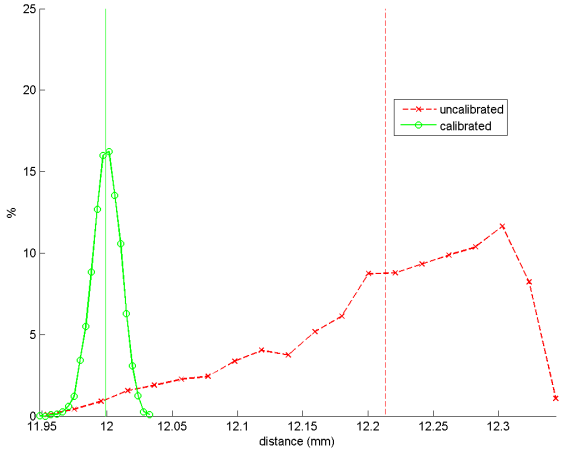

A.3.1 Histogram of distance between pairs of control points

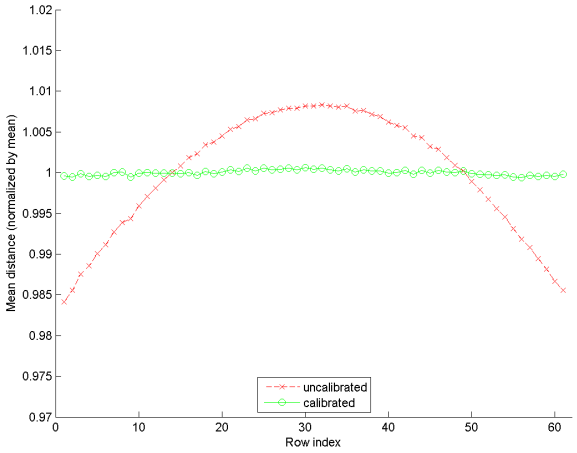

A.3.2 Normalised mean distance between horizontal pairs of control points per column

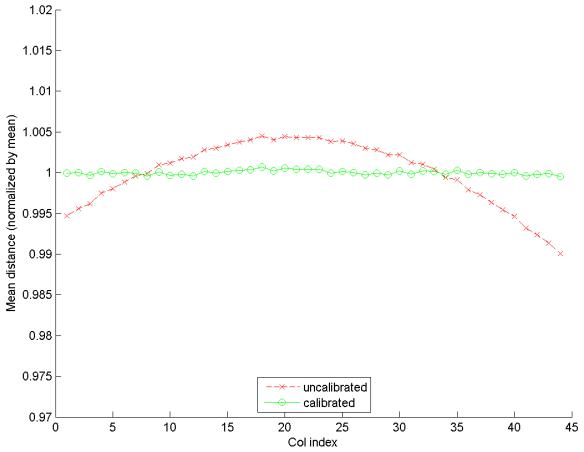

A.3.3 Normalised mean distance between vertical pairs of control points per row

FIGURE A.3: Diagnostic plots for camera calibration with SLSE.

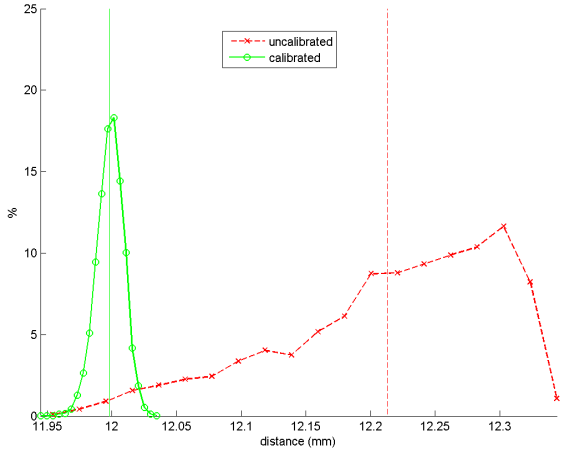

A.4.1 Histogram of distance between pairs of control points

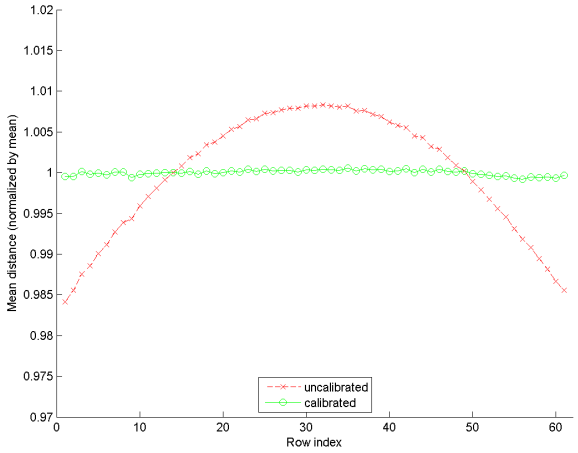

A.4.2 Normalised mean distance between horizontal pairs of control points per column

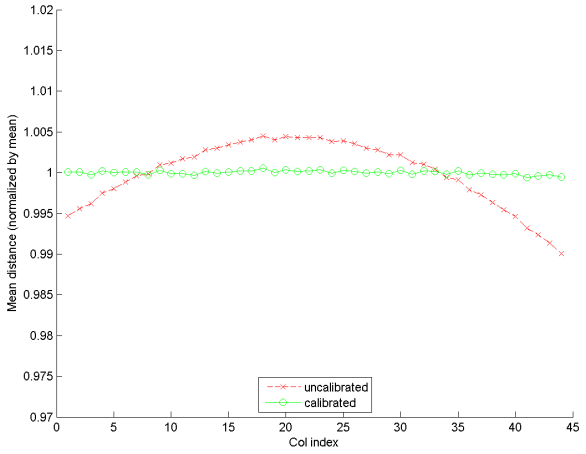

A.4.3 Normalised mean distance between vertical pairs of control points per row

FIGURE A.4: Diagnostic plots for camera calibration with PRM.

Appendix B

Rice Grain Contour Extraction Thumbnails

Table B.1 contains example images of the extracted contours from each method, back projected in bright green on the original grey level image. An example grain is given for each of the three levels of background quality, from black Teflon to one and two layers of rice dust (glued onto the background plate). Similarly, table B.2 contains example images of the extracted contours from each method for three different positions within the viewing area of the camera.

Method	Teflon Flat	1x Dust	2x Dust
NaiveThresh	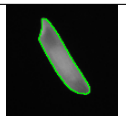	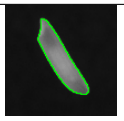	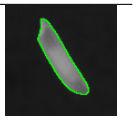
GlobalHist	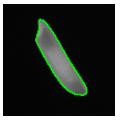	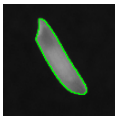	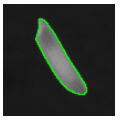
MinErrorThresh			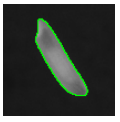
HybridHist	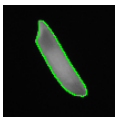	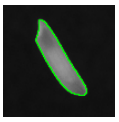	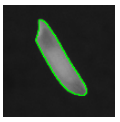
SmoothHybridHist	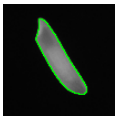	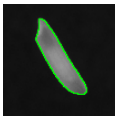	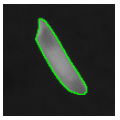
LocalVar	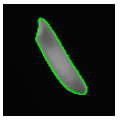	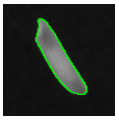	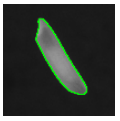
LocalVarRatio	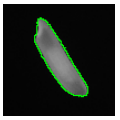		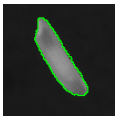
EdgeLoG	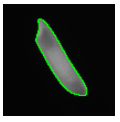	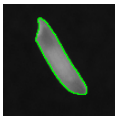	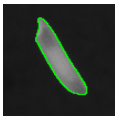
EdgeCanny	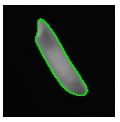	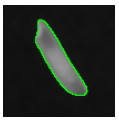	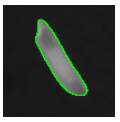

Table B.1: Sample rice grains with unstable contours extracted from 3 backgrounds.

Method	Centre	Centre Right	Far Right
NaiveThresh	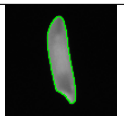	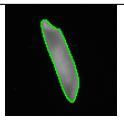	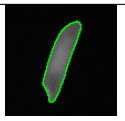
GlobalHist	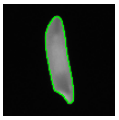	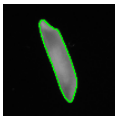	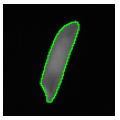
MinErrorThresh	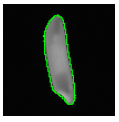		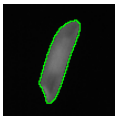
HybridHist	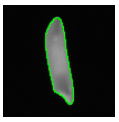	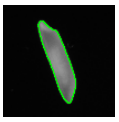	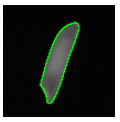
SmoothHybridHist	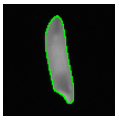	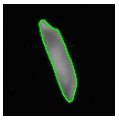	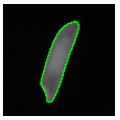
LocalVar	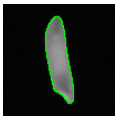	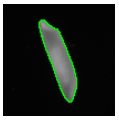	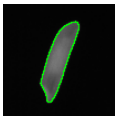
LocalVarRatio	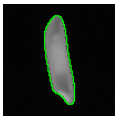	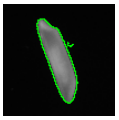	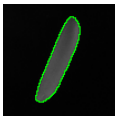
EdgeLoG	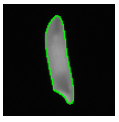	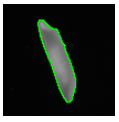	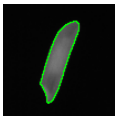
EdgeCanny	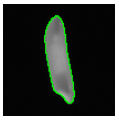		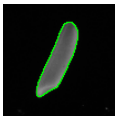

Table B.2: Sample rice grains with unstable contours, from 3 positions in the view.

Appendix C

Post Image Segmentation Filters & Test Cases

We include several test images that consist of: an empty background, a single grain, two grains, a mixture of sparse grains and lastly a mixture of touching grains, see figure C.1. These test images were as input samples for each contour extraction method. A set of output images for each test image is shown from tables C.1 to C.5, where an output image is shown after each of the main filter stages.

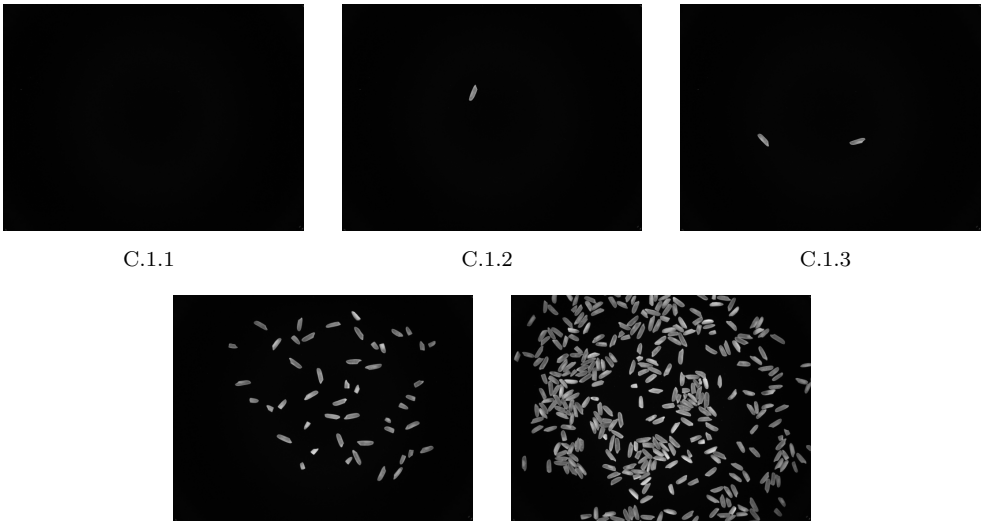

C.1.1 C.1.2 C.1.3

C.1.4 C.1.5

FIGURE C.1: A set of five test images for evaluating contour extraction of US Long Grain rice, consisting of: no presence signal, one grain, two grains, a mixture of broken and head rice, and lastly a random mix of touching broken and head rice.

Method	Output	Fill	Dust Filter	Clump Filter
NaiveThresh	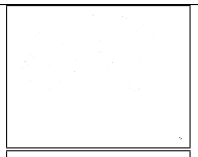	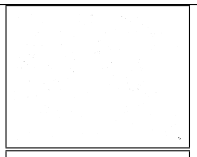		
GlobalHist	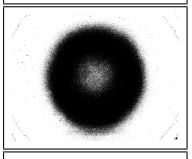	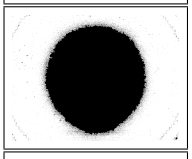	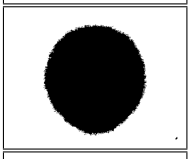	
MinErrorThresh	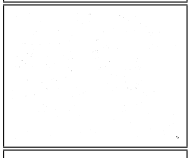	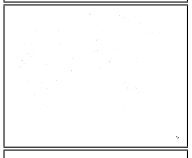		
HybridHist	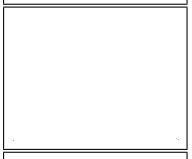	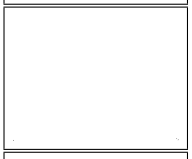	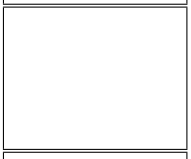	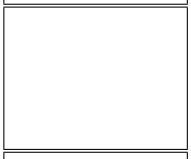
SmoothHybridHist	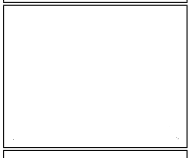	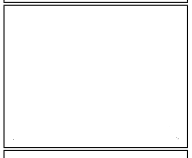	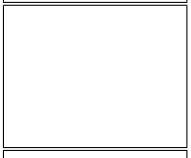	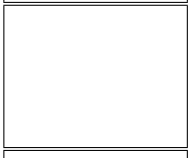
LocalVar	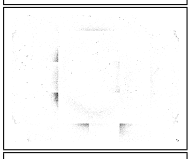	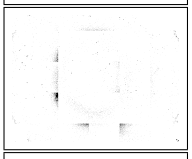	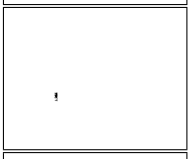	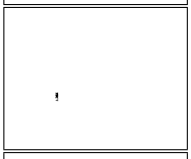
LocalVarRatio			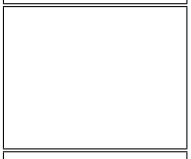	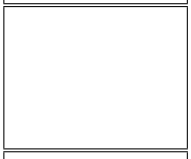
EdgeLoG	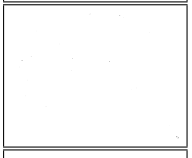	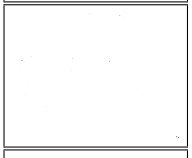		
EdgeCanny	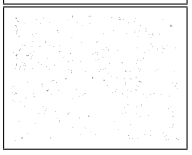	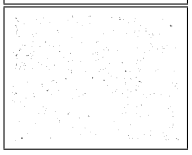		

Table C.1: Post contour extraction filters using a blank input image.

Method	Output	Fill	Dust Filter	Clump Filter
NaiveThresh	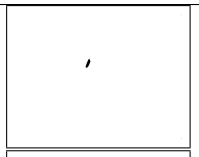	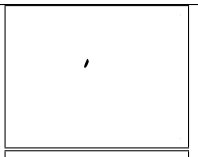	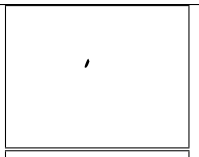	
GlobalHist		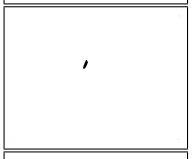		
MinErrorThresh	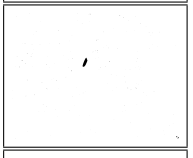	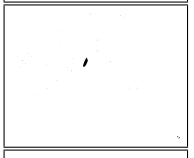		
HybridHist	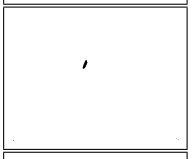	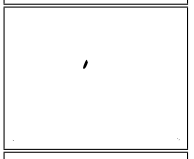	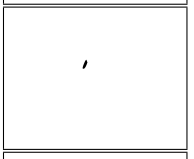	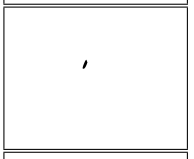
SmoothHybridHist	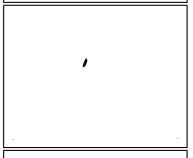	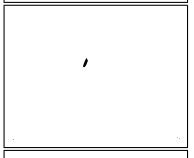	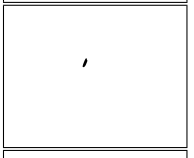	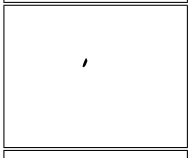
LocalVar	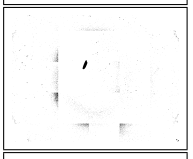	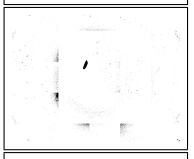	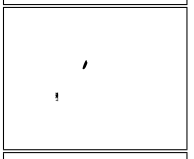	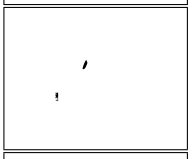
LocalVarRatio	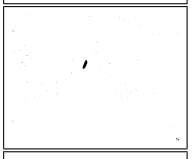	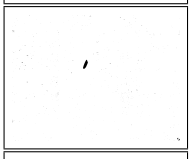	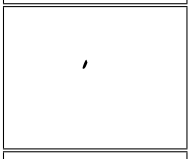	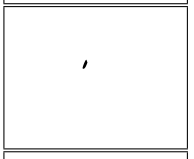
EdgeLoG	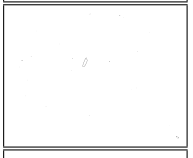	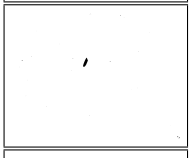	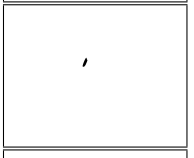	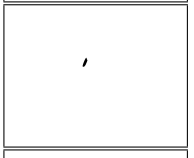
EdgeCanny	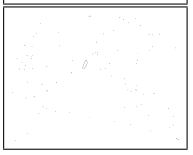	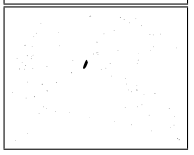	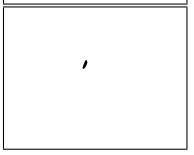	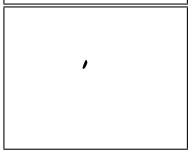

Table C.2: Post contour extraction filters using an input image of one grain of rice.

Method	Output	Fill	Dust Filter	Clump Filter
NaiveThresh				
GlobalHist				
MinErrorThresh	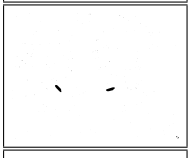	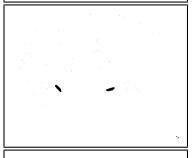		
HybridHist				
SmoothHybridHist	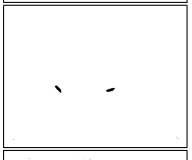	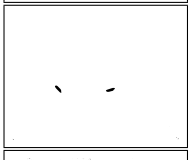	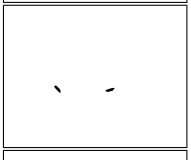	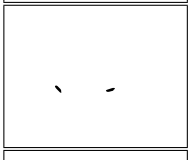
LocalVar	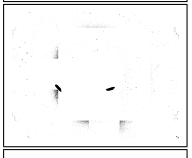	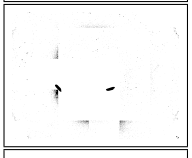		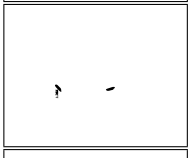
LocalVarRatio				
EdgeLoG	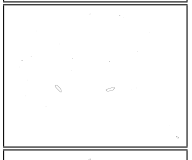	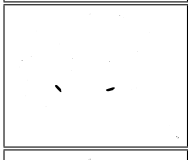		
EdgeCanny	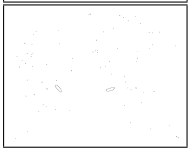	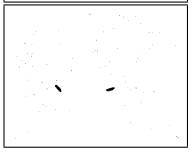		

Table C.3: Post contour extraction filters using an input image of two rice grains.

Method	Output	Fill	Dust Filter	Clump Filter
NaiveThresh	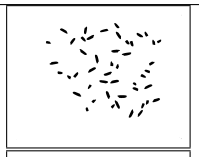		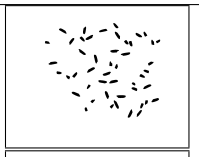	
GlobalHist	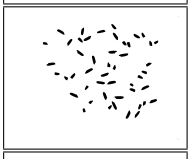	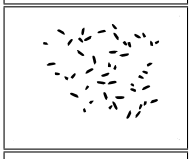	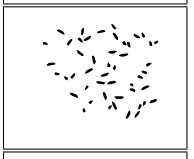	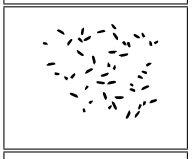
MinErrorThresh				
HybridHist	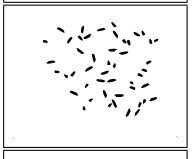	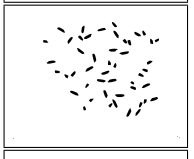	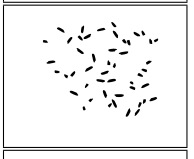	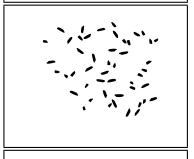
SmoothHybridHist	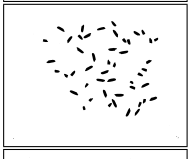	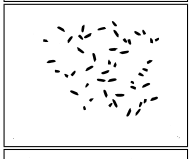	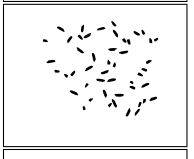	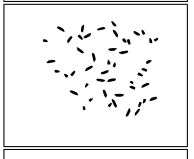
LocalVar	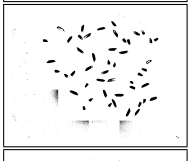	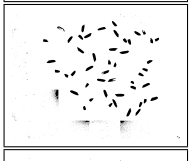		
LocalVarRatio				
EdgeLoG	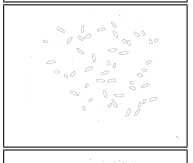			
EdgeCanny	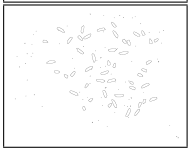	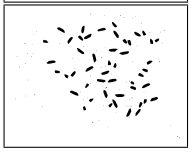		

Table C.4: Post contour extraction filters with an input image of mixed broken and head rice grains.

Method	Output	Fill	Dust Filter	Clump Filter
NaiveThresh				
GlobalHist				
MinErrorThresh				
HybridHist				
SmoothHybridHist				
LocalVar	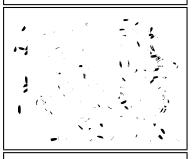	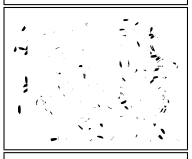	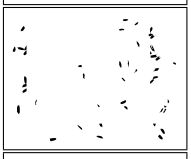	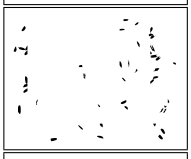
LocalVarRatio				
EdgeLoG	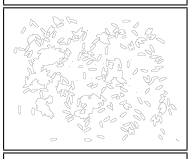			
EdgeCanny	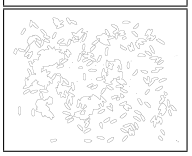	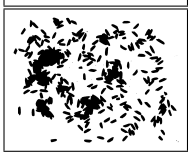	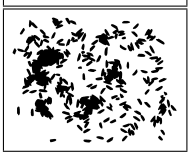	

Table C.5: Post contour extraction filters using an input image of mixed touching broken and head rice grains.

Appendix D

One-Hundred Plant Leaf Species Data Set

Figures D.1 and D.2 contain a sample binary image of each of the one-hundred plant species from the new data-set.

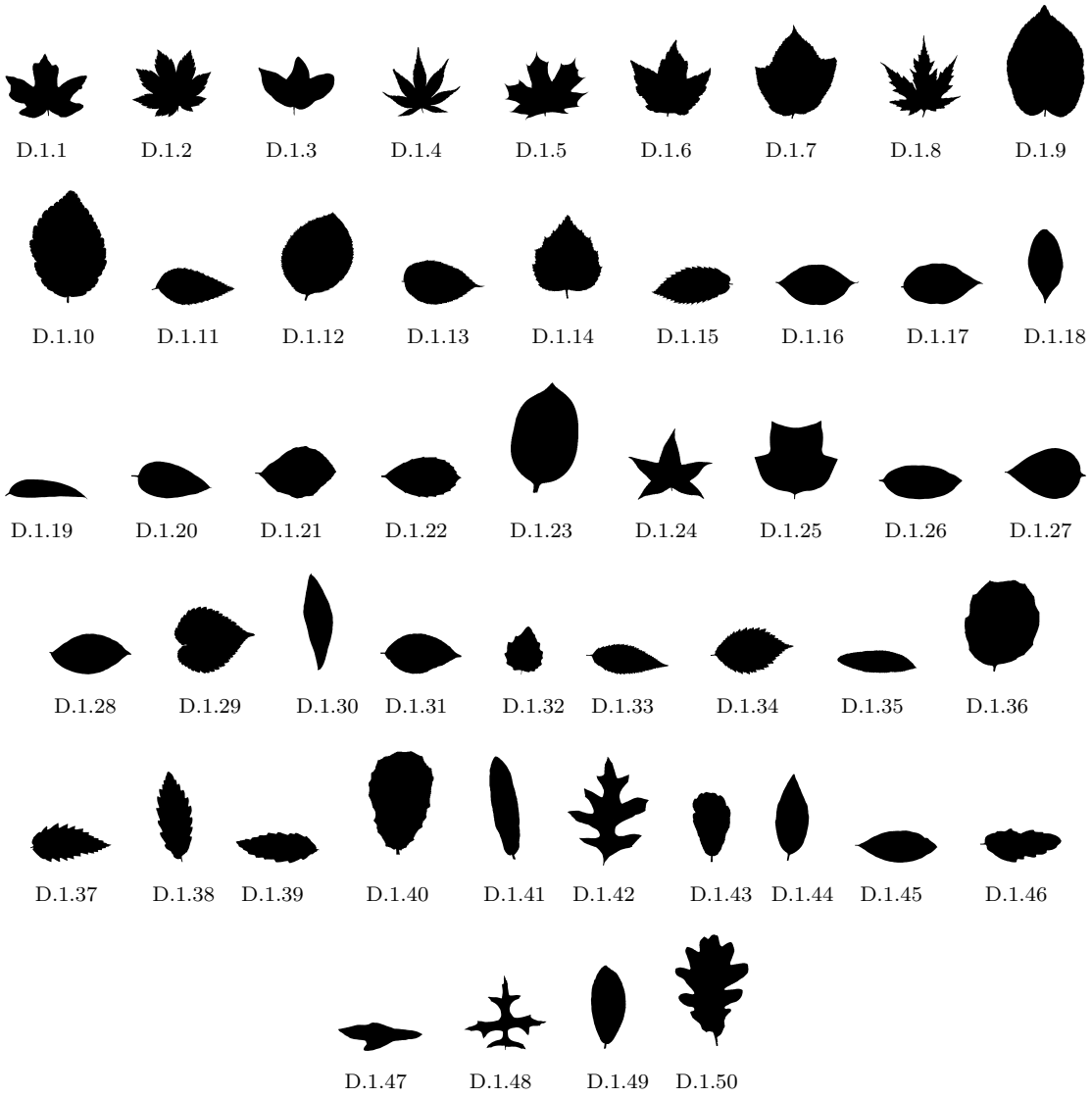

FIGURE D.1: A sample each of 50 species in the leaves data set: D.1.1 Acer Campestre. D.1.2 Acer Circinatum. D.1.3 Acer Mono. D.1.4 Acer Palmatum. D.1.5 Acer Platanoids. D.1.6 Acer Rubrum. D.1.7 Acer Rufinerve. D.1.8 Acer Saccharinum. D.1.9 Alnus Cordata. D.1.10 Alnus Rubra. D.1.11 Alnus Sieboldiana. D.1.12 Alnus Viridis. D.1.13 Betula Austrosinensis. D.1.14 Betula Pendula. D.1.15 Castanea Sativa. D.1.16 Cornus Chinensis. D.1.17 Cornus Macrophylla. D.1.18 Cytisus Battandieri. D.1.19 Eucalyptus Glaucescens. D.1.20 Eucalyptus Urnigera. D.1.21 Fagus Sylvatica. D.1.22 Ilex Aquifolium. D.1.23 Ilex Cornuta. D.1.24 Liquidambar Styraciflua. D.1.25 Liriodendron Tulipifera. D.1.26 Lithocarpus Cleistocarpus. D.1.27 Magnolia Heptapeta. D.1.28 Magnolia Salicifolia. D.1.29 Morus Nigra. D.1.30 Olea Europaea. D.1.31 Phildelphus. D.1.32 Populus Nigra. D.1.33 Prunus Avium. D.1.34 Prunus Shmittii. D.1.35 Pterocarya Stenoptera. D.1.36 Quercus Agrifolia. D.1.37 Quercus Brantii. D.1.38 Quercus Canariensis. D.1.39 Quercus Castaneifolia. D.1.40 Quercus Coccifera. D.1.41 Quercus Crassipes. D.1.42 Quercus Ellipsoidalis. D.1.43 Quercus Greggii. D.1.44 Quercus Ilex. D.1.45 Quercus Imbricaria. D.1.46 Quercus Infectoria. D.1.47 Ilex Aquifolium. D.1.48 Quercus Palustris. D.1.49 Quercus Phillyraeoides. D.1.50 Quercus Pubescens.

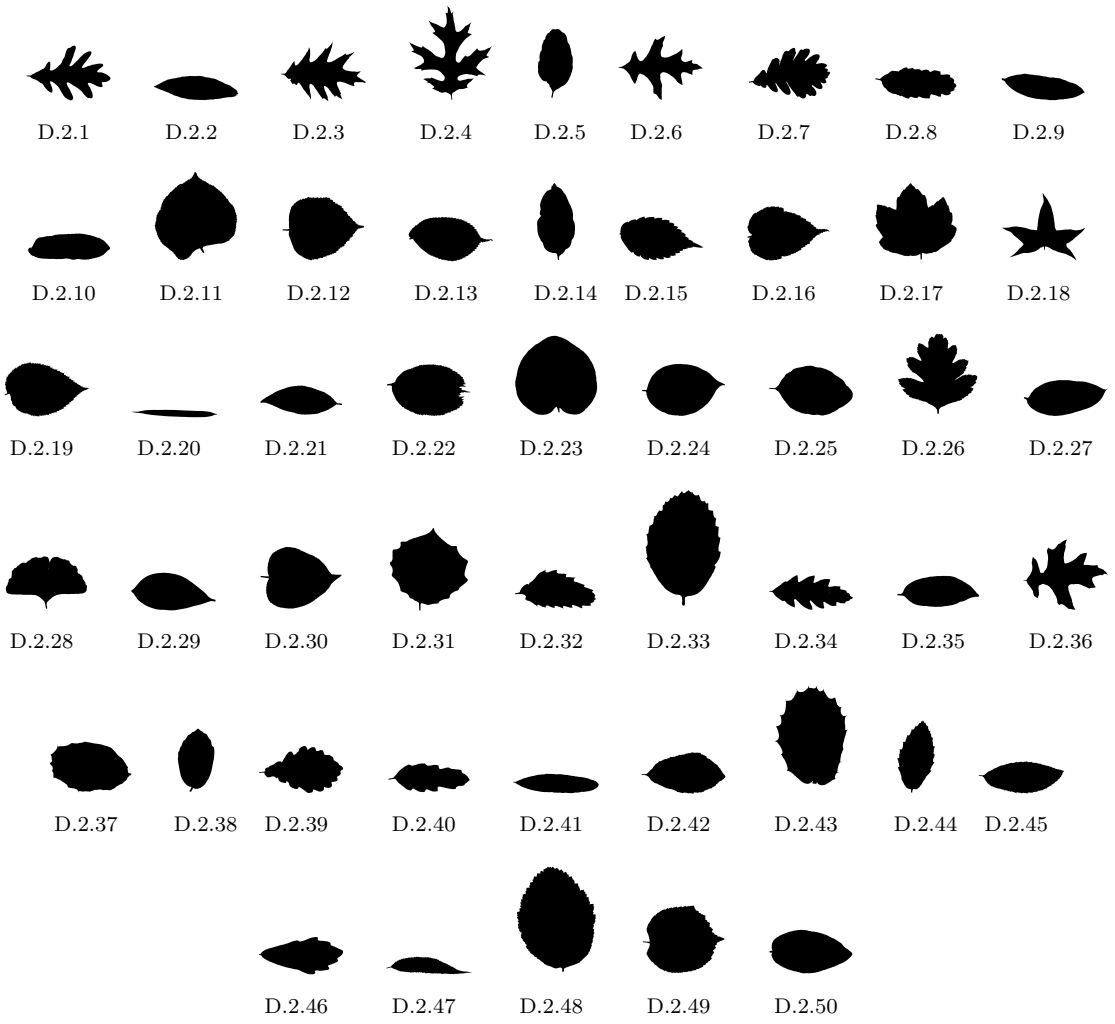

FIGURE D.2: A sample each of the remaining species in the data-set: D.2.1 Quercus Pyrenaica. D.2.2 Quercus Rhysophylla. D.2.3 Quercus Rubra. D.2.4 Quercus Shumardii. D.2.5 Quercus Suber. D.2.6 Quercus Texana. D.2.7 Quercus Vulcanica. D.2.8 Quercus Hispanica. D.2.9 Rhododendron Russellianum. D.2.10 Salix Intergra. D.2.11 Tilia Oliveri. D.2.12 Tilia Platyphyllos. D.2.13 Ulmus Bergmanniana. D.2.14 Viburnum Tinus. D.2.15 Zelkova Serrata. D.2.16 Acer Capillipes. D.2.17 Acer Opalus. D.2.18 Acer Pictum. D.2.19 Alnus Maximowiczii. D.2.20 Arundinaria Simonii. D.2.21 Callicarpa Bodinieri. D.2.22 Celtis Koraiensis. D.2.23 Cercis Siliquastrum. D.2.24 Cornus Controversa. D.2.25 Cotinus Coggygria. D.2.26 Crataegus Monogyna]. D.2.27 Eucalyptus Neglecta. D.2.28 Ginkgo Biloba. D.2.29 Lithocarpus Edulis. D.2.30 Populus Adenopoda. D.2.31 Populus Grandidentata. D.2.32 Quercus Afares. D.2.33 Quercus Alnifolia. D.2.34 Quercus Cerris. D.2.35 Quercus Chrysolepis. D.2.36 Quercus Coccinea. D.2.37 Quercus Crassifolia. D.2.38 Quercus Dolicholepis. D.2.39 Quercus Hartwissiana. D.2.40 Quercus Kewensis. D.2.41 Quercus Phellos. D.2.42 Quercus Pontica. D.2.43 Quercus Semecarpifolia. D.2.44 Quercus Trojana. D.2.45 Quercus Variabilis. D.2.46 Quercus Turneri. D.2.47 Salix Fragilis. D.2.48 Sorbus Aria. D.2.49 Tilia Tomentosa. D.2.50 Viburnum Rhytidophylloides.

Bibliography

[1] R. C. Bautista, T. J. Siebenmorgen, and P. A. Counce. Rice kernel dimensional variability trends. *Applied Engineering in Agriculture*, 23(2):207, 2007.

[2] J. N. Efferson. Rice quality in world markets. *Rice grain quality and marketing.International Rice Research Institute, PO Box*, 933:1–13, 1985.

[3] N. D. Cruz and GS Khush. Rice grain quality evaluation procedures. *Aromatic rices*, pages 15–28, 2000.

[4] G. S. Khush, C. M. Paule, and N. M. F De La Cruz. Rice grain quality evaluation and improvement at irri. In *Proceedings of the workshop on chemical aspects of rice grain quality*, pages 21–31, 1979.

[5] M. I. Saleh and J. F. MEULLENET. Effect of protein disruption using proteolytic treatment on cooked rice texture properties. *Journal of Texture Studies*, 38(4): 423–437, 2007.

[6] M. A. Monsoor and A. Proctor. Relative ffa formation and lipid oxidation of commercially milled unseparated, head, and broken rice. *Journal of the American Oil Chemists' Society*, 80(12):1183–1186, 2003.

[7] M. A. Monsoor, A. Proctor, and T. J. Siebenmorgen. Surface lipid and free fatty acids (ffa) content of head and broken rice produced by milling after different drying treatments. *Cereal Chemistry*, 81(6):705–709, 2004.

[8] N. T. W. Cooper, T. J. Siebenmorgen, and P. A. Counce. Effects of nighttime temperature during kernel development on rice physicochemical properties. *Cereal Chemistry*, 85(3):276–282, 2008.

[9] M. I. Saleh and J. F. Meullenet. Effect of moisture content at harvest and degree of milling (based on surface lipid content) on the texture properties of cooked long-grain rice. *Cereal Chemistry*, 84(2):119–124, 2007.

[10] The Economist. How to feed the world. (November 21st 2009):13–76–87, 2009.

[11] The Royal Society. Reaping the benefits. (October 2009), 2009. URL http://royalsociety.org/uploadedFiles/Royal_Society_Content/policy/publications/2009/4294967719.pdf;.

[12] National Physical Laboratory. Sustainability issue. *Metromnia*, (Autumn 2010): 2, 2010.

[13] F. Courtois, M. Faessel, and C. Bonazzi. Assessing breakage and cracks of parboiled rice kernels by image analysis techniques. *Food control*, 21(4):567–572, 2010.

[14] International Rice Research Institute. Rice basics, Dec 2012. URL http://www.irri.org/index.php?option=com_k2&view=item&layout=item&id=9081&lang=en.

[15] Professor Sir David Baulcombe. The food standards agency and the advocacy of genetically modified crops, 5th June 2010 2010. URL http://www.telegraph.co.uk/comment/letters/7803921/The-Food-Standards-Agency-and-the-advocacy-of-genetically-modified-crops.html.

[16] D. J. Feliz, A. Proctor, M. A. Monsoor, and R. L. Eason. The effects of damaged kernel caused by combine harvester settings on milled rice free fatty acid levels. *Journal of Food Science*, 70(6):c376–c379, 2005.

[17] Rice Knowledge Bank. Quality characteristics of milled rice, Dec 2012. URL http://www.knowledgebank.irri.org/rkb/quality-characteristics-of-milled-rice.html.

[18] Rice Knowledge Bank. Procedures for measuring quality of milled rice, Dec 2012. URL http://www.knowledgebank.irri.org/rkb/quality-characteristics-of-milled-rice/procedures-for-measuring-quality-of-milled-rice.html.

[19] Seedburo. Grainman rice sizing device, Dec 2012. URL http://www.seedburo.com/productDetail.asp_Q_catID_E_519_A_subCatID_E_2535_A_productID_E_3297_A_NO_2_Rice_Miller_E_NO_2_Rice_Miller.

[20] Serge Beucher and Fernand Meyer. The morphological approach to segmentation: the watershed transformation. *OPTICAL ENGINEERING-NEW YORK-MARCEL DEKKER INCORPORATED-*, 34:433–433, 1992.

[21] P. Lin, Y. Chen, and Y. He. Identification of broken rice kernels using image analysis techniques combined with velocity representation method. *Food and Bioprocess Technology*, pages 1–7, 2010.

[22] J. S. Aulakh and V. K. Banga. Percentage purity of rice samples by image processing. In *International conference on emerging trends in electrical, electronics and power engineering.*

[23] G. van Dalen. Determination of the size distribution and percentage of broken kernels of rice using flatbed scanning and image analysis. *Food Research International*, 37(1):51–58, 1 2004.

[24] B. K. Yadav and V. K. Jindal. Monitoring milling quality of rice by image analysis. *Computers and Electronics in Agriculture*, 33(1):19–33, 2001.

[25] H. Aghayeghazvini, A. Afzal, M. Heidarisoltanabadi, S. Malek, and L. Mollabashi. Determining percentage of broken rice by using image analysis. *Computer and Computing Technologies in Agriculture II, Volume 2*, pages 1019–1027, 2009.

[26] B. Ni, M. R. Paulsen, K. Liar, and J. F. Reid. Design of an automated corn kernel inspection system for machine vision. *Transactions of the ASAE*, 40(2):491–497, 1997.

[27] A. J. Cardarelli, Y. Tao, J. L. Bernhardt, and F. N. Lee. Nondestructive quantification of internal damage in rough rice caused by insects and fungus. In *Photonics East (ISAM, VVDC, IEMB)*, pages 111–118. International Society for Optics and Photonics, 1999.

[28] K. Liao, M. R. Paulsen, J. F. Reid, B. Ni, and E. Bonifacio. Corn kernel shape identification by machine vision using a neural network classifier. *Paper-American Society of Agricultural Engineers*, 1992.

[29] CVI Melles Griot. Machine vision lighting fundamentals - cvi melles griot technical guide, vol 2, issue 1. Technical Report Vol 2, Issue 1, CVI Melles Griot, 2009.

[30] D. Martin. A practical guide to machine vision lighting. Technical Report October, Advanced illumination, 2007.

[31] B. J. Lloyd, A. G. Cnossen, and T. J. Siebenmorgen. Evaluation of two methods for separating head rice from brokens for head rice yield determination. *Applied Engineering in Agriculture*, 17(5):643–648, 2001.

[32] R. Y. Tsai. An efficient and accurate camera calibration technique for 3d machine vision. In *Proceedings of IEEE Conference on Computer Vision and Pattern Recognition*, volume 1, pages 364–374. Miami: IEEE, 1986.

[33] A. David and J. Ponce. Computer vision: a modern approach, 2002.

[34] D. C. Brown. Decentering distortion of lenses. *American Society of Photogrammetry, Washington D. C.*, 32(7):444–462, 1966.

[35] J. Heikkila. Geometric camera calibration using circular control points. *IEEE Transactions on Pattern Analysis and Machine Intelligence*, 22(10):1066–1077, 2000.

[36] A. B. Forbes and I. M. Smith. Self-calibration and error separation techniques in metrology. In P. Ciarlini, M. G. Cox, E. Filipe, F. Pavese, and D. Richter, editors, *Advanced Mathematical and Computational Tools in Metrology V*, pages 149–163, Singapore, 2001. World Scientific.

[37] M. Sonka, V. Hlavac, and R. Boyle. *Image Processing, Analysis, and Machine Vision*. International Publishing Inc., 1999.

[38] O. D. Trier and T. Taxt. Evaluation of binarization methods for document images. *IEEE Transactions on Pattern Analysis and Machine Intelligence*, page 312, 1995.

[39] N. Otsu. A thresholding selection method from gray-level histogram. *IEEE transactions on systems, man, and cybernetics*, 9(1):62–66, 1979.

[40] J. Kittler and J. Illingworth. Minimum error thresholding. *Pattern Recognition*, 19(1):41–47, 1986.

[41] Wayne Niblack. *An Introduction to Digital Image Processing*. Prentice-Hall, Inc., Upper Saddle River, NJ, USA, 1990. ISBN 0134806743.

[42] S. D. Yanowitz and A. M. Bruckstein. A new method for image segmentation. *Computer Vision, Graphics, and Image Processing*, 46(1):82–95, 4 1989.

[43] Mehmet Sezgin and Bulent Sankur. Survey over image thresholding techniques and quantitative performance evaluation. *Journal of Electronic Imaging*, 13(1): 146–168, January 2004 2004.

[44] J. Sauvola, T. Seppanen, S. Haapakoski, and M. Pietikainen. Adaptive document binarization. *Document Analysis and Recognition*, 1:147 –152 vol.1, aug. 1997. doi: 10.1109/ICDAR.1997.619831.

[45] Faisal Shafait, Daniel Keysers, and Thomas M. Breuel. Efficient implementation of local adaptive thresholding techniques using integral images. volume 6815, page 681510. SPIE, 2008.

[46] J. Canny. A computational approach to edge detection. *Readings in computer vision: issues, problems, principles, and paradigms*, 184, 1987.

[47] R. M. Haralick and L. G. Shapiro. *Computer and robot vision*. Addison-Wesley Longman Publishing Co., Inc. Boston, MA, USA, 1992.

[48] W. A Yasnoff, J. K. Mui, and J. W. Bacus. Error measures for scene segmentation. *Pattern Recognition*, 9(4):217–231, 1977.

[49] M. Sezgin and B. Sankur. Selection of thresholding methods for nondestructive testing applications. In *Image Processing, 2001. Proceedings. 2001 International Conference on*, volume 3, pages 764–767. IEEE, 2001.

[50] M. P. Dubuisson and A. K. Jain. A modified hausdorff distance for object matching. In *Pattern Recognition, 1994. Vol. 1-Conference A: Computer Vision & Image Processing., Proceedings of the 12th IAPR International Conference on*, volume 1, pages 566–568. IEEE, 2002.

[51] ISO Standard. Bs iso 9276-6:2008: Representation of results of particle size analysis. descriptive and quantitative representation of particle shape and morphology. (1), 2008.

[52] H. G. Merkus. *Particle size measurements: fundamentals, practice, quality*. Springer Verlag, 2008.

[53] C. Washington. *Particle size analysis in pharmaceutics and other industries: theory and practice*. Taylor & Francis, 1992.

[54] L. R. Feret. *Assoc. Internat. pour l'Essai des Mat.*, 2(Group D), 1931.

[55] G. T. Toussaint. Solving geometric problems with the rotating calipers. In *Proc. IEEE Melecon*, volume 83, pages 1–4. Citeseer, 1983.

[56] P. A. Larsen and J. B. Rawlings. Maximum likelihood estimation of particle size distribution for high-aspect-ratio particles using in situ video imaging. *Technometrics*, pages 95–112, 2007.

[57] R. E. Miles. On the elimination of edge effects in planar sampling. *Stochastic Geometry*, pages 228–247, 1974.

[58] W. Wang and J. Paliwal. Separation and identification of touching kernels and dockage components in digital images. *Canadian biosystems engineering*, 48:7, 2006.

[59] N. S. Visen, N. S. Shashidhar, J. Paliwal, and D. S Jayas. Ae-automation and emerging technologies: Identification and segmentation of occluding groups of grain kernels in a grain sample image. *Journal of Agricultural Engineering Research*, 79(2):159–166, 2001.

[60] Q. Zhong, P. Zhou, Q. Yao, and K. Mao. A novel segmentation algorithm for clustered slender-particles. *Computers and Electronics in Agriculture*, 69(2):118–127, 2009.

[61] H. K Mebatsion and J. Paliwal. A fourier analysis based algorithm to separate touching kernels in digital images. *Biosystems Engineering*, 108(1):66–74, 2011.

[62] D. M Hobson, R. M Carter, and Y. Yan. Rule based concave curvature segmentation for touching rice grains in binary digital images. In *Instrumentation and Measurement Technology Conference, 2009. I2MTC'09. IEEE*, pages 1685–1689. IEEE, 2009.

[63] L. Yan, C. W. Park, S. R. Lee, and C. Y. Lee. New separation algorithm for touching grain kernels based on contour segments and ellipse fitting. *Journal of Zhejiang University-Science C*, 12(1):54–61, 2011.

[64] R. W. Scotland and A. H. Wortley. How many species of seed plants are there? *Taxon*, 52(1):101–104, 2003.

[65] R. Govaerts. How many species of seed plants are there? *Taxon*, 50(4):1085–1090, 2001.

[66] J. X. Du, X. F. Wang, and G. J. Zhang. Leaf shape based plant species recognition. *Applied mathematics and computation*, 185(2):883–893, 2007.

[67] Joao Camargo Neto. Plant species identification using elliptic fourier leaf shape analysis. *Computers and Electronics in Agriculture*, 50(2):121–134, 2 2006.

[68] Maria Persson and Bjorn Astrand. Classification of crops and weeds extracted by active shape models. *Biosystems Engineering*, 100(4):484–497, 8 2008.

[69] A. Hong, G. Chen, J. Li, Z. Chi, and D. Zhang. A flower image retrieval method based on roi feature. *Journal of Zhejiang University-Science A*, 5(7):764–772, 2004.

[70] N. Kumar, P. Belhumeur, A. Biswas, D. Jacobs, W. Kress, I. Lopez, and J. Soares. Leafsnap: A computer vision system for automatic plant species identification. *Computer VisionECCV 2012*, pages 502–516, 2012.

[71] C. C. Chen. Improved moment invariants for shape discrimination. *Pattern Recognition*, 26(5):683–686, 1993.

[72] B. V. Dasarathy. Nearest neighbor (NN) norms:NN pattern classification techniques. 1991.

[73] T. Denoeux. A k-nearest neighbor classification rule based on dempster-shafer theory. *Classic Works of the Dempster-Shafer Theory of Belief Functions*, pages 737–760, 2008.

[74] X. F. Wang, J. X. Du, and G. J. Zhang. Recognition of leaf images based on shape features using a hypersphere classifier. *Advances in Intelligent Computing*, pages 87–96, 2005.

[75] Z. Wang, Z. Chi, D. Feng, and Q. Wang. Leaf image retrieval with shape features. *Advances in Visual Information Systems*, pages 41–52, 2000.

[76] Y. Shen, C. Zhou, and K. Lin. Leaf image retrieval using a shape based method. *Artificial Intelligence Applications And Innovations*, pages 711–719, 2005.

[77] Y. Nam and E. Hwang. A shape-based retrieval scheme for leaf images. *Advances in Multimedia Information Processing-PCM 2005*, pages 876–887, 2005.

[78] J. Iivarinen and A. J. E. Visa. Shape recognition of irregular objects. In *Proceedings of SPIE*, volume 2904, page 25, 1996.

[79] A. El-ghazal, O. Basir, and S. Belkasim. Farthest point distance: A new shape signature for fourier descriptors. *Signal Processing: Image Communication*, 24(7): 572–586, 2009.

[80] I. Yahiaoui, N. Herve, and N. Boujemaa. Shape-based image retrieval in botanical collections. *Advances in Multimedia Information Processing-PCM 2006*, pages 357–364, 2006.

[81] S. Belongie, J. Malik, and J. Puzicha. Shape matching and object recognition using shape contexts. *IEEE Transactions on Pattern Analysis and Machine Intelligence*, pages 509–522, 2002.

[82] F. Mokhtarian, S. Abbasi, and J. Kittler. Efficient and robust retrieval by shape content through curvature scale space. *Series on Software Engineering and Knowledge Engineering*, 8:51–58, 1997.

[83] T. F. Cootes and C. J. Taylor. Statistical models of appearance for computer vision. *World Wide Web Publication, February*, 2001.

[84] H. T. Sogaard. Weed classification by active shape models. *Biosystems Engineering*, 91(3):271–281, 7 2005.

[85] André R. Backes and Odemir M. Bruno. Plant leaf identification using multi-scale fractal dimension. In *International Conference On Image Analysis And Processing*, pages 143–150. Springer Berlin / Heidelberg, 2009.

[86] André R. Backes, Wesley N. Gonçalves, Alexandre S. Martinez, and Odemir M. Bruno. Texture analysis and classification using deterministic tourist walk. *Pattern Recognition*, 43:685–694, 2010.

[87] Dalcimar Casanova, Jarbas Joaci de Mesquita Sá Junior, and Odemir M. Bruno. Plant leaf identification using Gabor wavelets. *International Journal of Imaging Systems and Technology*, 19:236–243, 2009.

[88] Jiandu Liu, Shanwen Zhang, and Shengli Deng. A method of plant classification based on wavelet transforms and support vector machines. *Emerging Intelligent Computing Technology and Applications*, 5754:253–260, 2009.

[89] J. Cope, P. Remagnino, S. Barman, and P. Wilkin. Plant texture classification using gabor co-occurrences. *Advances in Visual Computing*, pages 669–677, 2010.

[90] J. G. Daugman. Uncertainty relation for resolution in space, spatial frequency, and orientation optimized by two-dimensional visual cortical filters. *Optical Society of America, Journal, A: Optics and Image Science*, 2(7):1160–1169, 1985.

[91] Elio Ramos and Denny S. Fernandez. Classification of leaf epidermis microphotographs using texture features. *Ecological Informatics*, 4:177–181, 2009.

[92] André R. Backes, Jarbas Joac de Mesquita Sá Junior, Rosana M. Kolb, and Odemir M. Bruno. Plant species identification using multi-scale fractal dimension applied to images of adaxial surface epidermis. *Computer Analysis Of Images And Patterns*, 5702:680–688, 2009.

[93] Tracy McLellan and John A. Endler. The relative success of some methods for measuring and describing the shape of complex objects. *Systematic Biology*, 47: 264–281, 1998.

[94] J. S. Cope, D. Corney, J. Y. Clark, P. Remagnino, and P. Wilkin. Plant species identification using digital morphometrics: A review. *Expert Systems with Applications*, 39(8):7562–7573, 2012.

[95] T. Beghin, J. Cope, P. Remagnino, and S. Barman. Shape and texture based plant leaf classification. In *Advanced Concepts for Intelligent Vision Systems*, pages 345–353. Springer, 2010.

[96] Navneet Dalal and Bill Triggs. Histograms of oriented gradients for human detection. In *Computer Vision and Pattern Recognition, 2005. CVPR 2005. IEEE Computer Society Conference on*, volume 1, pages 886–893. IEEE, 2005.

[97] K. Q. Weinberger and L. K. Saul. Distance metric learning for large margin nearest neighbor classification. *The Journal of Machine Learning Research*, 10:207–244, 2009.

[98] W. J. Hwang and K. W. Wen. Fast knn classification algorithm based on partial distance search. *Electronics Letters*, 34(21):2062–2063, 1998.

[99] T. M. Cover, J. A. Thomas, and J. Wiley. *Elements of information theory*, volume 6. Wiley Online Library, 1991.

[100] K. Fukunaga and L. Hostetler. K-nearest-neighbor bayes-risk estimation. *Information Theory, IEEE Transactions on*, 21(3):285–293, 1975.

[101] A. F. Atiya. Estimating the posterior probabilities using the k-nearest neighbor rule. *Neural computation*, 17(3):731–740, 2005.

[102] A. K. Jain, R. P. W. Duin, and J. Mao. Statistical pattern recognition: A review. *Pattern Analysis and Machine Intelligence, IEEE Transactions on*, 22(1):4–37, 2000.

[103] J. P. Hoffbeck and D. A. Landgrebe. Covariance matrix estimation and classification with limited training data. *Pattern Analysis and Machine Intelligence, IEEE Transactions on*, 18(7):763–767, 1996.

[104] R. O. Duda and P. E. Hart. Pattern recognition and scene analysis. 1973.

[105] T. K. Moon. The expectation-maximization algorithm. *Signal Processing Magazine, IEEE*, 13(6):47–60, 1996.

[106] A. W. Bowman. A comparative study of some kernel-based nonparametric density estimators. *Journal of Statistical Computation and Simulation*, 21(3-4):313–327, 1985.

[107] J. N. Hwang, S. R. Lay, and A. Lippman. Nonparametric multivariate density estimation: a comparative study. *Signal Processing, IEEE Transactions on*, 42 (10):2795–2810, 1994.

[108] Tadhg Brosnan and Da-Wen Sun. Improving quality inspection of food products by computer visiona review. *Journal of Food Engineering*, 61(1):3–16, 1 2004.

[109] L. G. Shapiro and G. C. Stockman. *Computer Vision*. Prentence Hall, 2001.

[110] David G. Kleinbaum, Lawrence L. Kupper, Keith E. Muller, and Azhar Nizam. *Applied regression analysis and multivariable methods*. Duxbury Press 3rd Ed. Pacific Grove, 1998.

[111] Thomas Funkhouser. Image quantization, halftoning, and dithering. *Princeton University.¡ http://www. cs. princeton. edu/courses/archive/-fall99/cs426/lectures/dither/index. htm*, 2000.

[112] Paula M. Davis. Statistics for describing populations. *Handbook of sampling methods for arthropods in agriculture*, pages 33–54, 1994.

[113] E. A. Heinrichs and H. R. Rapusas. Levels of resistance to the whitebacked planthopper, sogatella furcifera (homoptera: Delphacidae), in rice varieties with different resistance genes. *Environmental entomology*, 12(6):1793–1797, 1983.

[114] W. H. Press, S. A. Teukolsky, W. T. Vetterling, and B. P. Flannery. *Numerical Recipes with Source Code CD-ROM 3rd Edition: The Art of Scientific Computing*. Cambridge University Press, 2007.

[115] W. S. Zheng, S. Gong, and T. Xiang. Person re-identification by probabilistic relative distance comparison. In *Computer Vision and Pattern Recognition (CVPR), 2011 IEEE Conference on*, pages 649–656. IEEE, 2011.

[116] R. A. Fisher. The use of multiple measurements in taxonomic problems. *Annals of Human Genetics*, 7(2):179–188, 1936.

[117] H. A. Guvenir and A. Akkus. Weighted k nearest neighbor classification on feature projections 1. 1997.

[118] P. Kulczycki and M. Charytanowicz. A complete gradient clustering algorithm. *Artificial Intelligence and Computational Intelligence*, pages 497–504, 2011.

[119] Charles Mallah, James Cope, and James Orwell. Plant leaf classification using probabilistic integration of shape, texture and margin features. *Signal Processing, Pattern Recognition and Applications*, 2013.